

CONTROLLED SYNTHESIS AND CHARACTERIZATION OF MAGNETIC  
CHALCOSPINELS NANOCRYSTALS

by

FARHAD AKBARI AFKHAMI

ARUNAVA GUPTA, COMMITTEE CHAIR  
GREROGY SZULCZEWSKI  
SHANLIN PAN  
JARED ALLRED  
GARY MANKEY

A DISSERTATION

Submitted in partial fulfillment of the requirements  
for the degree of Doctor of Philosophy  
in the Department of Chemistry  
in the Graduate School of  
The University of Alabama

TUSCALOOSA, ALABAMA

2020



## ABSTRACT

Binary and ternary metal chalcogenides have become well-known materials among chemists, physicists, material scientists, and other researchers of the field, and they have attracted significant attention because of their novel chemical, magnetic, electronic, mechanical and optical properties. Among the metal chalcogenides, chromium-based chalcospinels  $ACr_2X_4$  ( $A = Cu, Co, Fe, Cd, \text{ and } Hg$ ;  $X = S, Se, \text{ and } Te$ ) have gained significant attention because they are a notable class of magnetic materials such as semiconductors, magnetic metals, and insulators.

In this work, a general overview of binary and ternary metal chalcogenides and their nanocrystals has been provided. We have also provided an overview of the wet-chemical colloidal methods as an important approach to size and shape-controlled synthesis of nanocrystals. We have also discussed the importance of metal doping reactions as a pathway to create previously unavailable multielemental materials for high-performance applications. In this set of studies, colloidal nanocrystals of chromium-based chalcospinels of  $CuCr_2S_4$  and  $CuCr_2Se_4$  have been synthesized via hot-injection and heat-up methods and were characterized using experimental methodology comprised of different microstructural and structural tests.

The magnetic properties of these nanocrystals have also been studied. The next studied system was Cr-doped pyrite  $CuSe_2$  nanocrystals, eventually leading to the observation of significant enhancement of ferromagnetic moment by Cr-doping in octahedral sites of the pyrite structure. We performed a unique reaction in which nanocrystals of  $Cr_xCu_{1-x}Se_2$  ( $x = 0.1-0.5$ ) formed in the pyrite phase, which is not stable in bulk form. The host  $p-CuSe_2$  nanocubes did

also undergo a degradation influenced by the reaction temperature and the doping of  $\text{Cr}^{3+}$  ions in the pyrite crystal structure.

The Cr-doped nanocrystals of the pyrite phase were formed during the heat-up procedure and by increasing the reaction temperature transformed to  $\text{CuCr}_2\text{Se}_4$  spinel nanocrystals. To the best of our knowledge, no cationic substitution of chromium for copper has been reported on pyrite  $\text{CuSe}_2$  systems so far, likely due to the significant size difference between chromium and copper. Therefore, the results of this work are a powerful approach for the design and fabrication of new multielemental materials that may not be stable in the bulk form.

## DEDICATION

Dedicated to my beloved family. Their love and support helped me get through the difficult times in graduate school.

## LIST OF ABBREVIATIONS AND SYMBOLS

XRD	X-ray diffraction
TEM	Transmission electron microscopy
HRTEM	High-resolution transmission electron microscopy
HADDF	High-angle annular dark-field
STEM	Scanning transmission electron microscopy
EELS	Electron energy loss spectroscopy
EDS	Energy-dispersive X-ray spectroscopy
SAED	Selected area electron diffraction
SAD	Selected area diffraction
DP	Diffraction pattern
FEG	Field-emission electron gun
SEM	Scanning electron microscopy
SE	Secondary electron
BSE	Backscattered electron
XPS	X-Ray photoelectron spectroscopy

CCD	Charged coupled device
TGA	Thermal gravimetric analyses
UV	Ultraviolet
NIR	Near-infrared
PPMS	Physical properties measurement system
VSM	Vibrating sample magnetometer
$d$	Interplanar spacing
$\theta$	Bragg angle
$\lambda$	Wavelength
$n$	Integer
V	Volt
eV	Electron-volt
A	Ampere
$E_K$	Kinetic energy
$E_B$	Binding energy
$\phi$	Work function
P	Pressure
$^{\circ}\text{C}$	Celsius

K	Kelvin
g	Gram
ml	Milliliter
mol	Number of moles
M	Magnetization
M <sub>S</sub>	Saturation magnetization
SP	Superparamagnetism
Oe	Oersted
T <sub>C</sub>	Curie temperature
T <sub>b</sub>	Blocking temperature
GPA	Giga pascal
NC	Nanocrystal
NP	Nanoparticle
ND	Nanodisk
NR	Nanorod
HU	Heat-Up
HI	Hot-Injection
TMC	Transition metal chalcogenide

Å	Angstrom
nm	Nanometer
µm	Micrometer
OA	Oleic acid
OLA	Oleylamine
ODA	Octadecylamine
DDA	Dodecylamine
DDT	Dodecanethiol
1-DDT	1-Dodecanethiol
DDTC	Diethyldithiocarbamate
DMDTC	Dimethyldithiocarbamate
(TMS) <sub>2</sub> S	Bis(trimethylsilyl)sulphide
TOP	Tri-n-octylphosphine
TOPO	Tri-n-octylphosphine oxide
TOPh	Trioctylphosphite
ODE	1-Octadecene
TPP	Triphenylphosphine
TOAB	Tetraoctylammonium bromide

TEG	Triethylene glycol
TETA	Triethylenetetramine
HMDS	Hexamethyldisilazine
OE	Octyl ether
PVP	Polyvinylpyrrolidone
acac	Acetylacetonate
ac	Acetate
1D	One-dimension
2D	Two-dimension
HAD	Hexadecylamine
DBTU	N,N-di-n-butylthiourea
OctA	Octanoic acid
Pfn	Paraffin oil
MBTS	2,2-Dithiobisbenzothiazole
MA	Myristic acid
DOPO	Dioctylphosphine oxide
TBP	Tributylphosphine
EG	Ethylene glycol

DPP	Diphenylphosphine
DBE	Dibenzyl ether
QD	Quantum dot
O <sub>h</sub>	Octahedral
T <sub>d</sub>	Tetrahedral
fcc	Face-centered cubic
ICDD	International center of diffraction data
T	Temperature
%	Percentage
<i>p</i>	Pyrite
<i>m</i>	Marcasite

## ACKNOWLEDGEMENTS

I would like to take this opportunity to express my gratitude to all the remarkable individuals who assisted me with this research project. First and foremost, I would like to thank my advisor, Professor Arunava Gupta, for his outstanding management and leadership during all the years I was involved in this set of studies. Heartfelt gratitude to Prof. Gupta for believing in me and helping me to think critically and work independently towards problems. My gratitude also goes to Professor Jared Allred for the discussions throughout my Ph.D. study. I am highly indebted to Jared.

I am also grateful for my dissertation committee members, Professor Gregory Szulczewski, Professor Shanlin Pan, Professor Jared Allred, and Professor Gary Mankey for the time and effort they put into considering my dissertation and giving me valuable input and encouragement.

Next, I would like to thank our colleagues in the University of Alabama, Tyra Douglas, and Professor Jared Allred, and also our colleagues in the Washington University in St. Louis and Oak Ridge National Laboratory, led by Professor Rohan Mishra, whose collaboration was indispensable in the culmination of our project.

My thanks also go to my teammates, fellow lab members, and technical staff at the University of Alabama, whose help was essential in my progress toward finishing this dissertation.

This research would have been impossible without the unwavering support of my family. My wife, Elham, my son, Rayan, my father, Jafar, my mother, Shahla, and my brother, Saeed, always encouraged me in the challenging times to take one step further when the path became even more demanding. They are always in my heart, and I am eternally grateful to them. Without them, this dissertation could not have been realized.

Last but not least, I thank the Department of Chemistry and Biochemistry of the University of Alabama and the faculty members for the support they gave me all these years.

## CONTENTS

ABSTRACT.....	ii
DEDICATION.....	iv
LIST OF ABBREVIATIONS AND SYMBOLS .....	v
ACKNOWLEDGEMENTS.....	xi
LIST OF TABLES .....	xviii
LIST OF FIGURES .....	xx
LIST OF SCHEMES.....	xxviii
CHAPTER 1: INTRODUCTION.....	1
1.1 Colloidal Nanocrystals.....	1
1.2 Size and Shape Control of Colloidal NCs through HU and HI Methods .....	3
1.2.1 Kinetic Size and Shape Control.....	5
1.2.2 Capping Ligands .....	8
1.2.2.1 Oleylamine (OLA) and Octadecylamine (ODA).....	10
1.2.3 Precursors.....	11
1.2.3.1 Single-Source Precursors .....	14
1.3 Metal Chalcogenides.....	15
1.3.1 Binary Metal Chalcogenide NCs .....	16

1.3.2 Ternary and Quaternary Metal Chalcogenide NCs.....	19
1.3.3 Magnetic Metal Chalcogenides.....	23
1.4 Research Objectives and Thesis Organization.....	25
1.5 References.....	26
CHAPTER 2: EXPERIMENTAL METHODS .....	35
2.1 Synthesis of NCs.....	35
2.2 X-ray Diffraction Analyses.....	36
2.3 Electron Microscopy Methods.....	38
2.4 X-ray Photoelectron Spectroscopy (XPS) .....	43
2.5 Raman Spectroscopy.....	44
2.6 Magnetic Measurements .....	45
2.7 References.....	48
CHAPTER 3: Cr-INDUCED SYNTHESIS OF PYRITE $\text{Cr}_x\text{Cu}_{1-x}\text{Se}_2$ NANOCRYSTALS, ( $0 \leq x \leq 0.5$ ).....	49
3.1 Abstract.....	49
3.2. Introduction.....	49
3.2.1 Colloidal nanocrystals of Pyrite $\text{CuSe}_2$ .....	49
3.3 Experimental.....	53
3.4 Results and Discussion .....	55
3.4.1 Formation of the $\text{Cr}_x\text{Cu}_{1-x}\text{Se}_2$ NCs.....	56

3.4.2 Morphological Evolution .....	58
3.4.3 Understanding the formation mechanism of $\text{Cr}_x\text{Cu}_{1-x}\text{Se}_2$ .....	74
3.4.4 Magnetic Properties of $\text{Cr}_x\text{Cu}_{1-x}\text{Se}_2$ NCs; Cr-Induced Large Enhancement of Ferromagnetic Moment .....	80
3.5 Conclusion .....	83
3.6 References .....	84
<b>CHAPTER 4: TRANSFORMATION FROM PYRITE <math>\text{CuSe}_2</math> TO SPINEL <math>\text{CuCr}_2\text{Se}_4</math> NANOCRYSTALS</b> .....	<b>89</b>
4.1 Abstract .....	89
4.2 Introduction .....	89
4.2.1 Colloidal Nanocrystals of Spinel $\text{CuCr}_2\text{Se}_4$ .....	89
4.3 Magnetic Properties of the $\text{CuCr}_2\text{Se}_4$ NCs .....	92
4.4 Formation of $\text{CuCr}_2\text{Se}_4$ via Phase Transformation .....	94
4.5 Understanding the Mechanistic Details of Pyrite to Spinel Phase Transformation; Increasing Chromium Content versus Decreasing Copper and Selenium Contents .....	111
4.6 Phase Transformation and Raman Spectroscopy .....	114
4.7 Magnetic Properties of Spinel $\text{CuCr}_2\text{Se}_4$ NCs .....	115
4.8 Heat-Up versus Hot-Injection .....	116
4.9 Conclusion .....	117
4.10 References .....	119
<b>CHAPTER 5: CONTROLLED SYNTHESIS OF MAGNETIC <math>\text{CuCr}_2\text{S}_4</math> CHALCOSPINEL NANOCRYSTALS USING SINGLE SOURCE PRECURSORS</b> .....	<b>121</b>

5.1 Abstract .....	121
5.2 Introduction .....	122
5.2.1 Colloidal Nanocrystals of Spinel $\text{CuCr}_2\text{S}_4$ .....	122
5.2.2 Magnetic Properties of $\text{CuCr}_2\text{S}_4$ NCs .....	126
5.3 Synthesis and Characterization of $\text{CuCr}_2\text{S}_4$ NCs Using Single Source Precursors ...	128
5.3.1 Synthesis of the Precursors .....	128
5.3.2 Synthesis of NCs.....	130
5.4 Influence of the Reaction Parameters on the Formation of the Nanoparticles .....	130
5.4.1 Reaction Temperature .....	130
5.4.2 Reaction Time .....	135
5.4.3 Sulfur Source and Capping Agent .....	136
5.4.4 Synthesis Method; HU versus HI .....	139
5.4.5 Precursors.....	140
5.5 Stabilization of the Sulfur Rich Phase by Annealing.....	146
5.6 Magnetic Measurements .....	148
5.7 Conclusion .....	149
5.8 References.....	151
CHAPTER 6: CONCLUSION .....	153
6.1 Summary .....	153

6.2 Outlook .....	155
REFERENCES .....	156

## LIST OF TABLES

Table 1.1: A series of colloidal binary TMCs NCs prepared via HU and HI methods .....	18
Table 1.2: A series of colloidal ternary and quaternary TMCs NCs prepared via HU and HI methods .....	22
Table 3.1: Summary of the performed reactions and the effect of reagents concentration and reaction temperature on the composition and phase of $\text{Cr}_x\text{Cu}_{1-x}\text{Se}_2$ nanocrystals .....	65
Table 3.2: Elemental composition of the $\text{Cr}_x\text{Cu}_{1-x}\text{Se}_2$ NCs measured by EDS.....	66
Table 3.3: Extracted parameters from Curie-Weiß plots .....	82
Table 4.1: Reaction condition, morphology, size and saturation magnetization for NCs of $\text{CuCr}_2\text{Se}_4$ made by HI method .....	94
Table 4.2: Elemental composition of the $\text{Cu}_{1-x}\text{Cr}_x\text{Se}_2$ NCs measured by EDS.....	98
Table 4.3: Elemental composition of the nanocubes of $\text{Cr}_{0.5}\text{Cu}_{0.5}\text{Se}_2$ and nanoneedles of $\text{CuCr}_2\text{Se}_4$ measured by EDS .....	103
Table 4.4: Elemental composition of the nanorings of (a) $\text{CuCr}_{1.7}\text{Se}_4$ and (b) $\text{CuCr}_{1.4}\text{Se}_4$ measured by EDS.....	109
Table 4.5: EDS analyses of the selected points on the hollow ring (a) in figure 4.19, indicating a variety of chemical compositions in the range of $\text{Cr}_{0.5}\text{Cu}_{0.5}\text{Se}_2$ to $\text{Cu}_{0.5}\text{CrSe}_2$ ( $\text{CuCr}_2\text{Se}_4$ ).....	109
Table 4.6: EDS analyses of the selected points on the hollow ring (b) in figure 4.19, indicating a variety of chemical compositions in the range of $\text{Cr}_{0.5}\text{Cu}_{0.5}\text{Se}_2$ to $\text{Cu}_{0.5}\text{CrSe}_2$ ( $\text{CuCr}_2\text{Se}_4$ ).....	109

Table 4.7: EDS analyses of the selected points on the nanoneedles in selected areas in figure 4.21, indicating a variety of chemical compositions in the range of  $\text{Cr}_{0.5}\text{Cu}_{0.5}\text{Se}_2$  to  $\text{Cu}_{0.5}\text{CrSe}_2$  ( $\text{CuCr}_2\text{Se}_4$ ) .....111

Table 5.1: Elemental composition of the  $\text{CuCr}_2\text{S}_4$  nanocubes measured by EDS .....142

Table 5.2: Elemental composition of the spectra 1-3 .....144

## LIST OF FIGURES

Figure 1.1: Schematic diagram of the nucleation and growth stages the formation of colloidal NCs .....	4
Figure 1.2: Diagram of the growth rate versus radius. Depiction of two different modes of NCs growth process, ‘focusing’ and ‘defocusing’ related to the concentration of monomers .....	6
Figure 1.3: Kinetic shape control at (a) high rate of crystal growth and (b) through selective adhesion causes to the formation of nanorods and nanodisks .....	7
Figure 1.4: Schematic depiction of the surface of a spherical nanoparticle with commonly used hydrophilic capping ligands. Left to right: TOPO, TPP, DDT, TOAB, and OA .....	10
Figure 1.5: Effect of halide ions on the formation of 2D morphologies and influence of TOPO surfactant on the size distribution of $\text{Cu}_{2-x}\text{S}$ NCs .....	13
Figure 1.6: Influence of alkylammonium chlorides on the shape of $\text{Cu}_{2-x}\text{S}$ nanocrystals .....	13
Figure 1.7: Schematic synthesis pathway of metal sulfide NCs by thermal decomposition of metal-DDTC precursors .....	15
Figure 1.8: Spinel Crystal Structure.....	24
Figure 2.1: Experimental setup for colloidal synthesis of NCs .....	36
Figure 2.2: Schematic representation of the X-ray diffraction mechanism .....	38
Figure 2.3: Schematic representation of the X-ray diffractometer .....	38
Figure 2.4: Schematic diagram TEM.....	39
Figure 2.5: Schematic diagram of (a) diffraction mode and (b) image mode in TEM .....	41

Figure 2.6: Schematic diagram SEM .....	42
Figure 2.7: Schematic view of XPS system.....	44
Figure 2.8: A schematic representation of Raman spectroscopy system.....	45
Figure 2.9: Schematic depiction of VSM system .....	46
Figure 2.10: Schematic diagram of the sample measurement in PPMS .....	47
Figure 3.1: Pyrite crystal structure representing octahedral position of the metal cations and anion dimers.....	50
Figure 3.2: Octahedral nanoparticles of <i>p</i> -CuSe <sub>2</sub> synthesized with (a) TETA assisted HU method .....	51
Figure 3.3: Preparation process of HU synthesis of copper selenide crystals .....	52
Figure 3.4: XRD patterns of the Cr <sub>x</sub> Cu <sub>1-x</sub> Se <sub>2</sub> NCs formed in the temperature range of 250-300 °C .....	56
Figure 3.5: XRD patterns of the NCs synthesized at solution temperatures of 220, 240, and 250 °C indicating the formation of mixed pyrite and marcasite CuSe <sub>2</sub> phases at the temperatures below 250 °C.....	57
Figure 3.6: XRD patterns of NCs prepared in the absence of chromium indicating the formation of mixed-phase of <i>p</i> -CuSe <sub>2</sub> , <i>m</i> -CuSe <sub>2</sub> , CuSe, and some other impurities.....	58
Figure 3.7: Low-resolution TEM, high-resolution TEM (HRTEM) images and selected area diffraction (SAED) pattern of the isolated pristine nanocubes of <i>p</i> -CuSe <sub>2</sub> formed in the absence of chromium precursor .....	59
Figure 3.8: Morphological Degradation of Cr <sub>x</sub> Cu <sub>1-x</sub> Se <sub>2</sub> NCs as a function of reaction temperature and Cr-contents.....	61
Figure 3.9: HRTEM image of NCs of Cr <sub>0.3</sub> Cu <sub>0.7</sub> Se <sub>2</sub> that was formed at 250 °C confirming that the degradation starts from the edges of the cubes .....	61

Figure 3.10: HAADF-, EDS-STEM imaging, and EDS-diagram of $\text{Cr}_{0.1}\text{Cu}_{0.9}\text{Se}_2$ nanocubes formed at 220 °C .....	62
Figure 3.11: HAADF-, EDS-STEM imaging, and EDS-diagram of deformed nanocubes of $\text{Cr}_{0.3}\text{Cu}_{0.7}\text{Se}_2$ formed at 250 °C .....	63
Figure 3.12: HAADF-, EDS-STEM imaging, and EDS-diagram of nanoneedles of $\text{Cr}_{0.5}\text{Cu}_{0.5}\text{Se}_2$ formed at 300 °C .....	64
Figure 3.13: Wide field-of-view and atomic resolution HAADF images of $\text{Cr}_{0.3}\text{Cu}_{0.7}\text{Se}_2$ NCs along [001] with a part of the image superimposed with pyrite crystal structure.....	67
Figure 3.14: Wide field-of-view and atomic resolution HAADF images of $\text{Cr}_{0.3}\text{Cu}_{0.7}\text{Se}_2$ NCs along (a) [111], (b) $[\bar{2}11]$ , and (c) [120].....	68
Figure 3.15: (a) Atomic resolution HAADF image of $\text{Cr}_{0.3}\text{Cu}_{0.7}\text{Se}_2$ NCs along $[\bar{2}11]$ .....	69
Figure 3.16: TEM images of (a) $\text{Cr}_{0.1}\text{Cu}_{0.9}\text{Se}_2$ , (b) $\text{Cr}_{0.2}\text{Cu}_{0.8}\text{Se}_2$ , (c) $\text{Cr}_{0.3}\text{Cu}_{0.7}\text{Se}_2$ , (d) $\text{Cr}_{0.4}\text{Cu}_{0.6}\text{Se}_2$ , and (e) $\text{Cr}_{0.5}\text{Cu}_{0.5}\text{Se}_2$ NCs illustrating the disintegration process as a function of reaction temperature and Cr-content.....	70
Figure 3.17: TEM and HAADF-STEM images and SAED patterns (inset) of the NCs of $\text{Cr}_{0.1}\text{Cu}_{0.9}\text{Se}_2$ formed at 250 °C using only 0.1 mmol of Cr-precursor.....	71
Figure 3.18: XRD pattern of (a) $\text{Cr}_{0.3}\text{Cu}_{0.7}\text{Se}_2$ , (b) $\text{Cr}_{0.4}\text{Cu}_{0.6}\text{Se}_2$ , and (c) $\text{Cr}_{0.5}\text{Cu}_{0.5}\text{Se}_2$ NCs confirmed by the Rietveld refinement analysis to be in good agreement with the proposed pyrite model .....	73
Figure 3.19: Analysis of the oxidation state of Cu. XPS diagrams of $\text{Cr}_{0.4}\text{Cu}_{0.6}\text{Se}_2$ and $\text{Cr}_{0.5}\text{Cu}_{0.5}\text{Se}_2$ NCs.....	76
Figure 3.20: XPS spectra of Cr 2p and Se 3d of the $\text{Cr}_{0.4}\text{Cu}_{0.6}\text{Se}_2$ nanocrystals .....	77
Figure 3.21: EELS data acquired for the region highlighted (white box) in the HAADF image of pyrite NCs showing the presence of Cr, Cu, and Se.....	78

Figure 3.22: Comparing of (a) EELS fine structure of  $\text{Cu}_{0.45}\text{TaS}_2$  with (b)  $\text{Cu}^0$  and (c)  $\text{Cu}^{2+}$  spectra from ref. 57. The nearly sharp  $L_3$  edge in (a) is similar to  $\text{Cu}^{2+}$  .....79

Figure 3.23: EELS fine structure plots for  $\text{Cu}_{2.34}\text{GaSe}$  and  $\text{Cu}_{2.14}\text{In}_2\text{Se}_3$  along with reference plots for  $\text{Cu}^{2+}$ ,  $\text{Cu}^+$ , and  $\text{Cu}$ , confirming the zero-valent identity of the intercalated copper .....79

Figure 3.24: (a) Magnetization ( $M$ ) versus temperature ( $K$ ) measurements on  $\text{Cr}_{0.3}\text{Cu}_{0.7}\text{Se}_2$ , and  $\text{Cr}_{0.5}\text{Cu}_{0.5}\text{Se}_2$  NCs with applied field of 10 kOe (1 T). The same is shown for  $\text{CuSe}_2$  in inset, (b) Curie-Weiß plots for NCs of  $\text{Cr}_{0.3}\text{Cu}_{0.7}\text{Se}_2$  and  $\text{Cr}_{0.5}\text{Cu}_{0.5}\text{Se}_2$ , and (c) Magnetization ( $M$ ) versus magnetic field ( $H$ ) measurements on NCs of  $\text{Cr}_{0.3}\text{Cu}_{0.7}\text{Se}_2$  and  $\text{Cr}_{0.5}\text{Cu}_{0.5}\text{Se}_2$  at 1.8 K .....82

Figure 4.1: TEM images of nanocubes of  $\text{CuCr}_2\text{Se}_4$  .....90

Figure 4.2: (a) TEM image, (b,c) HRTEM, and (d) XRD pattern of the anisotropic NCs of  $\text{CuCr}_2\text{Se}_4$ , and (e) reaction pathway of formation of the nanocrystals .....91

Figure 4.3: (a) TEM and (b) HRTEM images of  $\text{CuCr}_2\text{Se}_4$  nanoparticles prepared from metal chloride precursors .....91

Figure 4.4: Magnetization ( $M$ ) as a function of external field ( $H$ ) at (a) 300 K and (b) 10 K for the 15 nm and 25 nm nanocubes of  $\text{CuCr}_2\text{Se}_4$  .....93

Figure 4.5: Magnetization ( $M$ ) as a function of external field ( $H$ ) for (a) NCs of  $\text{CuCr}_2\text{Se}_4$  with the average size of 20 nm reported by Pang et al., and (b) NCs of  $\text{CuCr}_2\text{Se}_4$  (green) with the average size of 10 nm reported by Ramasamy et al. ....93

Figure 4.6: XRD patterns of the  $\text{CuCr}_2\text{Se}_4$  nanoparticles formed at the range of 330-360 °C .....95

Figure 4.7: TEM images of the spinel  $\text{CuCr}_2\text{Se}_4$  nanorods prepared at (a) 360 °C and (b) 330 °C .....96

Figure 4.8: HRTEM and selected area diffraction (SAED) pattern of  $\text{CuCr}_2\text{Se}_4$  NCs The zone axis of the SAED pattern is in [111] direction .....96

Figure 4.9: HAADF-, EDS-STEM imaging, and EDS-diagram of nanorods of  $\text{CuCr}_2\text{Se}_4$

formed at 330 °C .....	97
Figure 4.10: Characterization of $\text{Cr}_{0.5}\text{Cu}_{0.5}\text{Se}_2/\text{CuCr}_2\text{Se}_4$ composites showing a decrease in the intensity of the pyrite phase peaks and increase on the intensity of spinel phase peaks by increasing the reaction temperature .....	99
Figure 4.11: The effect of reaction time on the composition of the NCs produced at 320 °C ....	100
Figure 4.12: TEM images of the NCs formed at 320 °C indicating deformed nanocubes and nanoneedles.....	101
Figure 4.13: TEM images of the hollow nanorings formed at 320 °C .....	101
Figure 4.14: HRTEM images of the hallow nanorings.....	102
Figure 4.15: Wide field-of-view and atomic resolution HAADF images of spinel $\text{CuCr}_2\text{Se}_4$ nanoneedles. In some atomic columns, it is possible to see all three atomic columns.....	102
Figure 4.16: HAADF-STEM, EDS-STEM images, SAED pattern, and EDS-diagram of the deformed nanocubes of $\text{Cr}_{0.5}\text{Cu}_{0.5}\text{Se}_2$ .....	104
Figure 4.17: HAADF-STEM, EDS-STEM images SAED pattern, and EDS-diagram of the deformed nanocubes of nanoneedles of $\text{CuCr}_2\text{Se}_4$ .....	105
Figure 4.18: HAADF-, EDS-STEM imaging, and EDS-diagram of hollow nanorings with the average chemical compositions of (a) $\text{CuCr}_{1.7}\text{Se}_4$ and (b) $\text{CuCr}_{1.4}\text{Se}_4$ .....	107
Figure 4.19: HAADF-STEM images of hollow nanorings formed via Kirkendall effect and randomly selected points for EDS analysis .....	108
Figure 4.20: SAED patterns extracted from a hollow nanoring (a,d) representing (b) spinel, (c) pyrite, and (e,f) multi-domain phases in the selected area .....	108
Figure 4.21: HAADF-STEM image of nanoneedles formed at 320 °C, and randomly selected points for EDS analysis.....	110
Figure 4.22: Phase transformation mechanism probed via HRTEM imaging.....	112

Figure 4.23: Raman Spectra of the NCs formed at 300, 310, and 330 °C, confirming the pyrite to spinel phase transformation by increasing the reaction temperature.....	115
Figure 4.24: Magnetization ( $M$ ) as a function of external field ( $H$ ) diagram at 300 K and 5 K for NCs of $\text{CuCr}_2\text{Se}_4$ , prepared by HU method at 360 °C .....	116
Figure 4.25: TEM images of triangular and hexagonal NCs of $\text{CuCr}_2\text{Se}_4$ made by HI method .....	117
Figure 5.1: The XRD patterns of (a) nanocubes and (b) nanoneedles of $\text{CuCr}_2\text{S}_4$ .....	124
Figure 5.2: The XRD pattern of the NCs prepared at 340 °C indicating the formation of the secondary phase of $\text{CuCrS}_2$ as impurity.....	125
Figure 5.3: TEM, HRTEM images, and FFT pattern of the nanocubes of $\text{CuCr}_2\text{S}_4$ formed in the presence of ODA.....	126
Figure 5.4: TEM and HRTEM images of the nanoclusters of $\text{CuCr}_2\text{S}_4$ formed in the presence of OLA .....	126
Figure 5.5: Magnetization ( $M$ ) as a function of temperature ( $T$ ) for (a) nanocubes and (b) nanoclusters and (c) as a function of field ( $H$ ) at (c) 300 K and (d) 5 K .....	127
Figure 5.6: The molecular structures of (a) $\text{Cu}(\text{DDTC})_2$ , and (b) $\text{Cr}(\text{DDTC})_3$ .....	128
Figure 5.7: XRD patterns of the layered $\text{CuCrS}_2$ nanoparticles formed at the temperature range of 310-330 °C (ICDD No. 23-0952) .....	131
Figure 5.8: XRD patterns of the prepared particles at (a) 340, and (b) 350 °C. The relative intensity of the $\text{CuCrS}_2$ peaks decreases by increasing the reaction temperature.....	133
Figure 5.9: XRD pattern of NCs synthesized at 360 °C .....	134
Figure 5.10: TEM images of $\text{CuCr}_2\text{S}_4$ nanocubes made by $\text{Cu}(\text{DDTC})_2$ and ODA as capping agent.....	135

Figure 5.11: Effect of reaction time on the formation of $\text{CuCr}_2\text{S}_4$ NCs. The XRD patterns of the NCs formed after (a) 15 min, (b) 30 min, (c) 45 min, and (d) 60 min .....	136
Figure 5.12: XRD pattern of the $\text{CuCr}_2\text{S}_4$ NCs prepared by using tert-DDT instead of 1-DDT .....	137
Figure 5.13: TEM images of $\text{CuCr}_2\text{S}_4$ nanoclusters made by $\text{Cu}(\text{DDTC})_2$ and OLA as capping agent .....	138
Figure 5.14: XRD pattern of the nanoparticles prepared by HU method indicating the formation of $\text{CuCrS}_2$ and sulfur along with $\text{CuCr}_2\text{S}_4$ phase .....	139
Figure 5.15: XRD patterns of the nanoparticles made by $\text{Cu}(\text{DMDTC})_2$ in the presence of (a) OLA, and (b) ODA, indicating the mixed phase of magnetic and nonmagnetic phases .....	140
Figure 5.16: XRD pattern of the $\text{CuCr}_2\text{S}_4$ NCs prepared by $\text{Cu}(\text{DDTC})_2$ and $\text{Cr}(\text{DDTC})_3$ single-source precursors.....	141
Figure 5.17: TEM images of $\text{CuCr}_2\text{S}_4$ nanocubes with the average size range of 20-30 nm made using $\text{Cu}(\text{DDTC})_2$ and $\text{Cr}(\text{DDTC})_3$ precursors and ODA.....	141
Figure 5.18: HRTEM image of the $\text{CuCr}_2\text{S}_4$ nanocubes.....	142
Figure 5.19: HAADF-, EDS-STEM imaging, and EDS-diagram of $\text{CuCr}_2\text{S}_4$ nanocubes.....	143
Figure 5.20: SEM image of $\text{CuCr}_2\text{S}_4$ nanocubes .....	144
Figure 5.21: SEM-EDS diagram of spectra 1-3 .....	145
Scheme 5.3: Depiction of annealing process of $\text{CuCr}_2\text{S}_4$ NCs under the atmosphere of sulfur vapor .....	146
Figure 5.22: XRD patterns of the as-synthesized colloidal (black) and annealed (red) $\text{CuCr}_2\text{S}_4$ NCs under the atmosphere of sulfur vapor .....	147

Figure 5.23: TEM images of annealed $\text{CuCr}_2\text{S}_4$ NCs .....	148
Figure 5.24: Magnetization ( $M$ ) as a function of field ( $H$ ) for nanocubes of $\text{CuCr}_2\text{S}_4$ at 300 K and 5 K .....	149

## LIST OF SCHEMES

Scheme 1.1: Essential stages of formation of nanocrystals during the thermal decomposition process.....	3
Scheme 3.1: Schematic drawing of the experimental setup used to synthesize NCs .....	54
Scheme 3.2: Representation of the reaction process for the synthesis of $\text{CuSe}_2$ and $\text{CuCr}_2\text{Se}_4$ NCs .....	55
Scheme 4.1: Schematic view of (a) the identical positions of Cr ions and (b) Cu ions diffusion into the neighboring vacant tetrahedral positions during the pyrite to spinel phase transformation .....	114
Scheme 4.2: Depiction of clustering of the initial nanocubes and pyrite to spinel phase transformation.....	118
Scheme 5.1: Schematic representation of the HI synthesis of $\text{CuCr}_2\text{S}_4$ NCs .....	122
Scheme 5.2: Depiction of synthesis process of $\text{Cu}(\text{DDTC})_2$ .....	129
Scheme 5.3: Depiction of annealing process of $\text{CuCr}_2\text{S}_4$ NCs under the atmosphere of sulfur vapor .....	146

## CHAPTER 1

### INTRODUCTION

#### 1.1 Colloidal Nanocrystals

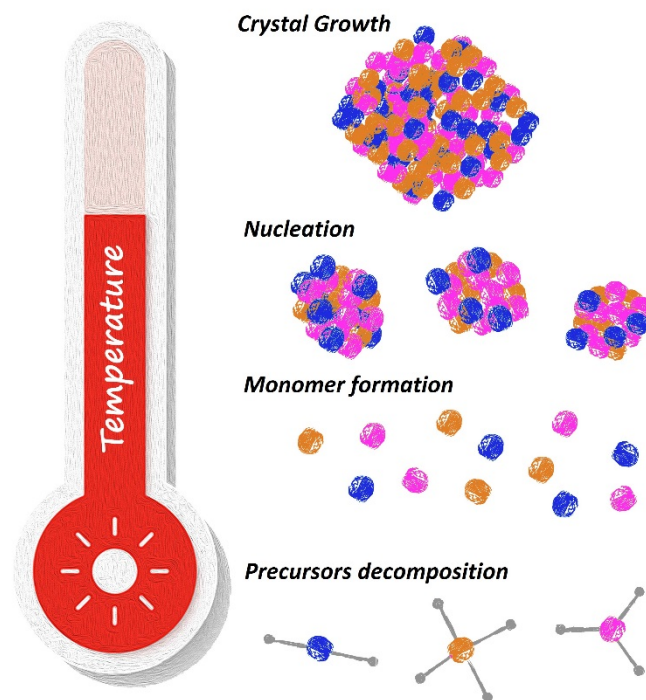
Nanocrystals (NCs) have attracted significant attention because they often show novel chemical, magnetic, electronic, mechanical, and optical properties that may not be found in the bulk materials. Therefore, controlling the size and shape of NCs is essential and plays a crucial role in optimizing their performance. Over the past 20 years, research efforts in nanocrystal synthesis have led to the development of synthetic pathways that allow precise control of the NCs composition, shape, size, and crystal structure.<sup>1,2</sup> Varieties of synthetic methods including solvothermal synthesis, microwave, and ultrasonic irradiation have been reported so far.<sup>3-5</sup> However, developing a general, simple, and inexpensive method for the preparation of NCs remains a challenge. The thermal-decomposition-based technique (also called wet-chemical colloidal synthesis) is one of the essential approaches to size- and shape-controlled synthesis of colloidal NCs.<sup>6-8</sup>

There are two main methods developed based on the thermal decomposition of the reagents, including heat-up (HU) synthesis and hot-injection (HI) method. In general, these methods need room temperature stable precursors and surfactants as the minimum set of requirements. In the HU synthesis method, all reagents are mixed into the same reaction container and heated to induce the nucleation, which leads to nanocrystals growth. Scheme 1.1 indicates the relation of the essential stages of nanocrystal formation to the temperature in a HU method. The precursors must rapidly decompose at temperatures where the surfactants are stable. As the temperature increases, the precursors form monomers and then nucleate to make small

nuclei. The small nuclei finally grow into mature NCs.<sup>7</sup> On the other hand, the HI method includes rapid injection of the reagents into a reaction vessel containing a hot solvent.<sup>8</sup> However, the essential stages of the formation mechanism of colloidal nanomaterials during the HI method are the same as HU synthesis, including decomposition of precursors, monolayer formation, and nucleation and crystal growth stages.<sup>7</sup>

One of the most critical challenges posed during the design of thermal-decomposition-based reactions is that the chemistry of the precursors and other parameters requires a significant level of attention to produce large quantities of nuclei in nanoscale within a relatively short time (relatively rapid process) and to reduce particles polydispersity via appropriate decoupling of the nucleation and growth stages.

Besides the chemistry and reactivity of precursors, other parameters such as reaction time and temperature, the composition of capping agents, and reaction solvent play significant roles in controlling the size, morphology, composition, and purity of the colloidal NCs. Control over these parameters is critical for achieving a product with the desired shape, composition, and phase purity. Although HI is of the most common methods to the growth of NCs, the formation of NCs using a HU approach circumvents all of the insurmountable drawbacks of HI method including (i) Reagent mixing time, (ii) Reaction cooling time, (iii) Practicality, (iv) Reproducibility,<sup>7</sup> and provides a possibility to fully controllable and scalable syntheses.



Scheme 1.1: Essential stages of the formation of nanocrystals during the thermal-decomposition process.

## 1.2 Size and Shape Control of Colloidal NCs through HU and HI Methods

Through controlled synthesis and surface chemistry engineering, colloidal NCs possess compelling benefits of low-cost, large-scale solution processing, and tunable properties.<sup>9</sup> Herein, we briefly discuss the effect of important parameters to control the size, size distribution, and morphology of the NCs obtained via HU and HI methods, including the reaction time and temperature, the chemistry, and concentration of the precursors, reaction solvent, capping ligands or surfactants, and injection temperature of the reagents in the case of HI method. Generally, nanocrystals size increases with increasing reaction time (as more materials add to nanocrystal surfaces), and temperature, because the rate of nucleation increases as a function of time and temperature.<sup>10,11</sup> The size distribution of NCs is highly correlated to the kinetics of nucleation

and growth processes. The nucleation stage can occur separately from the growth or be allowed to take place at the same time as growth.<sup>1</sup> According to the LaMer model, the formation process of NCs consists of two main stages, including nucleation and crystal growth (Figure 1.1).<sup>1,12,13</sup>

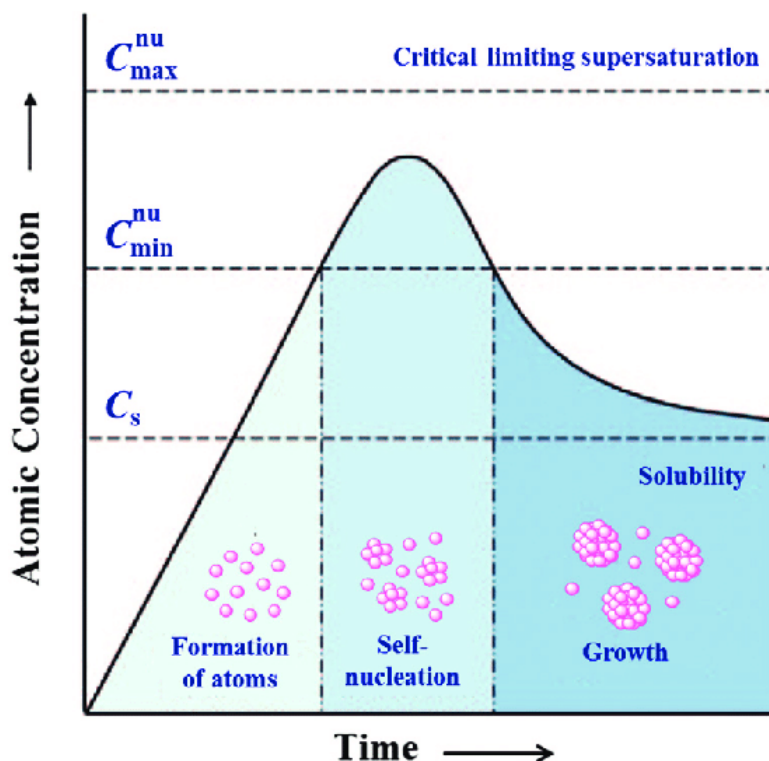


Figure 1.1: Schematic diagram of the nucleation and growth stages of the formation of colloidal NCs. Reprinted with permission from ref. 13.

The nucleation could occur either separately from or at the same time as the growth stage. Generally, the contemporaneity of the growth stage and nucleation stage leads to a poor size distribution. Therefore, to narrow the size distribution, the strategy of the separation of nucleation and growth stages is usually applied.<sup>9</sup> The hot-injection method is the best experimental strategy to separate the two steps. In 1993, Murray et al. introduced a successful HI method in which injecting precursors into solvents at high temperature, followed by a reduction of the reaction temperature. NCs of CdS within the range of 12–115 Å were synthesized via

rapid injection of precursors ( $\text{Cd}(\text{CH}_3)_2$ ) and bis(trimethylsilyl)sulfide ( $(\text{TMS})_2\text{S}$ ) into a hot solvent, inducing the mixture of (TOP) tri-n-octylphosphine and (TOPO) tri-n-octylphosphine oxide at high temperature (over 300 °C). The same method was also to prepare NCs of CdSe and CdTe.<sup>14</sup> Then after, the HI method widely extended to the synthesis of the nanocrystals of a large variety of materials, such as metallic NCs, metal oxides, binary, ternary, and quaternary metal chalcogenide and metal pnictogenide NCs, lanthanoid, and f-block containing NCs.

Apart from the HI, the HU method (also called non-injection) has also developed for the synthesis of colloidal NCs. In the HI method, separation of nucleation and growth is realized by slowly heating the solution in the presence of particular precursors.<sup>7</sup> In comparison with the HI method, the HU is far simpler without the injection step and provides an alternative way to obtain high-quality nanocrystals.<sup>9</sup> In 2005, Cao and coworkers prepared high-quality monodisperse NCs of CdSe and CdTe. The NCs were obtained by heating a mixture of cadmium myristate and selenium powder in the presence of 1-octadecene (ODE).<sup>15</sup> Nanocrystals of various types of materials such as metal oxides and metal chalcogenides have also been prepared by the HU synthesis method over the last few years.

### **1.2.1 Kinetic Size and Shape Control**

A key feature of NCs synthesis is the ability to prepare nanoparticles with a narrow size distribution. Figure 1.2 describes the concept of size distribution.<sup>16</sup> The left-hand side of the curve illustrates the dependence of the surface energy on the size of particles. According to the curve, small crystals indicating negative growth rate, are unstable due to their large fraction of active surface atoms. The right-hand side of the curve reveals that crystals with larger sizes are stable and grow because of the smaller surface-to-volume ratio. At the critical size (depends on the monomer concentration), the zero-crossing point occurs, where nanocrystals neither grow nor

shrink. In general, low monomer concentration favoring a larger critical size. The peak in growth rate versus radius on the right-hand side arises because of a geometric factor: increasing the radius of large crystals requires the incorporation of many more atoms that does increase the radius of smaller crystals. Depending upon the concentration of the monomers, the growth process of nanocrystals can occur in two different modes, ‘focusing’ and ‘defocusing.’

According to Howard Reiss prediction almost 70 years ago, and as illustrated in figure 1.2, at high monomer concentrations, the critical size is small so that all the particles grow.<sup>17</sup> In this case, smaller particles grow more rapidly than the larger ones. Eventually, the size distribution focuses, and the NCs could be nearly monodisperse. Moreover, secondary injection of the precursors could increase the monomer concentration. Although the distribution of NCs sizes present remains almost constant, but the critical size shifts to a smaller value, and as a result, the distribution will spontaneously narrow or ‘focus.’ At low monomer concentration (below a critical threshold), larger NCs grow whereas small nanocrystals are depleted, and the size distribution defocuses or broadens.<sup>16</sup>

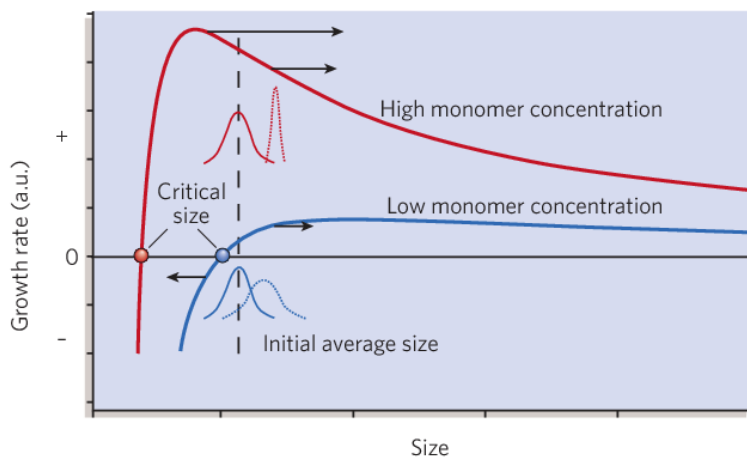


Figure 1.2: Diagram of the growth rate versus radius. Depiction of two different modes of NCs growth process, ‘focusing’ and ‘defocusing’ related to the concentration of monomers. Reprinted with permission from ref. 16.

Equilibrium NCs with low aspect ratios formed in the slow growth limit under thermodynamic control. However, the formation of the metastable nanocrystals requires a kinetic growth regime. At a low growth rate, defocusing is observed, and nearly round NCs with broad size distribution formed while focusing becomes more predominant at higher growth rate. In a kinetic regime, the high-energy facets grow faster than low energy facets. When the growth rate is increased just beyond the focusing regime, an astonishing variety of highly anisotropic shapes are obtained, such as rods and disks, arrows like and tetrapods. Using selective adhesion strategy in which an organic molecule could selectively adhere to a particular crystal facet slows the growth rate of that side relative to others, and eventually leads to the formation of rod- or disk-shaped NCs (Figure 1.3).<sup>16</sup>

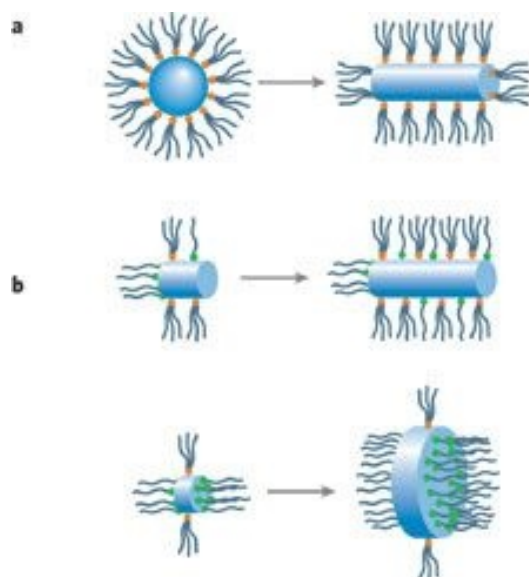


Figure 1.3: Kinetic shape control at (a) high rate of crystal growth and (b) through selective adhesion causes the formation of nanorods and nanodisks. Reprinted with permission from ref. 16.

In general, a colloidal synthesis system consists of three major components, including precursors, organic surfactants (also called capping ligands), and solvents. Many surfactants

could also be used as the solvent of the reaction. Hot organic capping ligands have a crucial role in determining the size and the morphology of the colloidal inorganic NCs. We will continue with a discussion of the organic-inorganic interface, knowing that a successful control depends on using suitable surfactants to manipulate the NCs surfaces.

### **1.2.2 Capping Ligands**

As already mentioned, colloidal nanocrystals are solution-grown inorganic nanoparticles that are stabilized by a layer of capping agents or surfactants attached to their surface. During the colloidal synthesis, the organic capping ligands bound to the surface of nanoparticles not only control the growth of the crystals but also effectively prevent the aggregation of the nanoparticles. Electrostatic repulsion, steric exclusion, or a hydration layer on the surface of nanoparticles could lead to a repulsive force between particles. Therefore, the choice of the right capping ligand may yield stable particles. Parameters such as the particle size, core materials, and the reaction solvent could usually guide to choose a suitable organic molecule as the capping ligand.<sup>18</sup>

First of all, the ligand should bind to the surface of the particle via physicochemical interactions such as electrostatic interactions, chemisorption, or hydrophobic interactions; therefore, the head group of the capping agent plays an essential role to form appropriate bonds. Organic ligands with electron-donating end groups of ligand molecules such as thiols, amines, and phosphines are the most common families of molecules were used for the colloidal synthesis of inorganic nanomaterials.<sup>19-23</sup> In general, polar or charged ligands provide more solubility in aqueous and polar solvents. In contrast, nanoparticles with nonpolar ligand groups are more soluble in nonpolar solvents such as chloroform, toluene, and hexane.<sup>18</sup> Figure 1.4 shows some different hydrophilic ligands that are commonly used as capping agents in colloidal nanoparticles

synthesis, including trioctylphosphine oxide (TOPO), triphenylphosphine (TPP), dodecanethiol (DDT), tetraoctylammonium bromide (TOAB) and oleic acid (OA). Ligand molecules can get off via the washing process or mass action by another incoming ligand. The washing procedure and further purification steps after the synthesis stage might affect the stability of the nanoparticles that might ultimately aggregate and precipitate. In general, strongly binding molecules could stabilize particles better than weakly binding ones, due to the formation of a denser layer around the particles.<sup>18</sup>

The capping agents not only bind to the surface of the growing NCs but also make a complex with the reactive monomer species formed during the heating procedure. The interaction between the organic ligands and the surface of inorganic NCs, therefore, the stability of these complexes, are strongly related to the reaction temperature.

Generally, increasing the temperature decreases the stability of the formed complexes while increasing the diffusion rates of the complexes, and it favors the nucleation and growth of the NCs. However, too high temperatures may lead to the uncontrolled growth of the crystals so that it is difficult to achieve precise control over the size distribution of the nanocrystals. Therefore, reaction temperature plays a predominant role, and choosing an appropriate range of temperature is one of the critical steps to control the colloidal NCs growth.<sup>16</sup>

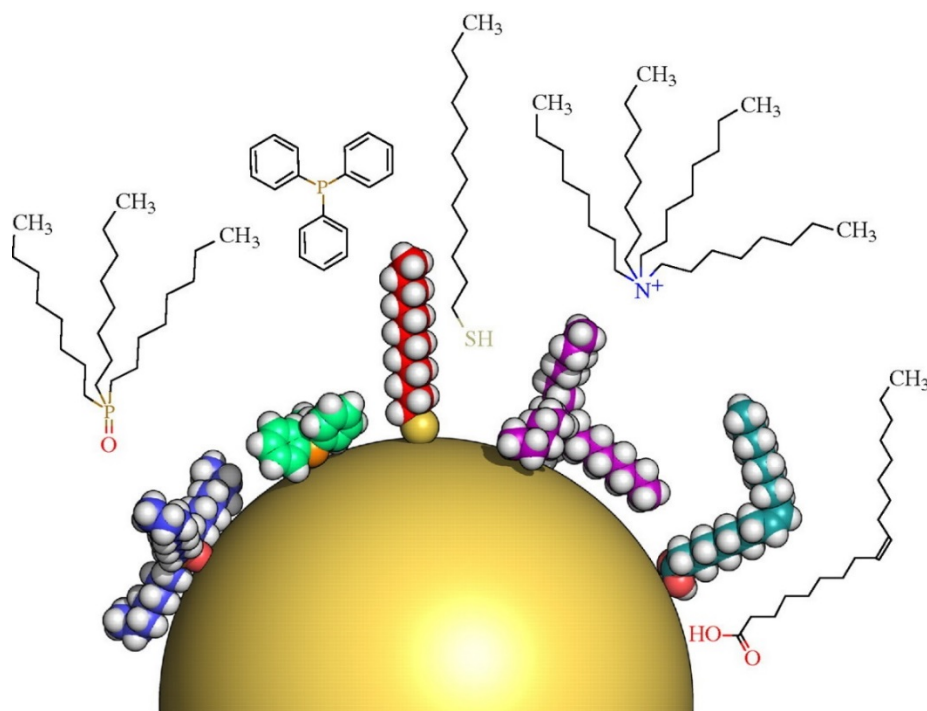


Figure 1.4: Schematic depiction of the surface of a spherical nanoparticle with commonly used hydrophilic capping ligands. Left to right: TOPO, TPP, DDT, TOAB, and OA. Reprinted with permission from ref. 18.

Next, we will focus on the chemistry and the critical aspects of the suitability and the versatility of the two of the most familiar capping agents that are widely used in the synthesis of various types of nanostructures, including oleylamine (OLA) and octadecylamine (ODA).

### 1.2.2.1 Oleylamine (OLA) and Octadecylamine (ODA)

OLA ( $C_{18}H_{37}N$ ) and ODA ( $C_{18}H_{39}N$ ) are multifunctional long-chain primary alkylamines, which can act as a solvent, surfactant, stabilizer, and reducing agent (electron donor) at elevated temperatures.<sup>24,25</sup> Existence of a double bond  $C=C$  in the middle of the molecule is the unique feature of OLA in comparison with ODA. Generally, and because of the similar structure of ODA and ODA, they exhibit similar basicity and affinity to metals through

their NH<sub>2</sub> functional groups. However, the size and morphology of the resulting nanoparticles can be significantly different. The lack of C=C bond in saturated structure of ODA could potentially limit its coordination with the surface of the nanoparticles.<sup>26</sup> The high boiling point of OLA and ODA (~350 °C) makes them great candidates to be used to strong heating conditions if necessary. OLA and ODA have been widely used in the synthesis of a broad range of NCs, e.g., metal oxides, metal chalcogenides, bimetallic magnetic materials, noble (nonplasmonic) metals, plasmonic metals (gold, silver, copper), semiconductors, heterostructures, and rare-earth-based materials.<sup>24</sup> Depending on the system under study, size, morphology, and composition of the obtained nanomaterials could be controlled by careful choice of additional reaction parameters.

### **1.2.3 Precursors**

The selection of suitable chemical reagents is one of the essential parameters that can significantly affect the resulting phase, size, and shape of the nanoparticles. As a requirement of HI and HU methods, the precursors need to react quickly or decompose at the growth temperature and yield reactive monomers, which then cause NCs nucleation and growth stages.<sup>7,15</sup>

Through a careful choice of chemical precursors along with surfactants, NCs of a series of semiconductors in different morphologies have been obtained from spherical dots to one-dimensional (1D) nanorods (NRs), tetrapods, and two-dimensional (2D) nanosheets.<sup>15,26,27</sup> A wide range of morphologies including 1D NRs, nanopyramids, 2D nanodisks (NDs), nanoplates, nanocubes, and noncentrosymmetric shapes have also been achieved in metal and metal chalcogenide NPs.<sup>28-34</sup>

Olesiak and coworkers indicated that a high reactivity of starting materials plays an essential role in preparing nanorods.<sup>34</sup> Using thiol as a sulfur source that decomposes easily, they could easily obtain NRs of colloidal CuS. In another work, Zhai and Shim examined how different Cu precursors, including CuCl<sub>2</sub>, CuAc, and Cu(NO<sub>3</sub>)<sub>2</sub>, influence the phase and the shape of resulting Cu<sub>2-x</sub>S nanocrystals.<sup>35</sup> According to this work, higher reactivity of the precursors (Cu(NO<sub>3</sub>)<sub>2</sub> along with thiol) favored 1D NRs and precursors with lower reactivity (e.g., CuAc and CuCl<sub>2</sub>) favored 2D NDs. Moreover, the application of a strong capping ligand, such as OLA, favored 2D disk shape NCs due to reducing the overall reactivity of the reagents.

In general, the introduction of halide ions reduces the rate of the formation of NCs (slowing growth kinetics) and eventually inhibits nucleation events, therefore favors the formation of 2D NCs.<sup>31,32</sup>

Donega and coworkers employed a method that yielded 2D nanosheets of Cu<sub>2-x</sub>S, in which a synergistic interaction between halides and a copper-thiolate precursor created a template that imposed 2D constraints, resulting in nucleation and growth of trigonal and hexagonal NCs, whereas, in the absence of halide, nearly spherical nanoparticles were obtained (Figure 1.5).<sup>32</sup> The lack of capping agent (TOPO) caused a change in the size and shape of the NCs dramatically, and yielded to large trigonal nanocrystals (3–4 μm).

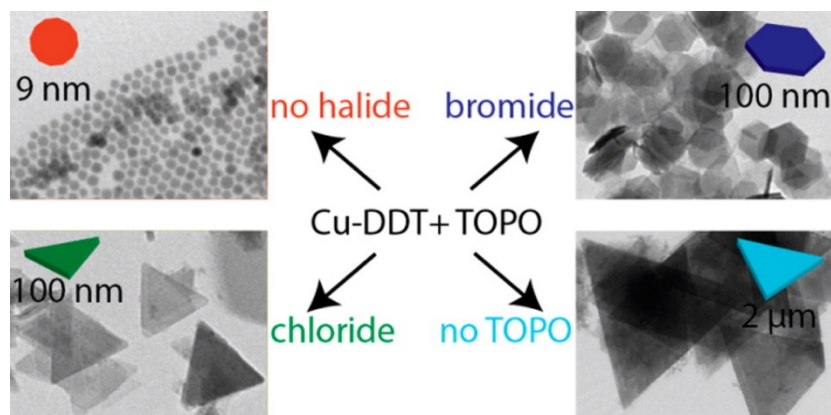


Figure 1.5: Effect of halide ions on the formation of 2D morphologies and influence of TOPO surfactant on the size distribution of  $\text{Cu}_{2-x}\text{S}$  NCs. Reprinted with permission from ref. 32.

Figure 1.6 illustrates that introducing chloride ion in the form of alkylammonium chloride suppresses or slows one-dimensional rod growth and promotes two-dimensional lateral growth. Alkylammonium derivatives are a type of surfactants that could form micelles or introduce other complications (such as chloride) into the growth mechanism.<sup>35</sup>

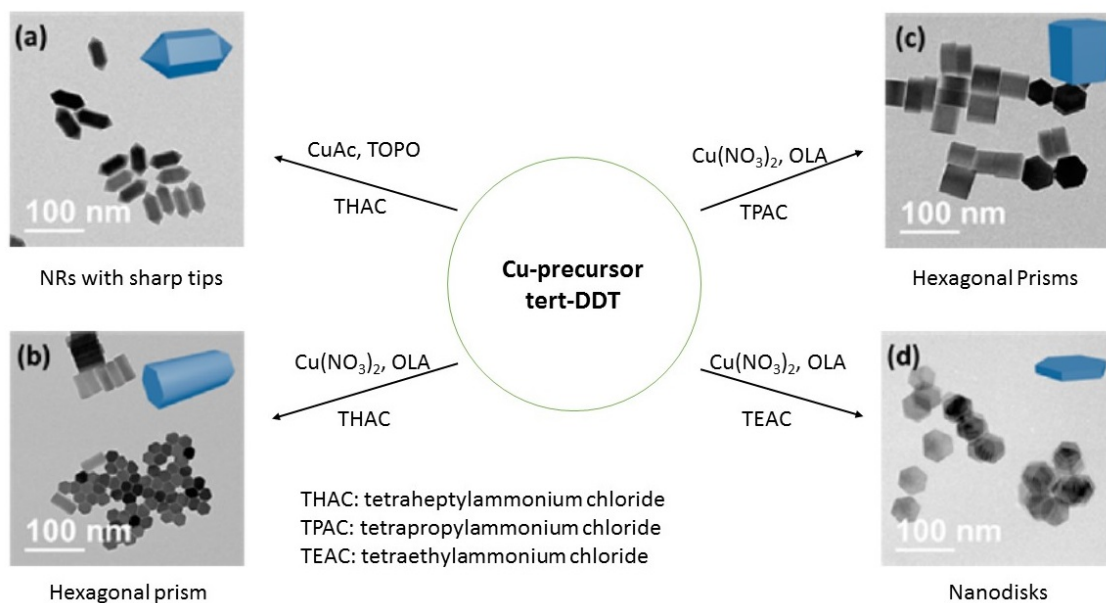


Figure 1.6: Influence of alkylammonium chlorides on the shape of  $\text{Cu}_{2-x}\text{S}$  nanocrystals. Reproduced with permission from ref. 35.

### 1.2.3.1 Single-Source Precursors

The single-source precursor method is one of the most suitable strategies because of its simplicity and the ability to control the nanoparticle size.<sup>36-39</sup> The most common examples of single-source precursors are urea, thiourea, biurets, phosphinates, carbamates, xanthates, and imidodiphosphinates.<sup>40-45</sup>

O'Brien et al. have synthesized binary CdS and ZnS NCs by thermal-decomposing of  $\text{Cd}[\text{S}_2\text{CN}(\text{C}_2\text{H}_5)_2]_2$  and  $\text{Zn}[\text{S}_2\text{CNMe}(\text{C}_6\text{H}_{13})]_2$  as the single-source precursors in the presence of trioctylphosphine and trioctylphosphine oxide.<sup>46,47</sup>

In another work, NCs of  $\text{AgInS}_2$  were prepared using phosphine based single-source of  $[(\text{Ph}_3\text{P})_2\text{AgIn}(\text{SCOPh})_4]$ .<sup>48</sup> In these studies, phosphorous surfactants such as TOPO and TOP (trioctylphosphine) were used to synthesize NCs of metal sulfides. Owen et al. have reported a tunable library of single-source precursors of metal complexes based on substituted thiourea to binary and ternary metal sulfide nanocrystals.<sup>49</sup>

Recently, thermal decomposition of metal-diethyl dithiocarbamate (metal-DDTC) based precursors were found as a facile and inexpensive way to the preparation of a wide range of binary and ternary metal sulfide NCs.<sup>50-54</sup> For example, Deng and coworkers reported a one-step heat-up based synthesis with metal-DDTCs as the precursors to synthesize several ternary metal sulfide NCs with uniform sizes and controlled morphologies.<sup>55</sup> Different NCs including orthorhombic  $\text{Cu}_3\text{BiS}_3$  nanosheets,  $\text{Cu}_3\text{BiS}_3$  nanoparticles,  $\text{Cu}_4\text{Bi}_4\text{S}_9$  nanowires and nanoribbons, wurtzite  $\text{CuInS}_2$  nanopenciles, cubic  $\text{AgBiS}_2$  nanocubes, orthorhombic  $\text{Ag}_8\text{SnS}_6$  nanoparticles, and orthorhombic  $\text{Cu}_3\text{SnS}_4$  nanorods were obtained. Figure 1.7 summarizes the relationship between the reaction conditions, structure, and morphology of the prepared nanoparticles.

Difficulty in individually controlling the kinetics of nucleation and growth stages is one of the main drawbacks with single monomer sources.<sup>7</sup>

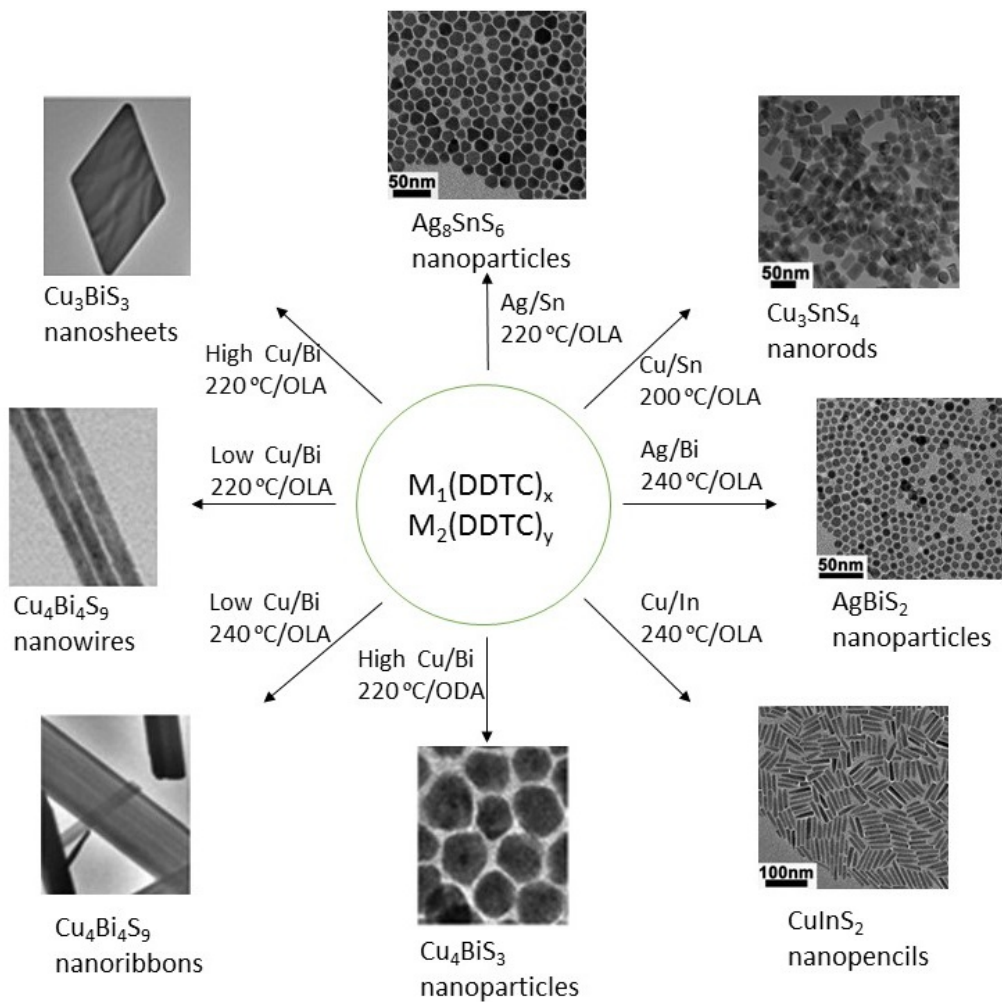


Figure 1.7: Schematic synthesis pathway of metal sulfide NCs by thermal decomposition of metal-DDTC precursors. Reproduced with permission from ref. 55.

### 1.3 Metal Chalcogenides

NCs of binary, ternary, and quaternary transition metal chalcogenides (TMCs) have attracted significant attention related to their synthesis and characterization because of their novel chemical, magnetic, electronic, mechanical and optical properties.<sup>49,55-60</sup>

In this section, a comprehensive library of HU and HI methods that were employed to obtain colloidal NCs of TMCs is provided. Tables 1-2 present a summary of the reaction conditions and resulting size and shape of a series of various types of colloidal TMCs nanocrystals.<sup>7</sup>

### 1.3.1 Binary Metal Chalcogenide NCs

The most widely investigated class of binary chalcogenides is group II-VI semiconductors. Early studies focused on the use of single-source precursors. However, these methods were not tremendously successful for growing monodisperse ensembles of particles.<sup>61,62</sup> In an early example, nanoclusters of CdTe formed during the rapid thermalizes of Cd(TePh)<sub>2</sub>(1,2-bis(diethylphosphino)ethane)<sub>2</sub> in 4-ethylpyridine.<sup>63</sup>

Cumberland et al. could successfully achieve full control on the nucleation and growth kinetics of the formation of ZnSe and CdSe NCs (size range of 2.5-9 nm) by modifying the solubility and reactivity of the Li<sub>4</sub>[Zn<sub>10</sub>Se<sub>4</sub>(SPh)<sub>16</sub>] and Li<sub>4</sub>[Cd<sub>10</sub>Se<sub>4</sub>(SPh)<sub>16</sub>] precursors via hexadecylamine (HDA).<sup>64</sup>

Cao's research team was the first to report on the HU method of both high-quality CdSe and CdTe NCs.<sup>65</sup> In comparison, more works were reported on the controlled synthesis of CdS nanoparticles via the HU method. Elemental sulfur has been used by many research group, although one of the major drawbacks with sulfur is that this element could react with capping ligands (e.g., 1-octadecene ODE) at low temperatures and it was found that for the growth of CdS NCs, a minimum temperature of 180 °C is needed to obtain high-quality CdS nanoparticles.<sup>66</sup>

Application of alternative sulfur sources such as N,N-di-n-butylthiourea (DBTU) made it possible to obtain desired nanocrystals of CdS at lower temperatures (e.g., 150 °C).<sup>67</sup> size- and shape-controlled nanoparticles of copper chalcogenides, e.g., Cu<sub>x</sub>S have also been investigated significantly. For the first time, the HU synthesis of Cu<sub>2</sub>S NRs was reported by Larsen et al. through the thermolysis of a copper dodecylthiolate precursor in the presence of octanoic acid (OctA) at 148 °C.<sup>68</sup> Other morphologies such as nanoplatelets and nanodiscs have also been synthesized employing copper thiolate and dodecanethiol (DDT) at 200 °C.<sup>69</sup>

In another work, heating copper oleate along with DDT at 230 °C formed monodispersed spherical NCs of Cu<sub>2</sub>S NCs.<sup>70</sup> NCs of Cu<sub>2-x</sub>Se with desired size and morphology were obtained through the use of copper stearate, Se, ODE, OLA, and ODA.<sup>71</sup> Table 1.1 shows more examples of successful works on the design and preparation of binary TMCs e.g., PbX (X=S, Se, Te), Ag<sub>2</sub>S, MnS, M<sub>n</sub>X<sub>m</sub> (M= Co, In, Bi, Ni, Fe, Sn, Pd), etc. The information on this table is gathered from ref. 7.

Table 1.1: A series of colloidal binary TMCs NCs prepared via HU and HI methods. The information on the table is collected from ref. 7 and the references therein. Other newer works and their references are also provided in the table.

Material	Temperature/Time	Chemistry	Size (nm)/Morphology
Ag <sub>2</sub> S	200 °C/30 min 120–200 °C/5 h 130-230 °C/1-60 min 200 °C/2 h 200 °C/30 min	Ag(DDTC), OA, ODA, ODE, OLA, TOPO Ag(CnDTP), OLA, n-decane, OA Ag(DDTC), 1-DDT Ag(OAc), 1-DDT AgNO <sub>3</sub> , 1-DDT	10-40 nm/ spheres 10-21 nm/spheres-cubes 2-7 nm/spheres 5-13 nm/spheres 3 nm/spheres
Bi <sub>2</sub> S <sub>3</sub>	225 °C/60 min 160 °C/60 min	Bi(OctA) <sub>3</sub> , 1-DDT Bi(OctA) <sub>3</sub> , S, 1-DDT	500-700 nm/wires 800 nm/rods
CdS	260 °C/unspecified 80-230 °C/0-4 h 240 °C/40 min 240 °C/ 0-60 min 180 °C/60 min 300 °C/30 min 180-250 °C/30 min	Cd(DDTC) <sub>2</sub> , OA, OLA, ODE ((CH <sub>3</sub> ) <sub>3</sub> NH) <sub>4</sub> [Cd <sub>10</sub> S <sub>4</sub> (SPh) <sub>16</sub> ], HDA Cd(S <sub>2</sub> PPh <sub>2</sub> ) <sub>2</sub> , Cd(MA) <sub>2</sub> , ODE Cd(OAc) <sub>2</sub> , S, OA, ODE Cd(OA) <sub>2</sub> , S, OA, ODE Cd(OA) <sub>2</sub> , DDT, OLA Cd(OAc) <sub>2</sub> , DDT, OA, OLA	5-16 nm/spheres, rods 2.5-5.5 nm/spheres 3.9-5.4 nm/spheres 2.5-4.0 nm/spheres 4.5 nm/spheres 10 nm/spheres 5 nm/spheres
CdSe	168 °C /0-84 h 220-240 °C/24 h 240 °C /2h 240 °C /2 h 180-290 °C/30–120 min 200-225 °C/100 min 220 °C/1-30 min 240 °C / 0-25 min	Cd[(SePh) <sub>2</sub> ] <sub>2</sub> [epe] <sub>2</sub> , Cd(SePh) <sub>2</sub> , EP (Li) <sub>4</sub> [Cd <sub>10</sub> Se <sub>4</sub> (SPh) <sub>16</sub> ], HDA Cd(MA) <sub>2</sub> , Se, OA, ODE Cd(MA) <sub>2</sub> , SeO <sub>2</sub> , OA, ODE Cd(ST) <sub>2</sub> , Se, Pfn Cd(DA) <sub>2</sub> or Cd(ST) <sub>2</sub> , Se, OA, Pfn CdO, Se, TOP, OA, Pfn Cd(TDPA) <sub>2</sub> , Cd(TDOA) <sub>2</sub> , TOPSe, TOPO, 1-ODA, ODE	2.5-4.0 nm/spheres 2.5-9.0 nm/spheres 2.0-4.5 nm/spheres 3.0-6.2 nm/spheres 1.8-3.0 nm/spheres 2.8-5.0 nm/spheres 6-12 nm/tetrapods 3-60 nm/rods, tetrapods
CdTe	168 °C/unspecified 240 °C/80 min 200 °C/100 min 220 °C /1 h	Cd[(TePh) <sub>2</sub> ] <sub>2</sub> [Et <sub>2</sub> PCH <sub>2</sub> CH <sub>2</sub> PET <sub>2</sub> ] <sub>2</sub> , EP Cd(ODPA) <sub>2</sub> , TBP-Te, ODE CdO, TOPO-Te, DA, Pfn Cd(acac) <sub>2</sub> , DOPO-Te, OA, OLA	3.5-5.0 nm/spheres 2.0-5.0 nm/spheres 4.0-8.3 nm/spheres 8 nm/tetrapods
CdS <sub>x</sub> Se <sub>1-x</sub>	240 °C/0-60 min	Cd(OAc) <sub>2</sub> , S, Se, MBTS, MA or OA, ODE	3-4 nm/spheres
CdS <sub>x</sub> Te <sub>1-x</sub>	120-280 °C/30 min 200 °C/100 min	Cd(OA) <sub>2</sub> , Cd(OctA) <sub>2</sub> , TOP-Se, TOP-Te, Pfn, ODE CdO, Se, TOPO-Te, DA, Pfn	2.3-5.2 nm/spheres 3.2-6.8 nm/spheres
Cu <sub>2</sub> S	140-200 °C/15-140 min 150-230 °C/15-140 min 200-250 °C/10-60 min 220 °C/unspecified 220 °C/unspecified 200-230 °C/1-2 h 200-250 °C/2 h 260 °C/1 h 200 °C/30 min	Cu(OctA) <sub>2</sub> , 1-DDT Cu(OA) <sub>2</sub> , 1-DDT, OLA Cu(acac) <sub>2</sub> , 1-DDT, OLA Cu(OAc) <sub>2</sub> , 1-DDT Cu(DDTC) <sub>2</sub> , 1-DDT Cu(acac) <sub>2</sub> , S, OLA Cu(acac) <sub>2</sub> , 1-DDT, OLA Cu(acac) <sub>2</sub> , S, OLA CuCl-thiolate complex, DDT	3-20 nm/spheres, disks 7-30 nm/spheres, disks 6–47 nm/spheres, disks 10 nm/spheres 6.5 nm / spheres 5-9 nm/spheres, hexagons 7-47 nm/spheres, hexagons 13 nm/spheres 20 nm/hexagons
Cu <sub>7</sub> S <sub>4</sub>	280 °C/unspecified	Cu(DDTC) <sub>2</sub> , OA	26 nm/spheres

Table 1.1: Continued.

Material	Temperature/Time	Chemistry	Size (nm)/Morphology
Cu <sub>2</sub> Se	120-200°C /2 h	Cu(ST) <sub>2</sub> , Se, OA, OLA, ODE	4-18 nm/spheres, discs
Cu <sub>2-x</sub> Se	220 °C/90 min 200 °C/10 min	Cu(ST) <sub>2</sub> , SA, OLA, ODE-Se, ODE Cu(acac) <sub>2</sub> , SeO <sub>2</sub> , Se, OA, ODE	12 nm/triangles 12 nm/polyhedra
CuSe <sub>2</sub>	210 °C/60 min 160 °C/45 min	CuCl <sub>2</sub> , Se, TEG, PVP, TETA CuCl, SeO <sub>2</sub> , EG, N <sub>2</sub> H <sub>4</sub>	400 nm/octahedra 808 nm/sheets
CuSe	160 °C/30 min	CuCl, SeO <sub>2</sub> , EG, N <sub>2</sub> H <sub>4</sub>	10-20 nm/nanoparticles
Cu <sub>2-x</sub> S <sub>y</sub> Te <sub>1-y</sub>	200–230 °C /30 min	Cu(acac) <sub>2</sub> , S, Te, 1-DDT, OA	3-8.5 nm/spheres
In <sub>2</sub> S <sub>3</sub>	215 °C/1 h	InCl <sub>3</sub> , S, OLA	22-63 nm/discs
MnS	290 °C/1 h 300-350 °C/2 h 250-320 °C/2-30min 280 °C/1 h	Mn(DDTC) <sub>2</sub> , Mn(DDTC) <sub>2</sub> (phen), OA, OLA, ODE (TMEDA)Mn(tbo) <sub>2</sub> , OLA, ODE Mn(OA) <sub>2</sub> , OLA, OA, ODE Mn(OA) <sub>2</sub> , 1-DDT, OLA	30-200 nm/polyhedra 25 nm/spheres, cubes 10-45 nm/spheres, starfish 11 nm /spheres
NiS	180 °C/1 h 150-190°C/5–300min	(TMEDA)Ni(tbo) <sub>2</sub> , OA, OLA, ODE Ni(OctA) <sub>2</sub> , 1-DDT	16-41 nm/polyhedra 6-20 nm/tetrahedra, rods
Ni <sub>3</sub> S <sub>4</sub>	250 °C/unspecified	Ni(OAc) <sub>2</sub> , 1-DDT, OLA, OA, ODE	20-50 nm/irregular
PbS	30-150 °C/15 min 230 °C/1 h 240 °C/10-80 min 220-240 °C/30 min 200-240 °C/10-80 min	PbX <sub>2</sub> (X = Cl, Br, I), OLA, (TMS) <sub>2</sub> S Pb(OA) <sub>2</sub> , 1-DDT, OLA Pb(DDTC) <sub>2</sub> , OLA, ODE Pb(OAc) <sub>2</sub> , 1-DDT, OA Pb(OAc) <sub>2</sub> , 1-DDT, ODE, OA, OLA	2-6 nm/spheres 50 nm/cubes 50 nm/cubes 30-120 nm/hexagons 40-160 nm/polyhedra
PbSe	40-80 °C/0-15 h 150 °C/0-30 min 180 °C /5 min 120-180 °C/20 min	Pb(OA) <sub>2</sub> , TOP-Se, DPP, ODE PbCl <sub>2</sub> , TBP-Se, (TMS) <sub>2</sub> Se, OLA Pb(OAc) <sub>2</sub> , SeO <sub>2</sub> , TOP, OA, ODE Pb(acac) <sub>2</sub> , ODE-Se, DA, OLA, Pfn	1-4 nm/clusters, spheres 2-6 nm/spheres 16 nm/spheres 6.5 nm/spheres
PbTe	180 °C/20 min	Pb(acac) <sub>2</sub> , TOPO-Te, DA or OA, OLA, Pfn	8.5 nm/spheres
PbS <sub>x</sub> Se <sub>1-x</sub>	60-80 °C /2-120 min	Pb(OA) <sub>2</sub> , TBP-Se, TA, DPP, ODE	2-4 nm/spheres
SnS	300 °C/unspecified	Sn(DDTC) <sub>2</sub> (phen), OLA, ODE	7 × 3 × 0.02 μm/nanosheets
SnS <sub>2</sub>	300 °C/unspecified	Sn(DDTC) <sub>2</sub> (phen), OA, OLA, ODE	150 × 6 nm/plates
ZnS	300 °C/unspecified 250 °C/unspecified 230-280 °C/2 h 310 °C/30 min	Zn(DDTC) <sub>2</sub> , OLA, OA, ODE Zn(OAc) <sub>2</sub> , 1-DDT, OLA, ODE ZnCl <sub>2</sub> , S, 1-DDT, OLA, DOE Zn(OA) <sub>2</sub> , 1-DDT, OLA	9.5 nm/spheres 3-5 nm/polyhedra 2-7 nm/spheres 10 nm/spheres
ZnSe	220-280 °C/24 h 280 °C/30 min 300 °C/5 h	(TMA) <sub>4</sub> [Zn <sub>10</sub> Se <sub>4</sub> (SPh) <sub>16</sub> ], HDA Zn(OA) <sub>2</sub> , TOP-Se, DPP-Se, DPP, ODE Zn(OAc) <sub>2</sub> , Se, OA, Pfn	2-5 nm/spheres 3.0 nm/spheres 5.5 nm/spheres
ZnSe	150 °C/3 h	ZnCl <sub>2</sub> , TOP-Te, OLA, Superhydride, DBE	5 × 30 nm/rods
ZnS <sub>x</sub> Se <sub>1-x</sub>	160-300 °C/20 min	Zn(OA) <sub>2</sub> , DPP-Se, DPP-S, ODE	5.0 nm/spheres
TiS <sub>2</sub> <sup>72</sup>	300 °C/1 h	TiCl <sub>4</sub> , CS <sub>2</sub> , OLA	150 nm/disks
ZrS <sub>2</sub> <sup>73</sup>	300 °C/1 h	ZrCl <sub>4</sub> , CS <sub>2</sub> , OLA	20 nm/disks
GeS <sup>74</sup>	320 °C/24 h	Gel <sub>4</sub> , HMDS, OA, OLA, 1-DDT	1 μm/sheets
InSe <sup>75</sup>	215 °C/5 h	InCl <sub>3</sub> , Se, OLA	7.8 nm/wires
SnSe <sup>76</sup>	180 °C/4 min	SnCl <sub>2</sub> , di-tert-butylselenide, DDA, 1-DDT	19 nm/anisotropic NCs
Bi <sub>2</sub> Te <sub>3</sub> <sup>77</sup>	150 °C/30 min	Bi-2-ethylhexanoate, Te, OE, TOP	200-300 nm/plates
NbSe <sub>2</sub> <sup>78</sup>	250-280 °C /4 h	NbCl <sub>5</sub> , Se, DDA	500 nm/plates

### 1.3.2 Ternary and Quaternary Metal Chalcogenide NCs

Design and engineering of the phase pure and homogenous multinary metal chalcogenides is more challenging than binary ones due to the difficulty in balancing the reactivity of the different precursors. Therefore, judicious selection of the reaction parameters such as solvents, surfactants, and heating conditions become even more critical. The case becomes more challenging in the HU method and requires much more consideration than in HI synthesis because the monomer of all the species becomes highly reactive at a similar time.<sup>7</sup> Therefore, to obtain multielemental materials via HU method, precursors with similar reactivities are favorable.

Uniform NCs of multinary TMCs can also be prepared with metal precursors showing different reactivities. At lower temperatures, most reactive metal species might act as a monomer source and less reactive metal precursors form monomer at higher temperatures and led to the formation of uniform “alloyed” composition.<sup>79</sup> However, in some cases, less reactive species may nucleate a secondary phase by increasing the temperature and eventually contaminate the final product.

An example of a simple ternary metal chalcogenide is  $\text{CdS}_x\text{Se}_{1-x}$  quantum dots (QDs) were first synthesized via HU procedure of  $\text{Cd}(\text{ac})_2$  and elemental S and Se in the presence of ODE.<sup>80</sup> Employment of phosphine based chalcogenide precursors of TOP-Se and TOP-Te complexes and  $\text{Cd}(\text{acetate})(\text{octanoate})$  in ODE formed homogeneously alloyed  $\text{CdSe}_x\text{Te}_{1-x}$  NCs at 180 °C.<sup>81</sup>

Purposefully and in order to synthesize nanocrystals of core/shell QDs, precursors with different reactivity have also been used. For example, the reaction of  $\text{Zn}(\text{NO}_3)_2$ , CdO, elemental S, and Se in TOP/ODE led to the formation of  $\text{CdSe}/\text{Zn}_x\text{Cd}_{1-x}\text{S}$  QDs at 250 °C.<sup>82</sup>

Because of the tunable band gap (1-2 eV) and low toxicity, nanocrystals of group I-III-VI TMCs based on copper, have gained attention as QDs for LED applications.<sup>83,84</sup> In a typical reaction, NCs of  $\text{CuInS}_2$  with sizes between 3-8 nm were synthesized by heating of copper and indium salts ( $\text{CuI}_2$  and  $\text{In}(\text{ac})_3$ ) in a solution of DDT and OLA/ODE as the capping agents heated to 210-260 °C.<sup>85,86</sup>

By using copper and indium oleate in DDT and OLA, Choi et al. could prepare uniform nanorods of  $\text{CuInS}_2$ .<sup>87</sup> In 2008, Panthani and coworkers have successfully used elemental S and Se in HU syntheses of  $\text{CuInS}_2$  and  $\text{CuInSe}_2$  nanoparticles.<sup>88</sup>

In 2015, Gupta and coworkers, for the first time, developed NCs of a new family of quaternary semiconductors  $\text{Cu}_2\text{ZnAS}_{4-x}$  and  $\text{CuZn}_2\text{AS}_4$  (A = Al, Ga, In) using HI method.<sup>89</sup> Rapid injection of a mixture of DDT to the preheated mixture of metal salts (acetylacetonate salts of Cu(II), Zn(II), and In(III)) at 150 °C, and consequent heating of the resulting solution to 250 °C led to the formation of NCs of  $\text{Cu}_2\text{ZnInS}_{4-x}$ . In another work, NCs of wurtzite and defect chalcopyrite phases of  $\text{CuMSnS}_4$  (M = In or Ga) have been successfully synthesized for the first time and through the HI method.<sup>90</sup> Table 1.2 shows more examples of successful works on design and preparation of ternary and quaternary TMCs, e.g.,  $\text{CuIn}_x\text{Ga}_{1-x}\text{S}_2$ ,  $\text{Cu}_2\text{ZnSnS}_4$ ,  $\text{Cu}_2\text{ZnGeSe}_4$ ,  $\text{AgInS}_2$ ,  $\text{AgIn}_x\text{Ga}_{1-x}\text{S}_2$ , etc. The information of this table is gathered from ref. 7.

Table 1.2: A series of colloidal ternary and quaternary TMCs NCs prepared via HU and HI methods. The information on the table is collected from ref. 7 and the references therein. Other newer works and their references are also provided in the table.

Material	Temperature/Time	Chemistry	Size(nm)/ morphology
AgBiS <sub>2</sub>	240 °C/1 h	Ag(DDTC), Bi(DDTC) <sub>3</sub> , ODA, ODE	7 nm/spheres
AgFeS <sub>2</sub>	150 °C/30 min	AgNO <sub>3</sub> , Fe(DDTC) <sub>3</sub> , OLA	15 nm/spheres
AgInS <sub>2</sub>	60–180 °C/2 min 180 °C/3 min 125–250 °C/2–16 h 200 °C/3–15 h 200 °C/2 h 120 °C/30 min 125–250 °C/2–16 h	AgNO <sub>3</sub> , In(OAc) <sub>3</sub> , 1-DDT, OA, TOP, ODE AgIn <sub>(1-x)</sub> (DDTC) <sub>(3-2x)</sub> , OLA [AgIn(SC[O]PhS)(Ph <sub>3</sub> P) <sub>2</sub> ], OA, 1-DDT, TOPO, OLA Ag(acac), In(acac) <sub>3</sub> , 1-DDT, OLA Ag(DDTC), In(DDTC) <sub>3</sub> , OA, 1-DDT AgNO <sub>3</sub> , In(OAc) <sub>3</sub> , 1-DDT, ODE, OA, TOP In(bipy)(tbo) <sub>3</sub> , Ag(tbo), 1-DDT, OA, TOPO, HDA	3-5 nm/spheres 4 nm/spheres 19-33 nm/polyhedra 15-80 nm/tadpoles, cones 12 nm/cones 2.5 nm/spheres 8-44 nm/irregular
AgGaS <sub>2</sub>	280 °C/2 h	Ag(DDTC), Ga(DDTC) <sub>3</sub> , 1-DDT	16 nm/trigonal pyramids
AgIn <sub>x</sub> Ga <sub>1-x</sub> S <sub>2</sub>	180–240 °C/30 min	AgIn <sub>x</sub> Ga <sub>1-x</sub> (DDTC) <sub>4</sub> , OLA	3-5 nm/spheres
AgInSe <sub>2</sub>	185 °C/17 h	[(PPh <sub>3</sub> ) <sub>2</sub> AgIn(tbo) <sub>4</sub> ], OA, 1-DDT	50 × 15 nm/rods
Ag <sub>8</sub> SnS <sub>6</sub>	220 °C/1 h	Ag(DDTC), Sn(DDTC) <sub>2</sub> (phen), OLA, 1-DDT	15 nm/polyhedra
Ag <sub>8</sub> Ge <sub>x</sub> Sn <sub>1-x</sub> S <sub>y</sub> Se <sub>6-y</sub>	220 °C/15 min	AgNO <sub>3</sub> , Ge/Sn[N(TMS) <sub>2</sub> ] <sub>2</sub> S, (TMS) <sub>2</sub> S(Se), OLA	10-13 nm/spheres
Cu <sub>3</sub> BiS <sub>3</sub>	220 °C/1 h	Cu(DDTC) <sub>2</sub> , Bi(DDTC) <sub>3</sub> , OLA, ODE, 1-DDT	25 nm/spheres
Cu <sub>4</sub> Bi <sub>4</sub> S <sub>9</sub>	220 °C/1 h	Cu(DDTC) <sub>2</sub> , Bi(DDTC) <sub>3</sub> , OLA, 1-DDT	micrometer wires/ribbons
CuInS <sub>2</sub>	230–250 °C/1 h 182 °C/1 h 240 °C/1–4 h 240 °C/0.5–60 min 240 °C/1–3 h 220 °C/12 h 160–240 °C/1–5 min	Cu(OA), In(OA) <sub>3</sub> , 1-DDT, OLA Cu(acac) <sub>2</sub> , In(acac) <sub>3</sub> , S, OLA, o-DCB Cu(OAc), In(OAc) <sub>3</sub> , 1-DDT, OA, ODE Cu(OAc), In(OAc) <sub>3</sub> , OLA-S, TOPO, ODE CuI, In(OAc) <sub>3</sub> , 1-DDT, OA, ODE CuI, In(OAc) <sub>3</sub> , 1-DDT, ODE CuI, InI <sub>3</sub> , S, OLA, 1-DDT	80-110 nm/rods 6-12 nm/spheres 2-4 nm/spheres, tetrahedra 5-15 nm/spheres, tetrahedra 3-8 nm/tetrahedra 9 nm/tetrahedra 4 nm/spheres
CuInSe <sub>2</sub>	240 °C/1 h 320 °C/1–2 min 240 °C/10 h	CuCl, InCl <sub>3</sub> , selenourea, OLA CuI, InCl <sub>3</sub> , TOP-Se, TOPh, TOP, HDA, ODE CuCl, InCl <sub>3</sub> , Se, TEA	16-18 nm/tetrahedra 1-6 nm/spheres 27-53 nm/spheres
CuInS <sub>x</sub> Se <sub>1-x</sub>	265 °C/90 min	CuCl, InCl <sub>3</sub> , S, Se, OLA	15-17 nm/spheres
Cu <sub>2</sub> SnS <sub>3</sub>	190–220 °C/12 h	CuI, Sn(OAc) <sub>2</sub> , 1-DDT, OLA or ODE	30-150 nm/spheres
Cu <sub>3</sub> SnS <sub>4</sub>	200 °C/1 h	Cu(DDTC) <sub>2</sub> , Sn(DDTC) <sub>4</sub> , OLA, 1-DDT	20 nm/rods
CuGaS <sub>2</sub>	280 °C/30 min	Cu(DDTC) <sub>2</sub> , Ga(DDTC) <sub>2</sub> , 1-DDT, OA, TOA	25 nm/tadpoles
CuIn <sub>x</sub> Ga <sub>1-x</sub> S <sub>2</sub>	150 °C/10-30 min	Cu(acac) <sub>2</sub> , In(acac) <sub>3</sub> , Ga(acac) <sub>3</sub> , 1-DDT, ODE, OLA	16-35 nm/rods, tadpoles
Cu <sub>2</sub> ZnSnS <sub>4</sub>	280 °C/1 h 120–300 °C/1 h 180 °C/1 h 190–220 °C/12 h 200 °C/1 h 200–250 °C/30 min	Cu(acac) <sub>2</sub> , Zn(OAc) <sub>2</sub> , SnCl <sub>2</sub> , S, OLA Cu(OAc) <sub>2</sub> , Zn(OAc) <sub>2</sub> , Sn(OAc) <sub>4</sub> , S, OLA CuCl <sub>2</sub> , ZnCl <sub>2</sub> , SnCl <sub>4</sub> , S, OLA CuI, ZnCl <sub>2</sub> , Sn(OAc) <sub>2</sub> , 1-DDT, OLA or ODE CuCl <sub>2</sub> , Zn(DDTC) <sub>2</sub> , Sn(DDTC) <sub>4</sub> , 1-DDT, OLA CuI, ZnCl <sub>2</sub> , SnCl <sub>4</sub> ·5H <sub>2</sub> O, CS <sub>2</sub> , 1-DDT, OLA	10.6 nm/spheres 5.1-6.6 nm/spheres 7-9 nm/spheres 5-25 nm/spheres 200 nm/rods 2-7 nm/spheres
Cu <sub>2</sub> ZnSnSe <sub>4</sub>	230 °C/90 min 255 °C/40 min	CuI, ZnCl <sub>2</sub> , SnI <sub>4</sub> , Se, TOPO, OLA or ODE Cu(OA) <sub>2</sub> , Sn(EHO) <sub>2</sub> , Zn(EHO) <sub>2</sub> , OLA, DPSe, Se	14-35 nm/spheres 20-80 nm/spheres, rods
Cu <sub>2</sub> ZnGeS(Se) <sub>4</sub>	310 °C/2 h	Cu(acac) <sub>2</sub> , Zn(acac) <sub>2</sub> , GeCl <sub>2</sub> ·dioxane, S, Se, OLA	10.6-13.6 nm/spheres
Cu <sub>2</sub> ZnGeS <sub>4</sub>	250 °C/30 min 300 °C/1 h	CuI, ZnCl <sub>2</sub> , [Ge(gly) <sub>2</sub> (H <sub>2</sub> O) <sub>2</sub> ], CS <sub>2</sub> , OLA, 1-DDT Cu(DDTC) <sub>2</sub> , Zn(OAc) <sub>2</sub> , GeCl <sub>2</sub> ·diox, t-DDT, OLA	6.5 nm/spheres 50-80 nm/rods
CuCr <sub>2</sub> S <sub>4</sub> <sup>91</sup>	360 °C/30 min	CuCl <sub>2</sub> , CrCl <sub>3</sub> , 1-DDT, OLA or ODA	20-31 nm/cubes, clusters
CuCr <sub>2</sub> Se <sub>4</sub> <sup>92,93</sup>	350 °C/1 h 300 °C/30 min	Cu(acac) <sub>2</sub> , Cr(acac) <sub>3</sub> , Se, OLA, ODE Cu(oleate) <sub>2</sub> , Cr(oleate) <sub>3</sub> , Se, TOA	15-30 nm/cubes 20 nm/triangles, hexagons

Table 1.2: Continued

Material	Temperature/Time	Chemistry	Size(nm)/ morphology
$\text{CuCr}_2\text{S}_{4-x}\text{Se}_x$ <sup>94</sup>	360 °C/30 min	$\text{CuCl}_2$ , $\text{CrCl}_3$ , 1-DDT, DPDS, OLA or ODA	12-21 nm/cubes,clusters
$\text{CuCr}_2\text{Te}_4$ <sup>95</sup>	350 °C/30 min	$\text{CuCl}_2$ , $\text{CrCl}_3$ , $\text{NaBH}_4$ , TOA, OLA	23 nm/cubes
$\text{Co}_x\text{Cu}_{1-x}\text{Cr}_2\text{S}_4$ <sup>96</sup>	360 °C/30 min	$\text{CuCl}_2$ , $\text{CoCl}_2$ , $\text{CrCl}_3$ , 1-DDT, OLA or ODA	20-31nm/cubes,clusters
$\text{CuSbS}_2$ <sup>97</sup>	170 °C/10 min	$\text{Cu}(\text{acac})_2$ , $\text{SbCl}_3$ , S, 1-DDT, t-DDT, OLA	340-450 nm/layers
$\text{CuSbSe}_2$ <sup>98</sup>	250 °C/10-30 min	$\text{Cu}(\text{acac})_2$ , $\text{SbCl}_3$ , DPDS, 1-DDT, t-DDT, OLA	45-50 nm/layers
$\text{CuSbS}_{2-x}\text{Se}_x$ <sup>98</sup>	250 °C/10-30 min	$\text{Cu}(\text{acac})_2$ , $\text{SbCl}_3$ , S, DPDS, 1-DDT, t-DDT, OLA	45-50 nm/layers
$\text{CuCo}_2\text{S}_4$ <sup>99</sup>	200 °C/1 h	$\text{Co}(\text{acac})_3$ , $\text{Cu}(\text{acac})_2$ , S, TOPO, OLA	6-14 nm/spheres
$\text{CuGaSe}_2$ <sup>100</sup>	250 °C/1 h	$\text{Cu}(\text{ac})_2$ , $\text{Ga}(\text{ac})_3$ , Se, OLA	11 nm/nanoparticles

### 1.3.3 Magnetic Metal Chalcogenides

Magnetic nanomaterials display unique nanosize-dependent properties including high field reversibility, high saturation field, and supermagnetism<sup>101</sup> and eventually have broad applicability in areas such as recording media, spin-based electronics, magneto-optics, and biomedical applications.<sup>102-105</sup> Ternary metal chalcogenides, especially chalcospinels, have attracted considerable attention because of their unique shape- and size-dependent properties and potential use in superconducting materials, photocatalysts, photovoltaics, solar cells, lasers, light-emitting diodes, and bio-labeling.<sup>60,106,107</sup>

Chalcospinels are the class of mixed metal materials of the general formulation of  $\text{A(II)B(III)}_2\text{X}_4$  (X= S, Se, Te) with the same crystal structure as shown in the traditional spinel materials ( $\text{AB}_2\text{O}_4$ ), which are crystallized in a cubic crystal system with the chalcogenide anions arranged in a cubic closed-packed lattice and the 2+ and 3+ cations partially occupying (1/8) of tetrahedral and (1/2) of the octahedral sites in the lattice respectively (Figure 1.8).

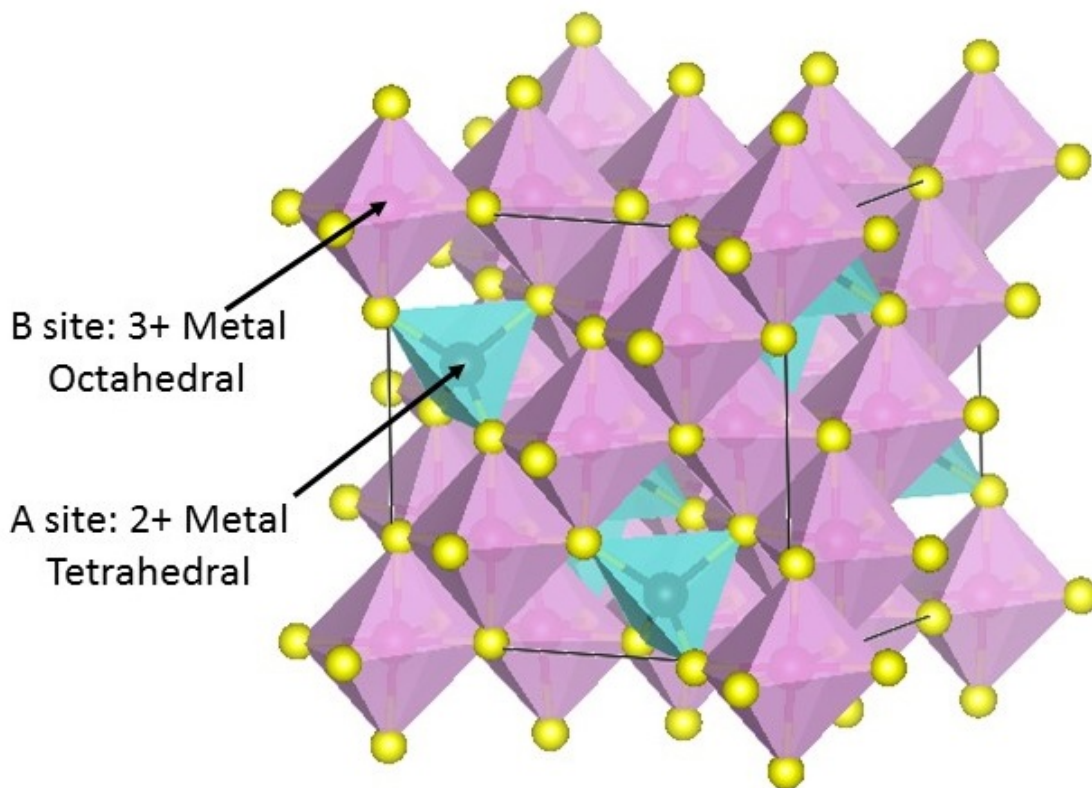


Figure 1.8: Spinel Crystal Structure.

Among the chalcospinels, chromium-based systems  $ACr_2X_4$  ( $A = Cu, Co, Fe, Cd,$  and  $Hg$ ;  $X = S, Se,$  and  $Te$ ) have gained significant attention because they encompass notable classes of electronic materials such as semiconductors, magnetic materials, and insulators.<sup>91-95</sup> Cu- and Cr-based chalcospinels ( $CuCr_2X_4$ ) are metallic and also ferromagnetic at room temperature with the Curie temperatures ( $T_C$ ) of  $CuCr_2S_4$  (377 K),  $CuCr_2Se_4$  (430 K), and  $CuCr_2Te_4$  (360 K) and these properties make them unique among the chalcospinels.<sup>108</sup> Due to the difficulties in finding a suitable sulfur and tellurium source and appropriate experimental conditions to design and construction of desirable spinel phase nanocrystals, there have been only a few reports on the thermal decomposition synthesis of S- and Te-based metal chalcogenide nanocrystals.<sup>92,109-111</sup>

## 1.4 Research Objectives and Thesis Organization

Although in recent years, a few reports on the solution-based synthesis of spinel  $\text{CuCr}_2\text{X}_4$  NCs have been published,<sup>91-95,111</sup> the exploration of a general and easy preparation method to design and construction of novel nanoparticles with desired morphology remains a challenge. Our objective concentrated on the design and preparation of nanoparticles of Cu- and Cr-based magnetic materials by using new methods to develop strategies to control the size and morphology of the phase-pure NCs and study their magnetic properties.

In chapters 3 and 4 of this study,  $\text{CuCr}_2\text{Se}_4$  NCs were synthesized using the HU method, and the formation mechanism and properties of the products were studied. We present a unique degradation mechanism of pyrite  $\text{CuSe}_2$  nanocubes formed through the heat-up synthesis of selenospinel  $\text{CuCr}_2\text{Se}_4$  nanoparticles. The degradation mechanism included doping of  $\text{Cr}^{3+}$  ions in the pyrite crystal structure and formation of  $\text{Cr}_x\text{Cu}_{1-x}\text{Se}_2$  ( $X = 0.1-0.5$ ) derivatives followed by clustering of the nanocubes.

The morphological evolution of the initial nanocubes as a function of reaction temperature was studied and correlated with the concentration of chromium. Finally, the formation mechanism of pure phase  $\text{CuCr}_2\text{Se}_4$  as the final product of the reaction pathway was discussed. Chapter 5 of this work describes the synthesis and characterization of  $\text{CuCr}_2\text{S}_4$  NCs prepared by employing single-source precursors. For this purpose, we have selected Cu- and Cr-diethyl dithiocarbamate (DDTC) complexes as the single-source precursors, and we have discussed the effect of different reaction parameters on the composition, phase purity, size, and shape of the resulting products.

## 1.5 References

1. Wang, X.; Zhuang, J.; Peng, Q.; Li, Y. A General Strategy for Nanocrystal Synthesis. *Nature* **2005**, *437*, 121–124.
2. Carbone, L.; Cozzoli, D. P. Colloidal Heterostructured Nanocrystals: Synthesis and Growth Mechanisms. *Nanotoday* **2010**, *5*, 449–493.
3. Lu, Q.; Hu, J.; Tang, K.; Qian, Y.; Zhou, G.; Liu, X. Synthesis of Nanocrystalline  $\text{CuMS}_2$  (M = In or Ga) Through a Solvothermal Process. *Inorg. Chem.* **2000**, *39*, 1606–1607.
4. Pang, C.; Gao, L.; Chaturvedi, A.; Bao, N.; Yanagisawa, K.; Shen, L.; Gupta, A. High-Temperature Solvothermal Synthesis and Magnetic Properties of Nearly Monodisperse  $\text{CdCr}_2\text{S}_4$  Nanocrystals. *J. Mater. Chem. C.* **2015**, *3*, 12077–12082.
5. Chen, D.; Shen, G.; Tang, K.; Jiang, X.; Huang, L.; Jin, Y.; Qian, Y. Microwave Synthesis of  $\text{AgBiS}_2$  Dendrites in Aqueous Solution. *Inorg. Chem. Commun.* **2003**, *6*, 710–712.
6. Kwon, S. G.; Hyeon, T. Formation Mechanisms of Uniform Nanocrystals via Hot-Injection and Heat-Up Methods. *Small.* **2011**, *7*, 2685–2702.
7. Embden, J. V.; Chesman, A. S. R.; Jasieniak, J. J. The Heat-Up Synthesis of Colloidal Nanocrystals. *Chem. Mater.* **2015**, *27*, 2246–2285.
8. Murray, C. B.; Sun, S.; Gaschler, W.; Doyle, H.; Betley, T. A.; Kagan, C. R. Colloidal Synthesis of Nanocrystals and Nanocrystal Superlattices. *IBM J. RES. & DEV.* **2001**, *45*, 47–56.
9. Chang, J.; Waclawik, E. R. Colloidal Semiconductor Nanocrystals: Controlled Synthesis and Surface Chemistry in Organic Media. *RSC Adv.*, **2014**, *4*, 23505–23527.
10. Murray, C. B.; Sun, S.; Gaschler, W.; Doyle, H.; Betley, T. A.; Kagan, C. R. Colloidal Synthesis of Nanocrystals and Nanocrystal Superlattices. *IBM J. RES. & DEV.* **2001**, *45*, 47–56.
11. Castro, S. L.; Bailey, S. G.; Raffaele, R. P.; Banger, K. K.; Hepp, A. F. Synthesis and Characterization of Colloidal  $\text{CuInS}_2$  Nanoparticles from a Molecular Single-Source Precursor. *J. Phys. Chem. B.* **2004**, *108*, 12429–12435.
12. LaMer, V. K.; Dinegar, R. H. Theory, Production and Mechanism of Formation of Monodispersed Hydrosols. *J. Am. Chem. Soc.*, **1950**, *72*, 4847–4854.
13. Jana, S. Advances in Nanoscale Alloys and Intermetallics: Low Temperature Solution Chemistry Synthesis and Application in Catalysis. *Dalton Trans.* **2015**, *44*, 18692–18717.

14. Murray, C. B.; Norris, D. J.; Bawendi, M. G. Synthesis and Characterization of Nearly Monodisperse CdE (E = Sulfur, Selenium, Tellurium) Semiconductor Nanocrystallites. *J. Am. Chem. Soc.*, **1993**, *115*, 8706–8715.
15. Yang, Y. A.; Wu, H.; Williams, K.R.; Cao, Y. C. Synthesis of CdSe and CdTe Nanocrystals without Precursor Injection. *Angew. Chem., Int. Ed.*, **2005**, *44*, 6712–6715.
16. Yin, Y.; Alivisatos, A. P. Colloidal Nanocrystal Synthesis and the Organic-Inorganic Interface. *Nature*, **2005**, *437*, 664–670.
17. Reiss, H. The Growth of Uniform Colloidal Dispersions. *J. Chem. Phys.* **1951**, *19*, 482–487.
18. Sperling, R. A.; Parak, W. J. Surface Modification, Functionalization and Bioconjugation of Colloidal Inorganic Nanoparticles. *Phil. Trans. R. Soc. A* **2010**, *368*, 1333–1383.
19. Weisbecker, C. S., Merritt, M. V.; Whitesides, G. M. Molecular Self-assembly of Aliphatic Thiols on Gold Colloids. *Langmuir* **1996**, *12*, 3763–3772.
20. Lin, S. Y., Tsai, Y. T., Chen, C.-C., Lin, C. M. & Chen, C.-H. Two-Step Functionalization of Neutral and Positively Charged Thiols onto Citrate-Stabilized Au Nanoparticles. *J. Phys. Chem. B* **2004**, *108*, 2134–2139.
21. Love, J. C., Estroff, L. A., Kriebel, J. K., Nuzzo, R. G. & Whitesides, G. M. Self-Assembled Monolayers of Thiolates on Metals as a Form of Nanotechnology. *Chem. Rev.* **2005**, *105*, 1103–1169.
22. Leff, D. V., Brandt, L. & Heath, J. R. Synthesis and Characterization of Hydrophobic, Organically-Soluble Gold Nanocrystals Functionalized with Primary Amines. *Langmuir* **1996**, *12*, 4723–4730.
23. Ji, X., Copenhaver, D., Sichmeller, C. & Peng, X. Ligand Bonding and Dynamics on Colloidal Nanocrystals at Room Temperature: The Case of Alkylamines on CdSe Nanocrystals. *J. Am. Chem. Soc.* **2008**, *130*, 5726–5735.
24. Mourdikoudis, S.; Liz-Marzán, S. M. Oleylamine in Nanoparticle Synthesis, *Chem. Mater.* **2013**, *25*, 1465–1476.
25. Wang, D.; Li, Y. Effective Octadecylamine System for Nanocrystal Synthesis. *Inorg. Chem.* **2011**, *50*, 5196–5202.
26. Ma, Y.; Zeng, J.; Li, W.; McKiernan, M.; Xe, Z.; Xia, Y. Seed-Mediated Synthesis of Truncated Gold Decahedrons with a AuCl/Oleylamine Complex as Precursor. *Adv. Mater.* **2010**, *22*, 1930–1934.

27. Xia, Y.; Xia, X.; Peng, H. C. Shape-Controlled Synthesis of Colloidal Metal Nanocrystals: Thermodynamic versus Kinetic Products. *J. Am. Chem. Soc.* **2015**, *137*, 7947–7966.
28. Zhang, Q.; Han, L.; Jing, H.; Blom, D. A.; Lin, Y.; Xin, H. L.; Wang, H. Facet Control of Gold Nanorods. *ACS Nano* **2016**, *10*, 2960–2974.
29. Hu, J.; Li, L.; Yang, W.; Manna, L.; Wang, L.; Alivisatos, A. P. Linearly Polarized Emission from Colloidal Semiconductor Quantum Rods. *Science* **2001**, *292*, 2060–2063.
30. Li, Y.; Zhang, L.; Yu, J. C.; Yu, S. H. Facet Effect of Copper(I) Sulfide Nanocrystals on Photoelectrochemical Properties. *Prog. Nat. Sci.* **2013**, *22*, 585–591.
31. Wu, W. Y.; Chakraborty, S.; Chang, C. K. L.; Guchhait, A.; Lin, M.; Chan, Y. Promoting 2D Growth in Colloidal Transition Metal Sulfide Semiconductor Nanostructures via Halide Ions. *Chem. Mater.* **2014**, *26*, 6120–6126.
32. Van der Stam, W.; Akkerman, Q. A.; Ke, X.; van Huis, M. A.; Bals, S.; de Mello Donega, C. Solution-Processable Ultrathin Size- and Shape-Controlled Colloidal  $\text{Cu}_{2-x}\text{S}$  Nanosheets. *Chem. Mater.* **2015**, *27*, 283–291.
33. Hsu, S. W.; Ngo, C.; Bryks, W.; Tao, A. R. Shape Focusing During the Anisotropic Growth of  $\text{CuS}$  Triangular Nanoprisms. *Chem. Mater.* **2015**, *27*, 4957–4963.
34. Kruszynska, M.; Borchert, H.; Bachmatiuk, A.; Rummeli, M. A.; Büchner, B.; Parisi, J.; Kolny-Olesiak, J. Predicting Nanocrystal Shape through Consideration of Surface-Ligand Interactions. *ACS Nano* **2012**, *6*, 5889–5896.
35. Zhai, Y.; Shim, M. Effects of Copper Precursor Reactivity on the Shape and Phase of Copper Sulfide Nanocrystals. *Chem. Mater.* **2017**, *29*, 2390–2397.
36. Trindade, T.; O'Brien, P.; Zhang, X. M.; Motevalli, M. Synthesis of  $\text{PbS}$  Nanocrystallites Using a Novel Single Molecule Precursors Approach: X-ray Single-Crystal Structure of  $\text{Pb}(\text{S}_2\text{CNEtPri})_2$ . *J. Mater. Chem.* **1997**, *7*, 1011–1016.
37. Tian, L.; Ng, M. T.; Venkatram, N.; Ji, W.; Vittal, J. J. Tadpole-Shaped  $\text{AgInSe}_2$  Nanocrystals from a Single Molecular Precursor and its Nonlinear Optical Properties. *Crysl Growth Des.* **2010**, *10*, 1237–1242.
38. Tian, L.; Elim, H. I.; Ji, W.; Vittal, J. J. One-Pot Synthesis and Third-Order Nonlinear Optical Properties of  $\text{AgInS}_2$  Nanocrystals. *Chem. Commun.* **2006**, 4276–4278.
39. Plante, I. J.; Zeid, T. W.; Yangab, P.; Mokari, T. Synthesis of Metal Sulfide Nanomaterials via Thermal Decomposition of Single-Source Precursors. *J. Mater. Chem.* **2010**, *20*, 6612–6617.

40. Tshemese, Z.; Khan, M. D.; Mlowe, S.; Revaprasadu, N. Synthesis and Characterization of PbS Nanoparticles in an Ionic Liquid Using Single and Dual Source Precursors. *Mater. Sci. Eng. B* **2018**, *227*, 116–121.
41. Saah, S. A.; Boadi, N. O.; Wilkins, C. Deposition of PbS Thin Films From Lead Hexadecyl and Octadecyl Xanthate Complexes Using The Spin Coating Method. *MRS Adv.* **2019**, *4*, 733–742.
42. Saah, S. A.; Khan, M. D.; McNaughter, P. D.; Awudza, J. A. M.; Revaprasadu, N.; O'Brien, P. Facile Synthesis of a  $\text{PbS}_{1-x}\text{Se}_x$  ( $0 \leq x \leq 1$ ) Solid Solution Using bis(N, Ndiethyl-N0 -naphthoylchalcogenoureato)lead(ii) complexes. *New J. Chem.* **2018**, *42*, 16 602–607.
43. Boadi, N. O.; Malik, M. A.; O'Brien, P.; Awudza, J. A. M. The Deposition of PbS and PbSe Thin Films From Lead Dichalcogenoimidophosphinates By AACVD. *Inorg. Chim. Acta* **2016**, *453*, 439–442.
44. Malik, S. N.; Akhtar, M.; Revaprasadu, N.; Qadeer, A.; Malik, M. A.; Dialkyldiselenophosphinatometal Complexes – A New Class of Single Source Precursors for Deposition of Metal Selenide Thin Films and Nanoparticles. *Mater. Sci. Eng.* **2014**, *64*, 1–9.
45. Cant, D. J. H. Surface Properties of Nanocrystalline PbS Films Deposited at The Water–Oil Interface: A Study of Atmospheric Aging. *Langmuir* **2015**, *31*, 1445–1453.
46. Trindade, T.; O'Brien, P. Synthesis of CdS and CdSe Nanoparticles by Thermolysis of Diethyldithio- or Diethyldiseleno-Carbamates of Cadmium. *J. Mater. Chem.* **1996**, *6*, 343–347.
47. Ludolph, B.; Malik, M. A.; O'Brien, P.; Revaprasadu, N. Novel Single Molecule Precursor Routes For The Direct Synthesis of Highly Monodispersed Quantum Dots of Cadmium or Zinc Sulfide or Selenide. *Chem. Commun.* **1998**, *17*, 1849–1850.
48. Tian, L.; Elim, H. I.; Ji, W.; Vittal, J. J. One-Pot Synthesis and Third-Order Nonlinear Optical Properties of  $\text{AgInS}_2$  Nanocrystals. *Chem. Commun.*, **2006**, *41*, 4276–4278.
49. Hendricks, M. P.; Campos, M. P.; Cleveland, G. T.; Plante, I. J.; Owen, J. S. A Tunable Library of Substituted Thiourea Precursors to Metal Sulfide Nanocrystals. *Science* **2015**, *348*, 1226–1230.
50. Castro, S. L.; Bailey, S. G.; Raffaella, R. P.; Banger K. K.; Hepp, A. F. Synthesis and Characterization of Colloidal  $\text{CuInS}_2$  Nanoparticles from a Molecular Single-Source Precursor. *J. Phys. Chem. B*, **2004**, *108*, 12429–12435.

51. Du, Y.; Xu, B.; Fu, T.; Cai, M.; Li, F.; Zhang, Y.; Wang, Q. Near-Infrared Photoluminescent Ag<sub>2</sub>S Quantum Dots From a Single Source Precursor. *J. Am. Chem. Soc.* **2010**, *132*, 1470–1471.
52. Zhang, Y.; Lu, J.; Shen, S.; Xu, H.; Wang, Q. Ultralarge Single Crystal SnS Rectangular Nanosheets. *Chem. Commun.* **2011**, *47*, 5226–5228.
53. Saah, S. A.; Boadi, N. O.; Adu-Poku, D.; Wilkins, C. Lead Ethyl Dithiocarbamates: Efficient Single-Source Precursors to PbS Nanocubes. *R. Soc. open sci.* **2019**, *6*, 190943.
54. Devendran, P.; Alagesan, T.; Ravindran, T. R.; Pandian, K. Synthesis of Spherical CdS Quantum Dots Using Cadmium Diethyldithiocarbamate as Single Source Precursor in Olive Oil Medium. *Current Nanoscience* **2014**, *10*, 302–307.
55. Deng, M.; Shen, S.; Zhang, Y.; Xu, H.; Wang, Q. A Generalized Strategy for Controlled Synthesis of Ternary Metal Sulfide Nanocrystals. *New J. Chem.* **2014**, *38*, 77–83.
56. Ido, H. Pnictides and Chalcogenides: Transition Metal Compounds, *Encyclopedia of Materials: Science and Technology* **2001**, *1*, 7121–7124.
57. Kumar, M.; Persson, C. Cu<sub>3</sub>BiS<sub>3</sub> as a Potential Photovoltaic Absorber with High Optical Efficiency. *Appl. Phys. Lett.* **2013**, *102*, 062109.
58. Li, L.; Coates, N.; Moses, D. Solution-Processed Inorganic Solar Cell Based on in Situ Synthesis and Film Deposition of CuInS<sub>2</sub> Nanocrystals. *J. Am. Chem. Soc.* **2010**, *132*, 22–23.
59. Pagan, E. H. A.; Leach, A. D. P.; Rhodes, J. M.; Sarkar, S.; Macdonald, J. E. A Synthetic Exploration of Metal–Semiconductor Hybrid Particles of CuInS<sub>2</sub>. *Chem. Mater.* **2015**, *27*, 7969–7976.
60. Miyakawa, M.; Kim, S. W.; Hirano, M.; Kohama, Y.; Kawaji, H.; Atake, T.; Ikegami, H.; Kono, K.; Hosono, H. Superconductivity in an Inorganic Electride 12CaO·7Al<sub>2</sub>O<sub>3</sub>:e<sup>-</sup>. *J. Am. Chem. Soc.* **2007**, *129*, 7270–7271.
61. Pradhan, N.; Efrima, S. Single-Precursor, One-Pot Versatile Synthesis under near Ambient Conditions of Tunable, Single and Dual Band Fluorescing Metal Sulfide Nanoparticles. *J. Am. Chem. Soc.* **2003**, *125*, 2050–2051.
62. Zhiguo, L.; Wei, C.; Jiehe, S. Large-Scale Preparation of CdS Quantum Dots by Direct Thermolysis of a Single-Source Precursor. *Nanotechnology* **2008**, *19*, 035602.
63. Brennan, J. G.; Siegrist, T.; Carroll, P. J.; Stuczynski, S. M.; Reynders, P.; Brus, L. E.; Steigerwald, M. L. Bulk and Nanostructure Group II-VI Compounds from Molecular Organometallic Precursors. *Chem. Mater.* **1990**, *2*, 403–409.

64. Cumberland, S. L.; Hanif, K. M.; Gregory, A. J.; Khitrov, A.; Strouse, G. F.; Woessner, S. M.; Yun, C. S. Inorganic Clusters as Single-Source Precursors for Preparation of CdSe, ZnSe, and CdSe/ZnS Nanomaterials. *Chem. Mater.* **2002**, *14*, 1576–1584.
65. Yang, Y. A.; Wu, H.; Williams, K. R.; Cao, Y. C. Synthesis of CdSe and CdTe Nanocrystals without Precursor Injection. *Angew. Chem., Int. Ed.* **2005**, *44*, 6712–6715.
66. Li, Z.; Peng, X. Size/Shape-Controlled Synthesis of Colloidal CdSe Quantum Disks: Ligand and Temperature Effects. *J. Am. Chem. Soc.* **2011**, *133*, 17248–17256.
67. Kanehara, M.; Arakawa, H.; Honda, T.; Saruyama, M.; Teranishi, T. Large-Scale Synthesis of High-Quality Metal Sulfide Semiconductor Quantum Dots with Tunable Surface-Plasmon Resonance Frequencies. *Chem. – Eur. J.* **2012**, *18*, 9230–9238.
68. Larsen, T. H.; Sigman, M.; Ghezelbash, A.; Doty, R. C.; Korgel, B. A. Solventless Synthesis of Copper Sulfide Nanorods by Thermolysis of a Single Source Thiolate-Derived Precursor. *J. Am. Chem. Soc.* **2003**, *125*, 5638–5639.
69. Du, X.-S.; Mo, M.; Zheng, R.; Lim, S.-H.; Meng, Y.; Mai, Y.-W. Shape-Controlled Synthesis and Assembly of Copper Sulfide Nanoparticles. *Cryst Growth Des.* **2008**, *8*, 2032–2035.
70. Choi, S.-H.; An, K.; Kim, E.-G.; Yu, J. H.; Kim, J. H.; Hyeon, T. Simple and Generalized Synthesis of Semiconducting Metal Sulfide Nanocrystals. *Adv. Funct. Mater.* **2009**, *19*, 1645–1649.
71. Shen, H.; Wang, H.; Yuan, H.; Ma, L.; Li, L. S. Size-, shape-, and Assembly-Controlled Synthesis of Cu<sub>2-x</sub>Se Nanocrystals via a Non-Injection Phosphine-Free Colloidal Method. *CrystEngComm.* **2012**, *14*, 555–560.
72. Jeong, S.; Han, J. H.; Jang, J. T.; Seo, J. W.; Kim, J. G.; Cheon, J. Transformative Two-Dimensional Layered Nanocrystals. *J. Am. Chem. Soc.* **2011**, *133*, 14500–14503.
73. Jang, J. T.; Jeong, S.; Seo, J. W.; Kim, M. C.; Sim, E.; Oh, Y.; Nam, S.; Park, B.; Cheon, J. Ultrathin Zirconium Disulfide Nanodiscs. *J. Am. Chem. Soc.* **2011**, *133*, 7636–7639.
74. Vaughn, D. D.; Patel, R. J.; Hickner, M. A.; Schaak, R. E. Single-Crystal Colloidal Nanosheets of GeS and GeSe. *J. Am. Chem. Soc.* **2010**, *132*, 15170–15172.
75. Park, K. H.; Jang, K.; Kim, S.; Kim, H. J.; Son, S. U. Phase-Controlled One-Dimensional Shape Evolution of InSe Nanocrystals. *J. Am. Chem. Soc.* **2006**, *128*, 14780–14781.
76. Franzman, M. A.; Schlenker, C. W.; Thomson, M. E.; Brutchey, R. L. Solution-Phase Synthesis of SnSe Nanocrystals for Use in Solar Cells. *J. Am. Chem. Soc.* **2010**, *132*, 4060–4061.

77. Lu, W.; Ding, Y.; Chen, Y.; Wang Z. L.; Fang, J. Bismuth Telluride Hexagonal Nanoplatelets and Their Two-Step Epitaxial Growth. *J. Am. Chem. Soc.* **2005**, *127*, 10112–10116.
78. Sekar, P.; Greyson, E. C.; Barton, J. E.; Odom, T. W. Synthesis of Nanoscale NbSe<sub>2</sub> Materials From Molecular Precursors. *J. Am. Chem. Soc.* **2005**, *127*, 2054–2055.
79. Liao, H.-C.; Jao, M. -H.; Shyue, J. -J.; Chen, Y. -F.; Su, W. -F. Facile Synthesis of Wurtzite Copper–Zinc–Tin Sulfide Nanocrystals from Plasmonic Djurleite Nuclei. *J. Mater. Chem. A* **2013**, *1*, 337–341.
80. Ouyang, J.; Vincent, M.; Kingston, D.; Descours, P.; Boivineau, T.; Zaman, M. B.; Wu, X.; Yu, K. Noninjection, One-Pot Synthesis of Photoluminescent Colloidal Homogeneously Alloyed CdSeS Quantum Dots. *J. Phys. Chem. C* **2009**, *113*, 5193–5200.
81. Wang, R.; Calvignanello, O.; Ratcliffe, C. I.; Donald, X. W.; Leek, M.; Zaman, M. B.; Kingston, D.; Ripmeester, J. A.; Yu, K. Homogeneously-Alloyed CdTeSe Single-Sized Nanocrystals with Bandgap Photoluminescence. *J. Phys. Chem. C* **2009**, *113*, 3402–3408.
82. Shen, H.; Niu, J.; Wang, H.; Song, L. L. One-pot Synthesis of High Quality CdE (E = Te, Te<sub>x</sub>Se<sub>1-x</sub>, Se) Nanocrystals without Using Pyrophoric Reagents. *Mater. Chem. Phys.* **2012**, *135*, 1122–1127.
83. Chiang, M.-Y.; Chang, S. -H.; Chen, C. -Y.; Yuan, F. -W.; Tuan, H. Y. Quaternary CuIn(S<sub>1-x</sub>Se<sub>x</sub>)<sub>2</sub> Nanocrystals: Facile Heating-Up Synthesis, Band Gap Tuning, and Gram-Scale Production. *J. Phys. Chem. C* **2011**, *115*, 1592–1599.
84. Song, W.-S.; Kim, J. -H.; Lee, J. -H.; Lee, H. -S.; Dob, Y. R.; Yang, H. Synthesis of Color-Tunable Cu–In–Ga–S Solid Solution Quantum Dots with High Quantum Yields for Application to White Light-Emitting Diodes. *J. Mater. Chem.* **2012**, *22*, 21901–21908.
85. Zhong, H.; Shun S. Lo, S. S.; Mirkovic, T.; Li, T.; Ding, Y.; Li, Y.; Scholes, G. D. Noninjection Gram-Scale Synthesis of Monodisperse Pyramidal CuInS<sub>2</sub> Nanocrystals and Their Size-Dependent Properties. *ACS Nano* **2010**, *4*, 5253–5262.
86. Zhong, H.; Zhou, Y.; Ye, M.; He, Y.; Ye, J.; He, C.; Yang, C.; Li, Y. Controlled Synthesis and Optical Properties of Colloidal Ternary Chalcogenide CuInS<sub>2</sub> Nanocrystals. *Chem. Mater.* **2008**, *20*, 6434–6443.
87. Connor, S. T.; Hsu, C. -M.; Weil, B. D.; Aloni, S.; Cui, Y. Phase Transformation of Biphasic Cu<sub>2</sub>S–CuInS<sub>2</sub> to Monophasic CuInS<sub>2</sub> Nanorods. *J. Am. Chem. Soc.* **2009**, *131*, 4962–4966.
88. Panthani, M. G.; Akhavan, V.; Goodfellow, B.; Schmidtke, J. P.; Dunn, L.; Dodabalapur, A.; Barbara, P. F.; Korgel, B. A. Synthesis of CuInS<sub>2</sub>, CuInSe<sub>2</sub>, and Cu(In<sub>x</sub>Ga<sub>1-x</sub>)Se<sub>2</sub> (CIGS) Nanocrystal “Inks” for Printable Photovoltaics. *J. Am. Chem. Soc.* **2008**, *130*, 16770–16777.

89. Ghosh, A.; Palchoudhury, S.; Thangavel, R.; Zhou, Z.; Naghibolashrafi, N.; Ramasamy, K.; Gupta, A. A new family of wurtzite-phase  $\text{Cu}_2\text{ZnAS}_{4-x}$  and  $\text{CuZn}_2\text{AS}_4$  (A = Al, Ga, In) Nanocrystals for Solar Energy Conversion Applications. *Chem. Commun.* **2016**, *52*, 264–267.
90. Ramasamy, K.; Shinde, P. S.; Naghibolashrafi, N.; Pan, S.; Gupta, A. Nanocrystals of  $\text{CuMSnS}_4$  (M = In or Ga) for Solar Energy Conversion Applications. *Chem. Commun.* **2018**, *54*, 11757–11760.
91. Ramasamy, K.; Mazumdar, D.; Zhou, Z.; Wang, Y. H. A.; Gupta, A. Colloidal Synthesis of Magnetic  $\text{CuCr}_2\text{S}_4$  Nanocrystals and Nanoclusters. *J. A. Chem. Soc.* **2011**, *133*, 20716–20719.
92. Wang, Y. H. A.; Bao, N.; Shen, L.; Padhan, P.; Gupta, A. Size-Controlled Synthesis of Magnetic  $\text{CuCr}_2\text{Se}_4$  Nanocrystals. *J. Am. Chem. Soc.* **2007**, *129*, 12408–12409.
93. Pang, C.; Yang, R.; Singh, A.; Chen, H.; Bowman, M. K.; Bao, N.; Shen, L.; Gupta, A. Colloidal Synthesis and Magnetic Properties of Anisotropic-Shaped Spinel  $\text{CuCr}_2\text{Se}_4$  Nanocrystals. *RSC Adv.* **2017**, *7*, 31173–31179.
94. Ramasamy, K.; Sims, H.; Keshavarz, S.; Naghibolashrafi, N.; Gupta, A. Nanocrystals of  $\text{CuCr}_2\text{S}_{4-x}\text{Se}_x$  Chalcospinels with Tunable Magnetic Properties. *J. Mater. Chem. C* **2016**, *4*, 3628–3639.
95. Ramasamy, K.; Mazumdar, D.; Bennett R. D.; Gupta, A. Syntheses and Magnetic Properties of  $\text{Cr}_2\text{Te}_3$  and  $\text{CuCr}_2\text{Te}_4$  Nanocrystals. *Chem. Commun.* **2012**, *48*, 5656–5658.
96. Ramasamy, K.; Sims, H.; Gupta, R. K.; Kumar, D.; Butler, W. H.; Gupta, A.  $\text{Co}_x\text{Cu}_{1-x}\text{Cr}_2\text{S}_4$  Nanocrystals: Synthesis, Magnetism, and Band Structure Calculations. *Chem. Mater.* **2013**, *25*, 4003–4009.
97. Ramasamy, K.; Sims, H.; Butler, W. H.; Gupta, A. Mono-, Few-, and Multiple Layers of Copper Antimony Sulfide ( $\text{CuSbS}_2$ ): A Ternary Layered Sulfide. *J. Am. Chem. Soc.* **2014**, *136*, 1587–1598.
98. Ramasamy, K.; Gupta, R. K.; Palchoudhury, S.; Ivanov, S.; Gupta, A. Layer-Structured Copper Antimony Chalcogenides ( $\text{CuSbSe}_x\text{S}_{2-x}$ ): Stable Electrode Materials for Supercapacitors. *Chem. Mater.* **2015**, *27*, 379–386.
99. Wilttrout, A. M.; Read, C. G.; Spencer, E. M.; Schaak, R. E. Solution Synthesis of Thiospinel  $\text{CuCo}_2\text{S}_4$  Nanoparticles. *Inorg. Chem.* **2016**, *55*, 221–226.
100. Tang, J.; Hinds, S.; Kelley, S. K.; Sargent, E. H. Synthesis of Colloidal  $\text{CuGaSe}_2$ ,  $\text{CuInSe}_2$ , and  $\text{Cu(InGa)Se}_2$  Nanoparticles. *Chem. Mater.* **2008**, *20*, 6906–6910.

101. Zarur, A. J.; Ying, J. Y. Reverse Microemulsion Synthesis of Nanostructured Complex Oxides for Catalytic Combustion. *Nature* **2000**, *403*, 65–67.
102. Berkovsky, B. M.; Medvedev, V. F.; Krovov, M. S. *Magnetic Fluids: Engineering Applications*; Oxford University Press: Oxford, U.K., **1993**.
103. Ziolo, R. F.; Giannelis, E. P.; Weinstein, M. P.; O'Horo, B. N.; Ganguly, M. V.; Russel, M. W.; Huffman, D. R. Matrix-Mediated Synthesis of Nanocrystalline  $\gamma$ -Fe<sub>2</sub>O<sub>3</sub>: A New Optically Transparent Magnetic Material. *Science* **1992**, *257*, 219–223.
104. Sun, S. H.; Murray, C. B.; Weller, D.; Folks, L.; Moser. Monodisperse FePt Nanoparticles and Ferromagnetic FePt Nanocrystal Superlattices. *Science* **2000**, *287*, 1989–1992.
105. Yoo, D.; Jeong, H.; Noh, S. H.; Lee, J. H.; Cheon, J. Magnetically Triggered Dual Functional Nanoparticles for Resistance-Free Apoptotic Hyperthermia. *Angew. Chem., Int. Ed.* **2013**, *52*, 13047–13051.
106. Li, L.; Coates, N.; Moses, D. Solution-Processed Inorganic Solar Cell Based on in Situ Synthesis and Film Deposition of CuInS<sub>2</sub> Nanocrystals. *J. Am. Chem. Soc.* **2010**, *132*, 22–23.
107. Pagan, E. H., A.; Leach, A. D., P.; Rhodes, J. M.; Sarkar, S.; Macdonald, J. E. A Synthetic Exploration of Metal–Semiconductor Hybrid Particles of CuInS<sub>2</sub>. *Chem. Mater.* **2015**, *27*, 7969–7976.
108. Baltzer, P. K.; Lehmann, H. W.; Robbins, M. Insulating Ferromagnetic Spinel. *Phys. Rev. Lett.* **1965**, *15*, 493–495.
109. Ramesha, K.; Seshadri, R. Solvothermal Preparation of Ferromagnetic Sub-Micron Spinel CuCr<sub>2</sub>Se<sub>4</sub> Particles. *Solid State Sci.* **2004**, *6*, 841–845.
110. Kim, D.; Gedanken, A.; Tver'yanovich, Y. S.; Lee, D. W.; Kim, B. K. Synthesis and Characterization of Nanocrystalline CuCr<sub>2</sub>Se<sub>4</sub> particles. *Mater. Lett.* **2006**, *60*, 2807–2809.
111. Lin, C. R.; Yeh, C. L.; Lu, S. Z.; Lyubutin, I. S.; Wang, S. C.; Suzdalev, I. P. Synthesis, Characterization and Magnetic Properties of Nearly Monodisperse CuCr<sub>2</sub>Se<sub>4</sub> Nanoparticles. *Nanotechnology* **2010**, *21*, 235603.

## CHAPTER 2

### EXPERIMENTAL METHODS

For our research, we adopted the colloidal synthesis of binary and ternary metal chalcogenides based on copper and chromium by the heat-up (HU) and hot-injection (HI) methods as a choice of process for the preparation of nanocrystals.

The next step, as it is usual with processing any novel material, was to characterize the NCs by the available structural and microstructural instrumental techniques including X-ray Diffraction (XRD), Transmission Electron Microscopy (TEM), Scanning Electron Microscopy (SEM), X-ray Photoelectron Spectroscopy (XPS), and Raman Spectroscopy. Finally, the magnetic behavior of these materials was studied using Vibrating Sample Magnetometry (VSM).

#### **2.1 Synthesis of NCs**

The NCs of metal chalcogenides were prepared using HU and HI methods. In chapter 1, we have described the fundamentals of these two strategies, along with their similarities and differences. The synthesis procedures were carried out using a standard Schlenk line setup in the fume hood and under the nitrogen atmosphere. Figure 2.1 represents the general view of the experimental setup we have used for the sample preparation. The reaction temperature was controlled with a multi-voltage temperature controller. The mixture of the reagents was degassed under vacuum at room temperature for almost 15 min and put back under nitrogen. The described process was repeated several times before increasing the reaction temperature. In the case of the hot-injection method, the chalcogenide sources, e.g., 1-dodecanethiol or selenium, were treated in a separate vessel under a similar condition.

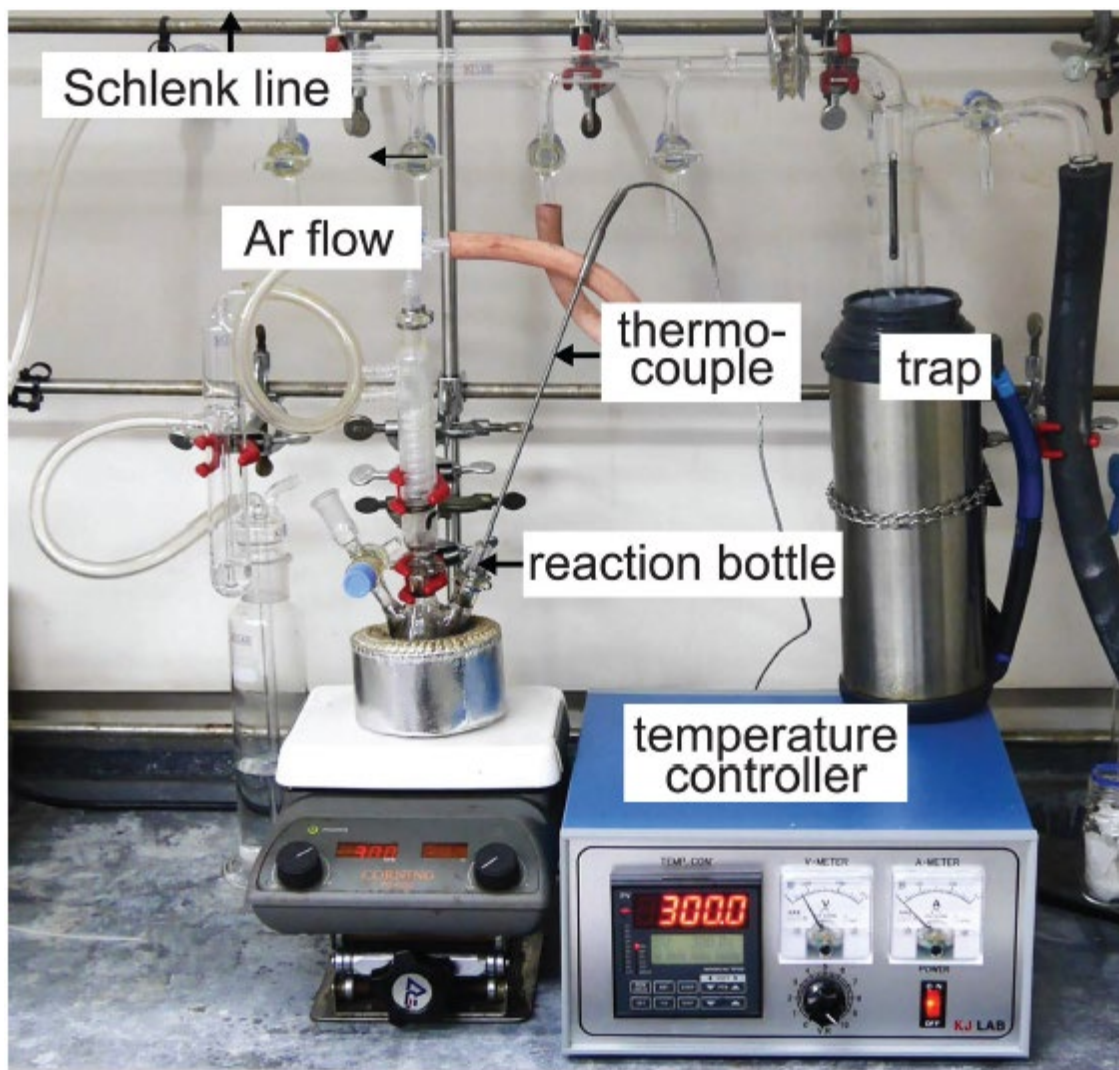


Figure 2.1: Experimental setup for the colloidal synthesis of NCs. Reprinted with permission from ref. 1.

## 2.2 X-ray Diffraction Analyses

X-ray diffraction technique or XRD is a fast, simple, and very useful method for characterizing crystalline materials. This technique is used to determine the crystal structure from the diffraction data of an incident X-ray beam on the surface of a crystalline material, and could provide structural parameters and crystal orientations.

A specific wavelength of a monochromatic X-ray impingement on a crystalline material and interacts with the electron cloud of the atoms within the material and scattered by them eventually. The scattered wave is called “the atomic scattering factor” and related to the number of the electrons within the atom and consequently differing from atom to atom. The scattered beams could be in phase or out of phase in one another. When the Bragg’s condition of diffraction is met ( $2d\sin\theta = n\lambda$ ), constructive interference occurs (Figure 2.2). Bragg law expresses the relationship between the wavelength,  $\lambda$ , and interplanar spacing,  $d$  in which  $n$  is the number of beam wavelengths from different atomic planes and usually is considered to be unit value.<sup>2,3</sup> The scattered waves must have a path difference related to an integer of the wavelength to the occurrence of diffraction. Out of phase, scattered waves cancel out each other. The X-ray diffraction pattern is yielded when the intensity of the diffracted X-ray beams is plotted as a function of  $2\theta$  angle of incident X-ray. The outcome is a spectrum unique to that material, and the position ( $2\theta$ ), and intensity of the peaks in an XRD pattern is a signature of a given phase of a material.

A schematic view of an X-ray diffractometer is shown in figure 2.3, indicating that the X-ray emitter and signal detector are placed on a circle, and the sample holder loaded with the test sample is located in the center of the circle. As represented in figure. 2.3 b, the sample holder could be rotated in three dimensions ( $\omega$ ,  $\psi$ ,  $\phi$ ). The XRD analysis was performed on a Bruker D2 PHASER using a Cu source ( $\text{CuK}_{\alpha 1}$ ,  $\lambda = 1.54059\text{\AA}$ ) operating at 30 kV and 10 mA.

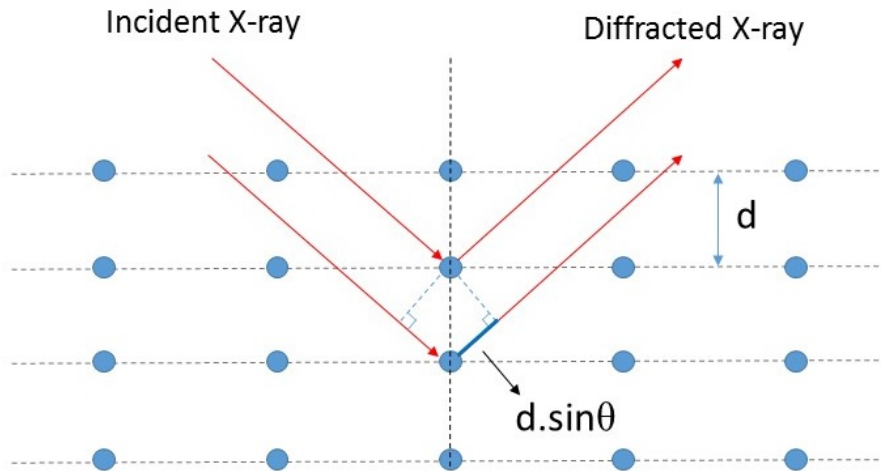


Figure 2.2: Schematic representation of the X-ray diffraction mechanism.

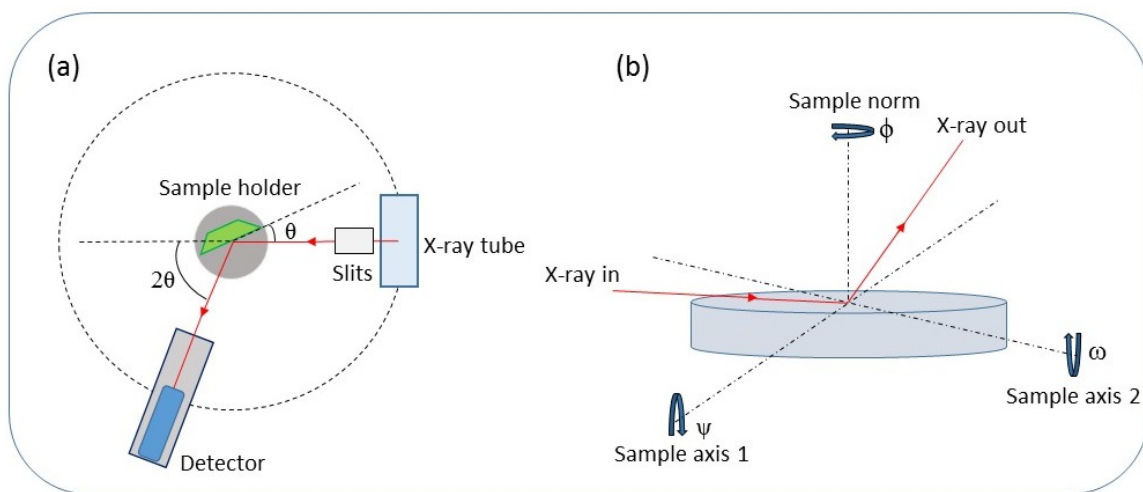


Figure 2.3: Schematic representation of the X-ray diffractometer.

## 2.3 Electron Microscopy Methods

In these studies, we have used electron microscopy techniques to characterize the microstructure of the nanocrystals and their features. The instruments used in this research were Transmission Electron Microscope (TEM) and Scanning Electron Microscope (SEM).

TEM uses transmitted electrons through samples to create images. The main parts of the TEM body are illumination system, objective lens and stage, and imaging system. The schematic depiction of the TEM setup is shown in figure 2.4.

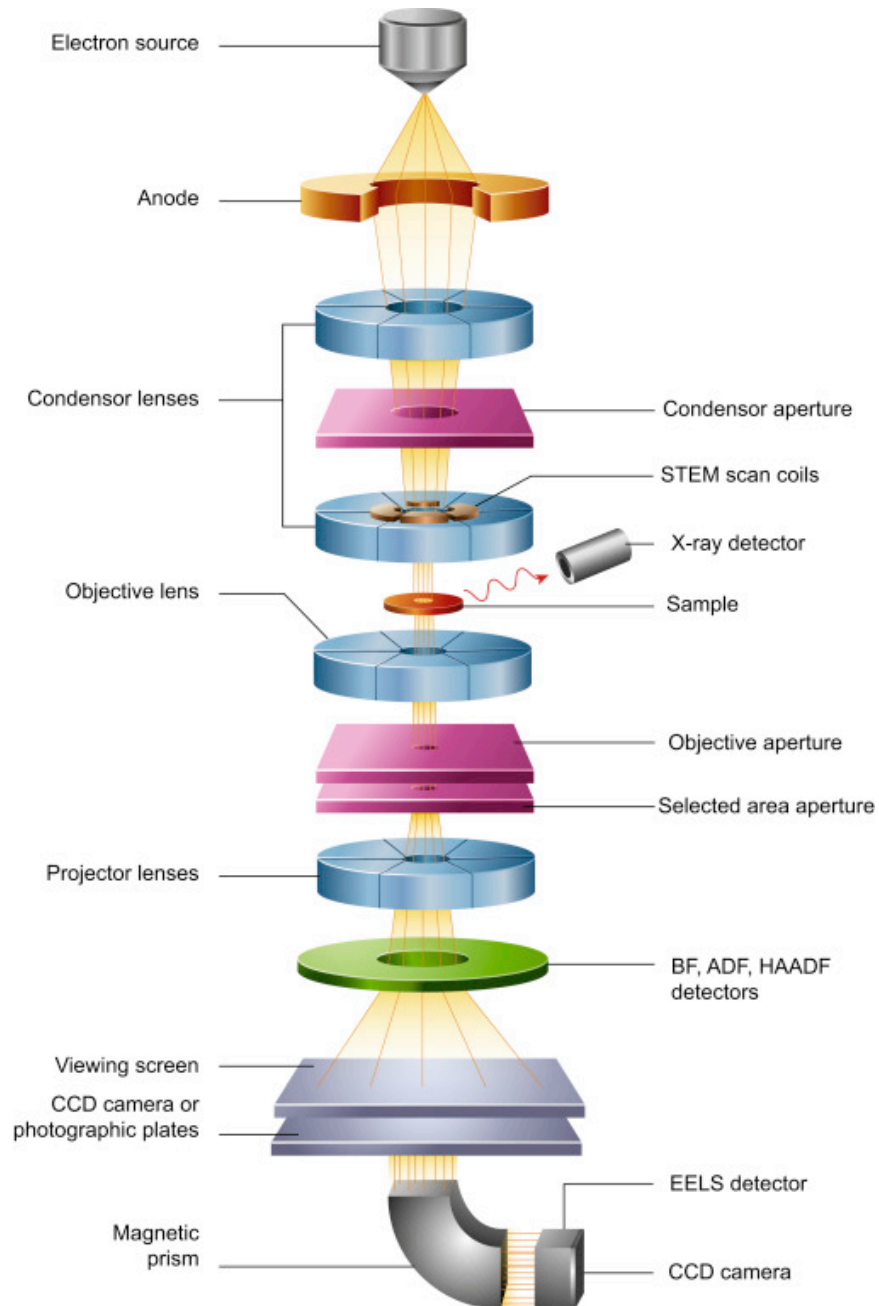


Figure 2.4: Schematic diagram of TEM. Reprinted with permission from ref. 4.

The illumination system takes the electrons from the gun source (FEG or thermionic), passes them through condenser lenses C1 & C2, and transfers them to the specimen. This system operates in parallel or convergent beam mode. The parallel beam mode is used in TEM imaging and selected area diffraction (SAD) patterns, whereas the convergent beam mode is used in scanning transmission electron microscopy (STEM). The TEM images and diffraction patterns are produced in the objective lens and stage (specimen holder).

The TEM alignment procedure starts from the top of the microscope column down to the last condenser, which is the objective lens. During the alignment of this part, the specimen height on the optic axis should be fixed well, so that focusing and under focusing of the objective lens controls the magnification of the image. Unwanted Scattered electrons are blocked by objective aperture and SAD aperture in order to create the high-contrast image and diffraction patterns (DP), respectively.<sup>5</sup> Figure 2.5 indicated the schematic view of the two basic operations of a TEM imaging system, including diffraction mode and image mode.

In this study, the samples have been prepared by dropping diluted hexane suspensions of nanoparticles onto carbon-coated nickel grids. TEM, High-Resolution TEM (HRTEM) imaging, High-Angle Annular Dark-Field (HAADF)- Scanning TEM (STEM) imaging, Energy-Dispersive X-ray Spectroscopy (EDS), and Selected Area Electron Diffraction (SAED) patterns were performed using an FEI-Tecnai, 200 kV transmission electron microscope equipped with a GATAN Rio camera.

Scanning Transmission Electron Microscopy (STEM) experiments were carried out using the aberration-corrected Nion UltraSTEM™ 200 (operating at 200 kV) at Oak Ridge National Laboratory. The microscope is equipped with a cold field-emission electron gun and a fifth-order aberration corrector. Electron energy loss spectra (EELS) were acquired using a dual-range

Gatan Enfimum spectrometer with a collection semi-angle of 33 mrad and energy dispersion of 0.5 eV. We used a power law to subtract the background signal from the characteristic core-loss edges for each element. The TEM grids were heated to 160° C prior to STEM experiments to remove excess solvent and impurities.

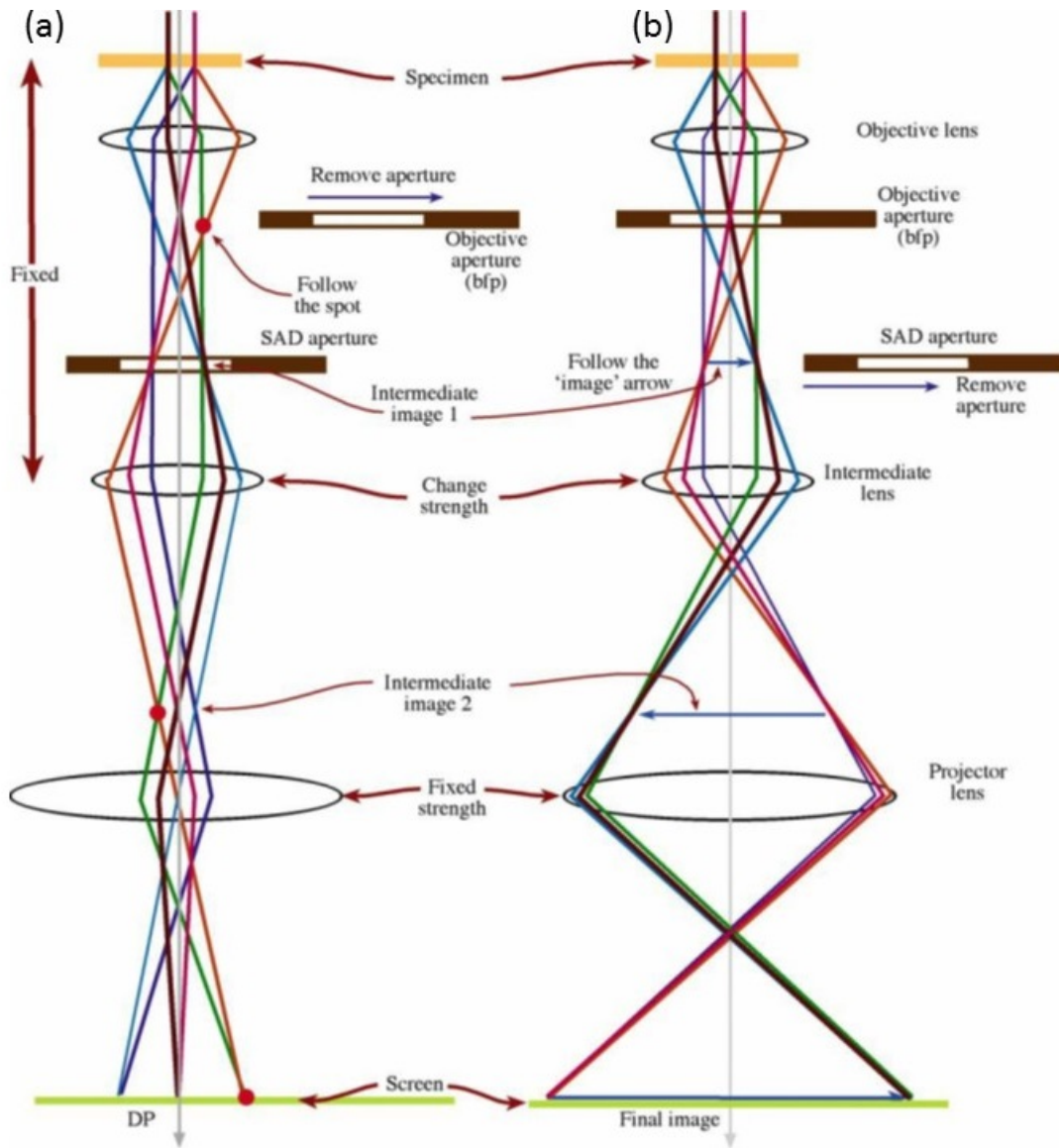


Figure 2.5: Schematic diagram of (a) diffraction mode and (b) image mode in TEM. Reprinted with permission from ref. 5.

The schematic depiction of SEM setup is shown in figure 2.6. In SEM electrons are focused into a small electron probe and scanned through the surface of the sample.

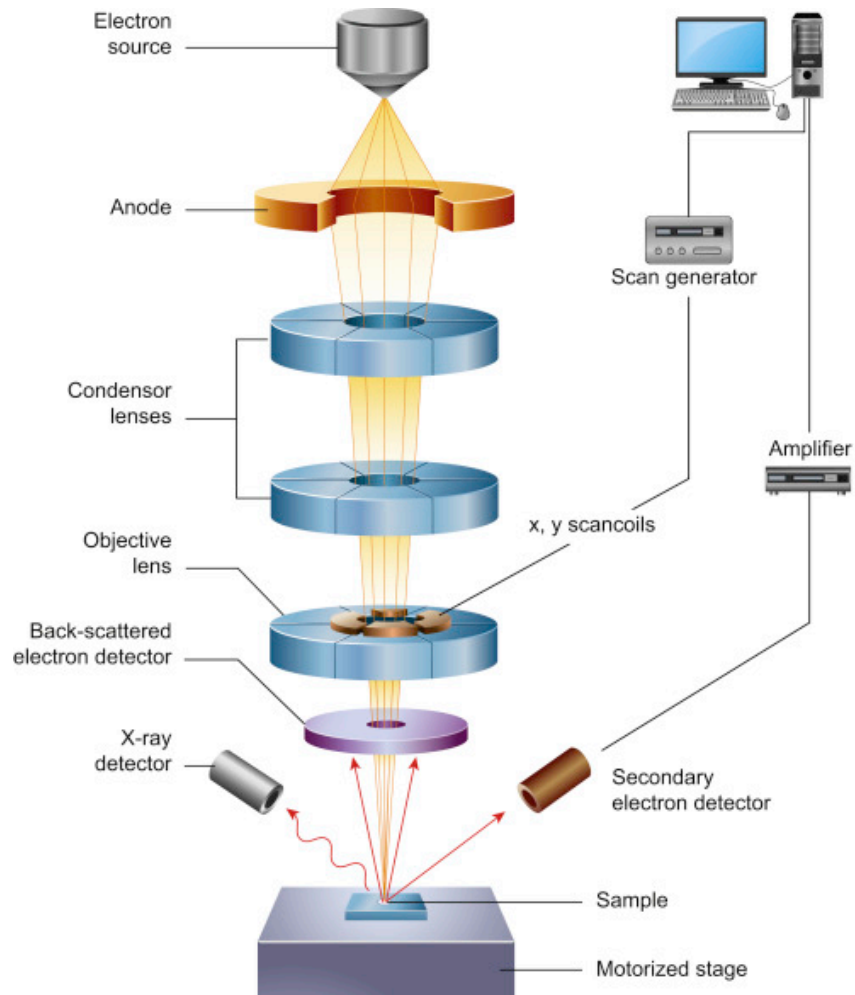


Figure 2.6: Schematic diagram of SEM. Reprinted with permission from ref. 4.

The incident beam of primary electron generates two main types of electrons during the interaction with the sample surface, so-called backscattered electrons (BSE) and secondary electrons (SE). BSE are primarily incident electrons reflected from the sample surface at angles between  $90^\circ$  to  $180^\circ$  with respect to the incident beam.<sup>6,7</sup> The energy of the BSE usually lies

between the energy of the incident beam and 50 eV. SE are resulting from the interaction of the beam with the specimen. SE have lower energy than BSE and could penetrate the sample weakly in about 3 to 10 nanometers.<sup>6</sup> The energy of the SE could be as near to zero as possible.

It is easy to collect secondary electrons, and the majority of the SEM images are taken in the SE mode. SE could generate a topographic image of the sample surface with resolutions of up to 1 nm. In this work, SEM analysis was performed using a JEOL 7000 FESEM equipped with an EDS detector.

#### **2.4 X-ray Photoelectron Spectroscopy (XPS)**

X-ray photoelectron spectroscopy is a surface-sensitive quantitative technique to measure the elemental composition, in which irradiating the sample via X-ray with constant energy ( $h\nu$ ) escapes electrons from the surface of the sample, and the spectrum obtained during the simultaneously measuring the kinetic energy and the number escaped electrons. In principle, XPS could easily detect all elements except hydrogen and helium. The relationship between the energy of the incident X-ray ( $h\nu$ ) and the kinetic energy of escaped electrons ( $E_K$ ) is expressed as  $h\nu = E_K + E_B + \phi$ ; where  $\phi$  is the work function of sample and  $E_B$  is the binding energy of the electron to nucleus. The  $E_B$  value, along with chemical shift, is utilized for the identification of an element. The XPS analysis needs to be performed under a high vacuum ( $P < 10^{-8}$  millibar) condition. Figure 2.7 represented the schematic view of the XPS system. In general, XPS instrument uses a focused beam of monochromic X-rays (Al K $\alpha$ ; diameter of 20-500  $\mu\text{m}$ ) or a broad beam of polychromatic X-rays (Al K $\alpha$  or Mg K $\alpha$ ; diameter of 10-30 mm).<sup>8</sup>

In this work, XPS data were measured using a Kratos Axis Ultra DLD equipped with Al-monochromatic source (15 kV, 10 mA). The selected regions were scanned using a pass energy

of 40 eV. Specimens were loaded into a transfer chamber and evacuated for 12 h (base pressure was kept under  $3 \times 10^{-10}$  Torr).

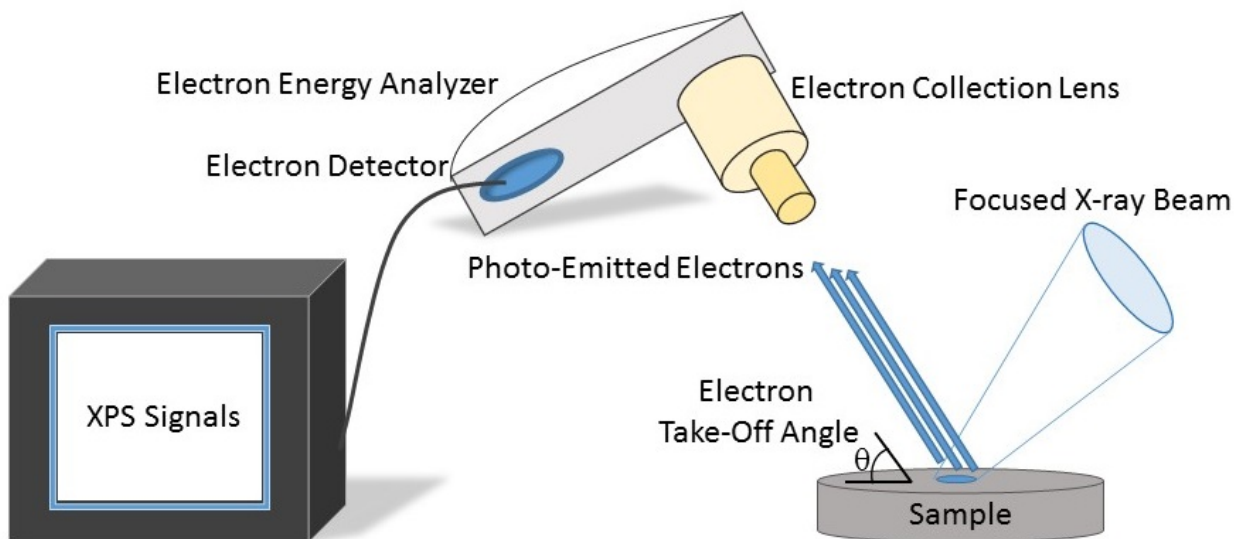


Figure 2.7: Schematic view of XPS system.

## 2.5 Raman Spectroscopy

Raman spectroscopy is a technique used to determine vibrational modes of materials and is based upon the interaction of photons with the chemical bonds within the molecules. The schematic view of a Raman spectrometer is shown in figure 2.8. Modern Raman setups use laser as the excitation light source. In general, the sample is illuminated with the laser and causes electromagnetic radiation that is collected from the illuminated spot with a lens and sent and passed through a monochromator. Elastically scattered radiation called Rayleigh scattered lines that have the same wavelength corresponding to the laser line is filtered, and the rest of the collected light is dispersed onto a Charged Coupled Device (CCD) detector. The interaction of the laser light with the vibrational states of the sample resulting in the energy of the photons of

the laser is increased or decreased, and this energy shift gives information about the vibrational modes of the sample.<sup>9</sup>

Raman spectroscopy characterization was performed on a Horiba Jobin Yvon LabRAM HR800 using 532 nm laser as the excitation laser. The laser light was focused into a line on the sample through a cylindrical lens and an air objective lens.

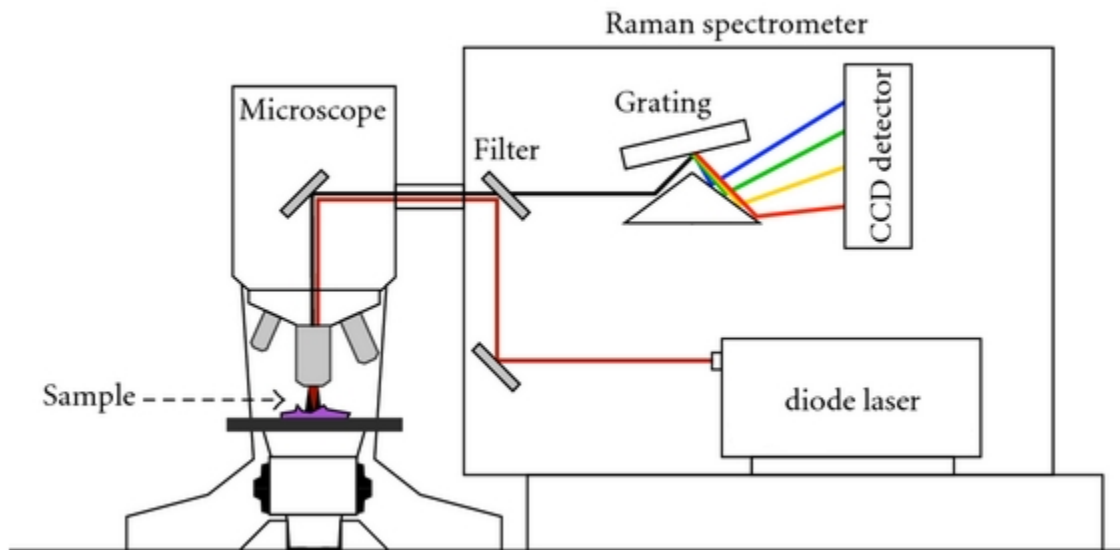


Figure 2.8: A schematic representation of Raman spectroscopy system. Reprinted with permission from ref. 10.

## 2.6 Magnetic Measurements

Vibrating Sample Magnetometer (VSM) system is one of the widely used techniques for measuring magnetization and hysteresis loops of magnetic materials. VSM is fast and easy to use and has excellent features, including high sensitivity and versatility. The basic principle of a VSM is based on Faraday's Law of Induction, which means that a changing magnetic field will generate an electric field. The VSM instrument has a source of a magnetic field, which is usually

an electromagnet. The magnetometer measures the magnetic moment as a function of an applied magnetic field, time, and temperature. Figure 2.9 shows a schematic diagram of a VSM system.

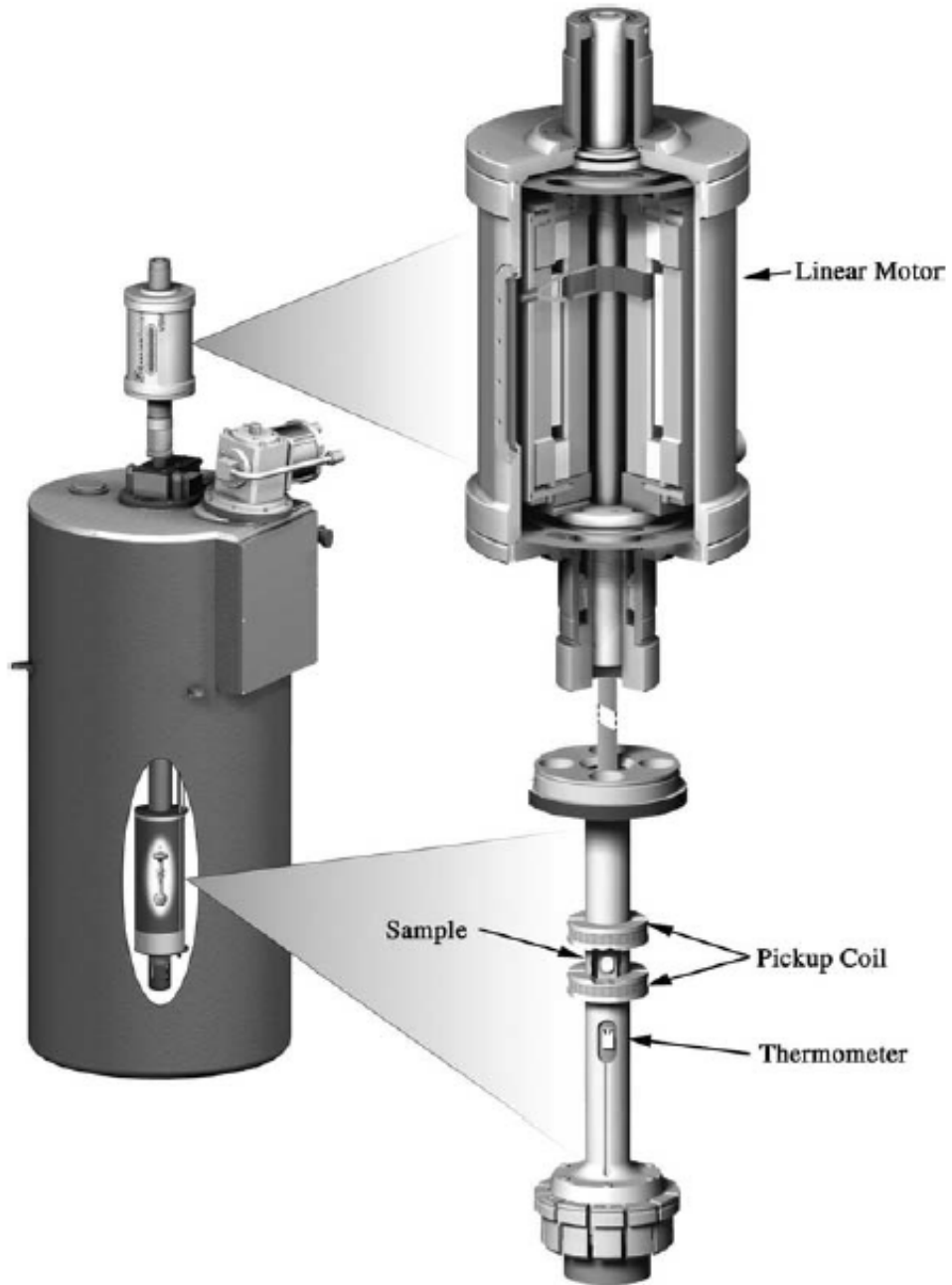


Figure 2.9: Schematic depiction of VSM system. Reprinted with permission from ref. 12.

The VSM system is based on the change in the flux in a coil when a magnetized sample is vibrated near it.<sup>12</sup> The applied magnetic field sets on a constant value. The magnetization of the sample will change with the movement of the sample during vibration. The change of the mentioned magnetic flux induces a voltage in the sensing coils. The induced voltage is proportional to the sample's magnetization. The graph of magnetization ( $M$ ) as a function of an external magnetic field ( $H$ ) is called hysteresis loop and is widely used to represent the magnetic behavior of magnetic materials. The VSM could operate in a wide range of temperatures from near 0 K up to 1000 K.<sup>11</sup> This characteristic makes VSM useful in deriving the magnetic thermal behavior of materials such as Curie temperature ( $T_C$ ).

For this study, the measurements were performed using a Quantum Design Dynacool Physical Properties Measurement System (PPMS) equipped with Vibrating Sample Magnetometer (VSM). Figure 2.10 displays the stacking model diagram of the sample measurement using a PPMS.<sup>13</sup>

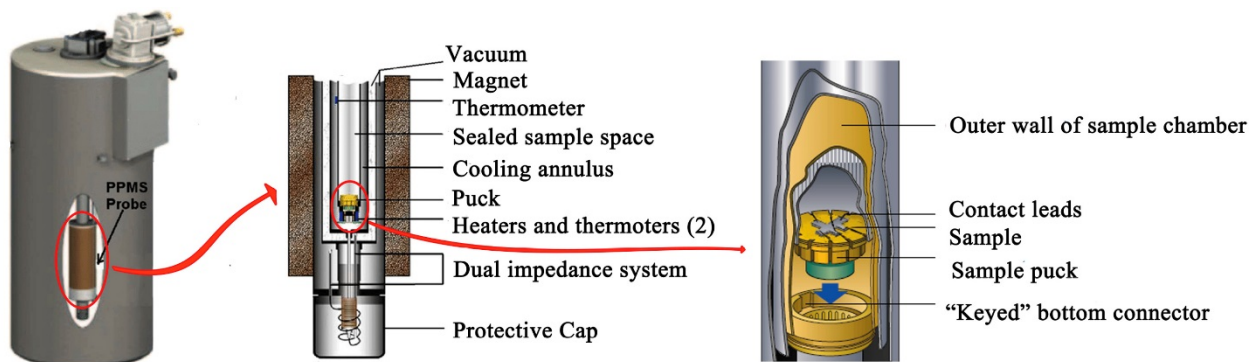


Figure 2.10: Schematic diagram of the sample measurement in PPMS. Reprinted with permission from ref. 13.

## 2.7 References

1. Kim, J. W.; Seo, D.; Lee, J.; Southard, K. M.; Lim, Y.; Kim, D.; Gartner, Z. J.; Jun, Y.; and Cheon, J. Single Cell Mechanogenetics Using Monovalent Magnetoplasmonic Nanoparticles. *Nat Protoc.* **2017**, *12*, 1881–1889.
2. Guinebretiere, R. X-Ray Diffraction by Polycrystalline Materials, Iste Ltd. **2007**.
3. Will, G. Powder Diffraction: Rietveld Method and Two-Stage Method, Springer Verlag, Berlin Heidelberg **2006**.
4. Inkson, B. J. Scanning Electron Microscopy (SEM) and Transmission Electron Microscopy (TEM) for Materials Characterization. Materials Characterization Using Nondestructive Evaluation (NDE) Methods. Woodhead Publishing **2016**, 17–43.
5. Williams, D. B.; Carter, C. B. Transmission Electron Microscopy A Textbook for Materials Science. Springer Springer-Verlag US **2009**.
6. Joy, D. C. Electron Microscopy : Principles and Fundamentals , Edited by Amelinckx, S., Van Dyck, D.; Van Landuyt, J.; Van Tendeloo, G. VCH Verlagsgesellschaft mbH **1997**.
7. Egerton, R. F. Physical Principles of Electron Microscopy: An Introduction to TEM, SEM and AEM, Springer Science+Business Media, Inc. **2005**.
8. Fadley, C. S. X-ray Photoelectron Spectroscopy: Progress and Perspectives. *Journal of Electron Spectroscopy and Related Phenomena* **2010**, *178–179*, 2–32.
9. Hirschfeld, T.; Chase, B. FT-Raman Spectroscopy: Development and Justification. *Applied Spectroscopy* **1986**, *40*, 133–137.
10. Fenn, M. B.; Xanthopoulos, P.; Pyrgiotakis, G.; Grobmyer, S. R.; Pardalos, P. M.; Hench, L. L. Raman Spectroscopy for Clinical Oncology, *Advances in Optical Technologies* **2011**, 213783.
11. Foner, S. The Vibrating Sample Magnetometer: Experiences of a Volunteer (invited). *J. Appl. Phys.* **1996**, *79*, 4740–4745.
12. Cullity, B. D.; Graham, C. D. Introduction to Magnetic Materials, A John Wiley & Sons, Inc. **2009**.
13. Zhang, Q. F.; Wang, L. S.; Zheng, H. F.; Su, A. M.; Liu, X.; Xie, J.; Chen, Y. Z.; Peng, D. L. Effect of in Situ Low-Temperature Annealing on Anomalous Hall Effect in Co Nanocluster-Assembled Granular Film. *Journal of Alloys and Compounds* **2018**, *748*, 922–928.

## CHAPTER 3

### Cr-INDUCED SYNTHESIS OF PYRITE $\text{Cr}_x\text{Cu}_{1-x}\text{Se}_2$ NANOCRYSTALS, ( $0 \leq x \leq 0.5$ )

#### 3.1 Abstract

We studied the formation of colloidal pyrite  $\text{CuSe}_2$  ( $p\text{-CuSe}_2$ ) nanoparticles involving the replacement of  $\text{Cu}^{2+}$  with  $\text{Cr}^{3+}$ , which is uncommon substitution within nanocrystals (NCs). Herein, the first ternary pyrite  $\text{Cr}_x\text{Cu}_{1-x}\text{Se}_2$  ( $x = 0.1\text{-}0.5$ ) were prepared as NCs and a degradation of the host  $p\text{-CuSe}_2$  nanocubes is discussed. The degradation mechanism includes substitution of  $\text{Cr}^{3+}$  ions in the pyrite crystal structure and formation of  $\text{Cr}_x\text{Cu}_{1-x}\text{Se}_2$  derivatives followed by aggregation of the nanocubes. The reaction temperature determines the concentration of the chromium and the morphological evolution of the initial nanocubes. The pyrite phase forms in the temperature range of 250-300 °C, and the structure preserved regardless of the degree of doping. Occupation of the octahedral sites of the pyrite structure of the host  $\text{CuSe}_2$  via  $\text{Cr}^{3+}$  ions led a large enhancement of ferromagnetic moment.

#### 3.2. Introduction

##### 3.2.1 Colloidal Nanocrystals of Pyrite $\text{CuSe}_2$

Binary transition metal chalcogenides (TMCs) with a cubic pyrite structure have gained considerable attention because of their unique optical, magnetic, and electronic properties.<sup>1-3</sup> Figure 3.1 represents the cubic crystal structure of pyrite, in which metal cations occupy one face-centered cubic (fcc) sub-lattice, and the mass center in another fcc sub-lattice is occupied by dichalcogenide anions (dimers). Six neighbor anions surround each metal center in an octahedral

geometry.  $\text{CuSe}_2$  exists in two polymorphs, including the high-pressure phase, pyrite ( $p\text{-CuSe}_2$ ), and marcasite ( $m\text{-CuSe}_2$ ).

Among the binary TMCs with pyrite crystal structure  $\text{MX}_2$  ( $\text{M} = \text{Fe}, \text{Co}, \text{Ni}, \text{Cu}, \text{Zn}, \text{Cd}; \text{X} = \text{S}, \text{Se}$ ), only copper pyrites known to be superconducting.<sup>2,4,5</sup> Superconducting transition of  $p\text{-CuSe}_2$  is  $T_c = 2.4 \text{ K}$ , and this material shows weak ferromagnetism at temperatures below 31 K, which is assumed to depend on the presence of structural defects.<sup>6-9</sup>  $p\text{-CuSe}_2$  is metastable under ambient conditions and its preparation in the bulk requires the application of high temperature (1000 °C) and high pressure (1.2 GPa).<sup>4,9</sup> There are also a few reports on the solution synthesis of metastable  $p\text{-CuSe}_2$  in the form of nanoparticles.<sup>10,11</sup>

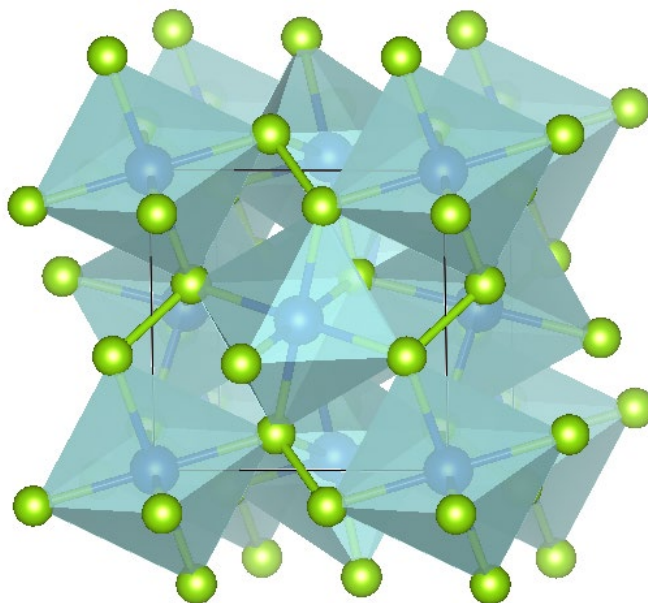


Figure 3.1: Pyrite crystal structure representing the octahedral position of the metal cations and anion dimers.

Datta et al. have reported the first solution based synthesized nanoparticles of  $p\text{-CuSe}_2$  via sonication and using Cu-aminoclay and  $\text{NaHSe}$ .<sup>12</sup> In 2013, the first reported colloidal NCs of

*p*-CuSe<sub>2</sub> had been obtained by Liu et al. using CuCl<sub>2</sub> and elemental Se in the presence of triethylene glycol (TEG; solvent), and polyvinylpyrrolidone (PVP) (capping ligand), and triethylenetetramine (TETA). The nanoparticles of *p*-CuSe<sub>2</sub> in the octahedral-shape and edge length range of 350 nm–400 nm were formed at 210 °C (Figure 3.2).<sup>10</sup> Both TEG and TETA acted as reducing agents to reduce elemental Se to Se<sub>2</sub><sup>2-</sup> which contributed to the formation of CuSe<sub>2</sub>. The XRD pattern of the products formed in the absence of TETA indicated the presence of Se, which could be attributed to its low reactivity due to insufficient reducibility, indicating the importance of TETA as the basic assisting agent.

In another work, copper selenide crystals with various phases (CuSe nanoparticles, Cu<sub>2</sub>Se nanoplates, and *p*-CuSe<sub>2</sub> nanosheets) and shapes were prepared through HU procedure at 160 °C using CuCl and SeO<sub>2</sub> precursors and ethylene glycol (EG) and hydrazine hydrate (N<sub>2</sub>H<sub>4</sub>.H<sub>2</sub>O) as the reaction solvent and reducing agent, respectively. Various phases of copper selenide particles were obtained by changing the molar ratio of the reaction precursors (Figure 3.3).<sup>11</sup>

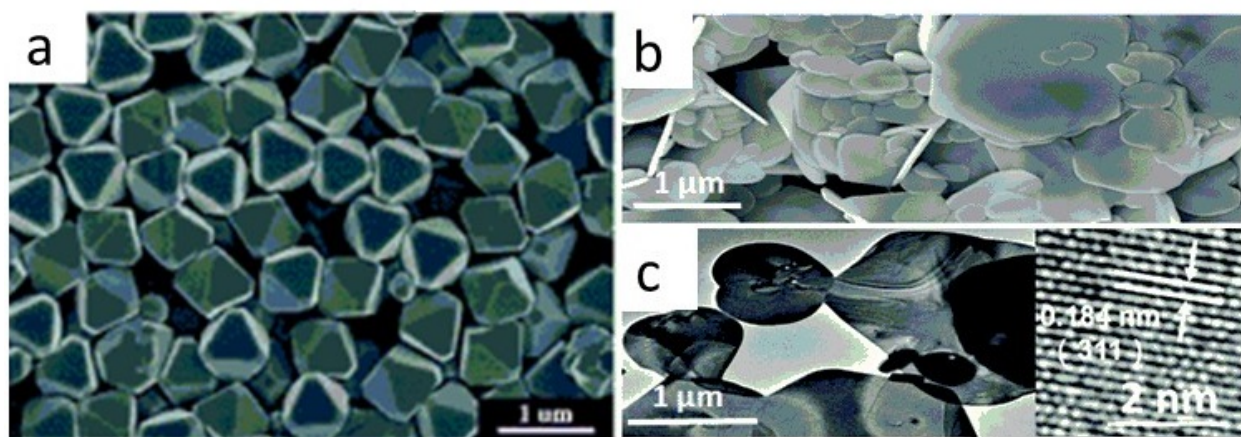


Figure 3.2: Octahedral nanoparticles of *p*-CuSe<sub>2</sub> synthesized with (a) TETA assisted HU method at 210 °C using CuCl<sub>2</sub> and Se and (b,c) *p*-CuSe<sub>2</sub> nanosheets obtained at 160 °C using CuCl and SeO<sub>2</sub> precursors and N<sub>2</sub>H<sub>4</sub>.H<sub>2</sub>O reducing agent. Reproduced with permission from refs. 10 and 11.

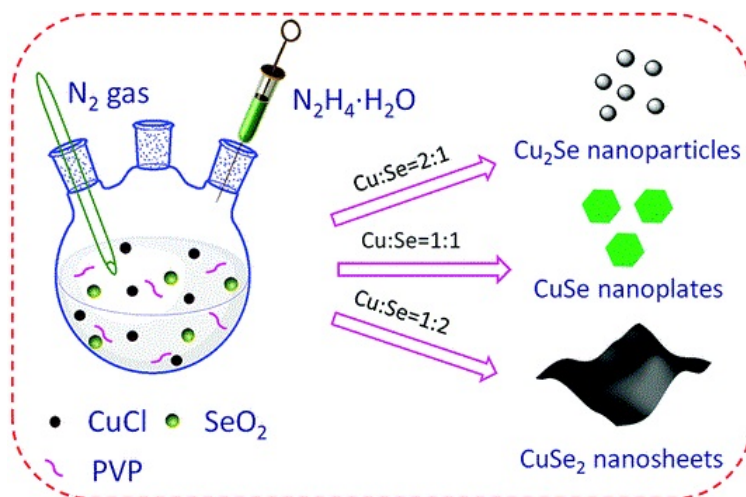


Figure 3.3: Preparation process of HU synthesis of copper selenide crystals. Reprinted with permission from ref. 11.

Magnetic nanomaterials display unique size- and shape-dependence properties, including high field reversibility, high saturation field, and superparamagnetism. These characteristics have broad applicability in areas such as recording media, spin-based electronics, magneto-optics, and biomedical applications.<sup>13-17</sup> In particular, magnetic materials that display semiconducting or insulating characteristics are highly desirable, but their choices are presently limited. Doping materials with selective transition metal ions is an effective approach that provides access to a wide variety of new properties and characteristics not obtainable by other strategies. Therefore, advances in selective cationic substitutions provides a pathway to create novel materials and enables tailoring of electronic, optical, and magnetic properties. Cr<sup>3+</sup> ions exhibit high-spin configuration, which potentially can play an important role in producing large magnetic moments. Well-known examples include the chromium-based spinel oxides and chalcogenides  $M\text{Cr}_2\text{X}_4$  ( $X = \text{O}, \text{S}, \text{Se}, \text{Te}$ ), in which the partial occupation of the octahedral sites of the spinel

structure by Cr<sup>3+</sup> magnetic ions ( $t_2g^3$ ) leads to the formation of an interesting family of magnetic materials.<sup>18-27</sup>

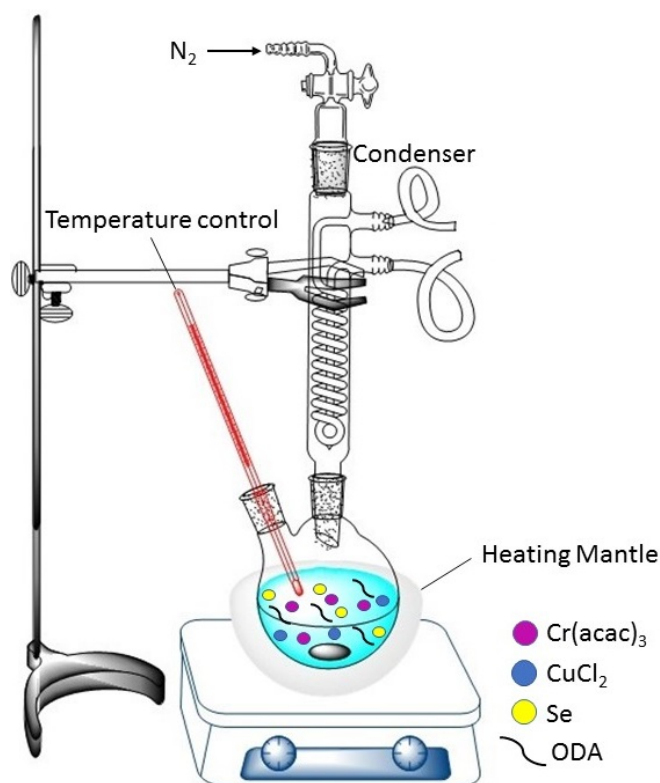
In recent years, there has also been significant efforts to induce magnetic characteristics in binary oxides and nitrides, such as ZnO, In<sub>2</sub>O<sub>3</sub>, GaN, and AlN, by Cr<sup>3+</sup> doping.<sup>28-32</sup> The synthesis and magnetic properties of transition metal substituted *p*-CuSe<sub>2</sub> remains unexplored. Herein, we illustrated the influence of the reaction conditions (e.g., synthesis methodology, temperature, time, etc.) on the composition and morphology of the products. The results indicated that the reaction temperature plays a critical role in the formation mechanism of the NCs. Our study represented that by increasing the reaction temperature, Cr<sup>3+</sup> ions partially occupied the octahedral positions in the pyrite structure and formed Cr<sub>*x*</sub>Cu<sub>1-*x*</sub>Se<sub>2</sub> NCs and by reaching the temperature to above 300 °C, the 50% doped pyrite phase Cr<sub>0.5</sub>Cu<sub>0.5</sub>Se<sub>2</sub> transformed to spinel CuCr<sub>2</sub>Se<sub>4</sub> NCs. This unique cationic substitution in colloidal pyrite followed with occupation of the octahedral positions of the pyrite structure with Cr<sup>3+</sup> ions induced the direct structural transformation from pyrite to spinel phase. We will discuss the phase transformation in chapter 4.

### 3.3 Experimental

All chemicals and solvents including copper chloride (CuCl<sub>2</sub>, 99%, Alfa Aesar), chromium acetylacetonate (Cr(acac)<sub>3</sub>, 99.99%, Sigma-Aldrich), selenium powder (Se, 99.99%, Sigma-Aldrich), octadecylamine (ODA, 97%, Sigma-Aldrich), *n*-hexane, and ethanol, were obtained from commercial sources and were used as received without further purification.

The synthesis process was carried out in a fume hood using the standard Schlenk technique and under N<sub>2</sub> atmosphere (Scheme 3.1). To synthesis of *p*-Cr<sub>*x*</sub>Cu<sub>1-*x*</sub>Se<sub>2</sub> NCs, a mixture of 0.25 mmol CuCl<sub>2</sub>, 0.5 mmol Cr(acac)<sub>3</sub>, and 2.0 mmol Se was dissolved into 10 g ODA, and

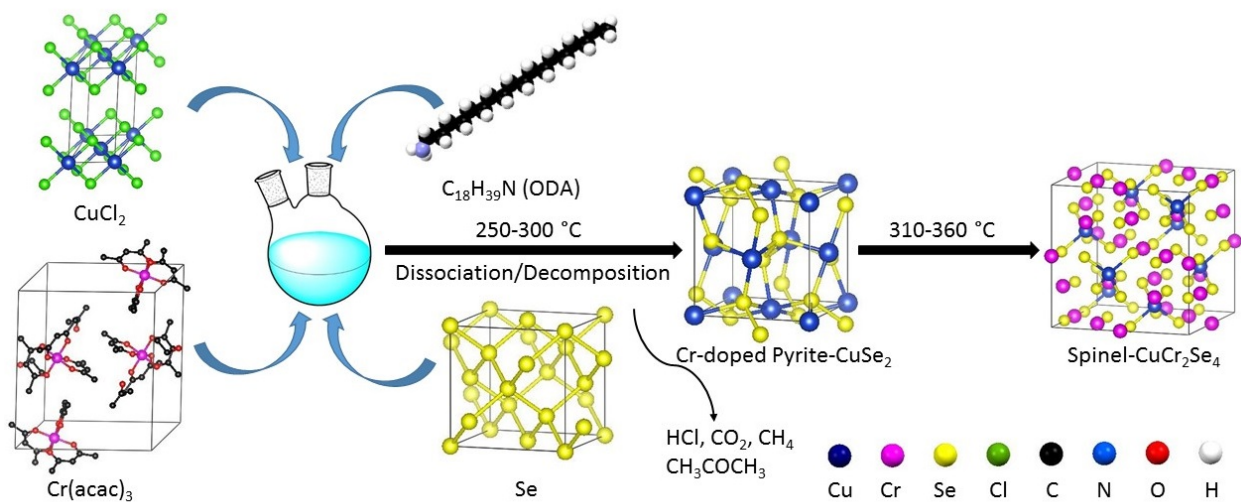
was deaerated at room temperature for 10 minutes and then back-filled with N<sub>2</sub> for 10 more minutes. The mixture was stirred and heated to 250 °C and was kept at this temperature for 30 min. After the resulting black mixture was cooled slowly down to room temperature, a mix of ethanol (10 mL) and *n*-hexane (10 mL) was added to the solution to participate in the product. The product was collected via centrifugation (8000 rpm, 5 min) and washed three times. The same procedure has been repeated at 260, 270, 280, 290, and 300 °C. The phase-pure pyrite Cr<sub>x</sub>Cu<sub>1-x</sub>Se<sub>2</sub> compositions are formed in the temperature range of 250-300 °C. Increasing the temperature of the same solution to the range of 330-360 °C led to the formation of CuCr<sub>2</sub>Se<sub>4</sub> NCs.



Scheme 3.1: Schematic drawing of the experimental setup used to synthesize NCs.

### 3.4 Results and Discussion

Scheme 3.2 illustrated the reaction process for the synthesis of  $\text{Cr}_x\text{Cu}_{1-x}\text{Se}_2$  and  $\text{CuCr}_2\text{Se}_4$  nanocrystals schematically. The colloidal nanoparticles have been synthesized by a heat-up method in which the reaction temperature plays a critical role and influences the composition and structure of the products. Although, the pure  $p\text{-CuSe}_2$  phase is a high-pressure phase,<sup>4,9</sup> the cubic pyrite phase of  $\text{Cr}_x\text{Cu}_{1-x}\text{Se}_2$  was successfully formed under this colloidal conditions. The predominant phase formed at the temperature range of 250-300 °C was  $p\text{-Cr}_x\text{Cu}_{1-x}\text{Se}_2$ , whereas at the range of 330-360 °C the spinel phase has been formed. The XRD patterns (Figure 3.4) of the products prepared at solution temperatures of 250-300 °C revealed the formation of pyrite single-phase.



Scheme 3.2: Representation of the reaction process for the synthesis of  $p\text{-CuSe}_2$  and  $\text{CuCr}_2\text{Se}_4$  NCs.

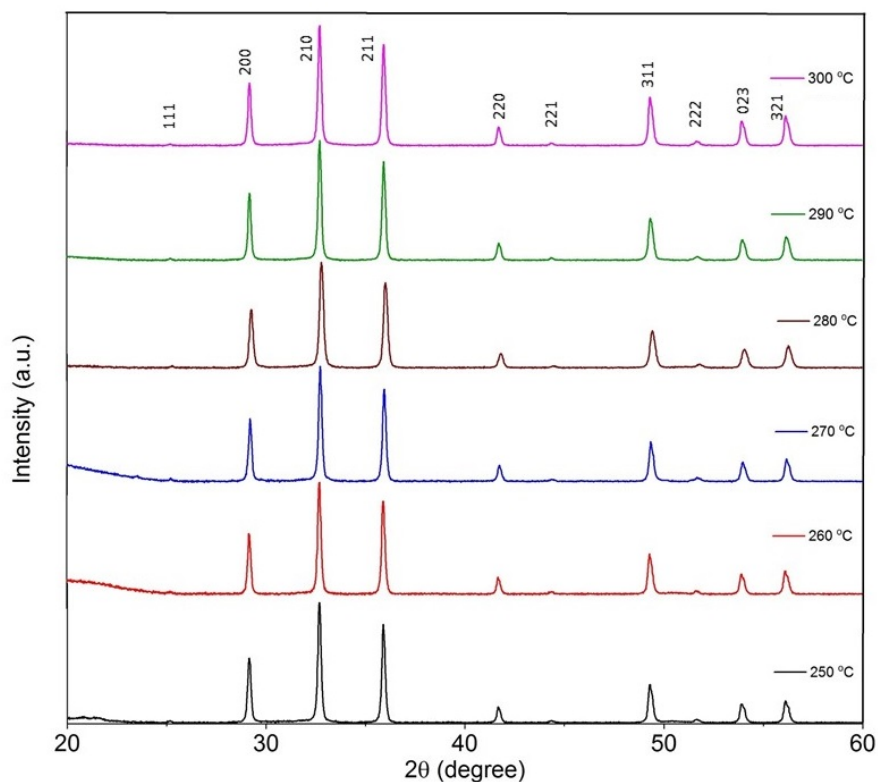


Figure 3.4: XRD patterns of the  $\text{Cr}_x\text{Cu}_{1-x}\text{Se}_2$  NCs formed in the temperature range of 250-300 °C.

### 3.4.1 Formation of the $\text{Cr}_x\text{Cu}_{1-x}\text{Se}_2$ NCs

The pyrite phase formed at the temperatures lower than 250 °C (e.g., 220 °C) was not phase pure (Figure 3.5). Moreover, the same heat-up reaction procedure using only the copper and selenium precursors does not lead to formation of pure pyrite phase, with impurities such as the marcasite phase of  $\text{CuSe}_2$  ( $m\text{-CuSe}_2$ ) and  $\text{CuSe}$  being detected in the X-ray diffraction (XRD) patterns of the products (Figure 3.6). Therefore, the presence of chromium plays a significant role in the formation of phase-pure pyrites, even when it is incorporated in small concentrations. Energy-dispersive X-ray spectroscopy (EDX) analysis confirms the existence of chromium in the structure of  $p\text{-CuSe}_2$ , and it increases in concentration with increasing reaction temperature.

The chemical composition of the pyrite nanoparticles formed at temperature ranges of 250-260, 270-280, and 290-300 °C, are determined to be  $\text{Cr}_{0.3}\text{Cu}_{0.7}\text{Se}_2$ ,  $\text{Cr}_{0.4}\text{Cu}_{0.6}\text{Se}_2$ , and  $\text{Cr}_{0.5}\text{Cu}_{0.5}\text{Se}_2$ , respectively.

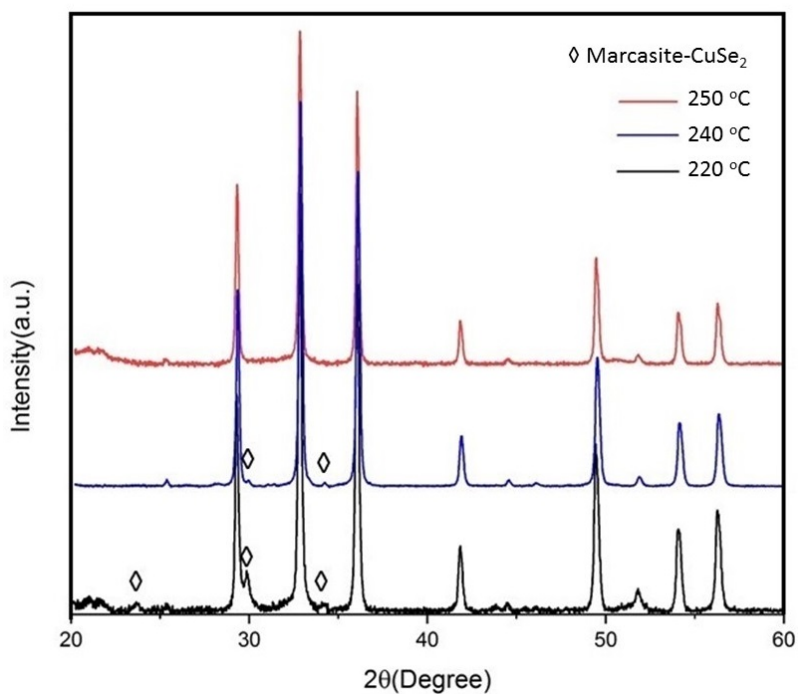


Figure 3.5: XRD patterns of the NCs synthesized at solution temperatures of 220, 240, and 250 °C indicating the formation of mixed pyrite and marcasite  $\text{CuSe}_2$  phases at the temperatures below 250 °C.

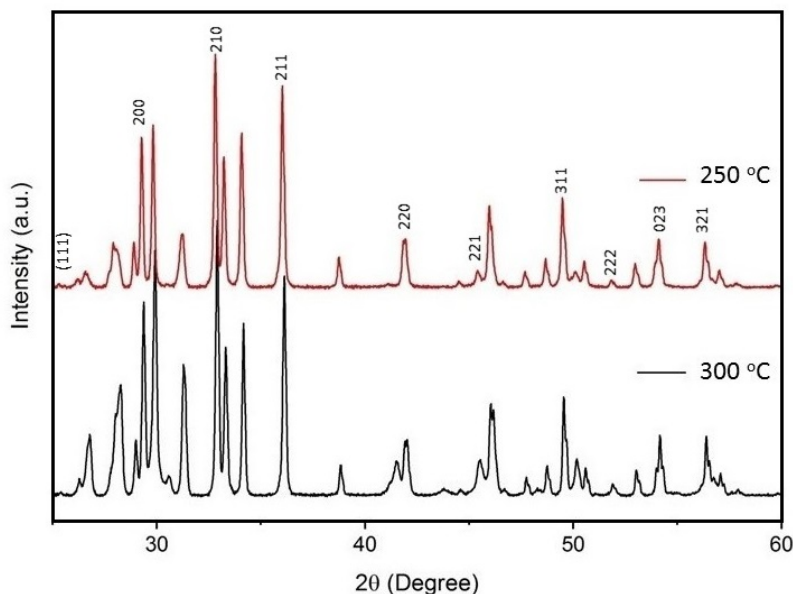


Figure 3.6: XRD patterns of NCs prepared in the absence of chromium indicating the formation of mixed-phase of  $p$ -CuSe<sub>2</sub>,  $m$ -CuSe<sub>2</sub>, CuSe, and some other impurities.

### 3.4.2 Morphological Evolution

The minimum temperature necessary to obtain phase-pure Cr<sub>x</sub>Cu<sub>1-x</sub>Se<sub>2</sub> nanocrystals is ~250 °C at which nanocubes of Cr<sub>0.3</sub>Cu<sub>0.7</sub>Se<sub>2</sub> in the size range of 100-500 nm are formed. The high-resolution TEM (HRTEM) micrographs of isolated  $p$ -CuSe<sub>2</sub> formed at 250 °C in the absence of the Cr-precursor, showed perfect cubic shape NCs without any disintegration. Figure 3.7 indicates an HRTEM image of a representative  $p$ -CuSe<sub>2</sub> nanocrystal, highlighting the 0.25 nm lattice fringes that correspond to (2 1 1) planes.

However, the TEM images of Cr<sub>0.3</sub>Cu<sub>0.7</sub>Se<sub>2</sub> formed at the same temperature clearly show broad size distribution and agglomeration (Figure 3.8). The degradation occurs at the edges of the nanocubes (Figure 3.9). The Cr concentration in the nanocrystals systematically increases with increasing reaction temperature, with distortion and subsequent disintegration of the nanocubes surface and ejection of small nanoneedle-like structures at higher concentrations. The

highest temperature at which the phase pure Cr-doped pyrite is still formed is 300 °C, at which the composition of the product is  $\text{Cr}_{0.5}\text{Cu}_{0.5}\text{Se}_2$ . Disintegration of the relatively large nanocubes to nanoneedles is essentially complete at this temperature and composition although some deformed cubic shape particles are still observable.

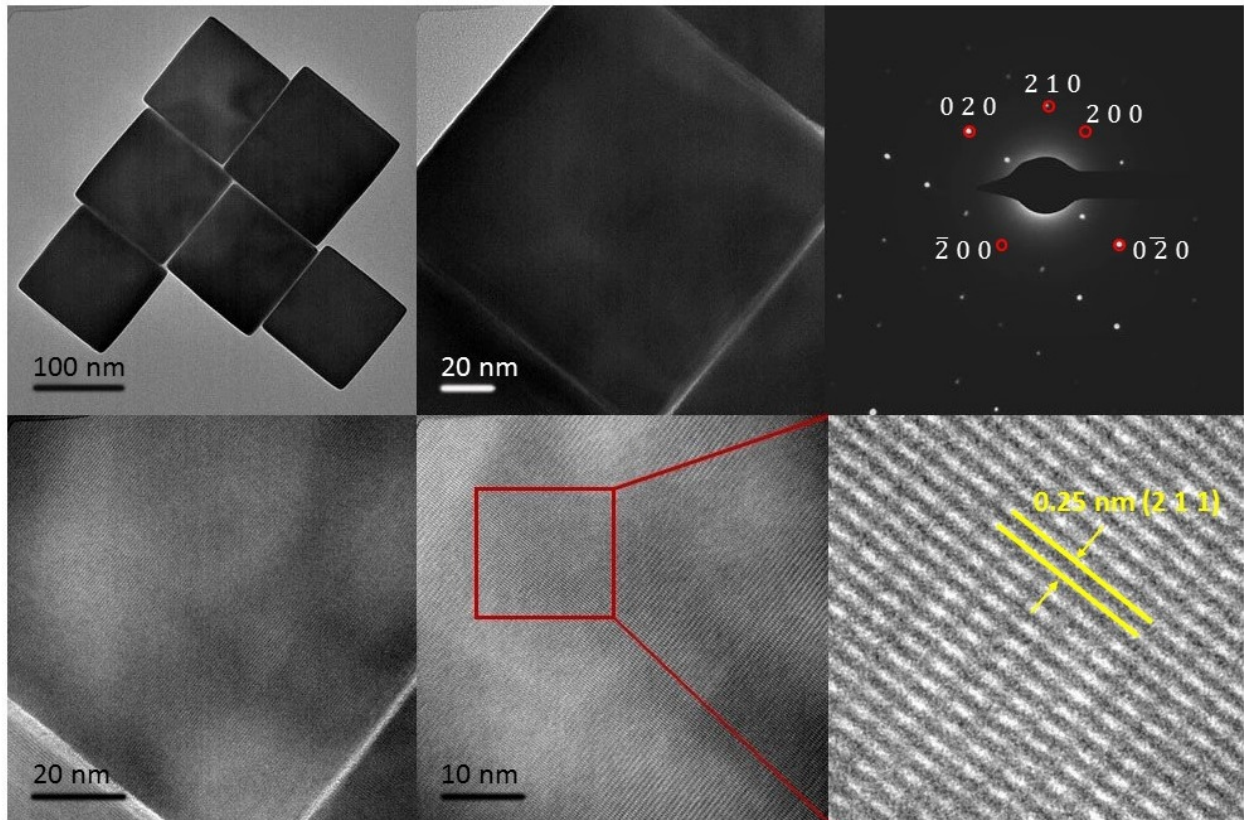


Figure 3.7: Low-resolution TEM, high-resolution TEM (HRTEM) images and selected area diffraction (SAED) pattern of the isolated pristine nanocubes of  $p\text{-CuSe}_2$  formed in the absence of chromium precursor. The zone axis of the SAED pattern is in  $[001]$  direction.

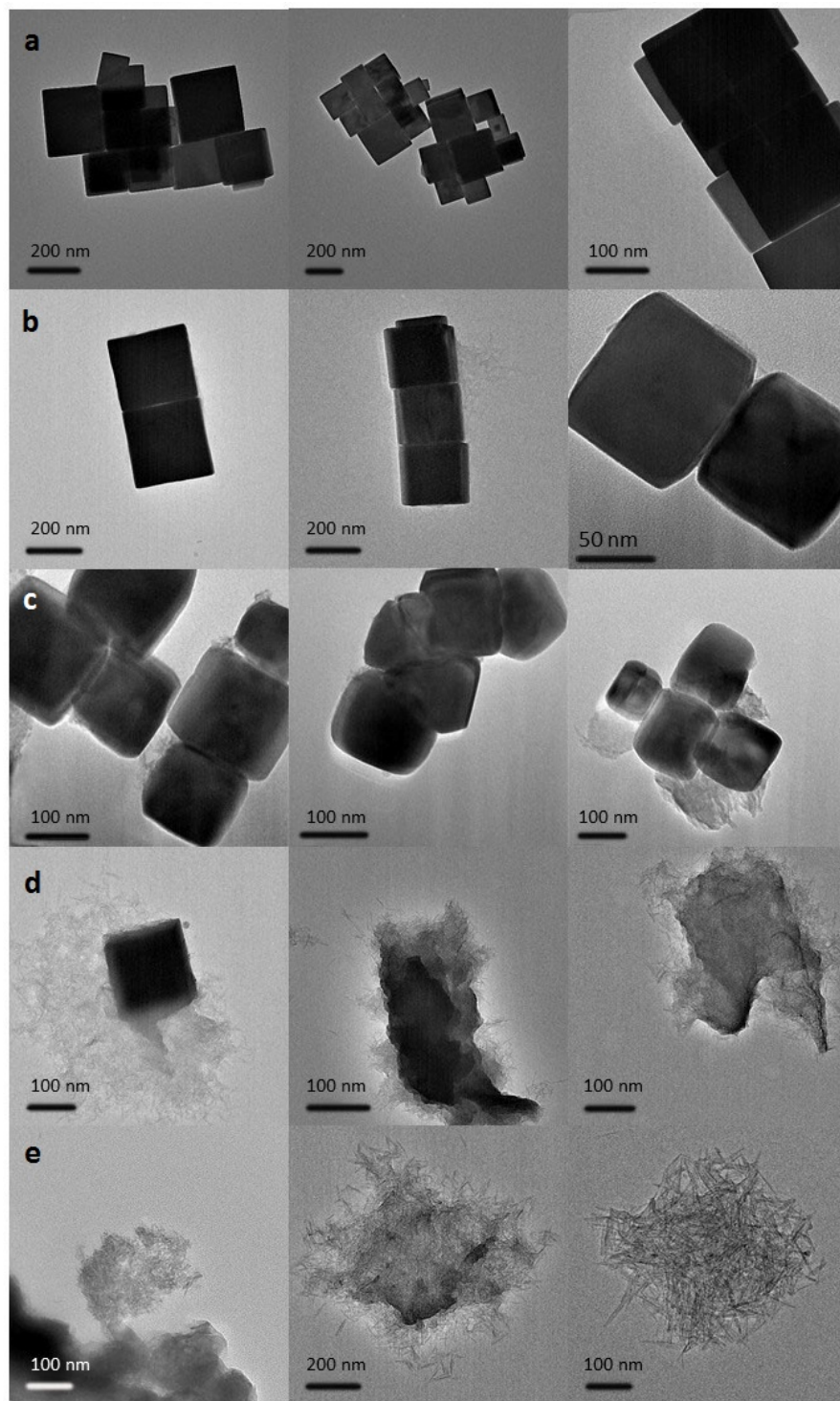


Figure 3.8: Morphological Degradation of  $\text{Cr}_x\text{Cu}_{1-x}\text{Se}_2$  NCs as a function of reaction temperature and Cr-contents. TEM images of the (a)  $\text{Cr}_{0.1}\text{Cu}_{0.9}\text{Se}_2$ , (b)  $\text{Cr}_{0.2}\text{Cu}_{0.8}\text{Se}_2$ , (c)  $\text{Cr}_{0.3}\text{Cu}_{0.7}\text{Se}_2$ , (d)  $\text{Cr}_{0.4}\text{Cu}_{0.6}\text{Se}_2$ , and (e)  $\text{Cr}_{0.5}\text{Cu}_{0.5}\text{Se}_2$  NCs indicating morphological evolution of NCs during increasing the reaction temperature and chromium content.

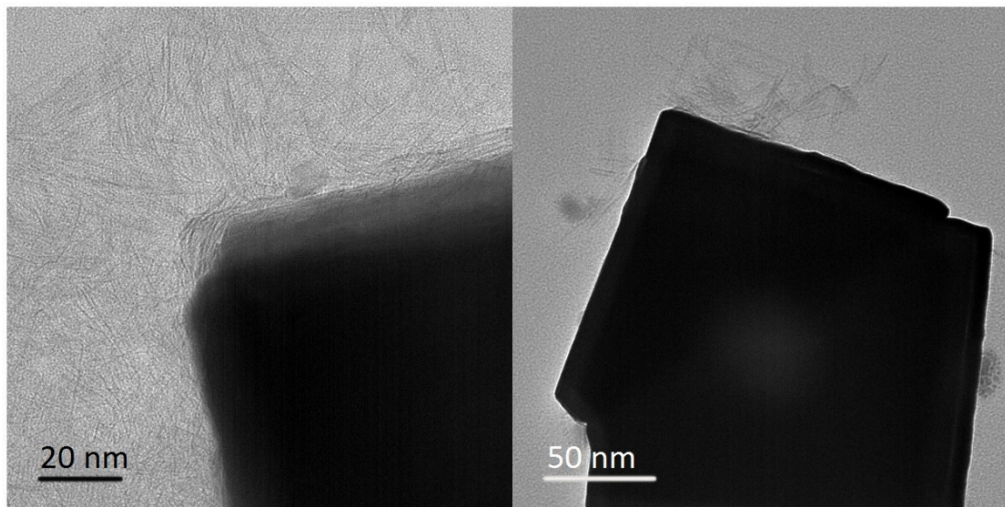


Figure 3.9: HRTEM image of NCs of  $\text{Cr}_{0.3}\text{Cu}_{0.7}\text{Se}_2$  that was formed at 250 °C, confirming that the degradation occurs at the edges of the cubes.

In order to correlate the concentration of the doped chromium with the reaction temperature, we have performed EDS analysis on the pyrite crystals formed at the temperatures below 250 °C. For instance, the elemental composition of the isolated pyrite particles formed at 220 °C showed only a 10% doped pyrite  $\text{Cr}_{0.1}\text{Cu}_{0.9}\text{Se}_2$  phase. HAADF-, EDS-STEM imaging, and EDS-diagrams of the NCs of  $\text{Cr}_{0.1}\text{Cu}_{0.9}\text{Se}_2$ ,  $\text{Cr}_{0.3}\text{Cu}_{0.7}\text{Se}_2$ , and  $\text{Cr}_{0.5}\text{Cu}_{0.5}\text{Se}_2$ , respectively formed at 220 °C, 250 °C, and 300 °C are represented in figures 3.10-3.12.

Table 3.1 summarized the effect of the reaction temperature and the concentration of the precursors on the composition and phase of the prepared NCs. Table 3.2 represents the elemental composition of the  $\text{Cr}_x\text{Cu}_{1-x}\text{Se}_2$  NCs measured by EDS.

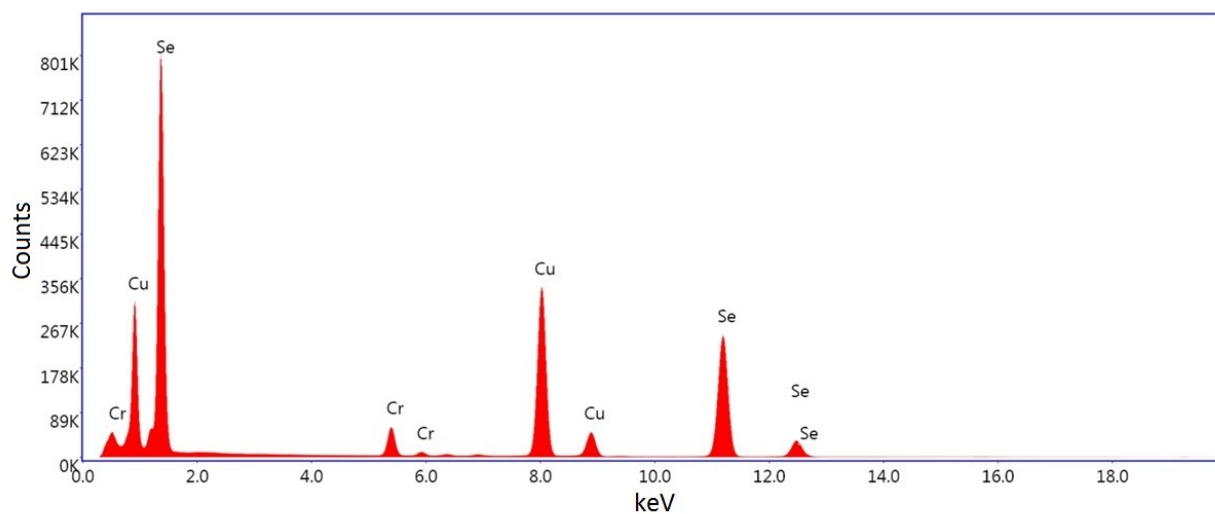
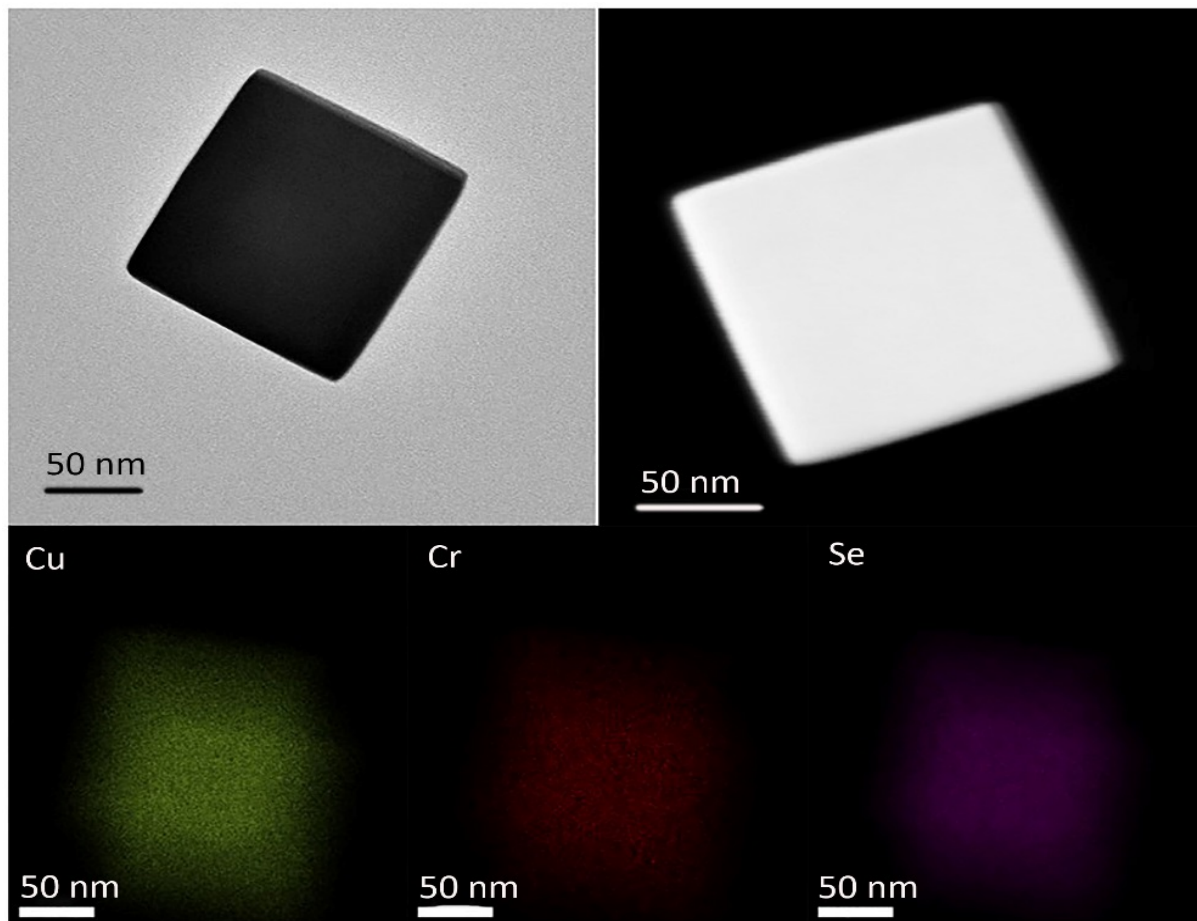


Figure 3.10: HAADF-, EDS-STEM imaging, and EDS-diagram of  $\text{Cr}_{0.1}\text{Cu}_{0.9}\text{Se}_2$  nanocubes formed at 220 °C.

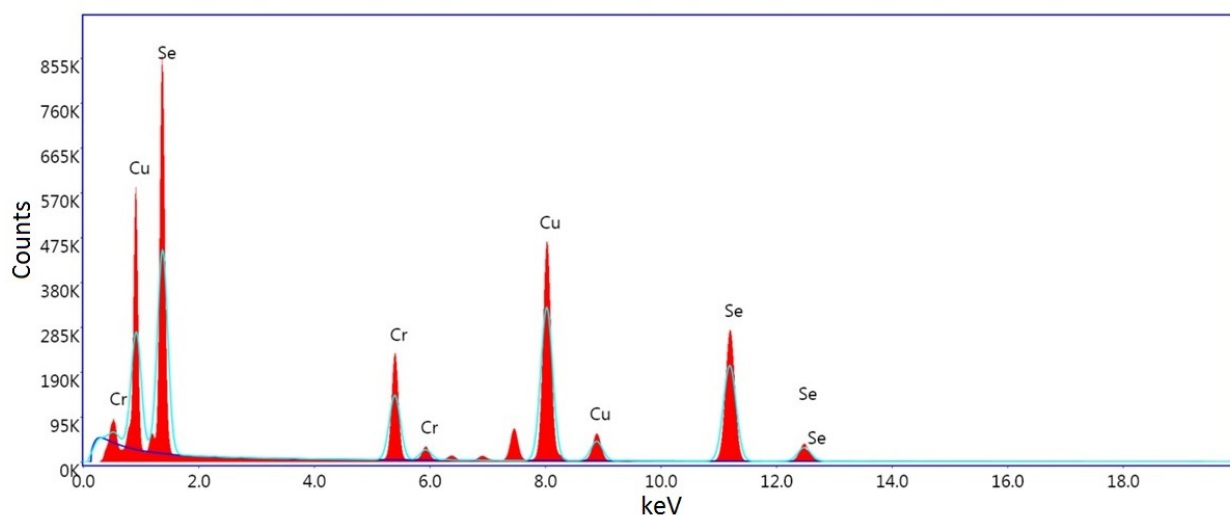
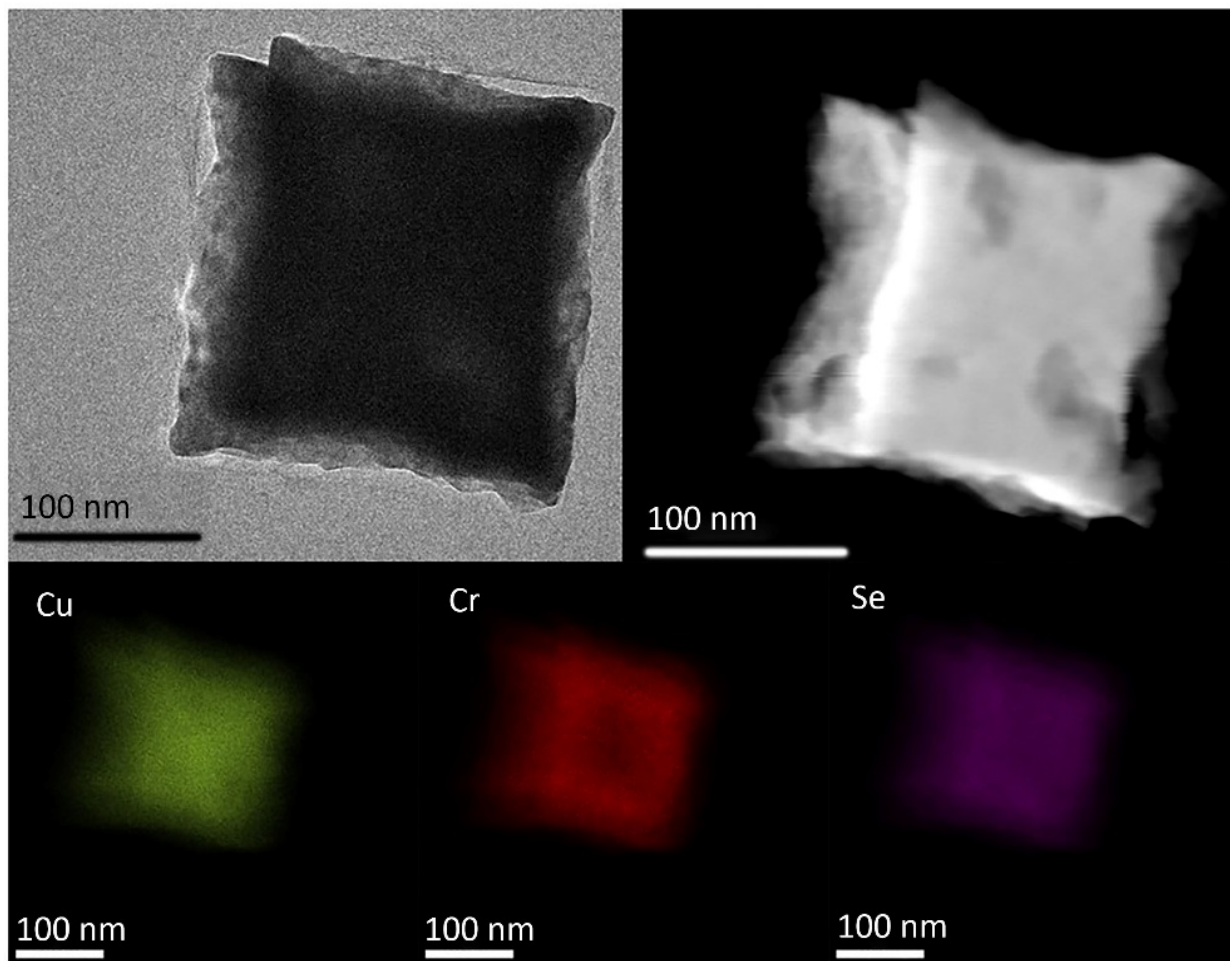


Figure 3.11: HAADF-, EDS-STEM imaging, and EDS-diagram of deformed nanocubes of  $\text{Cr}_{0.3}\text{Cu}_{0.7}\text{Se}_2$  formed at 250 °C.

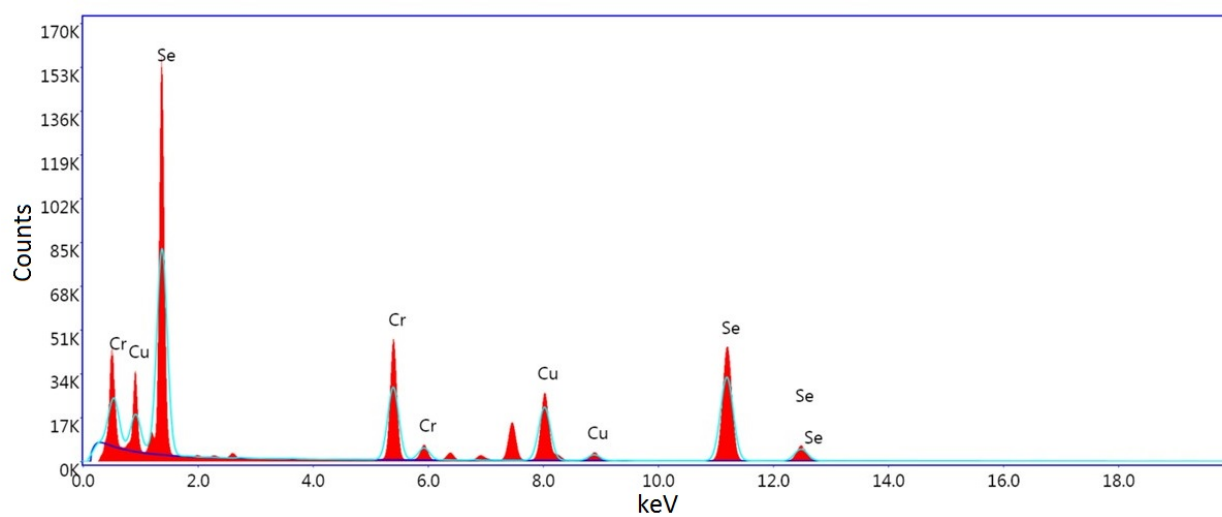
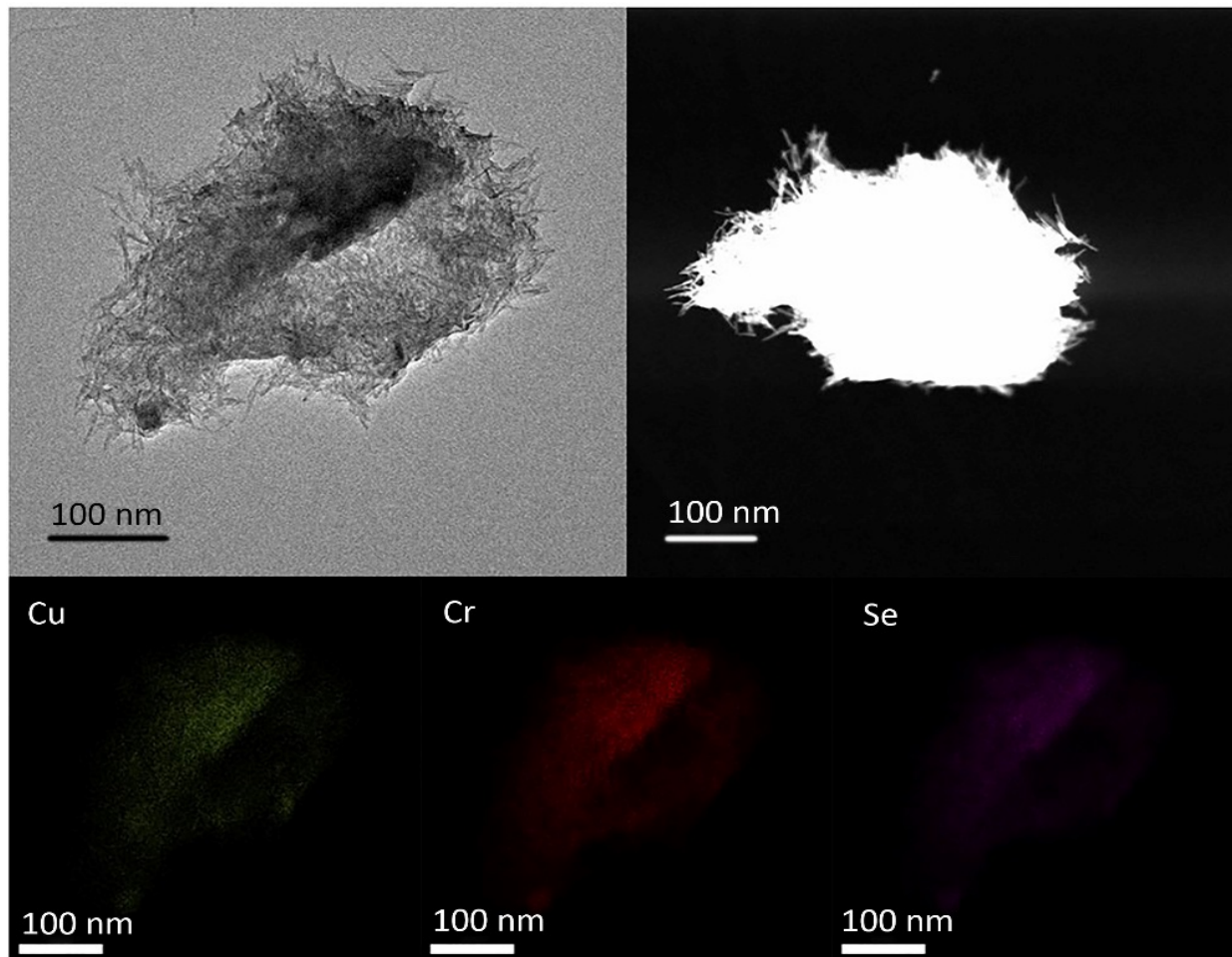


Figure 3.12: HAADF-, EDS-STEM imaging, and EDS-diagram of nanoneedles of  $\text{Cr}_{0.5}\text{Cu}_{0.5}\text{Se}_2$  formed at 300 °C.

Table 3.1: Summary of the performed reactions and the effect of reagents concentration and reaction temperature on the composition and phase of  $\text{Cr}_x\text{Cu}_{1-x}\text{Se}_2$  nanocrystals.

Precursors (mmol)	Reaction Temperature	Products	Measured Composition of Pyrite Phase	Cu: Cr: Se Ratio of Pyrite Phase
[Cu <sup>2+</sup> ] (0.25) [Cr <sup>3+</sup> ] (0.50)	220 °C	Pyrite/Marcasite	Cr <sub>0.1</sub> Cu <sub>0.9</sub> Se <sub>2</sub>	1.0: 0.11: 2.27
[Cu <sup>2+</sup> ] (0.25) [Cr <sup>3+</sup> ] (0.50)	240 °C	Pyrite/Marcasite	Cr <sub>0.2</sub> Cu <sub>0.8</sub> Se <sub>2</sub>	1.0: 0.28: 2.54
[Cu <sup>2+</sup> ] (0.25) [Cr <sup>3+</sup> ] (0.50)	250 °C	Pyrite	Cr <sub>0.3</sub> Cu <sub>0.7</sub> Se <sub>2</sub>	1.0: 0.44: 2.97
[Cu <sup>2+</sup> ] (0.25) [Cr <sup>3+</sup> ] (0.10)	250 °C	Pyrite	Cr <sub>0.1</sub> Cu <sub>0.9</sub> Se <sub>2</sub>	1.0: 0.12: 2.28
[Cu <sup>2+</sup> ] (0.25) [Cr <sup>3+</sup> ] (0.50)	260 °C	Pyrite	Cr <sub>0.3</sub> Cu <sub>0.7</sub> Se <sub>2</sub>	1.0: 0.46: 2.91
[Cu <sup>2+</sup> ] (0.25) [Cr <sup>3+</sup> ] (0.50)	270 °C	Pyrite	Cr <sub>0.4</sub> Cu <sub>0.6</sub> Se <sub>2</sub>	1.0: 0.63: 3.17
[Cu <sup>2+</sup> ] (0.25) [Cr <sup>3+</sup> ] (0.50)	280 °C	Pyrite	Cr <sub>0.4</sub> Cu <sub>0.6</sub> Se <sub>2</sub>	1.0: 0.75: 3.24
[Cu <sup>2+</sup> ] (0.25) [Cr <sup>3+</sup> ] (0.50)	290 °C	Pyrite	Cr <sub>0.5</sub> Cu <sub>0.5</sub> Se <sub>2</sub>	1.0: 0.93: 3.87
[Cu <sup>2+</sup> ] (0.25) [Cr <sup>3+</sup> ] (0.50)	300 °C	Pyrite	Cr <sub>0.5</sub> Cu <sub>0.5</sub> Se <sub>2</sub>	1.0: 0.97: 3.93
[Cu <sup>2+</sup> ] (0.25) [Cr <sup>3+</sup> ] (0.50)	>300 °C	Pyrite/Spinel	Cr <sub>0.5</sub> Cu <sub>0.5</sub> Se <sub>2</sub>	1.0: 0.93: 3.95
[Cu <sup>2+</sup> ] (0.25) No Cr <sup>3+</sup>	250 °C	Pyrite/Marcasite/CuSe	-	-
[Cu <sup>2+</sup> ] (0.25) No Cr <sup>3+</sup>	300 °C	Pyrite/Marcasite/CuSe	-	-

Table 3.2: Elemental composition of the  $\text{Cr}_x\text{Cu}_{1-x}\text{Se}_2$  NCs measured by EDS.

Material	Temperature	Element	Weight %	Atomic %	Ratio
$\text{Cr}_{0.1}\text{Cu}_{0.9}\text{Se}_2$	220 °C	Cr K	2.39	3.38	0.11
		Cu K	25.56	29.56	1.00
		Se L	72.05	67.06	2.27
$\text{Cr}_{0.2}\text{Cu}_{0.8}\text{Se}_2$	240 °C	Cr K	5.16	7.24	0.28
		Cu K	22.81	26.19	1.00
		Se L	72.03	66.57	2.54
$\text{Cr}_{0.3}\text{Cu}_{0.7}\text{Se}_2$	250 °C	Cr K	7.18	10.05	0.44
		Cu K	19.77	22.64	1.00
		Se L	73.05	67.31	2.97
$\text{Cr}_{0.4}\text{Cu}_{0.6}\text{Se}_2$	270 °C	Cr K	9.45	13.12	0.63
		Cu K	18.34	20.84	1.00
		Se L	72.21	66.04	3.17
$\text{Cr}_{0.5}\text{Cu}_{0.5}\text{Se}_2$	300 °C	Cr K	11.93	16.51	0.97
		Cu K	14.94	16.90	1.00
		Se L	73.13	66.59	3.94

We have further performed scanning transmission electron microscopy (STEM) experiments to determine the quality of the pyrite NCs. We used the high-angle annular dark-field (HAADF) imaging mode, where intensity is approximately proportional to the squared atomic number ( $\sim Z^2$ ).<sup>33</sup> The crystal structure of NCs was resolved using atomic resolution HAADF images. We confirm the presence of Cr, Cu, and Se using electron energy loss spectroscopy (EELS).

Figures 3.13, 3.14a, 3.14b, and 3.14c show the atomic resolution HAADF images of the pyrite crystal structure along [011], [111],  $[\bar{2}11]$ , and [120], respectively, with their crystal structure model shown below the images.<sup>34</sup> From atomic resolution HAADF image and EELS, we find that Cr is fully incorporated into the pyrite crystal structure. Interestingly, we find that incorporation of Cr into the (Cu-Cr)Se<sub>2</sub> pyrite system results in NCs without any planar defects.

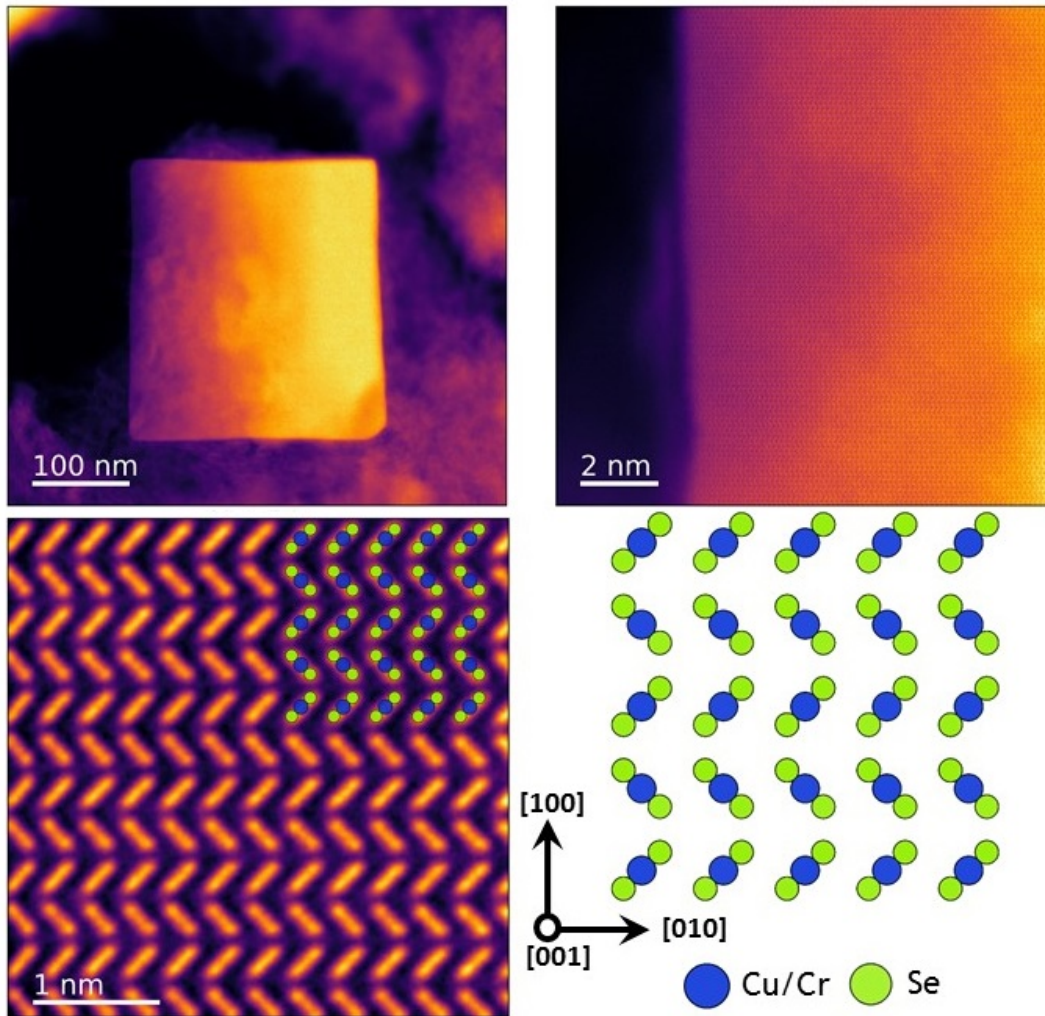


Figure 3.13: Wide field-of-view HAADF images showing various NCs. Atomic resolution HAADF images of NCs along  $[001]$  with its respective atomic models shown below the corresponding HAADF images.

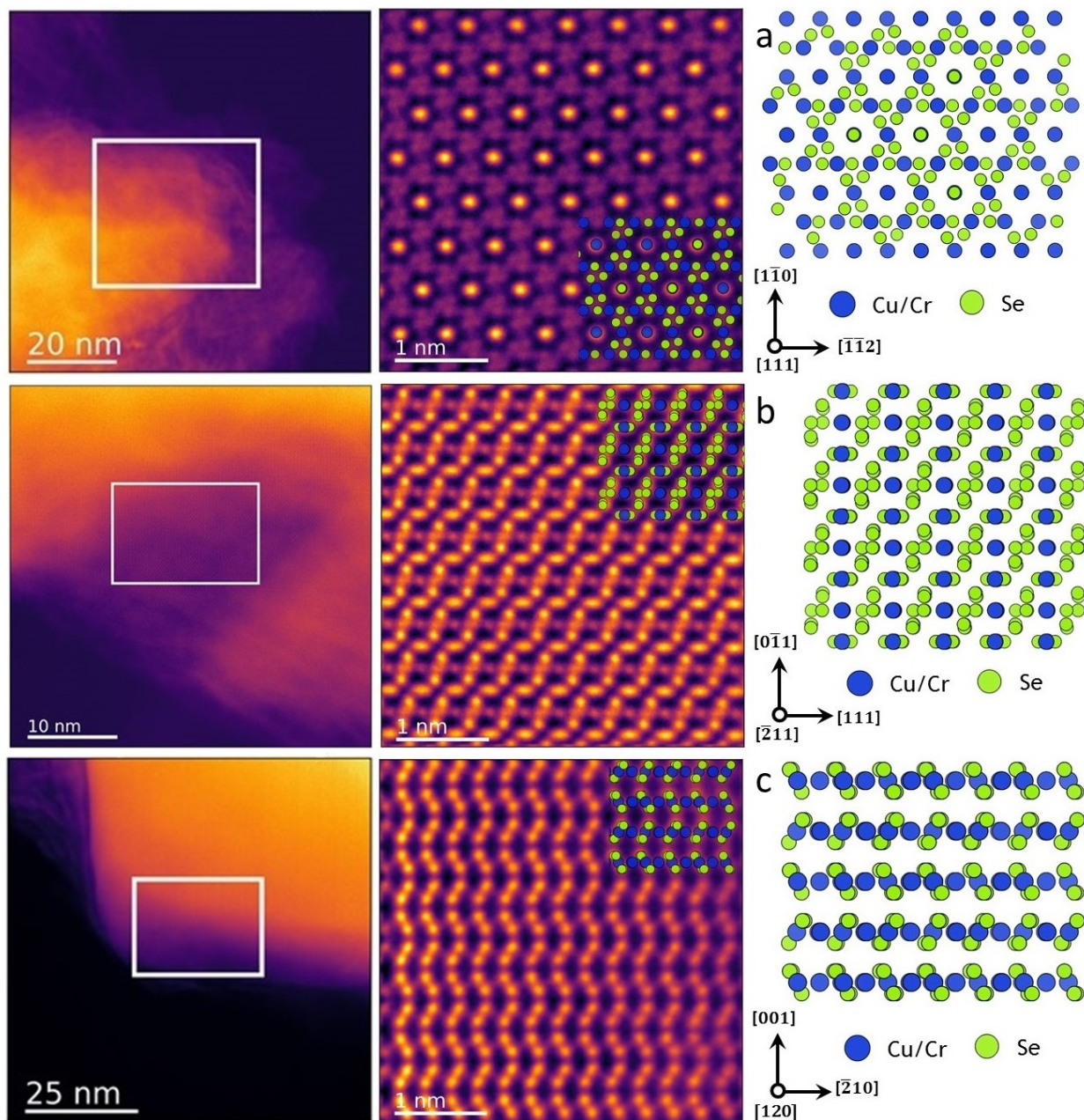


Figure 3.14: Wide field-of-view and atomic resolution HAADF images of pyrite  $\text{Cu}_{0.7}\text{Cr}_{0.3}\text{Se}_2$  NCs along (a)  $[111]$ , (b)  $[\bar{2}11]$ , and (c)  $[120]$ .

We can label the atomic columns in a HAADF image based on their intensity, as shown in figure 3.15 for a crystal viewed along  $[\bar{2}11]$ . Here, the dimmest (type-3) columns correspond to Cr/Cu atomic columns. The next brightest (type-2) columns correspond to pure Se atomic

columns. The brightest atomic columns (type-1) have a combination of Cr/Cu and Se atoms. Incorporation of Cr into the (Cu-Cr)Se<sub>2</sub> pyrite system results in NCs without any planar defects. Due to spatial resolution limitations, some of the individual atomic columns cannot be resolved, which results in multiple atomic columns within type-1 and type-2 to be labeled as single columns.

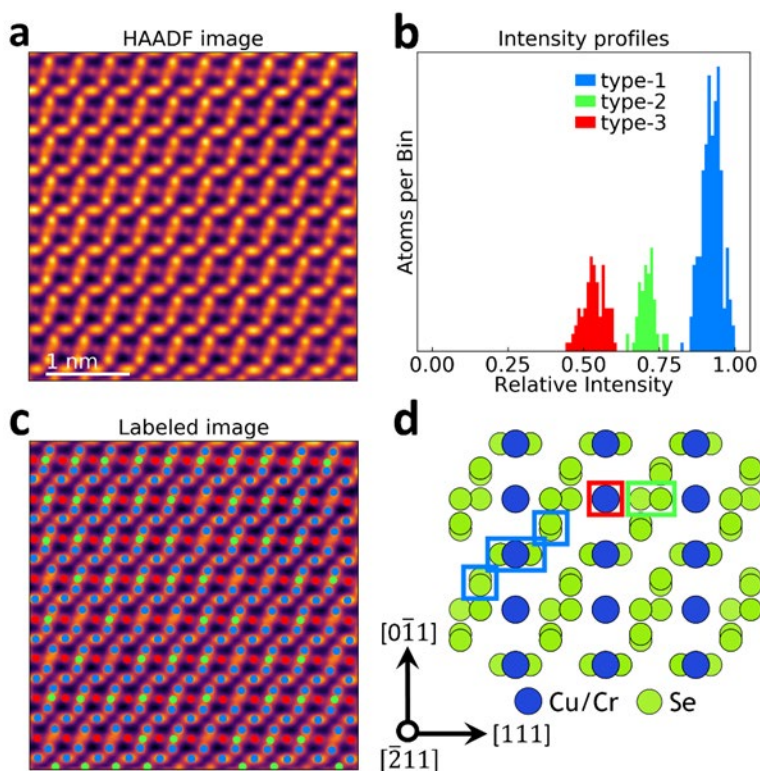


Figure 3.15: (a) Atomic resolution HAADF image of Cr<sub>0.3</sub>Cu<sub>0.7</sub>Se<sub>2</sub> NCs along  $[\bar{2}11]$ . (b) HAADF intensity profiles of various atomic columns for the image shown in (a). (c) HAADF image (same as shown in (a)) with labeled atomic columns corresponding to the HAADF intensity profiles. (d) The corresponding atomic model with three types of atomic columns highlighted as red, green and blue boxes.

We have used TEM and HRTEM images to understand the morphological changes of the Cr-doped pyrites formed at different temperatures and to determine the main parameters that induce break down of the nanocubes to form nanoneedles. The TEM images indicate that by

increasing the reaction temperature, the number of the aggregated nanoparticles increases, therefore the reaction temperature is a likely candidate that potentially influences the disintegration. The degree of Cr-substitution increases with increasing reaction temperature. Comparing the morphologies of  $\text{CuSe}_2$  (Figure 3.7) and  $\text{Cr}_{0.3}\text{Cu}_{0.7}\text{Se}_2$  (Figure 3.8 and 3.9), both formed at 250 °C, illustrates the role of Cr-content in the degradation of the nanocube morphology. The composition of isolated pyrite phase nanoparticles formed at lower reaction temperatures of 220 °C and 240 °C are determined to be  $\text{Cr}_{0.1}\text{Cu}_{0.9}\text{Se}_2$  and  $\text{Cr}_{0.2}\text{Cu}_{0.8}\text{Se}_2$ , respectively. These nanoparticles exhibit close to a nanocube morphology, like that of pure  $\text{CuSe}_2$ , and the degeneration is not significant for these compositions (Figures 3.10, 3.16). Thus, both the reaction temperature and chromium content play a role in the morphological degradation of the nanocubes. Figure 3.8 shows the morphological disintegration of pristine nanocubes and the formation of nanoneedles as a function of reaction temperature and Cr-contents. Close inspection of HRTEM images indicates that the degradation initiates at the edges of the nanocubes (Figure 3.9), leading to the initial rounding of the edges, as illustrated in Fig. 3.16 b.

Figure 3.16 shows the morphological degradation of the pristine nanocubes and the formation of nanoneedles as a function of reaction temperature and Cr-content.

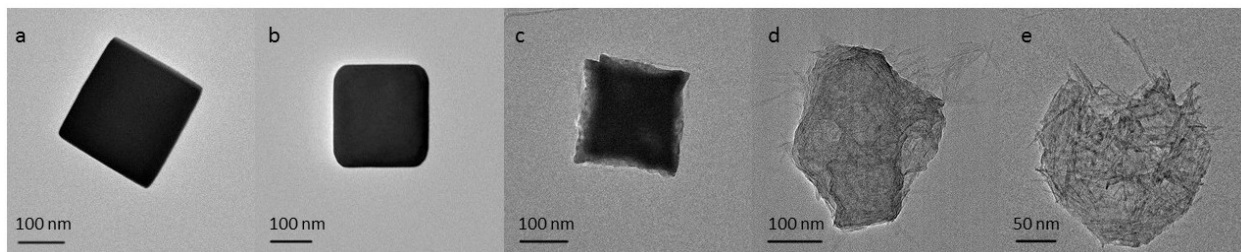


Figure 3.16: TEM images of (a)  $\text{Cr}_{0.1}\text{Cu}_{0.9}\text{Se}_2$ , (b)  $\text{Cr}_{0.2}\text{Cu}_{0.8}\text{Se}_2$ , (c)  $\text{Cr}_{0.3}\text{Cu}_{0.7}\text{Se}_2$ , (d)  $\text{Cr}_{0.4}\text{Cu}_{0.6}\text{Se}_2$ , and (e)  $\text{Cr}_{0.5}\text{Cu}_{0.5}\text{Se}_2$  NCs illustrating the disintegration process as a function of reaction temperature and Cr-content.

As mentioned, the molar ratio of Cu:Cr precursors was used to synthesis  $\text{Cr}_x\text{Cu}_{1-x}\text{Se}_2$  NCs was 1:2, where the excess amount of Cr-precursor was used. Decreasing the amount of Cr-precursor from 0.5 mmol to 0.1 mmol at the reaction temperature of 250 °C led to the formation of  $\text{Cr}_{0.1}\text{Cu}_{0.9}\text{Se}_2$  NCs indicating a significant decrease on the amount of doped  $\text{Cr}^{3+}$  in comparison with NCs of  $\text{Cr}_{0.3}\text{Cu}_{0.7}\text{Se}_2$  were formed at the same temperature but in the presence of excess Cr-precursors (0.5 mmol). However, we did not have good control on the shape of the prepared particles under the explained condition, and different deformed morphologies with big sizes were obtained (Figure 3.17). The NCs of  $\text{Cr}_{0.1}\text{Cu}_{0.9}\text{Se}_2$  formed at 220 °C with the excess amount of  $\text{Cr}^{3+}$  was much more uniform (Figures 3.8 and 3.10). Therefore and as expected, increasing the concentration of the Cr-precursor induces and facilitates the formation of  $\text{Cr}_x\text{Cu}_{1-x}\text{Se}_2$  products.

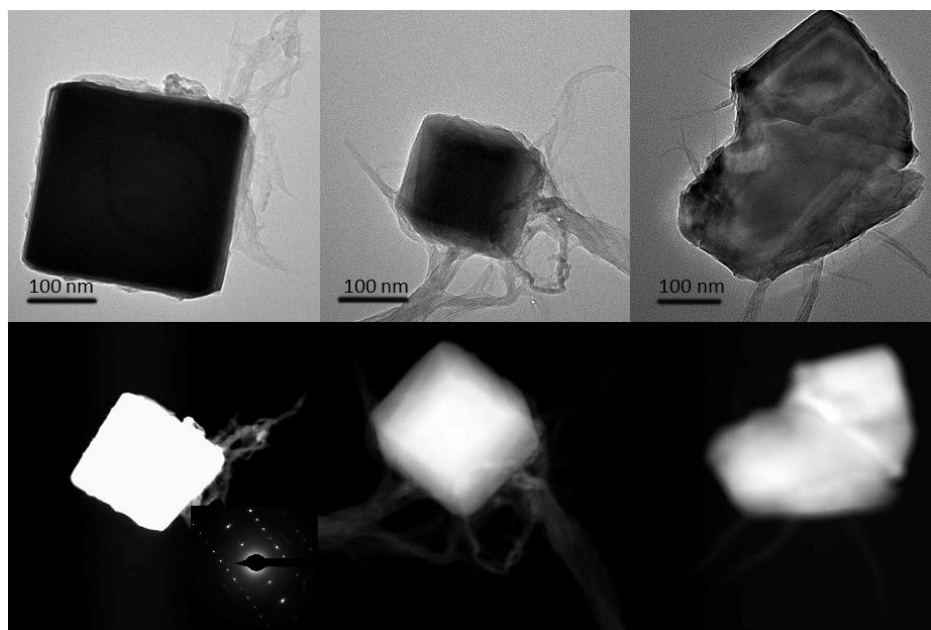


Figure 3.17: TEM and HADDF-STEM images and SAED patterns (inset) of the NCs of  $\text{Cr}_{0.1}\text{Cu}_{0.9}\text{Se}_2$  formed at 250 °C using only 0.1 mmol of Cr-precursor indicating the formation of some big size particles and some amorphous phase around the deformed nanocubes. The uniformity of the prepared NCs is much less than the same materials made in the excess amount (0.5 mmol) of Cr-precursor.

The XRD pattern of the NCs of  $\text{Cr}_x\text{Cu}_{1-x}\text{Se}_2$  ( $x = 0.3-0.5$ ) confirmed by the Rietveld refinement analysis with good agreement with the proposed structural models (Figure 3.18). The Rietveld refinement was carried out through a Match! Software<sup>35</sup> based on the FullProf algorithm.<sup>36</sup> The determined lattice parameters were 6.1252(2) Å, 6.12585(18) Å, and 6.12824(11) Å for  $x = 0.30, 0.40,$  and  $0.50,$  respectively, which are slightly larger than the reported  $p\text{-CuSe}_2$  lattice parameters 6.116 Å (JCPDS: 26-1115).

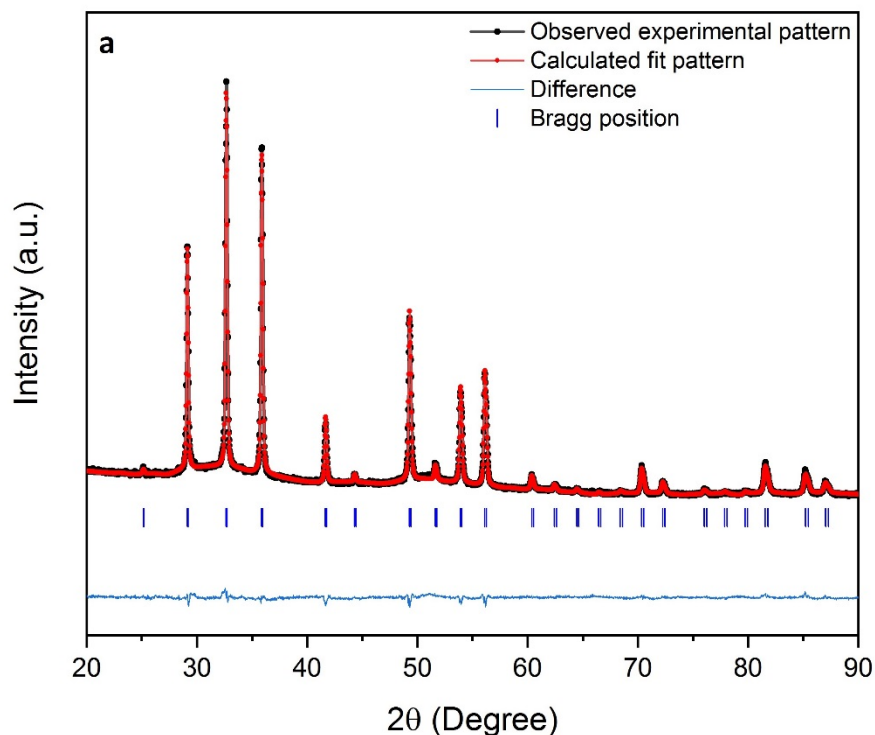


Figure 3.18: XRD pattern of (a)  $\text{Cr}_{0.3}\text{Cu}_{0.7}\text{Se}_2$ , (b)  $\text{Cr}_{0.4}\text{Cu}_{0.6}\text{Se}_2$ , and (c)  $\text{Cr}_{0.5}\text{Cu}_{0.5}\text{Se}_2$  NCs confirmed by the Rietveld refinement analysis to be in good agreement with the proposed pyrite model.

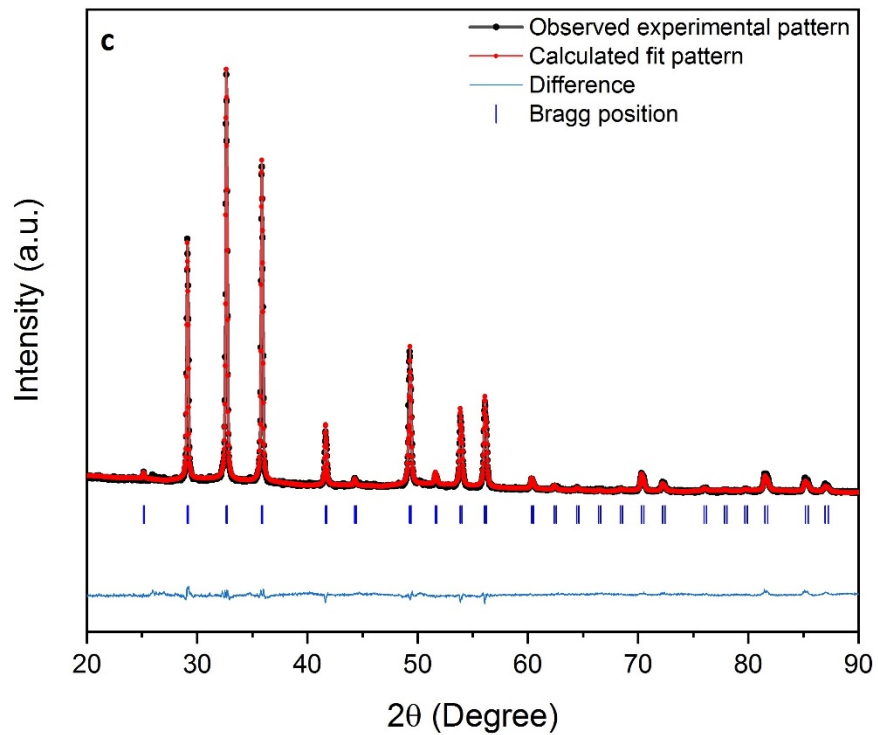
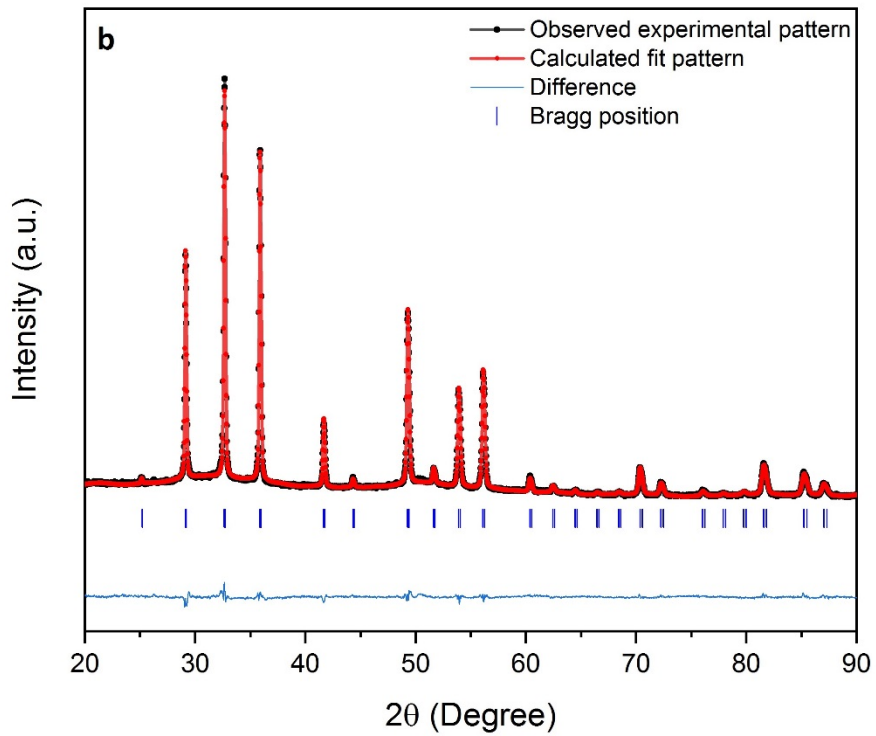


Figure 3.18: Continued.

### 3.4.3 Understanding the Formation Mechanism of $\text{Cr}_x\text{Cu}_{1-x}\text{Se}_2$ NCs

The next purpose of this work is to discuss the formation of  $\text{Cr}_x\text{Cu}_{1-x}\text{Se}_2$  NCs in which guest  $\text{Cr}^{3+}$  ions partially occupied the original octahedral positions of  $\text{Cu}^{2+}$  ions.

Although there are numerous reported studies of cationic substitution and cation exchange reactions, they usually involve isovalent ions, i.e, partial replacement of the host cations with ions of the same charge.<sup>37,38</sup> However, incorporation of an aliovalent guest ion, as in the case of  $\text{Cr}_x\text{Cu}_{1-x}\text{Se}_2$ , presents complications in maintaining charge balance and either reduction of the elements (Cu, Cr, or Se) or formation of vacancies should be considered in order to attain charge neutrality. Regardless of the degree of substitution, the pyrite  $\text{Cr}_x\text{Cu}_{1-x}\text{Se}_2$  structure is preserved for  $x = 0.1-0.5$ , as confirmed by Rietveld refinement of the X-ray diffraction patterns. Furthermore, based on EDX analyses of the different composition  $\text{Cr}_{1-x}\text{Cu}_x\text{Se}_2$  NCs, the atomic concentration for the sum of the cations (Cr, Cu) is within error about twice that for the anion (Se) for all the samples, suggesting no significant variations from the pyrite stoichiometry. The atomic resolution TEM images of the substituted NCs also show well-ordered lattices without defects. Thus, the valence reduction of the elements is more likely than vacancy formation. The stability of  $\text{Cr}^{3+}$  is significantly higher than  $\text{Cr}^{2+}$ , and the reduction of stable  $\text{Cr}^{3+}$  ion is not favorable, and this implies the reduction of  $\text{Cu}^{2+}$  to  $\text{Cu}^+$  ions. Therefore, a simple substitutional incorporation of the  $\text{Cr}^{3+}$  can be favorable in which both the metal cations occupy the octahedral sites. We propose that occupation of octahedral sites by  $\text{Cr}^{3+}$  plus partial reduction of  $\text{Cu}^{2+}$  to  $\text{Cu}^+$  results in the formation of stable  $\text{Cr}_x\text{Cu}_{1-x}\text{Se}_2$  NCs. In the synthesis reaction, ODA serves as a reducing agent and as the source of electrons involved in the reduction of  $\text{Cu}^{2+}$  to  $\text{Cu}^+$ .<sup>39,40</sup> Thus, depending on the amount of Cr-substitution, NCs of  $\text{Cr}^{3+}_{0.3}\text{Cu}^+_{0.3}\text{Cu}^{2+}_{0.2}\text{Se}_2$ ,  $\text{Cr}^{3+}_{0.4}\text{Cu}^+_{0.4}\text{Cu}^{2+}_{0.2}\text{Se}_2$ , and  $\text{Cr}^{3+}_{0.5}\text{Cu}^+_{0.5}\text{Se}_2$  are obtained.

By increasing the reaction temperature, the  $\text{Cu}^{2+}$  reduction becomes more favorable that induces the  $\text{Cr}^{3+}$  inclusion and replacement process. Finally, between 290-330 °C, the NCs of nominal composition  $\text{Cr}_{0.5}\text{Cu}_{0.5}\text{Se}_2$  are formed in which all copper ions are nominally in the +1 oxidation state. Although a larger fraction of the  $\text{Cu}^{2+}$  ions are reduced to  $\text{Cu}^+$  with substitution, the oxidation state of the guest  $\text{Cr}^{3+}$  remains constant. Moreover, the pyrite phase of  $\text{Cr}_x\text{Cu}_{1-x}\text{Se}_2$  maintains its cubic structure, regardless of the degree of substitution and no phase transformation is observed.

In order to support the above proposed mechanism, the change in the oxidation state of copper ions with Cr substitution has been confirmed by X-ray photoelectron spectroscopy (XPS). The spectrum of  $\text{Cr}_{0.5}\text{Cu}_{0.5}\text{Se}_2$  exhibits two main peaks at 932.4 and 952.1 eV corresponding to  $2p_{3/2}$  and  $2p_{1/2}$ , respectively, which are ascribed to  $\text{Cu}^+$ .<sup>41</sup> Whereas, in the case of  $\text{Cr}_{0.4}\text{Cu}_{0.6}\text{Se}_2$  an additional peak is observed at 933.3 eV, corresponding to  $\text{Cu}^{2+}$  (Figure 3.19).<sup>10,42</sup> Therefore, generation of  $\text{Cu}^+$  derived from the reduction of  $\text{Cu}^{2+}$  during the formation of Cr-substituted pyrite NCs is confirmed.

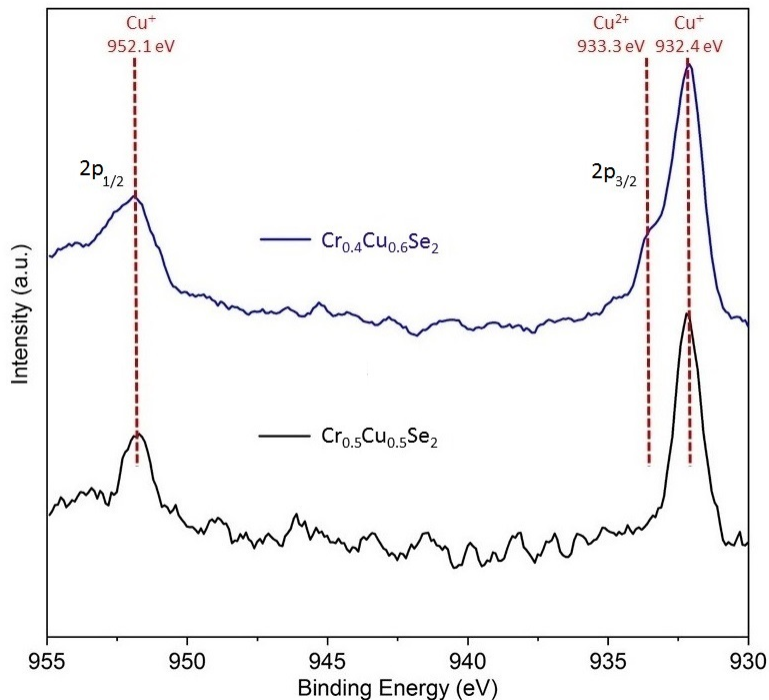


Figure 3.19: Analysis of the oxidation state of Cu. XPS diagrams of  $\text{Cr}_{0.4}\text{Cu}_{0.6}\text{Se}_2$  and  $\text{Cr}_{0.5}\text{Cu}_{0.5}\text{Se}_2$  NCs. The presence of  $\text{Cu}^+$  in the samples is validated by the appearance of two intense peaks at around 932.4 eV and 952.1 eV on the XPS spectra corresponding to  $2p_{3/2}$  and  $2p_{1/2}$ , respectively. The  $2p_{3/2}$  shoulder peak on the spectrum of  $\text{Cr}_{0.4}\text{Cu}_{0.6}\text{Se}_2$  NCs at 933.3 eV corresponds to  $\text{Cu}^{2+}$  ion.

The XPS spectrum of Cr 2p exhibits a spin-orbit separation of 9.7 eV between the  $2p_{3/2}$  and  $2p_{1/2}$  states, indicative of  $\text{Cr}^{3+}$  (Figure 3.20).<sup>43,44</sup> Two representative peaks in the observed XPS spectrum of Se are generally attributed to Se  $3d_{5/2}$  and  $3d_{3/2}$  confirming the existence of  $\text{Se}_2^{2-}$ .<sup>45-47</sup> In addition to the major Se 3d peaks, a minor broad peak (shoulder) was observed indicated partially surface oxidation. Similar surface oxidations were already observed in some reported pyrite  $\text{MSe}_2$  systems.<sup>45-47</sup>

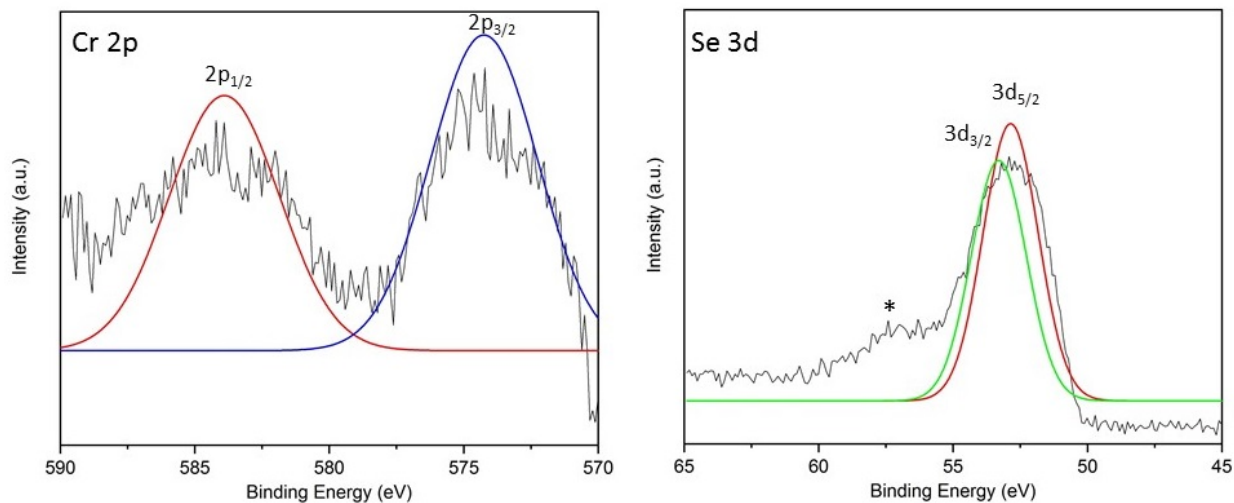


Figure 3.20: XPS spectra of Cr 2p and Se 3d of the  $\text{Cr}_{0.4}\text{Cu}_{0.6}\text{Se}_2$  nanocrystals.

We confirmed the presence of Cr, Cu, and Se using EELS. The oxidation state of the copper has also been studied by Electron Energy Loss Spectroscopy (EELS). Figure 3.21 shows the EELS data of Cr L, Cu L, and Se L edge maps for the highlighted region. EELS can be a powerful technique for the identification of the oxidation states of elements. Especially for transition metals, from analyzing the near-edge fine structure. Because of the electronic transition from 2p state of transition metals to unoccupied 3d level, their L ionization edges should display sharp peaks in the near-edge region (due to the unoccupied states in 3d bands).<sup>48,49</sup> In general, the L<sub>3</sub> and L<sub>2</sub> edges indicating transitions from 2p<sub>1/2</sub> to 3d<sub>3/2</sub> and 2p<sub>3/2</sub> to 3d<sub>5/2</sub>, respectively should exhibit nearly sharp and intense peaks for Cu<sup>2+</sup>, whereas Cu<sup>0</sup> shows broad edges because of its completely filled 3d band.<sup>50-52</sup>

Since the spectrum of the Cu L edge is noisy, we could not clearly determine the position of the peaks. It seems that this is a common issue in Cu L edge, especially in nanoparticles. Liu et al. have compared the EELS spectrum of Cu<sup>2+</sup> containing materials with standard spectra, and

based on the similarities detected between their work and references, they approved the existence of  $\text{Cu}^{2+}$  in their materials (Figure 3.22). They have prepared  $\text{Cu}_{0.45}\text{TaS}_2$  via intercalating copper into two dimensional (2D) layered  $\text{TaS}_2$  nanoflakes.<sup>53</sup>

In another work, Motter et al. intercalate zero-valent  $\text{Cu}^0$  into 2D layered materials of  $\text{GaSe}$  and  $\text{In}_2\text{Se}_3$ . As indicated in figure 3.23, the authors illustrated that according to the similarities between the EELS fine structure plots of the prepared  $\text{Cu}_{2.34}\text{GaSe}$  and  $\text{Cu}_{2.14}\text{In}_2\text{Se}_3$  with Cu L edge in  $\text{Cu}^0$  spectrum, and detection of no sharp peaks, the intercalated copper is in zero-valent.<sup>54</sup> Figure 3.22 also represented the  $\text{Cu}^+$  spectrum, in which the  $L_3$  and  $L_2$  look sharper than in  $\text{Cu}^{2+}$  spectrum.

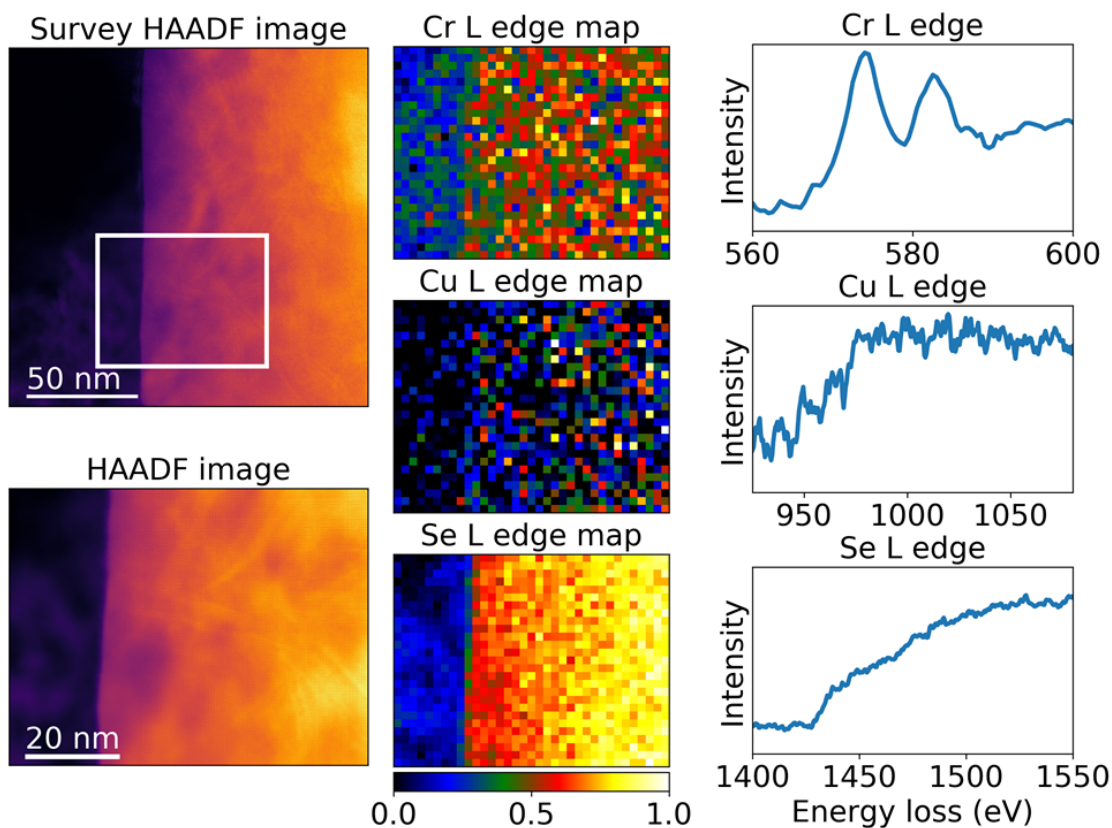


Figure 3.21: EELS data acquired for the region highlighted (white box) in the HAADF image of pyrite NCs showing the presence of Cr, Cu, and Se.

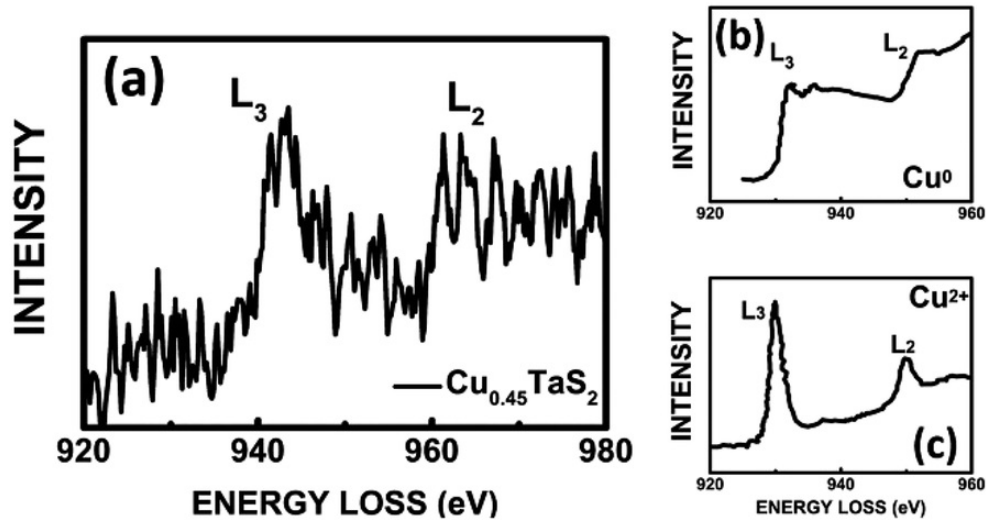


Figure 3.22: Comparing of (a) EELS fine structure of  $\text{Cu}_{0.45}\text{TaS}_2$  with (b)  $\text{Cu}^0$  and (c)  $\text{Cu}^{2+}$  spectra from ref. 53. The nearly sharp  $L_3$  edge in (a) is similar to  $\text{Cu}^{2+}$ . Reprinted with permission from ref. 53.

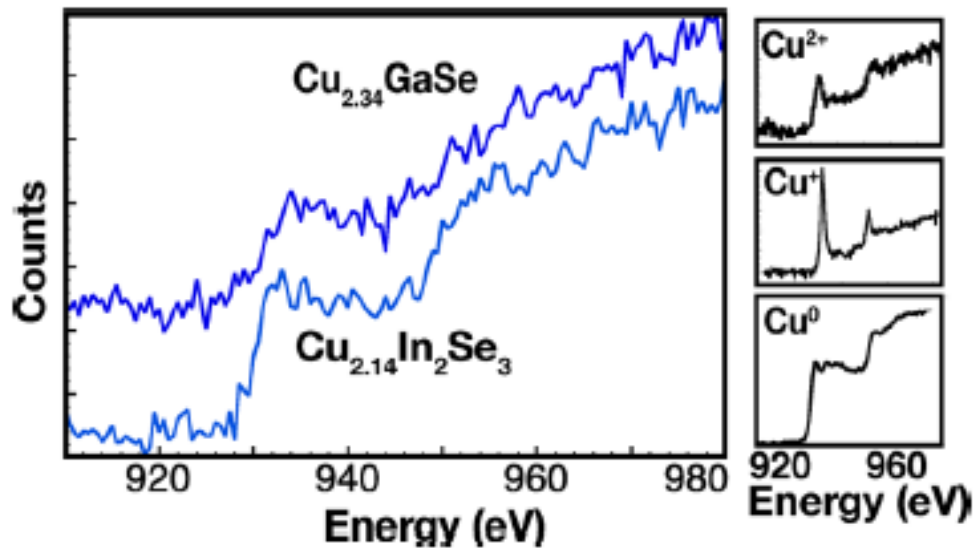


Figure 3.23: EELS fine structure plots for  $\text{Cu}_{2.34}\text{GaSe}$  and  $\text{Cu}_{2.14}\text{In}_2\text{Se}_3$  along with reference plots for  $\text{Cu}^{2+}$ ,  $\text{Cu}^+$ , and  $\text{Cu}^0$ , confirming the zero-valent identity of the intercalated copper. Reprinted with permission from ref. 54.

Using the same strategy, we have compared the EELS fine structure plot of pyrite NCs with reference plots in order to study the oxidation state of the copper ions. The appearance of the multiple nearly sharp peaks in the Cu L edge is suggesting the existence of both  $\text{Cu}^+$  and

Cu<sup>2+</sup> ions in the structure of NCs. However, the EELS fine structure spectrum of Cu L edge was too noisy to let us extract the position of the L<sub>2</sub> and L<sub>3</sub> ionization edges.

Comparing to copper, two intense peaks corresponding to L<sub>3</sub> and L<sub>2</sub> edges of chromium are observed that matches well with that for Cr<sup>3+</sup> in the octahedral geometry.<sup>55-57</sup> As expected, Se edge EELS plot shows a broad L edge.<sup>58,59</sup>

### 3.4.4 Magnetic Properties of Cr<sub>x</sub>Cu<sub>1-x</sub>Se<sub>2</sub> NCs; Cr-Induced Large Enhancement of Ferromagnetic Moment

The magnetic properties of the NCs of Cr<sub>0.3</sub>Cu<sub>0.7</sub>Se<sub>2</sub> and Cr<sub>0.5</sub>Cu<sub>0.5</sub>Se<sub>2</sub> were measured using a Physical Properties Measurement System (PPMS) equipped with a Vibrating Sample Magnetometer (VSM) and compared to CuSe<sub>2</sub>.

Magnetization (*M*) as a function of temperature (*T*) measured at 10 kOe for CuSe<sub>2</sub> (inset) and two different Cr substituted Cr<sub>x</sub>Cu<sub>1-x</sub>Se<sub>2</sub> compositions are shown in figure 3.24 a. The general shape of the Cr<sub>0.3</sub>Cu<sub>0.7</sub>Se<sub>2</sub> and Cr<sub>0.5</sub>Cu<sub>0.5</sub>Se<sub>2</sub> curves are similar to that of CuSe<sub>2</sub>, except with a large enhancement (~10<sup>2</sup> fold) in the magnetization, which increases with increasing Cr<sup>3+</sup> concentration. Additionally, the temperature at which the magnetic phase transition occurs increases with increasing Cr<sup>3+</sup> concentration. Figure 3.24 c shows Curie-Weiß fits for Cr<sub>0.3</sub>Cu<sub>0.7</sub>Se<sub>2</sub> and Cr<sub>0.5</sub>Cu<sub>0.5</sub>Se<sub>2</sub> NCs and the related extracted parameters are summarized in table 3.4. The effective magnetic moment ( $\mu_{\text{eff}}$ ) per formula unit for Cr<sub>0.3</sub>Cu<sub>0.7</sub>Se<sub>2</sub> and Cr<sub>0.5</sub>Cu<sub>0.5</sub>Se<sub>2</sub> is 2.4818(17) and 2.5881(13)  $\mu_{\text{B}}$ , respectively. Assuming *S* = 3/2, 1/2, and 0 local moments for Cr<sup>3+</sup>, Cu<sup>2+</sup>, and Cu<sup>+</sup> species, respectively, the  $\mu_{\text{eff}}$  is expected to vary weakly between 1.75 and 2.74  $\mu_{\text{B}}$  for compositions above 5% Cr. Specifically, the predicted effective moment for Cr<sup>3+</sup><sub>0.3</sub>Cu<sup>2+</sup><sub>0.4</sub>Cu<sup>+</sup><sub>0.3</sub>Se<sub>2</sub> is 2.39  $\mu_{\text{B}}$  and for Cr<sup>3+</sup><sub>0.5</sub>Cu<sup>+</sup><sub>0.5</sub>Se<sub>2</sub> it is 2.74  $\mu_{\text{B}}$ .

Hysteresis loops of NCs of  $\text{Cr}_{0.3}\text{Cu}_{0.7}\text{Se}_2$  and  $\text{Cr}_{0.5}\text{Cu}_{0.5}\text{Se}_2$  and non-substituted pyrite  $\text{CuSe}_2$  measured at 1.8 K are presented in figure 3.24 b. Both  $\text{Cr}_{0.3}\text{Cu}_{0.7}\text{Se}_2$  and  $\text{Cr}_{0.5}\text{Cu}_{0.5}\text{Se}_2$  NCs show ferromagnetic-like behavior with low coercivity. Magnetic saturation does not occur in these NCs, which could be an indication of either a more complex magnetic structure, particularly at the surface of the NCs, or superparamagnetism. Consistent with the  $M(T)$  curves, an increase in  $\text{Cr}^{3+}$  concentration causes an increase in magnetization. The large effective moments suggest that the magnetic properties are intrinsic to the main phase since a  $J = 3/2$  impurity would need to be between 25 and 50% of the mass of the sample and thus be readily apparent in the diffraction patterns. Moreover, the magnetic properties are reminiscent of  $p$ - $\text{CuSe}_2$ , suggesting continuity in the electronic phase diagram. The magnetic response also could not be attributed to  $\text{CuCr}_2\text{Se}_4$  or any known Cr-Se phases such as  $\text{CrSe}_2$ ,  $\text{CrSe}$ ,  $\text{Cr}_7\text{Se}_8$ , or  $\text{Cr}_2\text{Se}_3$ , nor are aware of any Cr oxides or hydrates that would explain the magnetic response.

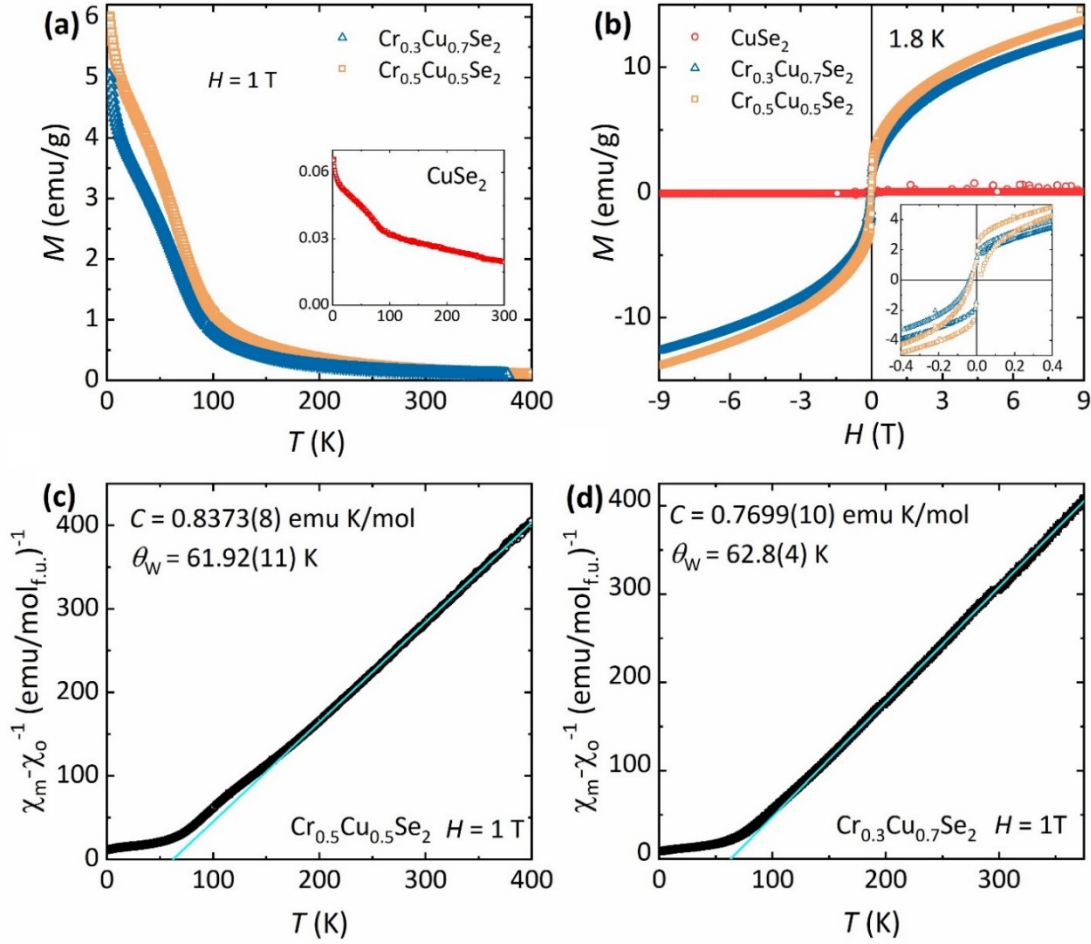


Figure 3.24: (a) Magnetization ( $M$ ) versus temperature ( $K$ ) measurements on  $\text{Cr}_{0.3}\text{Cu}_{0.7}\text{Se}_2$ , and  $\text{Cr}_{0.5}\text{Cu}_{0.5}\text{Se}_2$  NCs with applied field of 10 kOe (1 T). The same is shown for  $\text{CuSe}_2$  in inset, (b) Curie-Weiss plots for NCs of  $\text{Cr}_{0.3}\text{Cu}_{0.7}\text{Se}_2$  and  $\text{Cr}_{0.5}\text{Cu}_{0.5}\text{Se}_2$ , and (c) Magnetization ( $M$ ) versus magnetic field ( $H$ ) measurements on NCs of  $\text{Cr}_{0.3}\text{Cu}_{0.7}\text{Se}_2$  and  $\text{Cr}_{0.5}\text{Cu}_{0.5}\text{Se}_2$  at 1.8 K.

Table 3.3: Extracted parameters from Curie-Weiss plots.

Sample	C (emu*K/f.u.*Oe)	$\Theta_w$ (K)	$\mu_{\text{eff}}$ ( $\mu_B/\text{f.u.}$ )
$\text{Cr}_{0.3}\text{Cu}_{0.7}\text{Se}_2$	0.7699(10)	62.8(4)	2.4818(17)
$\text{Cr}_{0.5}\text{Cu}_{0.5}\text{Se}_2$	0.8373(8)	61.92(7)	2.5881(13)

### 3.5 Conclusion

Further development in the knowledge of the formation of novel nanomaterials unstable in a bulk phase will enable further design and engineering of previously unavailable multielemental compounds for unique high-performance applications. In summary, Cr-substituted *p*-CuSe<sub>2</sub> (Cr<sub>x</sub>Cu<sub>1-x</sub>Se<sub>2</sub>,  $x = 0.1-0.5$ ) NCs, which exhibit robust ferromagnetic order, have been synthesized and their magnetism correlated with the Cr<sup>3+</sup> content. To the best of our knowledge, there have been no previous reports of cationic substitution of Cr for Cu in the *p*-CuSe<sub>2</sub> system, likely due to the large size difference between Cr<sup>3+</sup> (crystal radius 0.755) and Cu<sup>2+</sup> (crystal radius 0.87). Our work has also shown that increase in Cr-content with increasing reaction temperature induces fragmentation of the Cr<sub>x</sub>Cu<sub>1-x</sub>Se<sub>2</sub> nanocubes to form small nanoneedles. The results of this work offer a novel approach for the design and synthesis of new multielement materials that may not be stable in bulk form. The XRD patterns of NCs formed at temperatures above 300 °C show that the intensity of peaks from the phase decreases gradually with increasing temperature and reaction time and temperature, with a corresponding increase in the intensity of peaks corresponding to spinel CuCr<sub>2</sub>Se<sub>4</sub> phase. It appears that the pyrite phase is saturated at 50% Cr-content, and then a new ternary phase (CuCr<sub>2</sub>Se<sub>4</sub> spinel) is formed for higher Cr concentrations. The mechanistic details of pyrite to spinel phase transformation will be discussed in chapter 4.

### 3.6 References

1. Bither, T. A.; Bouchard, R. J.; Cloud, W. H.; Donohue, P. C.; Siemons, W. J. Transition metal pyrite dichalcogenides. High-Pressure Synthesis and Correlation of Properties. *Inorg. Chem.* **1968**, *7*, 2208–2220.
2. Ogawa, S. Magnetic Properties of 3d Transition-Metal Dichalcogenides with the Pyrite Structure. *Journal of Applied Physics* **1979**, *50*, 2308–2311.
3. Faber, M. S.; Lukowski, M. A.; Ding, Q.; Kaiser, N. S.; Song Jin, S. Earth-Abundant Metal Pyrites (FeS<sub>2</sub>, CoS<sub>2</sub>, NiS<sub>2</sub>, and their alloys) for Highly Efficient Hydrogen Evolution and Polysulfide Reduction Electrocatalysis. *J. Phys. Chem. C* **2014**, *118*, 21347–21356.
4. Martinolich, A. J.; Kurzman, J. A.; Neilson, J. R. Polymorph Selectivity of Superconducting CuSe<sub>2</sub> through Kinetic Control of Solid-State Metathesis. *J. Am. Chem. Soc.* **2015**, *137*, 3827–3833.
5. Martinolich, A. J.; Higgins, R. F.; Shores, M. R.; Neilson, J. R. Lewis Base Mediated Polymorph Selectivity of Pyrite CuSe<sub>2</sub> through Atom Transfer in Solid-State Metathesis. *Chem. Mater.* **2016**, *28*, 1854–1860.
6. Bither, T.; Prewitt, C.; Gillson, J.; Bierstedt, P.; Flippen, R.; Young, H. New Transition Metal Dichalcogenides Formed at High Pressure. *Solid State Commun.* **1966**, *4*, 533–535.
7. Martinolich, A. J.; Neilson, J. R. Pyrite Formation via Kinetic Intermediates through Low-Temperature Solid-State Metathesis. *J. Am. Chem. Soc.* **2014**, *136*, 15654–15659.
8. Seo, Y. -H.; Jo, Y.; Choi, Y.; Yoon, K. H.; Ryu, B. -H. Ahn, S. J.; Jeong, S. Thermally-Derived Liquid Phase Involving Multiphase Cu(In,Ga)Se<sub>2</sub> Nanoparticles for Solution-Processed Inorganic Photovoltaic Devices. *RSC Adv.* **2014**, *4*, 18453–18459.
9. G. Krill, G.; Panissod, P.; Lapiere, M. F. Magnetic Properties and Phase Transitions of the Metallic CuX<sub>2</sub> dichalcogenides (X=S, Se, Te) with Pyrite Structure. *J. Phys. C: Solid State Phys.* **1976**, *9*, 1521–1535.
10. Liu, T.; Jin, Z.; Li, J.; Wang, J.; Wang, D.; Laia, J.; Du, H. Monodispersed Octahedral-Shaped Pyrite CuSe<sub>2</sub> Particles by Polyol Solution Chemical Synthesis. *CrystEngComm.* **2013**, *15*, 8903–8906.
11. Wang, X.; Miao, Z.; Ma, Y.; Chen, H.; Qian, H.; Zha, Z. One-Pot Solution Synthesis of Shape-Controlled Copper Selenide Nanostructures and Their Potential Applications in Photocatalysis and Photothermal Therapy. *Nanoscale* **2017**, *9*, 14512–14519.
12. Datta, K. K. R.; Kulkarni, C.; Eswaramoorthy, M. Aminoclay: A Permselective Matrix to Stabilize Copper Nanoparticles. *Chem. Commun.* **2010**, *46*, 616–618.

13. Zarur, A. J.; Ying, J. Y. Reverse Microemulsion Synthesis of Nanostructured Complex Oxides for Catalytic Combustion. *Nature* **2000**, *403*, 65–67.
14. Berkovsky, B. M.; Medvedev, V. F.; Krovov, M. S. *Magnetic Fluids: Engineering Applications*; Oxford University Press: Oxford, U.K., **1993**.
15. Ziolo, R. F.; Giannelis, E. P.; Weinstein, M. P.; O'Horo, B. N.; Ganguly, M. V.; Russel, M. W.; Huffman, D. R. Matrix-Mediated Synthesis of Nanocrystalline  $\gamma$ -Fe<sub>2</sub>O<sub>3</sub>: A New Optically Transparent Magnetic Material. *Science* **1992**, *257*, 219–223.
16. Sun, S. H.; Murray, C. B.; Weller, D.; Folks, L.; Moser. Monodisperse FePt Nanoparticles and Ferromagnetic FePt Nanocrystal Superlattices. *Science* **2000**, *287*, 1989–1992.
17. Yoo, D.; Jeong, H.; Noh, S. H.; Lee, J. H.; Cheon, J. Magnetically Triggered Dual Functional Nanoparticles for Resistance-Free Apoptotic Hyperthermia. *Angew. Chem., Int. Ed.* **2013**, *52*, 13047–13051.
18. Kocsis, V.; Bordács, S.; Varjas, D.; Penc, K.; Abouelsayed, A.; Kuntscher, A.; Ohgushi, K.; Tokura, Y.; Kézsmárki, I. Magnetoelasticity in ACr<sub>2</sub>O<sub>4</sub> Spinel Oxides. *Physical Review. B* **2013**, *87*, 064416.
19. Pagan, E, H, A.; Leach, A, D, P.; Rhodes, J, M.; Sarkar, S.; Macdonald, J, E. A Synthetic Exploration of Metal–Semiconductor Hybrid Particles of CuInS<sub>2</sub>. *Chem. Mater.* **2015**, *27*, 7969–7976.
20. Baltzer, P. K.; Lehmann, H. W.; Robbins, M. Insulating Ferromagnetic Spinel. *Phys. Rev. Lett.* **1965**, *15*, 493–495.
21. Ramesha, K.; Seshadri, R. Solvothermal Preparation of Ferromagnetic Sub-Micron Spinel CuCr<sub>2</sub>Se<sub>4</sub> Particles. *Solid State Sci.* **2004**, *6*, 841–845.
22. Kim, D.; Gedanken, A.; Tver'yanovich, Y. S.; Lee, D. W.; Kim, B. K. Synthesis and Characterization of Nanocrystalline CuCr<sub>2</sub>Se<sub>4</sub> particles. *Mater. Lett.* **2006**, *60*, 2807–2809.
23. Lin, C. R.; Yeh, C. L.; Lu, S. Z.; Lyubutin, I. S.; Wang, S. C.; Suzdalev, I. P. Synthesis, Characterization and Magnetic Properties of Nearly Monodisperse CuCr<sub>2</sub>Se<sub>4</sub> Nanoparticles. *Nanotechnology* **2010**, *21*, 235603.
24. Ramasamy, K.; Mazumdar, D.; Zhou, Z.; Wang, Y. H. A.; Gupta, A. Colloidal Synthesis of Magnetic CuCr<sub>2</sub>S<sub>4</sub> Nanocrystals and Nanoclusters. *J. A. Chem. Soc.* **2011**, *133*, 20716–20719.
25. Ramasamy, K.; Mazumdar, D.; Bennett R. D.; Gupta, A. Syntheses and Magnetic Properties of Cr<sub>2</sub>Te<sub>3</sub> and CuCr<sub>2</sub>Te<sub>4</sub> Nanocrystals. *Chem. Commun.* **2012**, *48*, 5656–5658.

26. Wang, Y. H. A.; Bao, N.; Shen, L.; Padhan, P.; Gupta, A. Size-Controlled Synthesis of Magnetic  $\text{CuCr}_2\text{Se}_4$  Nanocrystals. *J. Am. Chem. Soc.* **2007**, *129*, 12408–12409.
27. Pang, C.; Yang, R.; Singh, A.; Chen, H.; Bowman, M. K.; Bao, N.; Shen, L.; Gupta, A. Colloidal Synthesis and Magnetic Properties of Anisotropic-Shaped Spinel  $\text{CuCr}_2\text{Se}_4$  nanocrystals. *RSC Adv.* **2017**, *7*, 31173–31179.
28. Li, G. M.; Tang, X. B.; Lou, S. Y.; Zhou, S. M. Large Enhancement of Ferromagnetism by Cr Doping in  $\text{Mn}_2\text{O}_3$  Nanowires. *Appl. Phys. Lett.* **2014**, *104*, 173105.
29. Xing, G.; Yi, J.; Wang, D.; Liao, L.; Yu, T.; Shen, Z.; Huan, C.; Sum, T.; Ding, J.; Wu, T. Strong Correlation between Ferromagnetism and Oxygen Deficiency in Cr-Doped  $\text{In}_2\text{O}_{3-\delta}$  Nanostructures. *Phys. Rev. B* **2009**, *79*, 174406.
30. Liu, H.; Zhang, X.; Li, L.; Wang, Y.; Gao, K.; Li, Z.; Zheng, R.; Ringer, S.; Zhang, B.; Zhang, X. Role of Point Defects in Room-Temperature Ferromagnetism of Cr-doped ZnO. *Appl. Phys. Lett.* **2007**, *91*, 072511.
31. Liu, H.; Wu, S. Y.; Singh, R.; Gu, L.; Smith, D. J.; Newman, N.; Dilley, N.; Montes, L.; Simmonds, M. Observation of Ferromagnetism above 900K in Cr–GaN and Cr–AlN. *Appl. Phys. Lett.* **2004**, *85*, 407.
32. Farvid, S. S.; Ju, L.; Worden, M.; Radovanovic, P. V. Colloidal Chromium-Doped  $\text{In}_2\text{O}_3$  Nanocrystals as Building Blocks for High- $T_C$  Ferromagnetic Transparent Conducting Oxide Structures. *J. Phys. Chem. C* **2008**, *112*, 17755–17759.
33. Pennycook, S.; Jesson, D., High-resolution Z-contrast imaging of crystals. *Ultramicroscopy* **1991**, *37* (1-4), 14–38.
34. Johan, Z., Picot, P., Pierrot, R.; Kvacek, M. La krutaïte,  $\text{Cu Se}_2$ , un nouveau minéral du groupe de la pyrite. *Bulletin de Minéralogie*, **1972**, *95*(4), 475–481.
35. Putz, H.; Brandenburg, K. Phase Identification from Powder Diffraction, Crystal Impact, Kreuzherrenstr. Bonn, Germany, *102*, 53227.
36. Rodriguez-Carvajal, J. "FULLPROF: A Program for Rietveld Refinement and Pattern Matching Analysis", Abstracts of the Satellite Meeting on Powder Diffraction of the XV Congress of the IUCr. Toulouse, France **1990**, 27.
37. Gupta, S.; Kershaw, S. V.; Rogach, A. L. 25th Anniversary Article: Ion Exchange in Colloidal Nanocrystals. *Adv. Mater.* **2013**, *25*, 6923.
38. De Trizio, L.; Manna, L. Forging Colloidal Nanostructures via Cation Exchange Reactions. *Chem. Rev.* **2016**, *116*, 10852–10887.

39. Wang, D.; Li, Y. Effective Octadecylamine System for Nanocrystal Synthesis. *Inorg. Chem.* **2011**, *50*, 5196–5202.
40. Mourdikoudis, S.; Liz-Marzán, S. M. Oleylamine in Nanoparticle Synthesis. *Chem. Mater.* **2013**, *25*, 1465–1476.
41. Olvera, A.; Sahoo, P.; Tarczynski, S.; Poudeu, P. F. P. Topochemical Solid-State Reactivity: Redox-Induced Direct Structural Transformation from CuSe<sub>2</sub> to CuInSe<sub>2</sub>. *Chem. Mater.* **2015**, *27*, 7179–7186.
42. Huang, J.; Hörmann, N.; Oveisi, E.; Loiudice, A.; De Gregorio, G. L.; Andreussi, O.; Marzari, N.; Buonsanti, R. Potential-induced nanoclustering of metallic catalysts during electrochemical CO<sub>2</sub> reduction. *Nature Comm.* **2018**, *9*, 3117.
43. Pang, C.; Yang, R.; Singh, A.; Chen, H.; Bowman, M. K.; Bao, N.; Shen, L.; Gupta, A. Colloidal synthesis and magnetic properties of anisotropic-shaped spinel CuCr<sub>2</sub>Se<sub>4</sub> nanocrystals. *RSC Adv.* **2017**, *7*, 31173–31179.
44. Malicka, E.; Waskowska, A.; Heimann, J.; Sitko, R.; Kaczorowski, D. Structural and magnetic properties of CuCr<sub>2</sub>Se<sub>4</sub> single crystals diluted with Sb(III). *J. Alloys Compd.* **2012**, *513*, 353–358.
45. Wang, L. C.; Chen, L. Y.; Luo, T.; Bao, K. Y.; Tian, Y. T. A facile method to the cube-like MnSe<sub>2</sub> microcrystallines via a hydrothermal process. *Solid State Commun.* **2006**, *138*, 72–75.
46. Xu, J.; Jang, K.; Lee, J.; Kim, H. J.; Jeong, J.; Park, J. G.; Son, S. U. Phase-Selective Growth of Assembled FeSe<sub>2</sub> Nanorods from Organometallic Polymers and Their Surface Magnetism. *Cryst. Growth Des.* **2011**, *11*, 2707–2710.
47. Hamdadou, N.; Khelil, A.; Morsli, M.; Bernàde, J. C. Iron diselenide thin films synthesized by soft selenization of iron films. *Vacuum* **2005**, *77*, 151–156.
48. Yu, J. H.; Liu, X.; Kweon, K. E.; Joo, J.; Park, J.; Ko, K.-T.; Lee, D. W.; Shen, S.; Tivakornsasithorn, K.; Son, J. S.; Park, J.-H.; Kim, Y.-W.; Hwang, G. S.; Dobrowolska, M.; Furdyna, J. K.; Hyeon, T. Giant Zeeman splitting in nucleation-controlled doped CdSe:Mn<sup>2+</sup> quantum nanoribbons. *Nat. Mater.* **2010**, *9*, 47–53.
49. Beberwyck, B. J.; Surendranath, Y.; Alivisatos, A. P. Cation Exchange: A Versatile Tool for Nanomaterials Synthesis. *J. Phys. Chem. C* **2013**, *117*, 19759–19770.
50. Pease, D. M.; Bader, S. D.; Brodsky, M. B.; Budnick, J. I.; Morrison, T. I.; Zaluzec, N. J. Anomalous L<sub>3</sub>L<sub>2</sub> White Line Ratios and Spin Pairing in 3d Transition Metals and Alloys: Cr Metal and Cr<sub>20</sub>Au<sub>80</sub>. *Phys. Lett. A* **1986**, *114*, 491–494.

51. Krivanek, O. L.; Paterson, J. H. Elms of 3d Transition-Metal Oxides: I. Variations across the Periodic Table. *Ultramicroscopy* **1990**, *32*, 313–318.
52. Leapman, R. D.; Grunes, L. A.; Fejes, P. L. Study of the L<sub>23</sub> Edges in the 3d Transition Metals and Their Oxides by Electron-Energy-Loss Spectroscopy with Comparisons to Theory. *Phys. Rev. B: Condens. Matter Mater. Phys.* **1982**, *26*, 614–635.
53. Liu, R.; Wang, C.; Li, Y.; Xie, Y.; Chen, Q.; Chen, Z.; Liu, Q. Intercalating Copper into Layered TaS<sub>2</sub> van der Waals Gaps. *RSC Adv.* **2017**, *7*, 46699–46703.
54. Motter, J. P.; Koski, K. J.; Cui, Y. General Strategy for Zero-Valent Intercalation into Two-Dimensional Layered Nanomaterials. *Chem. Mater.* **2014**, *26*, 2313–2317.
55. Daultona, T. L.; Little, B. J. Determination of Chromium Valence over the Range Cr(0)–Cr(VI) by Electron Energy Loss Spectroscopy. *Ultramicroscopy* **2006**, *106*, 561–573.
56. Asa, M.; Vinai, G.; Hart, J. L.; Autieri, C.; Rinaldi, C.; Torelli, P.; Panaccione, G.; Taheri, M. L.; Picozzi, S.; Cantoni, M. Interdiffusion-Driven Synthesis of Tetragonal Chromium (III) Oxide on BaTiO<sub>3</sub>. *Phys. Rev. Mater.* **2018**, *2*, 033401.
57. Jiang, N.; Silcox, J. Observations of Reaction Zones at Chromium/Oxide Glass Interfaces. *J. App. Phys.* **2000**, *87*, 3768–3776.
58. Li, Y.; Bi, H.; Du, Y.; Che, R. Synthesis and Thermoelectric Properties of Defect Containing PbSe-PbTe Heterojunction Nanostructures. *RSC Adv.* **2017**, *7*, 53855–53860.
59. Xia, X.; Ling, L.; Zhang, W. –X. Genesis of Pure Se(0) Nano- and Micro-Structures in Wastewater with Nanoscale Zero-Valent Iron (nZVI). *Environ. Sci.: Nano* **2017**, *4*, 52–59.

## CHAPTER 4

### TRANSFORMATION FROM PYRITE $\text{CuSe}_2$ TO SPINEL $\text{CuCr}_2\text{Se}_4$ NANOCRYSTALS

#### 4.1 Abstract

In chapter 3, we performed a reaction in which pyrite  $p\text{-Cr}_x\text{Cu}_{1-x}\text{Se}_2$  nanocrystals (NCs) were formed, and by increasing the reaction temperature, more  $\text{Cr}^{3+}$  ions occupied the octahedral sites of the pyrite structure. The formation of  $p\text{-Cr}_x\text{Cu}_{1-x}\text{Se}_2$  NCs provides a trajectory to phase transformation to ternary spinel  $\text{CuCr}_2\text{Se}_4$  NCs at high temperatures (above 300 °C). The morphological changes and magnetic properties of the produced NCs are studied in this chapter. The mechanistic details of the pyrite-spinel phase transformation are also discussed. Through scanning transmission electron microscopy (STEM), energy-dispersive X-ray spectroscopy (EDS), high-resolution TEM (HRTEM), and X-ray diffraction (XRD), we observe that the structural template that is provided by  $p\text{-Cr}_x\text{Cu}_{1-x}\text{Se}_2$  serves as a pathway to construct spinel  $\text{CuCr}_2\text{Se}_4$  phase.

#### 4.2. Introduction

##### 4.2.1 Colloidal Nanocrystals of Spinel $\text{CuCr}_2\text{Se}_4$

Three successful works in order to the synthesis of colloidal  $\text{CuCr}_2\text{Se}_4$  chalcospinels have been previously reported by our research group, in which the hot-injection method has been used as the synthesis strategy.<sup>1-3</sup> In this work,  $\text{CuCr}_2\text{Se}_4$  NCs were synthesized using the heat-up method instead, and the formation mechanism and properties of the products have been studied. Wang et al. have reported the first colloidal synthesized NCs of  $\text{CuCr}_2\text{Se}_4$  during thermal decomposition of Cu-, and Cr-acetylacetonate (acac) precursors and selenium in the presence of

the mixture of OLA and/or 1-octadecene (ODE; C<sub>18</sub>H<sub>36</sub>).<sup>1</sup> Selenium powder was dissolved in OLA/ODE solvent at 330 °C. On the other hand, the mixture of metal salts was dissolved in OLA at 175 °C separately. The metal salts mixture was injected into the selenium mixture, and the resulting mixture was heated to 350 °C in 30 minutes and kept at this temperature for 60 more minutes. The average size of CuCr<sub>2</sub>Se<sub>4</sub> NCs was related to the ratio of OLA and ODE in the solvent mixture. Figure 4.1 indicates the TEM image of the relatively monodisperse nanocubes of CuCr<sub>2</sub>Se<sub>4</sub> with an average size of 25 nm. These NCs were synthesized with the solvent mixture volume ratio of 1:1.

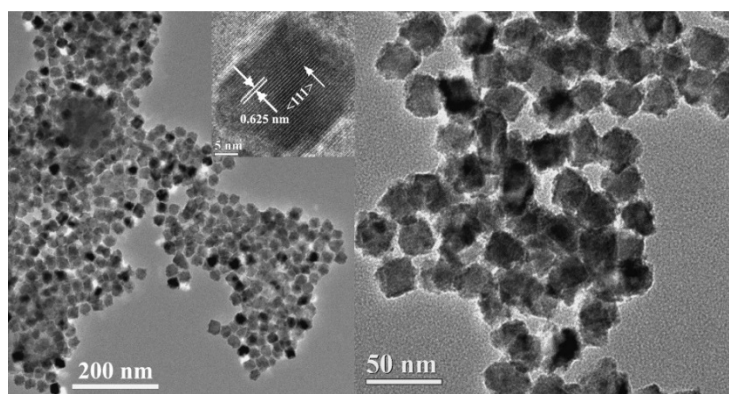


Figure 4.1: TEM images of nanocubes of CuCr<sub>2</sub>Se<sub>4</sub>. Reprinted with permission from ref. 1.

In another case, HI of the mixture of precursors including Cu- and Cr-oleate dissolved in trioctylamine (TOA; C<sub>18</sub>H<sub>37</sub>N) into the solution of Se in TOA at the temperature of 300 °C formed anisotropic-shaped nanocrystals of CuCr<sub>2</sub>Se<sub>4</sub>.<sup>2</sup> TOA as a capping agent coordinated to the elemental Se and made organo-Se intermediate. Figure 4.2 represented the reaction pathway of the formation of the nanocrystals. The prepared nanocrystals exhibit a mixture of close to triangular and hexagonal morphology, with an average size of 20 nm. The reaction at a temperature range of 250-300 °C led to the formation of nonmagnetic phase CuCrSe<sub>2</sub>. The next

effort to prepare  $\text{CuCr}_2\text{Se}_4$  nanoparticles was using metal salt precursors of  $\text{CuCl}$  and  $\text{CrCl}_3 \cdot 6\text{H}_2\text{O}$  under the same condition of the hot-injection strategy used to make  $\text{CuCr}_2\text{S}_4$  that reported by Ramasamy et al.<sup>3</sup> Quick injection of diphenyldiselenide (DPDS) as the source of selenium in the mix of precursors dissolved in OLA (or ODA) led to the formation of  $\text{CuCr}_2\text{Se}_4$  nanocrystals (Figure 4.3).

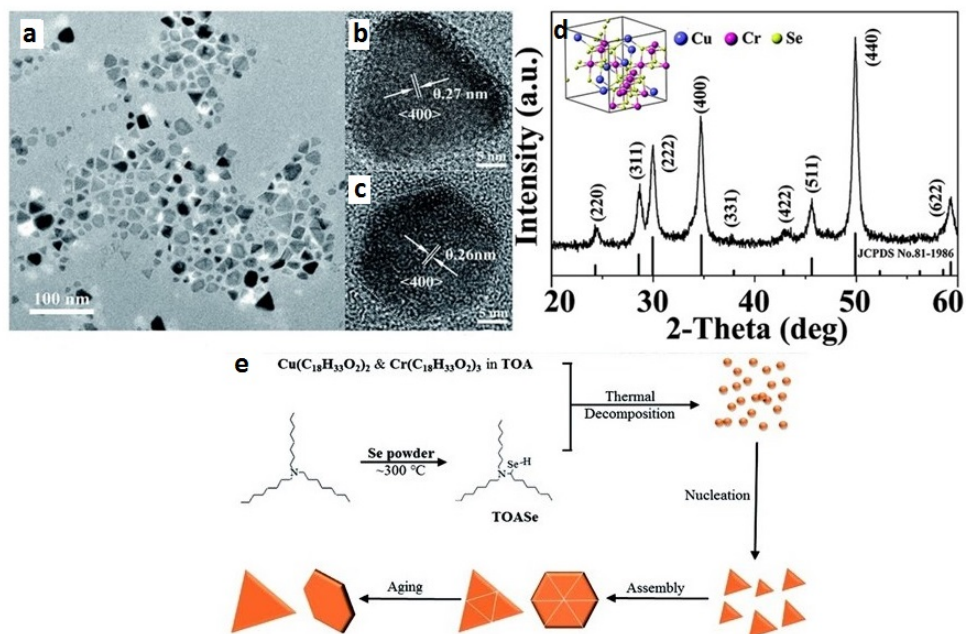


Figure 4.2: (a) TEM image, (b,c) HRTEM, and (d) XRD pattern of the anisotropic NCs of  $\text{CuCr}_2\text{Se}_4$ , and (e) reaction pathway of formation of the nanocrystals. Reprinted with permission from ref. 2.

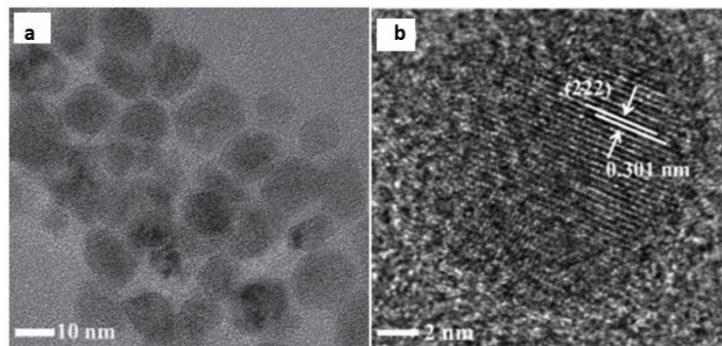


Figure 4.3: (a) TEM and (b) HRTEM images of  $\text{CuCr}_2\text{Se}_4$  nanoparticles prepared from metal chloride precursors. Reprinted with permission from ref. 3.

### 4.3 Magnetic Properties of the $\text{CuCr}_2\text{Se}_4$ NCs

The magnetic properties of the mentioned NCs of  $\text{CuCr}_2\text{Se}_4$  have been measured via PPMS equipped with VSM. Magnetization as a function of the applied magnetic field has been measured. Figure 4.4 shows hysteresis loops for the cubic NCs made by  $\text{Cu}(\text{acac})_2$  and  $\text{Cr}(\text{acac})_3$  with average sizes of 15 nm and 20 nm, measured at 300 K and 10 K.<sup>1</sup> The NCs are superparamagnetic at 300K, but they show hysteretic behavior at 10 K with relatively low coercivity. Figure 4.5 shows hysteresis loops for  $\text{CuCr}_2\text{Se}_4$  NCs made by different methods.<sup>2,3</sup> As expected, both types of NCs exhibit superparamagnetic behavior at room temperature (300 K) and ferromagnetic behavior at 5 K with low coercivity ( $\sim 1$  kOe).<sup>2,3</sup> The superparamagnetic behavior of the NCs at 300 K is not unexpected, because of their small crystalline size.

Table 4.1 summarize the reaction condition, size, and shape of the prepared NCs and their saturation magnetization values. The reported values for the saturation magnetization are somewhat lower than the value of  $56 \text{ emu g}^{-1}$  reported in the bulk. Because the smaller average size of the obtained NCs (10 nm), the value reported by Ramasamy et al. ( $23 \text{ emu g}^{-1}$ )<sup>3</sup> is significantly lower than what has been obtained for the NCs synthesized via the methods employed by Wang et al. and Pang et al.<sup>1,2</sup>

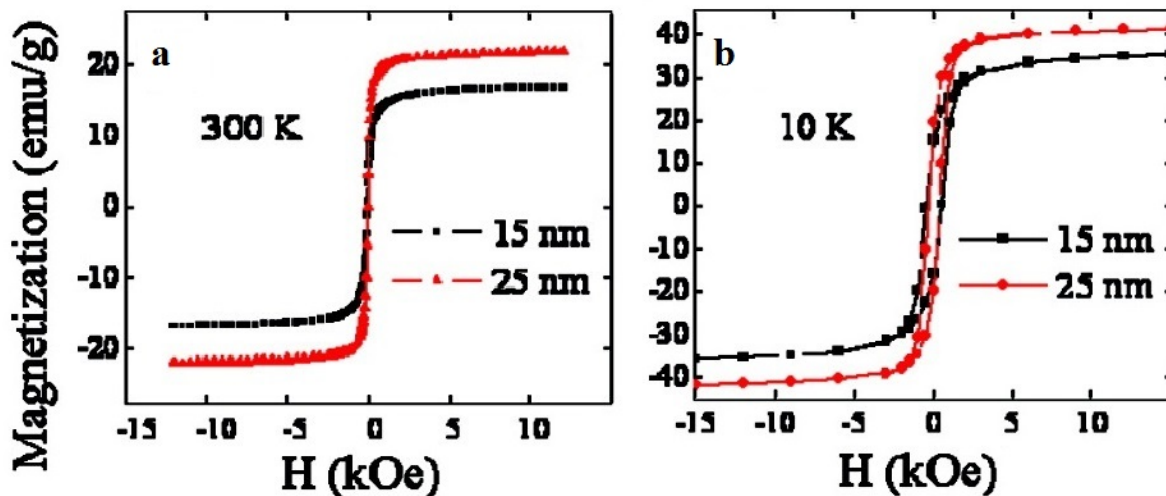


Figure 4.4: Magnetization ( $M$ ) as a function of an external field ( $H$ ) at (a) 300 K and (b) 10 K for the 15 nm and 25 nm nanocubes of  $\text{CuCr}_2\text{Se}_4$ . Reprinted with permission from ref. 1.

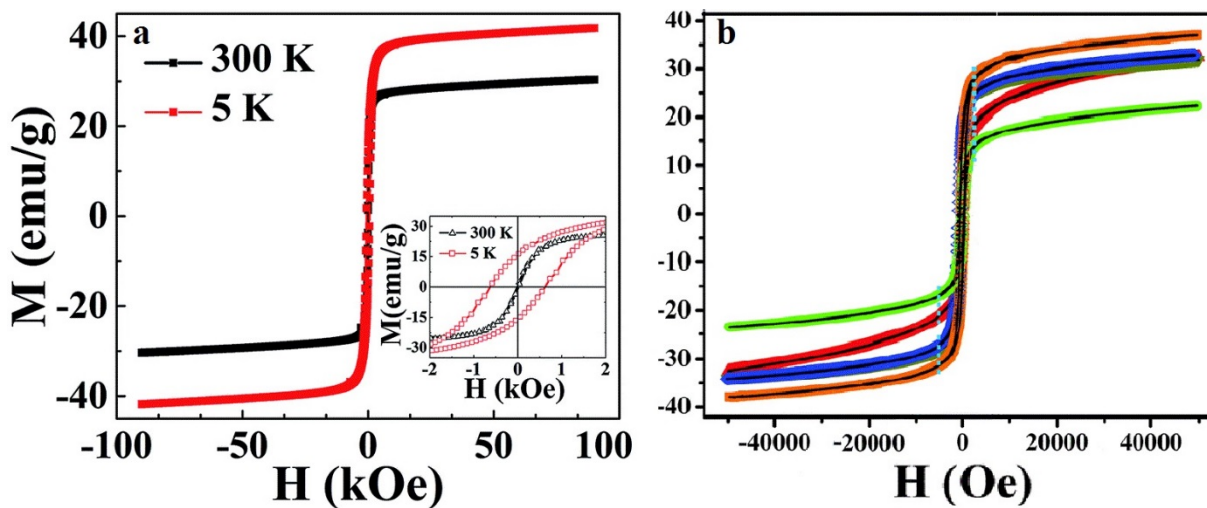


Figure 4.5: Magnetization ( $M$ ) as a function of an external field ( $H$ ) for (a) NCs of  $\text{CuCr}_2\text{Se}_4$  with the average size of 20 nm reported by Pang et al.,<sup>30</sup> and (b) NCs of  $\text{CuCr}_2\text{Se}_4$  (green) with the average size of 10 nm reported by Ramasamy et al. Reprinted with permission from ref. 3.

Table 4.1: Reaction condition, morphology, size and saturation magnetization for NCs of  $\text{CuCr}_2\text{Se}_4$  made by HI method.<sup>1-3</sup>

Precursors and Temperature	Solvent	Size and Morphology	Saturation Magnetization
$\text{Cu}(\text{acac})_2$ , $\text{Cr}(\text{acac})_3$ , Se, 350 °C	OLA, ODE	20 nm/cubes	43 emu g <sup>-1</sup>
		15 nm/cubes	37 emu g <sup>-1</sup>
$\text{Cu}(\text{oleate})_2$ , $\text{Cr}(\text{oleate})_3$ , Se, 300 °C	TOA	20 nm/triangular-hexagonal	43 emu g <sup>-1</sup>
$\text{CuCl}$ , $\text{CrCl}_3 \cdot 6\text{H}_2\text{O}$ , DPDS, 360 °C	OLA, ODA	10 nm/triangular-hexagonal	23 emu g <sup>-1</sup>

#### 4.4 Formation of $\text{CuCr}_2\text{Se}_4$ via Phase Transformation

The experimental details of the heat-up synthesis were explained in chapter 3. Increasing the temperature of the same HU procedure to the range of 310-360 °C led to the formation of spinel  $\text{CuCr}_2\text{Se}_4$  NCs. The predominant phase formed at the temperature range of 250-300 °C was  $\text{Cr}_x\text{Cu}_{1-x}\text{Se}_2$ , whereas the pure spinel phase was formed at the range of 330-360 °C (Figure 4.6).

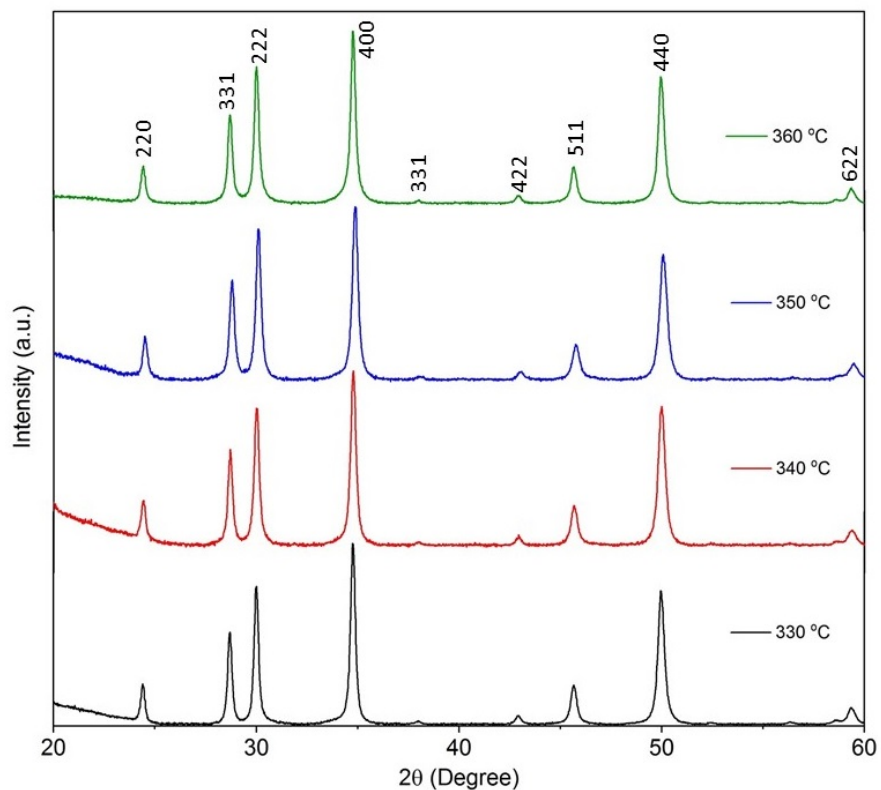


Figure 4.6 XRD patterns of the CuCr<sub>2</sub>Se<sub>4</sub> nanoparticles formed at the range of 330-360 °C.

The TEM images of the spinel NCs reveal that they are in nanorod morphology with an average length of 50 nm. Comparing the shape and size of the nanorods formed at 330 and 360 °C indicated that their width increases by increasing the reaction temperature (Figure 4.7). HRTEM, SAED pattern, HAADF-, EDS-STEM imaging, and EDS-diagrams of the NCs of the prepared CuCr<sub>2</sub>Se<sub>4</sub> are represented in figures 4.8 and 4.9. The lattice spacing of 0.31 nm corresponding to (3 1 1) lattice planes was observed in HRTEM. The zone axis of the SAED pattern is in [111] direction. Table 4.2 shows the elemental composition of the CuCr<sub>2</sub>Se<sub>4</sub> NCs measured by EDS.

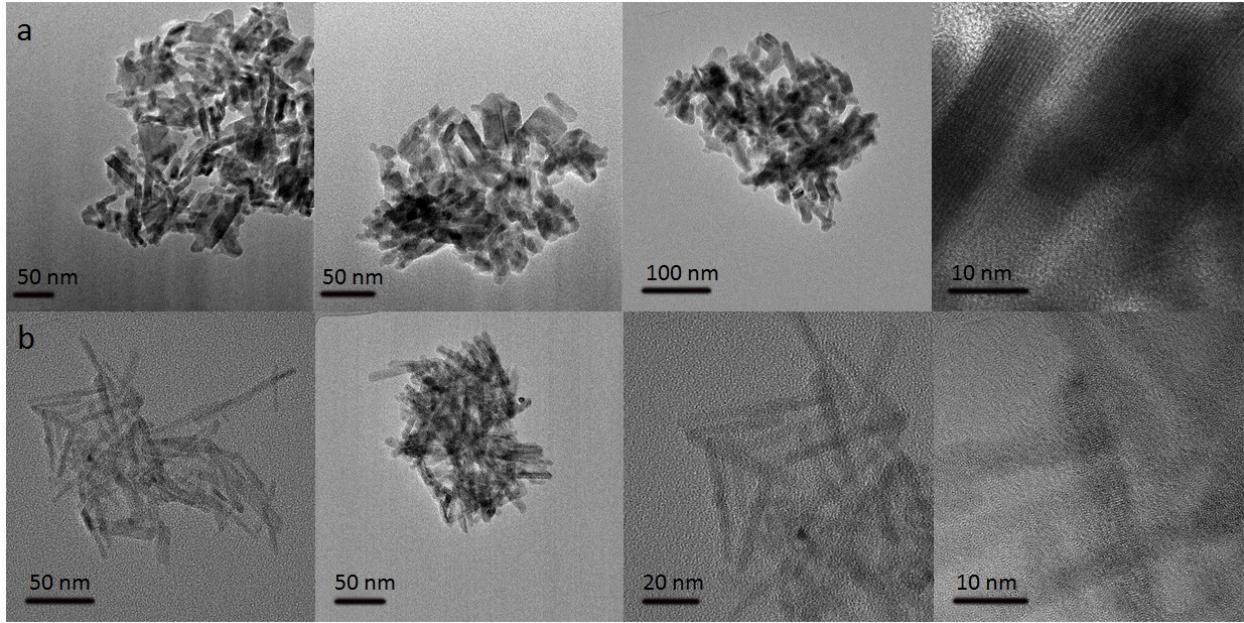


Figure 4.7: TEM images of the spinel  $\text{CuCr}_2\text{Se}_4$  nanorods prepared at (a) 360 °C and (b) 330 °C.

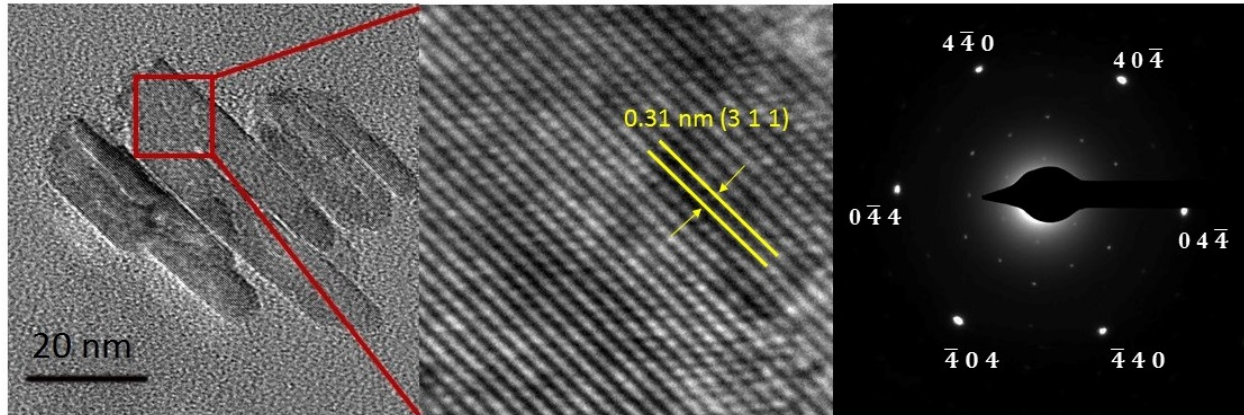


Figure 4.8: HRTEM and selected area diffraction (SAED) pattern of  $\text{CuCr}_2\text{Se}_4$  NCs. The zone axis of the SAED pattern is in  $[111]$  direction.

The XRD pattern of the particles prepared at the temperature range between 300 to 330 °C indicated the mix of the pyrite and spinel phase (Figure 4.10). Since  $\text{Cr}_{0.5}\text{Cu}_{0.5}\text{Se}_2$  (formed at 300 °C) has the highest chromium content for the pyrite phase, this suggests that the  $\text{Cr}_{0.5}\text{Cu}_{0.5}\text{Se}_2$  as a structural template results in the formation of  $\text{CuCr}_2\text{Se}_4$  during the pyrite to

spinel phase transformation. The proposed mechanism is supported by the XRD patterns of the intermediate compositions, which shows that the relative intensity of peaks corresponding to the pyrite phase gradually decreases with the reaction temperature, whereas the intensity of peaks from the spinel phase increases. It seems that the pyrite phase becomes saturated by reaching the Cr-content to 50%, and then the spinel phase forms.

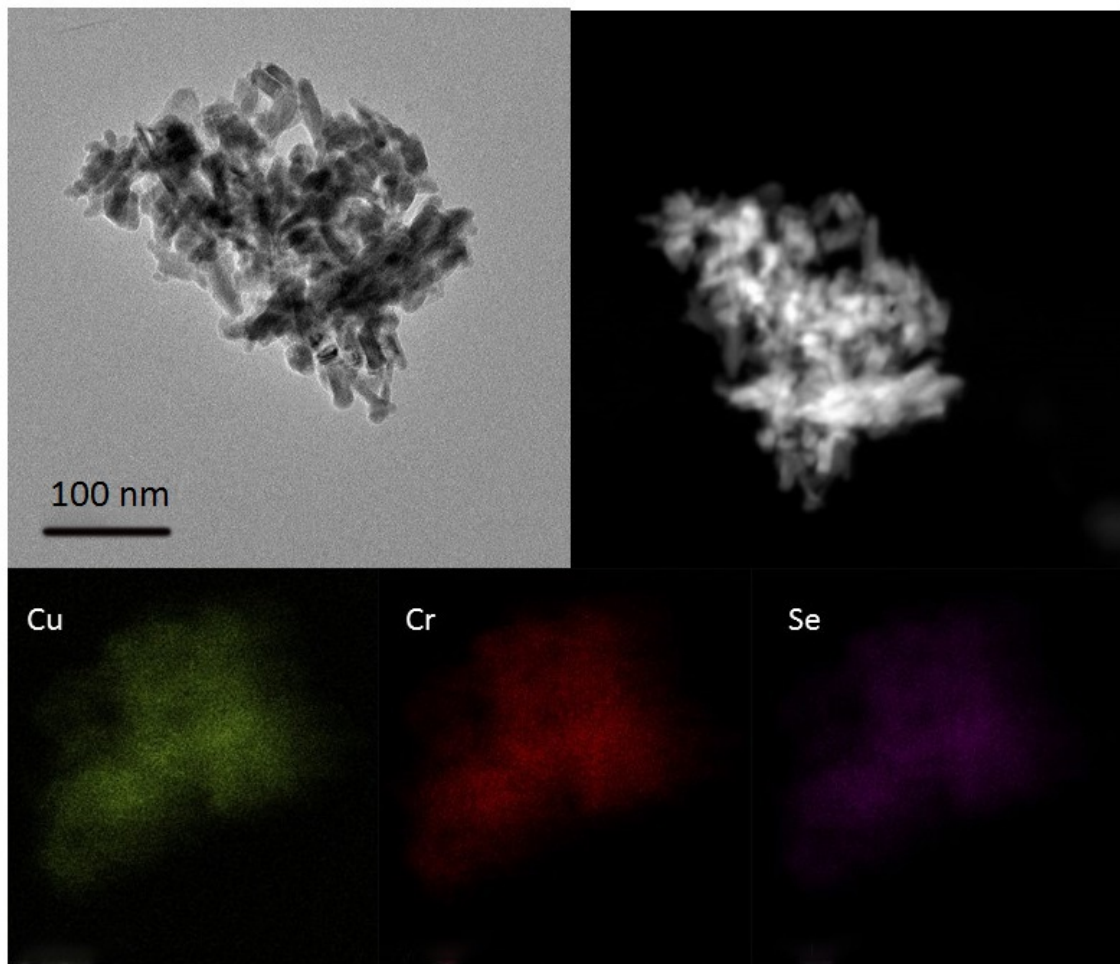


Figure 4.9: HAADF-, EDS-STEM imaging, and EDS-diagram of nanorods of CuCr<sub>2</sub>Se<sub>4</sub> formed at 330 °C.

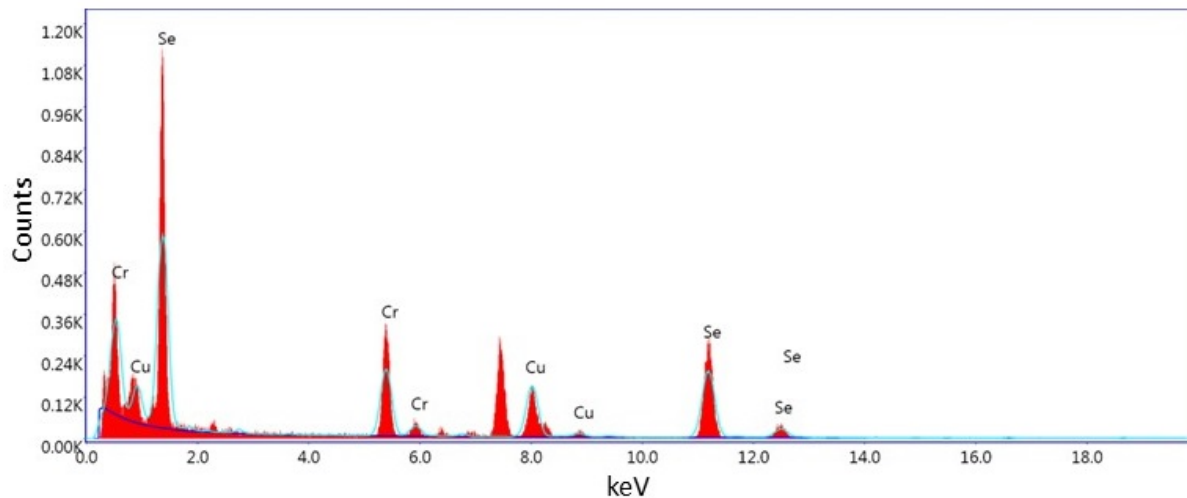


Figure 4.9: Continued.

Table 4.2: Elemental composition of the  $\text{CuCr}_2\text{Se}_4$  NCs measured by EDS.

Material	Temperature	Element	Weight %	Atomic %	Ratio
$\text{CuCr}_2\text{Se}_4$	330 °C	Cr K	21.22	28.25	2.05
		Cu K	12.67	13.80	1.00
		Se L	66.11	57.95	4.20

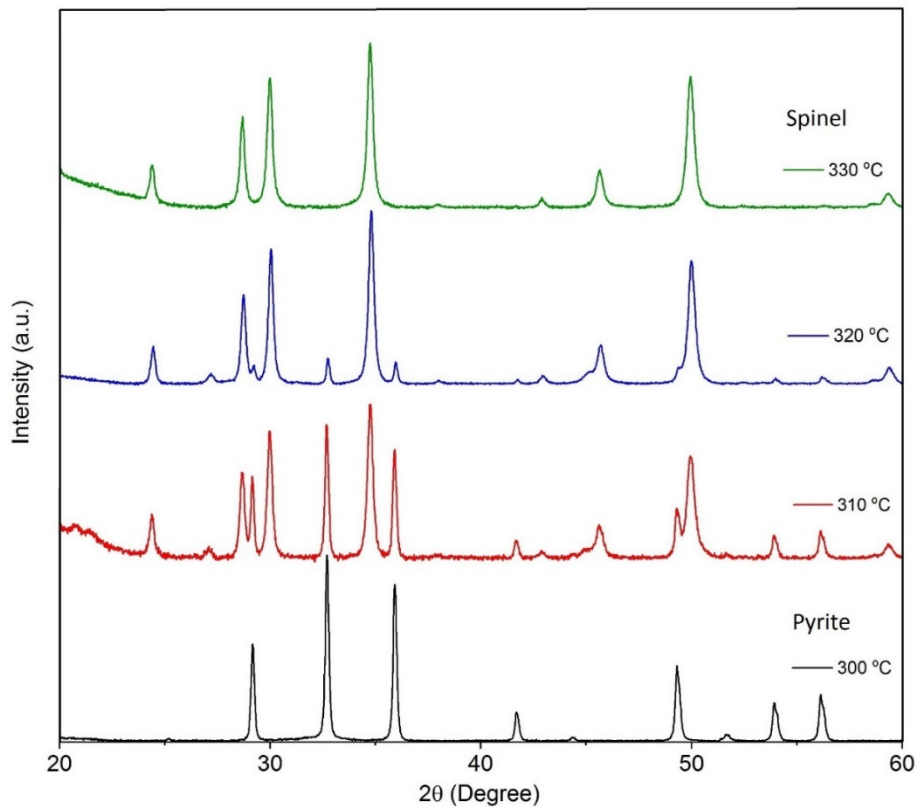


Figure 4.10: Characterization of  $\text{Cr}_{0.5}\text{Cu}_{0.5}\text{Se}_2/\text{CuCr}_2\text{Se}_4$  composites showing a decrease in the intensity of the pyrite phase peaks and an increase in the intensity of the spinel phase peaks by increasing the reaction temperature.

The HU reaction at 320 °C was performed at four different reaction times, including 30, 60, 90, and 120 min, and the results indicated that by increasing the reaction time, the spinel phase becomes more predominant and the only phase that exists after 120 min is spinel (Figure 4.11). The XRD patterns of the intermediate compositions show that the relative intensity of peaks corresponding to the pyrite phase gradually decreases with the reaction time, whereas the intensity of peaks from the spinel phase increases.

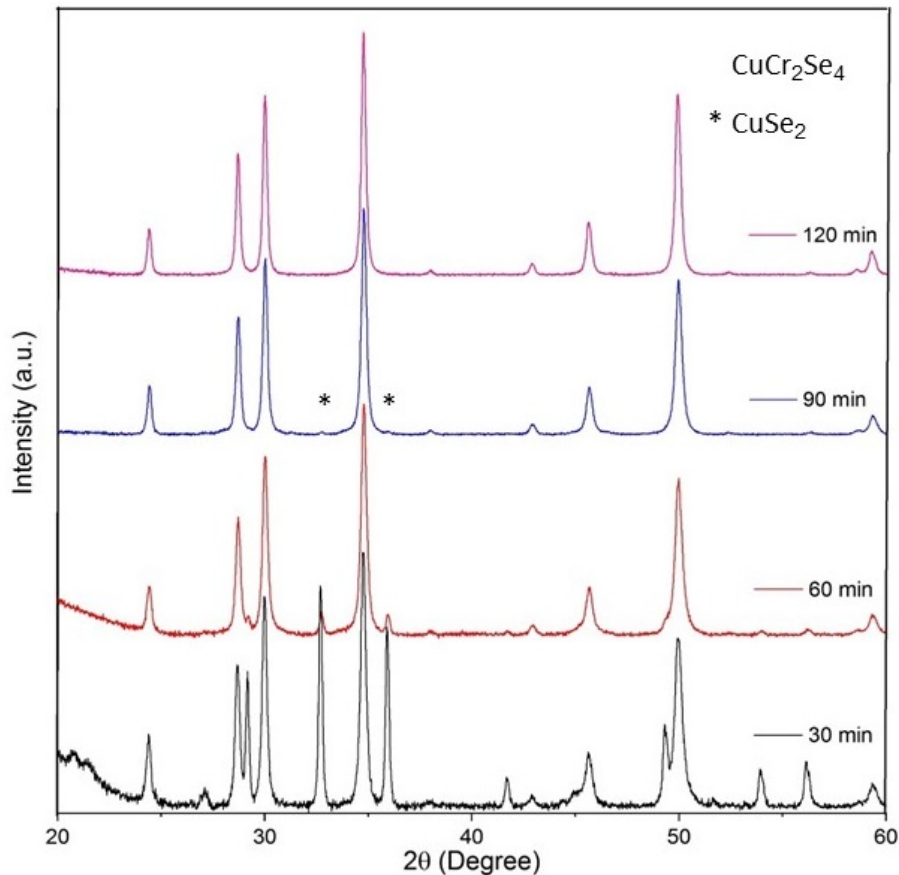


Figure 4.11: The effect of reaction time on the composition of the NCs produced at 320 °C.

To gain more insights into the phase transformation from pyrite ( $\text{Cr}_{0.5}\text{Cu}_{0.5}\text{Se}_2$ ) to spinel ( $\text{CuCr}_2\text{Se}_4$ ) structure, we performed detailed HRTEM, HAADF-STEM, and EDS-STEM characterizations on the intermediate products formed at 310 and 320 °C. As expected, EDS shows increasing chromium amount as the reaction proceeds.

Three distinct particles were detected by TEM, including deformed nanocubes, nanoneedles, and hollow nanorings (Figures 4.12-4.14). Deformed nanocubes are  $\text{Cr}_{0.5}\text{Cu}_{0.5}\text{Se}_2$ , whereas nanoneedles of both pyrite and spinel structures were detected separately. Figure 4.15 shows atomic resolution images of the spinel  $\text{CuCr}_2\text{Se}_4$  nanoneedles formed at 320 °C.

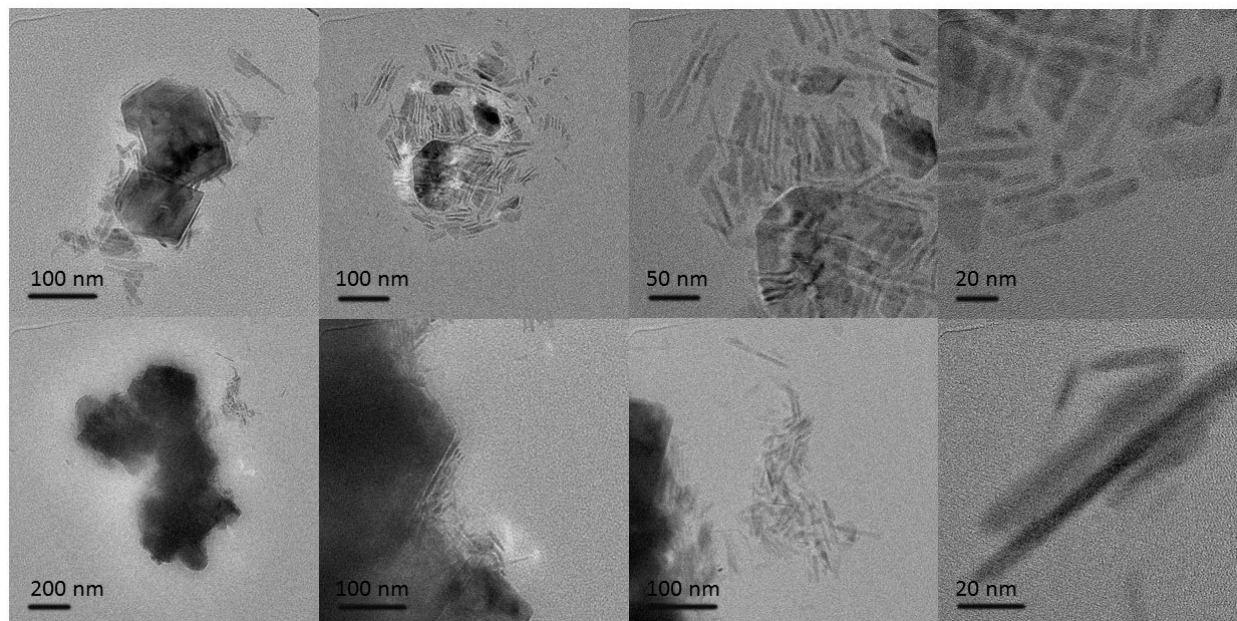


Figure 4.12: TEM images of the NCs formed at 320 °C, indicating deformed nanocubes and nanoneedles.

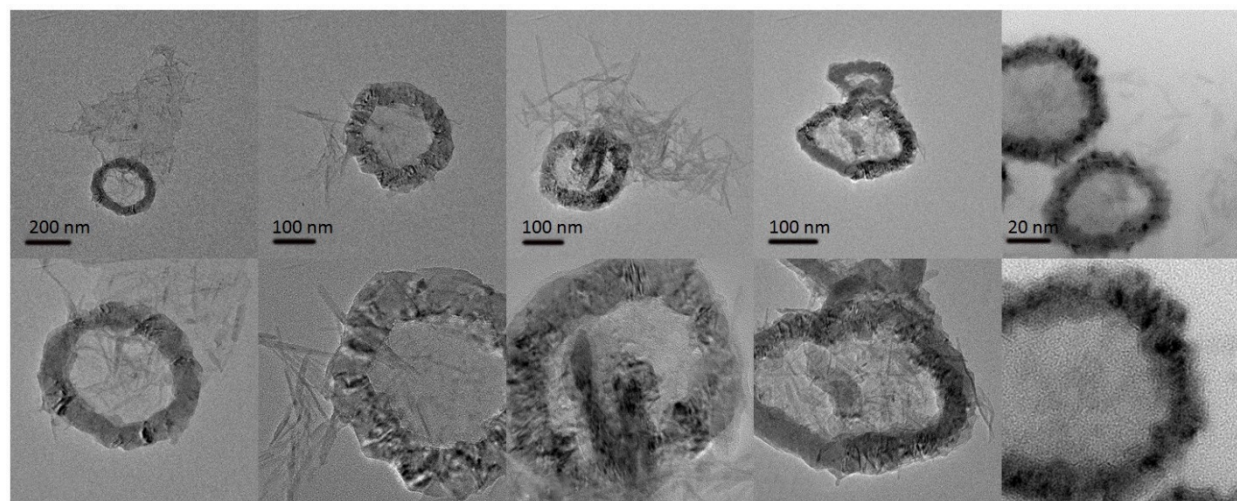


Figure 4.13: TEM images of the hollow nanorings formed at 320 °C.

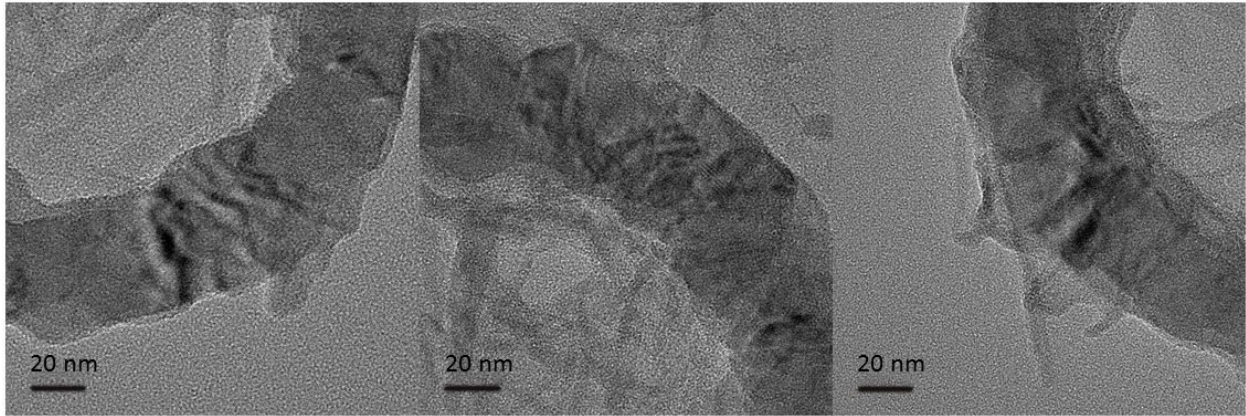


Figure 4.14: HRTEM images of the hollow nanorings.

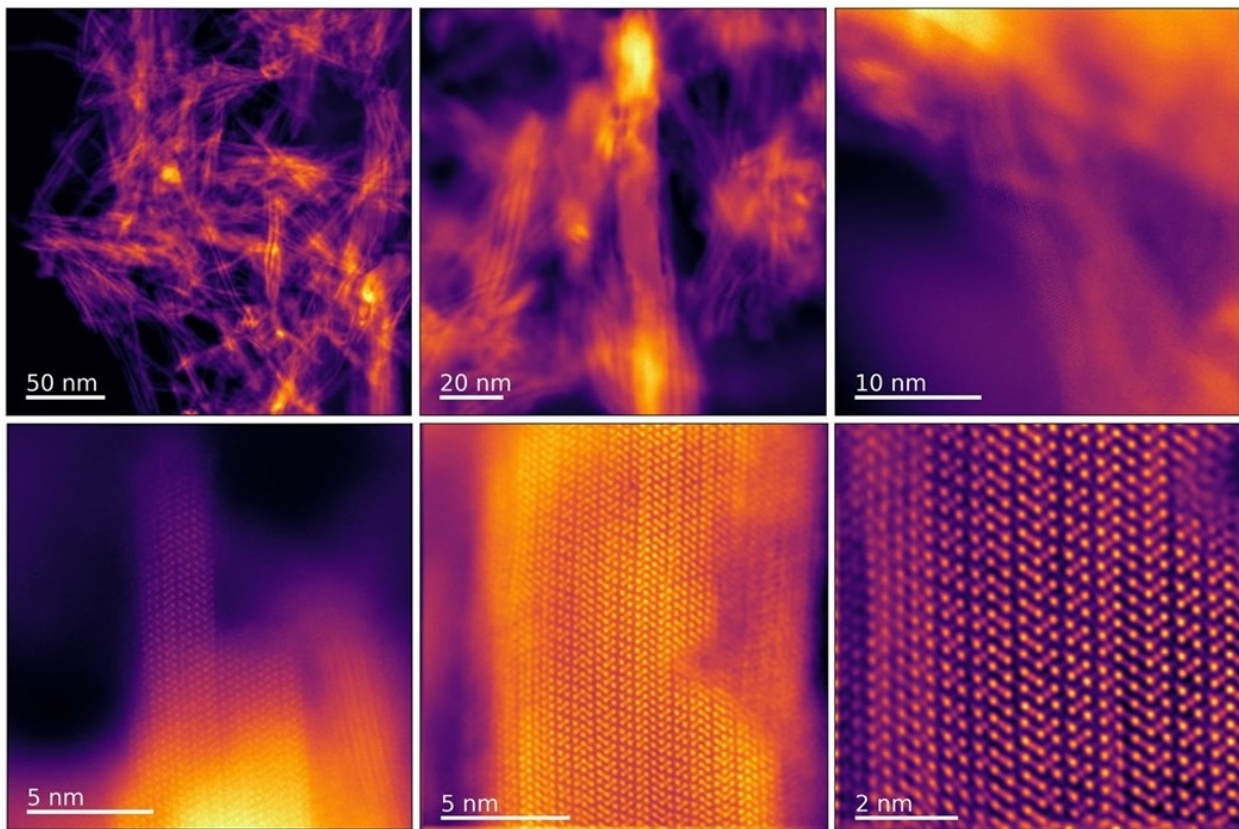


Figure 4.15: Wide field-of-view and atomic resolution HAADF images of spinel  $\text{CuCr}_2\text{Se}_4$  nanoneedles.

Figures 4.16 and 4.17 reveals HAADF-STEM, EDS-STEM images and SAED patterns of the deformed nanocubes of  $\text{Cr}_{0.5}\text{Cu}_{0.5}\text{Se}_2$  and nanoneedles of  $\text{CuCr}_2\text{Se}_4$ , respectively. The elemental analyses were summarized in table 4.3.

Table 4.3: Elemental composition of the nanocubes of  $\text{Cr}_{0.5}\text{Cu}_{0.5}\text{Se}_2$  and nanoneedles of  $\text{CuCr}_2\text{Se}_4$  measured by EDS.

Material	Temperature	Element	Weight %	Atomic %	Ratio
$\text{Cr}_{0.5}\text{Cu}_{0.5}\text{Se}_2$	320 °C	Cr K	12.25	16.92	1.03
		Cu K	14.58	16.49	1.00
		Se L	73.17	66.59	4.04
$\text{CuCr}_2\text{Se}_4$	320 °C	Cr K	19.27	25.85	1.79
		Cu K	13.17	14.46	1.00
		Se L	67.56	59.69	4.13

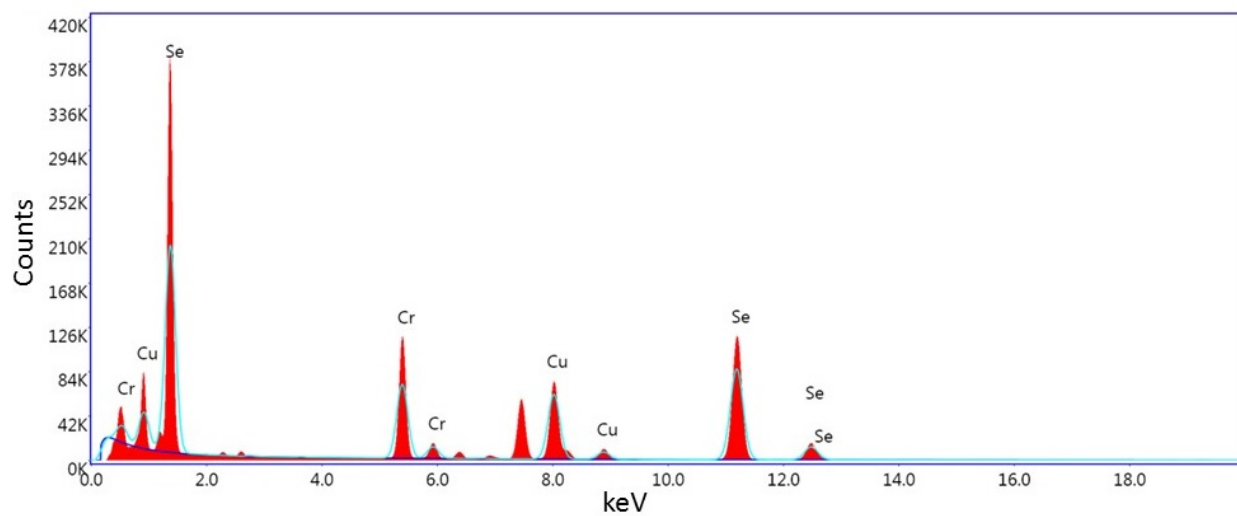
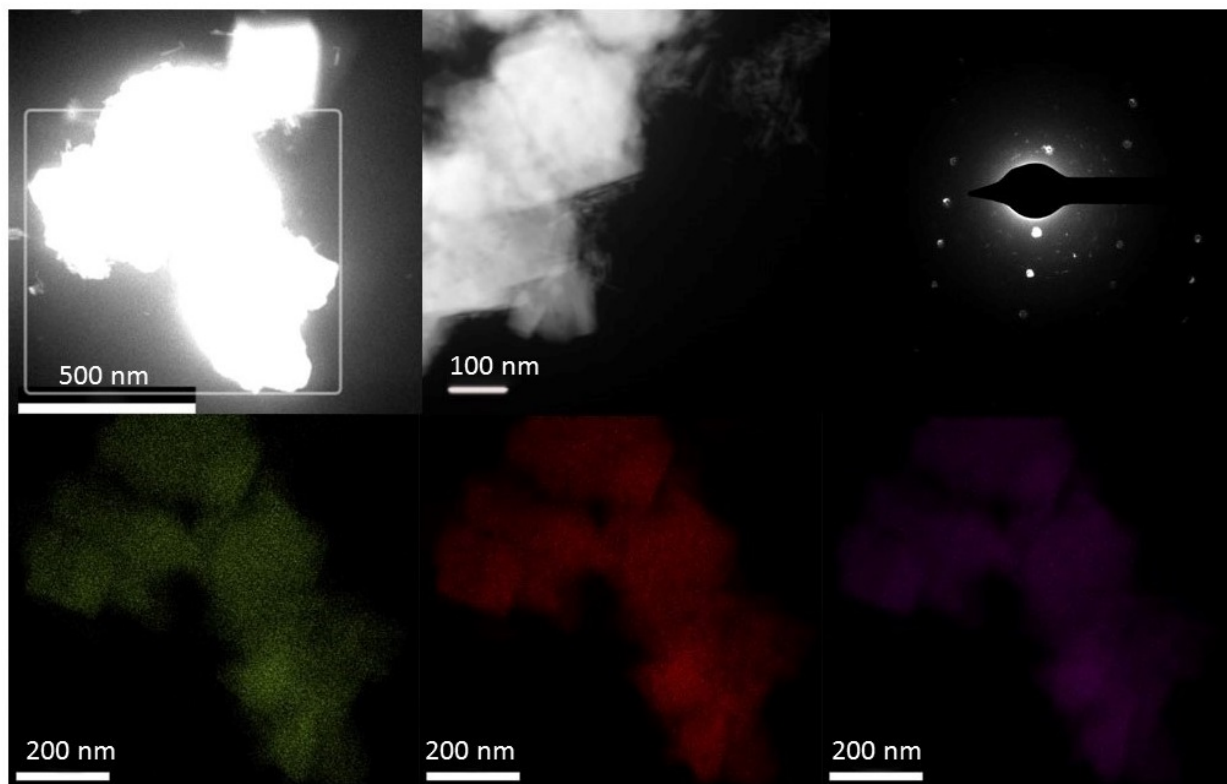


Figure 4.16: HAADF-STEM, EDS-STEM images, SAED pattern, and EDS-diagram of the deformed nanocubes of  $\text{Cr}_{0.5}\text{Cu}_{0.5}\text{Se}_2$ .

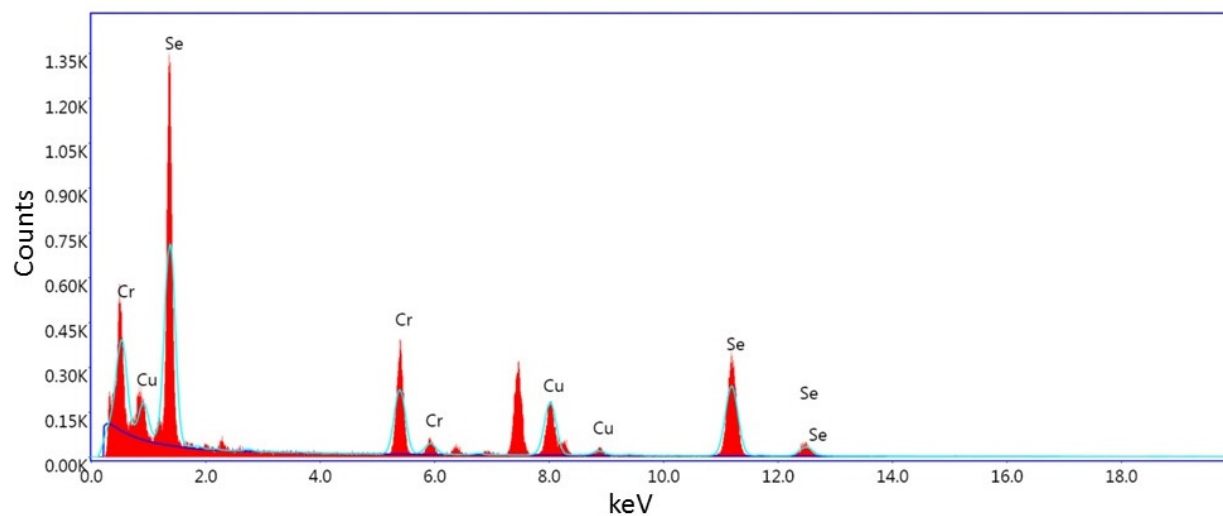
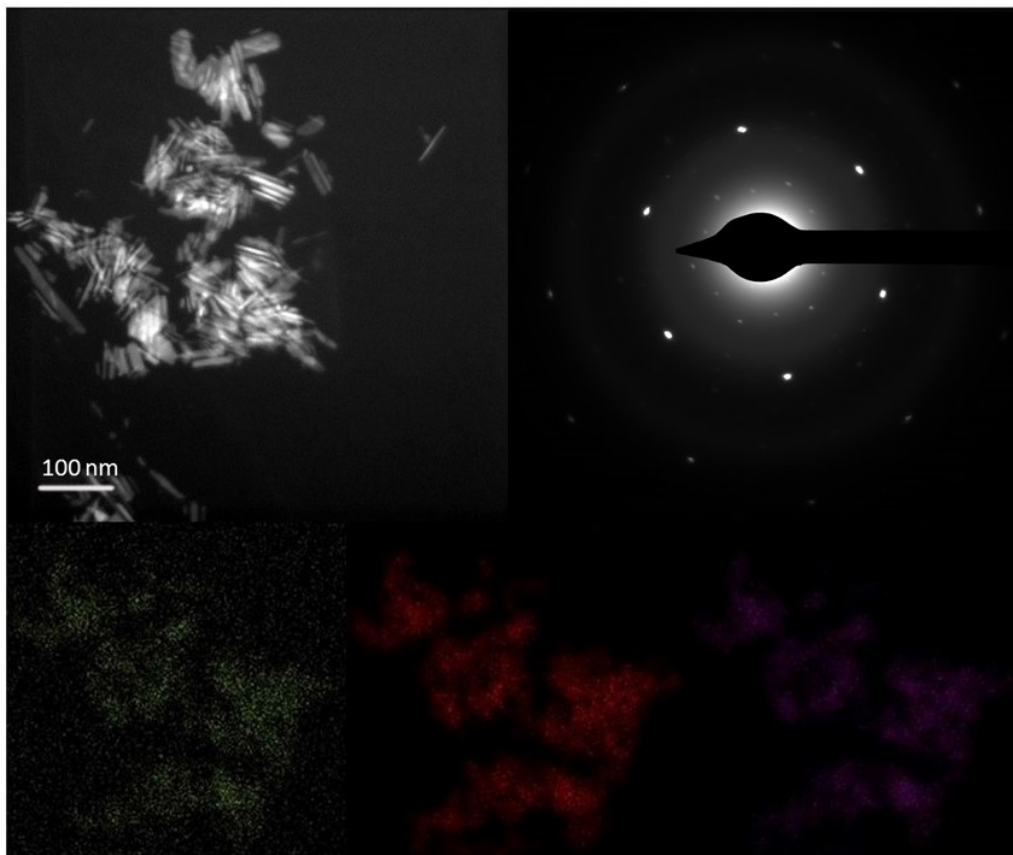


Figure 4.17: HAADF-STEM, EDS-STEM images SAED pattern, and EDS-diagram of the deformed nanocubes of nanoneedles of  $\text{CuCr}_2\text{Se}_4$ .

Perhaps the most interesting results extracted from the hollow nanorings that contain useful information and provide the complete picture on the transformation mechanism. Since the size of the hollow rings is comparable with the size of initial  $\text{CuSe}_2$  nanocubes, they should form via the Kirkendall effect driven by the ionic diffusion in the pyrite structure. Generally, the Kirkendall effect entails a process in which the imbalance in the ion diffusion rate causes the formation of voids or defects within colloidal NCs and pores to form due to the difference in diffusion rates of ions.<sup>4-9</sup>

The HRTEM and HAADF-STEM micrograph of the nanorings indicated that the hollow particles also undergo the degradation to small nanoneedles.

Figure 4.18 shows the EDS mapping of two representative nanorings in which the average compositions of the components are  $\text{CuCr}_{1.7}\text{Se}_4$  and  $\text{CuCr}_{1.4}\text{Se}_4$  (Table 4.4), which are between  $\text{Cr}_{0.5}\text{Cu}_{0.5}\text{Se}_2$  (or  $\text{Cu}_{0.5}\text{Cr}_{0.5}\text{Se}_2$ ) and spinel- $\text{CuCr}_2\text{Se}_4$  (or  $\text{Cu}_{0.5}\text{CrSe}_2$ ). The elemental analyses of the nanorings have been summarized in table 4.4. The point EDS (Tables 4.5 and 4.6) analysis of the randomly selected points of nanorings reveals different Cu-, Cr-, and Se-compositions in the range of  $\text{Cu}_{0.5}\text{Cr}_{0.5}\text{Se}_2$  to  $\text{Cu}_{0.5}\text{CrSe}_2$  exhibiting an increase in the chromium contents of the pyrite that influences the phase transformation leading to the formation of spinel phase (Figure 4.19). Figure 4.20 shows the corresponding SAED patterns of a hollow nanoring indicating distinguished spinel and pyrite patterns, and diffraction patterns representing the coexistence of the two phases. The represented SAED patterns show the distribution of both pyrite and spinel phases in real space.

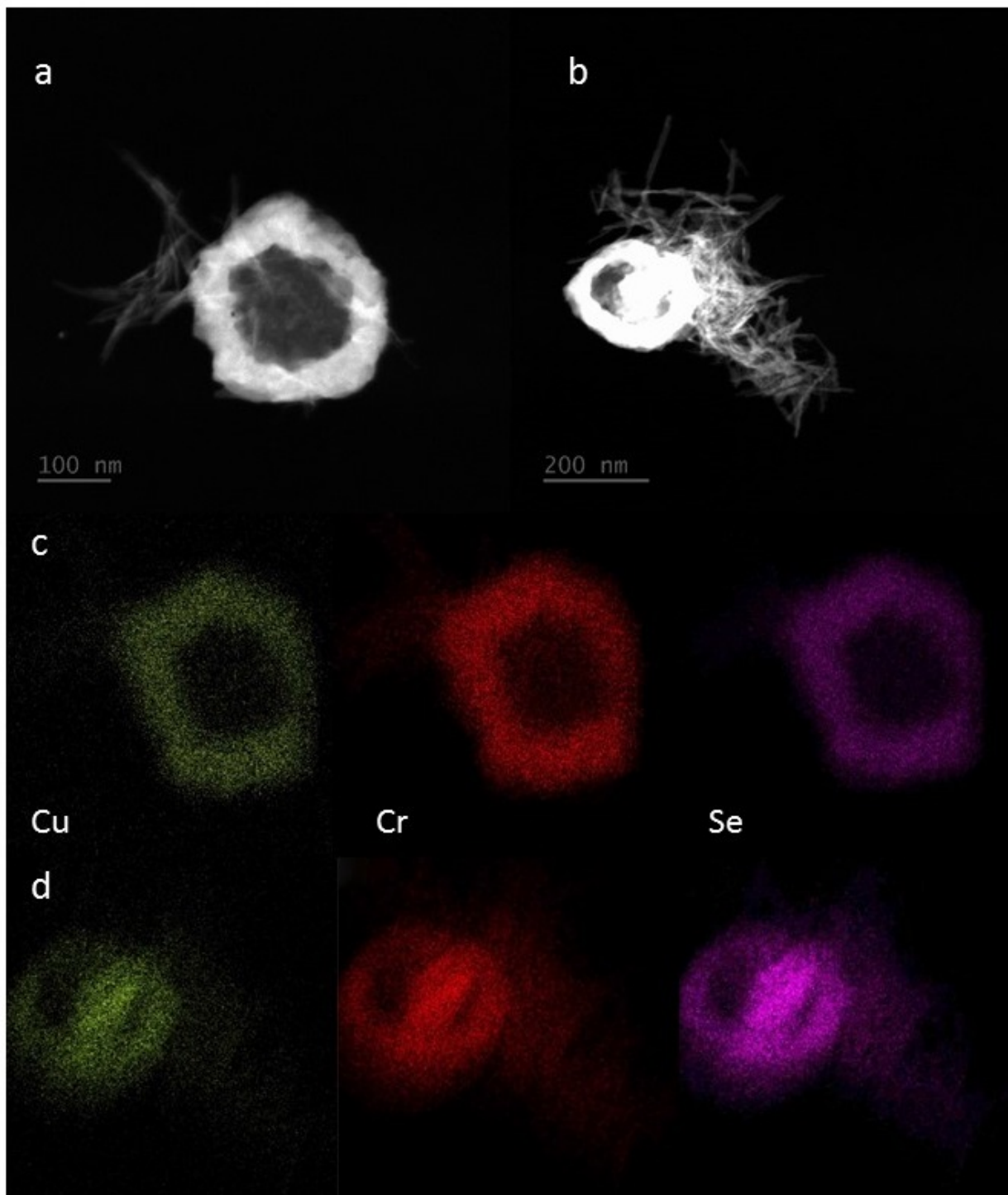


Figure 4.18: HAADF-, EDS-STEM imaging, and EDS-diagram of hollow nanorings with the average chemical compositions of (a)  $\text{CuCr}_{1.7}\text{Se}_4$  and (b)  $\text{CuCr}_{1.4}\text{Se}_4$ .

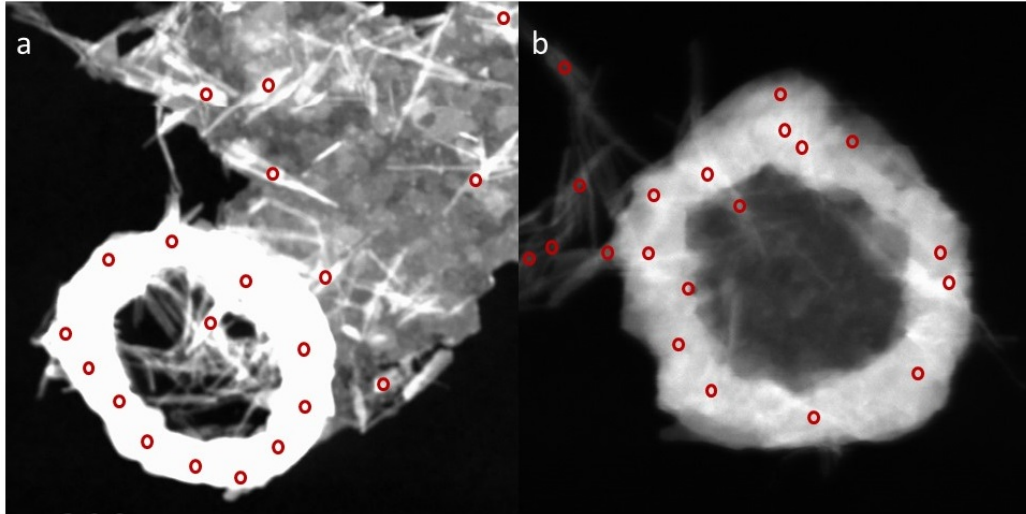


Figure 4.19: HAADF-STEM images of hollow nanorings formed via Kirkendall effect and randomly selected points for EDS analysis.

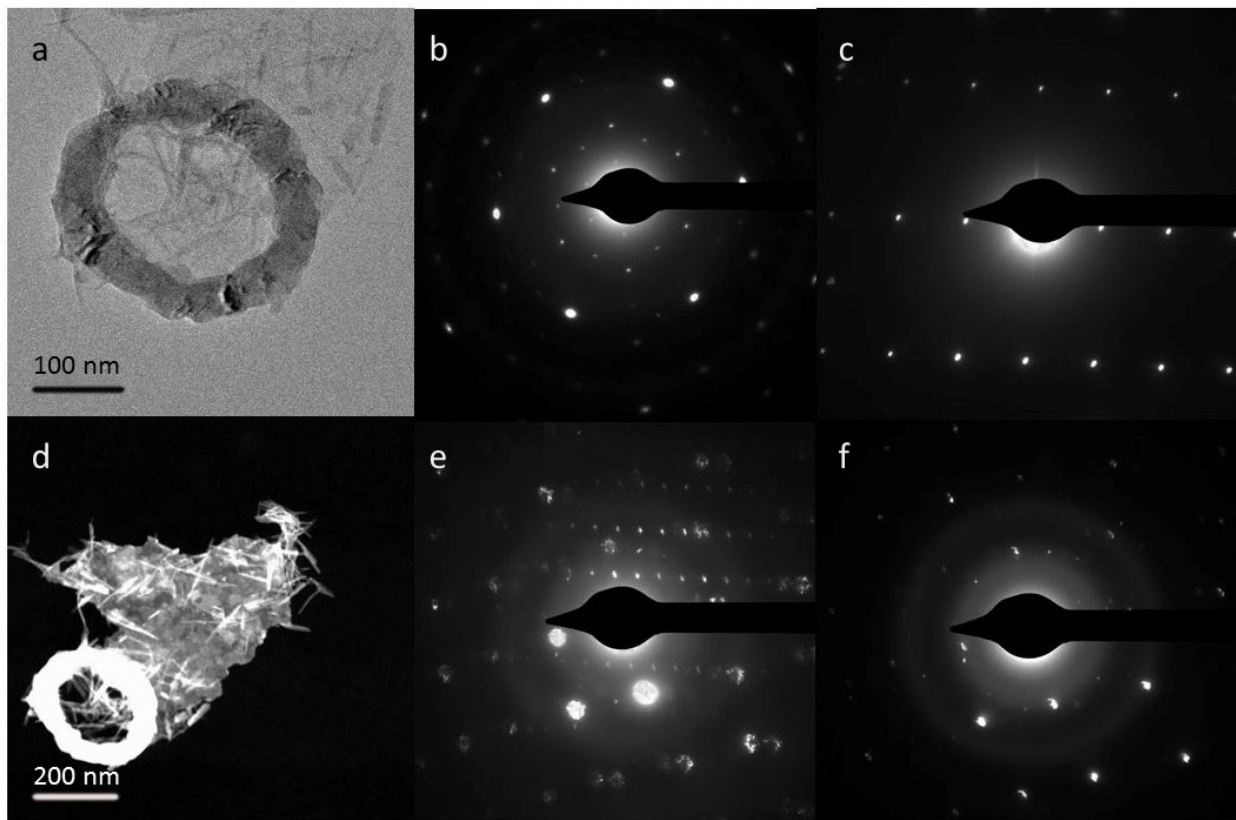


Figure 4.20: SAED patterns extracted from a hollow nanoring (a,d) representing (b) spinel, (c) pyrite, and (e,f) multi-domain phases in the selected area.

Table 4.4: Elemental composition of the nanorings of (a)  $\text{CuCr}_{1.7}\text{Se}_4$  and (b)  $\text{CuCr}_{1.4}\text{Se}_4$  measured by EDS.

Material	Temperature	Element	Weight %	Atomic %	Ratio
$\text{Cu}_{0.5}\text{Cr}_{0.85}\text{Se}_2$ (or $\text{CuCr}_{1.7}\text{Se}_4$ )	320 °C	Cr K	18.70	25.15	1.73
		Cu K	13.21	14.54	1.00
		Se L	68.09	60.31	4.15
$\text{Cu}_{0.5}\text{Cr}_{0.7}\text{Se}_2$ (or $\text{CuCr}_{1.4}\text{Se}_4$ )	320 °C	Cr K	16.62	22.52	1.44
		Cu K	14.14	15.68	1.00
		Se L	69.24	61.80	3.94

Table 4.5: EDS analyses of the selected points on the hollow ring (a) in figure 4.19, indicating a variety of chemical compositions in the range of  $\text{Cr}_{0.5}\text{Cu}_{0.5}\text{Se}_2$  to  $\text{Cu}_{0.5}\text{CrSe}_2$  ( $\text{CuCr}_2\text{Se}_4$ ).

Selected Point	Cu	Cr	Se	Selected Point	Cu	Cr	Se
1	1.0	1.73	4.15	9	1.0	1.30	4.27
2	1.0	1.77	4.21	10	1.0	2.13	4.21
3	1.0	1.43	3.91	11	1.0	1.66	3.83
4	1.0	1.48	3.92	12	1.0	1.69	3.89
5	1.0	1.72	4.35	13	1.0	1.51	4.23
6	1.0	1.93	4.22	14	1.0	1.48	4.14
7	1.0	1.93	3.95	15	1.0	1.28	4.11
8	1.0	1.10	4.06	16	1.0	1.13	3.90

Table 4.6: EDS analyses of the selected points on the hollow ring (b) in figure 5.19, indicating a variety of chemical compositions in the range of  $\text{Cr}_{0.5}\text{Cu}_{0.5}\text{Se}_2$  to  $\text{Cu}_{0.5}\text{CrSe}_2$  ( $\text{CuCr}_2\text{Se}_4$ ).

Selected Point	Cu	Cr	Se	Selected Point	Cu	Cr	Se
1	1.0	1.37	4.23	11	1.0	1.42	4.21
2	1.0	1.42	4.22	12	1.0	1.53	4.35
3	1.0	1.17	3.82	13	1.0	1.63	4.05
4	1.0	1.30	3.94	14	1.0	1.32	4.00
5	1.0	1.32	3.93	15	1.0	1.77	4.02
6	1.0	1.23	3.87	16	1.0	1.13	3.90
7	1.0	1.33	4.10	17	1.0	1.97	4.15
8	1.0	1.34	4.16	18	1.0	1.44	4.03
9	1.0	1.07	3.92	19	1.0	1.04	3.84
10	1.0	1.27	4.01	20	1.0	1.44	3.93

Several nanoneedles (Figure 4.21) with the intermediate compositions were also detected, supporting the idea of the formation of spinel NCs from the nanoneedles of pyrite during the phase transformation mechanism (Table 4.7).

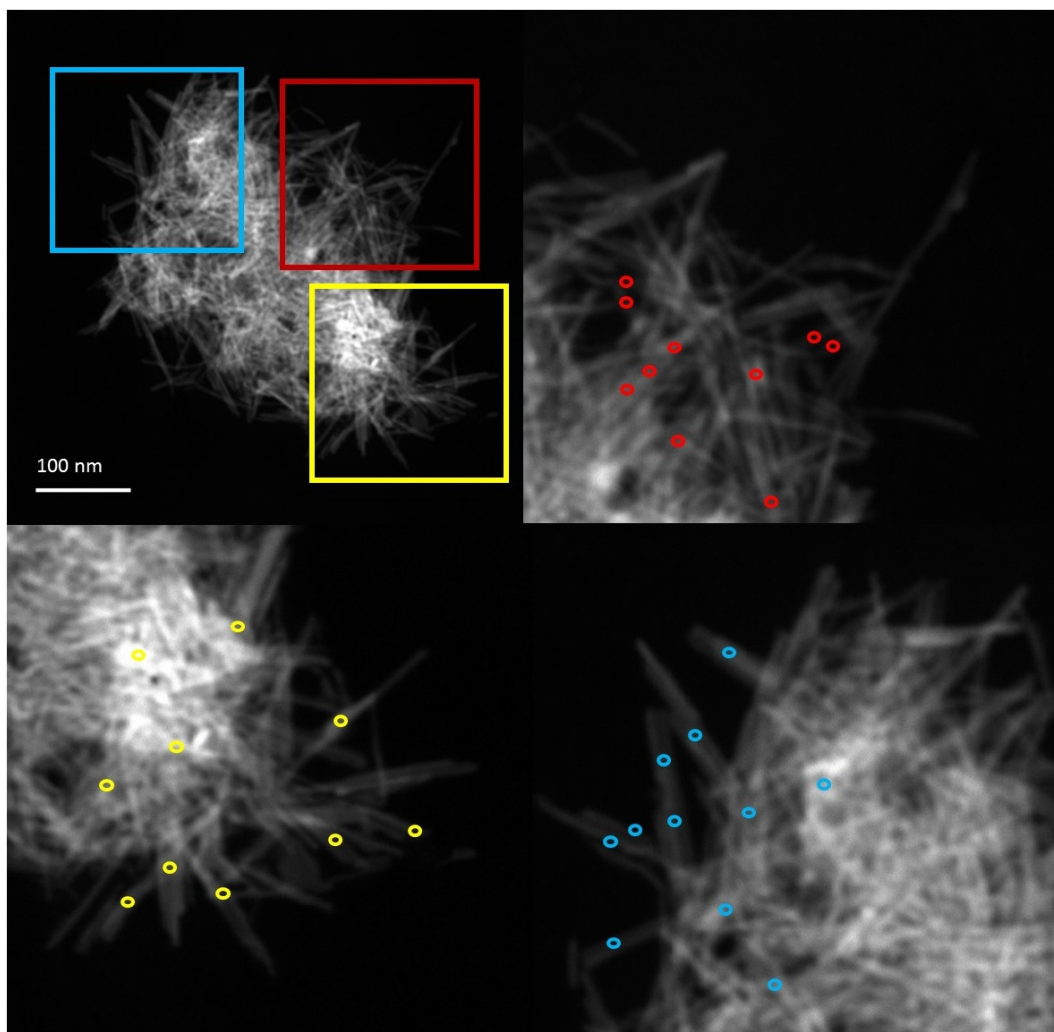


Figure 4.21: HAADF-STEM image of nanoneedles formed at 320 °C, and randomly selected points for EDS analysis.

Table 4.7: EDS analyses of the selected points on the nanoneedles in selected areas in figure 4.21, indicating a variety of chemical compositions in the range of  $\text{Cr}_{0.5}\text{Cu}_{0.5}\text{Se}_2$  to  $\text{Cu}_{0.5}\text{CrSe}_2$  ( $\text{CuCr}_2\text{Se}_4$ ).

Red Points	Cu	Cr	Se	Red Points	Cu	Cr	Se
1	1.00	1.45	3.98	6	1.00	1.74	4.14
2	1.00	1.15	4.06	7	1.00	1.59	4.15
3	1.00	1.33	4.09	8	1.00	1.63	3.93
4	1.00	1.53	4.19	9	1.00	1.83	4.19
5	1.00	1.20	3.88	10	1.00	1.89	4.04
Blue Points	Cu	Cr	Se	Blue Points	Cu	Cr	Se
1	1.00	1.18	4.19	7	1.00	1.27	3.90
2	1.00	1.17	3.90	8	1.00	1.30	3.99
3	1.00	1.29	3.93	9	1.00	1.35	3.96
4	1.00	1.40	4.00	10	1.00	1.48	4.15
5	1.00	1.39	4.05	11	1.00	1.29	3.91
6	1.00	1.57	4.17	-	-	-	-
Yellow Points	Cu	Cr	Se	Yellow Points	Cu	Cr	Se
1	1.00	1.63	4.16	6	1.00	1.38	3.90
2	1.00	1.55	4.03	7	1.00	1.87	4.08
3	1.00	1.50	3.97	8	1.00	1.29	3.82
4	1.00	1.55	4.06	9	1.00	1.53	4.07
5	1.00	1.45	3.89	10	1.00	1.49	3.97

#### 4.5 Understanding the Mechanistic Details of Pyrite to Spinel Phase Transformation; Increasing Chromium Content versus Decreasing Copper and Selenium Contents

Figure 4.22 shows phase transformation mechanism probed via HRTEM imaging and SAED on a selected area of a hollow ring showing the coexistence of pyrite and spinel phases. The SAED pattern includes three sets of diffraction spots, which are associated with the pyrite (left), spinel (right), and heterostructure (middle). SAED patterns and HRTEM image of the selected area distinguished the interface between the two structures emphasizing on  $\text{Cr}_{0.5}\text{Cu}_{0.5}\text{Se}_2$  phase (green contrast) from  $\text{CuCr}_2\text{Se}_4$  (pink contrast).

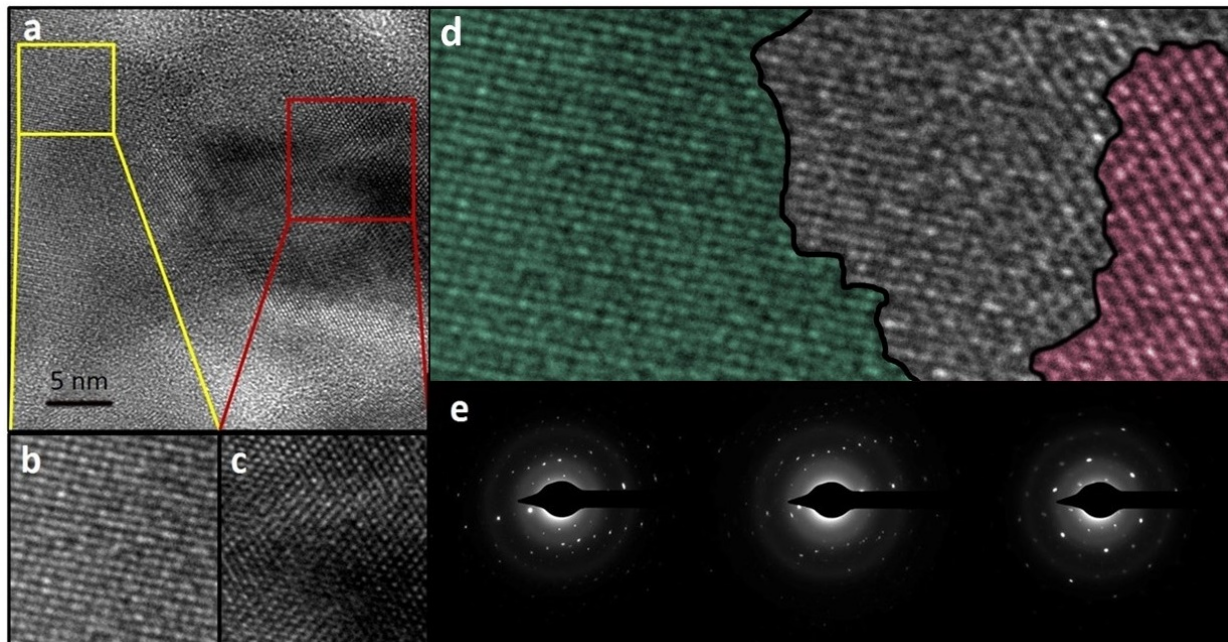


Figure 4.22: Phase transformation mechanism probed via HRTEM imaging. HRTEM image showing multi-domain intermediate phases during the transformation of  $\text{Cr}_{0.5}\text{Cu}_{0.5}\text{Se}_2$  to  $\text{CuCr}_2\text{Se}_4$  with an interface between the two domains indicated by a black line. (a) A part of a hollow nanoring, HRTEM images of the (b) pyrite and (c) spinel domains, (d) Multi-domain phase intermediate area with the interface between the pyrite (green) and spinel (pink) domains, and (e) Three sets of SAED patterns extracted from the represented multi-domain area showing the coexistence of pyrite and spinel phases.

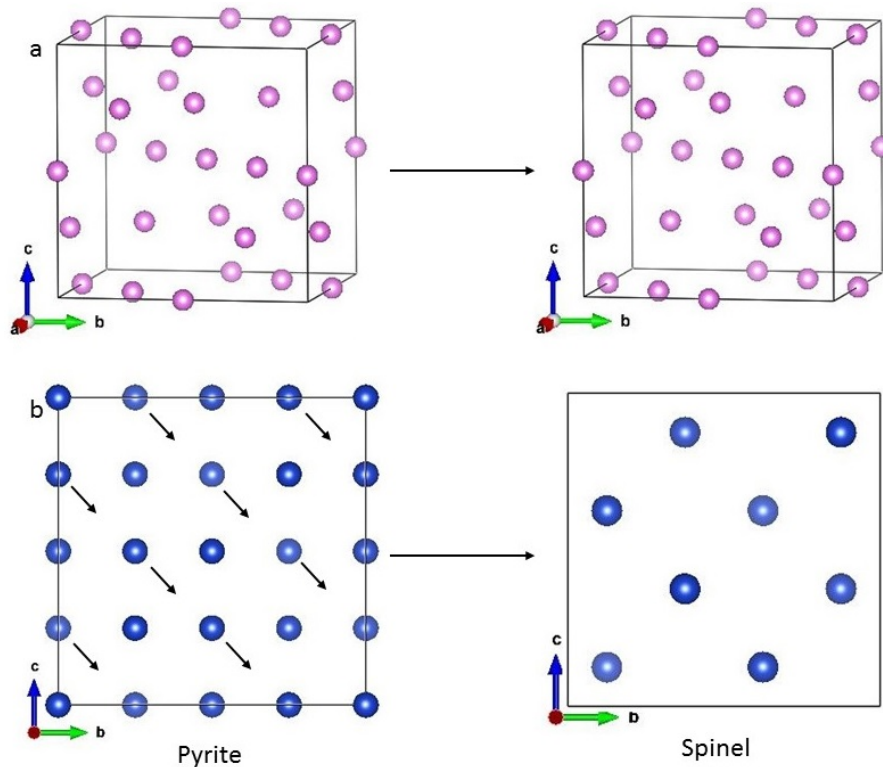
Based on the suggested pyrite structure for  $\text{Cu}_{0.5}\text{Cr}_{0.5}\text{Se}_2$ , half of the four octahedral sites should be occupied by  $\text{Cu}^+$  (2 positions), and the remaining half should be occupied by  $\text{Cr}^{3+}$  ions (2 positions). Assembly of eight pyrite unit cells ( $Pa-3$ ,  $a = 6.116 \text{ \AA}$ ) forms a  $2 \times 2 \times 2$  fcc superlattice including 16  $\text{Cr}^{3+}$  ions. Comparing this fabricated unit cell with the cubic unit cell of spinel  $\text{CuCr}_2\text{Se}_4$  ( $Fd-3m$ ,  $a = 10.337 \text{ \AA}$ ) shows that the same number of  $\text{Cr}^{3+}$  ions are located in the similar octahedral sites (Scheme 4.1). Using this pattern to rationalize the phase transformation mechanism shows that the total number of copper and selenium ions should be decreased in half (from 16 to 8, and 64 to 32, respectively) from pyrite to spinel phase. Importantly, the Se atoms in the pyrite structure are in their less stable oxidation state ( $\text{Se}_2^{2-}$ ) and,

therefore, can be viewed as electrophilic centers and will readily reduce into their most stable  $\text{Se}^{2-}$  oxidation state in the spinel structure.<sup>10</sup>

The reduction of diselenide ( $\text{Se}_2^{2-}$ ) is followed by the oxidation of  $\text{Cu}^+$  to  $\text{Cu}^{2+}$  ions. The reduction of  $\text{Se}_2^{2-}$  in  $\text{Cr}_{0.5}\text{Cu}_{0.5}\text{Se}_2$  structure during the transformation would break up the Se-Se covalent bonds.<sup>11</sup>  $\text{Cu}^{2+}$  ions located in the octahedral position in the structure of  $\text{Cr}_{0.5}\text{Cu}_{0.5}\text{Se}_2$  upon reduction of  $\text{Cu}^+$  diffuse into the neighboring vacant tetrahedral position. Simultaneously,  $\text{Se}^{2-}$  ions resulting from the reduction of the dimers of  $\text{Se}_2^{2-}$  diffuse into the neighboring sites. The short length of the  $\text{Cu}^+$  and  $\text{Se}^{2-}$  ions diffusion path could be the driving force that facilitates the complete transformation from Cr-doped pyrite to the spinel phase.<sup>11</sup> The changes in the oxidation states and decreasing the amounts of the Cu and Se ions followed by the formation of spinel structure is shown by this equation:



Based on this proposed mechanism, the total amount of the chromium does not decrease and remains constant. Therefore no more  $\text{Cr}^{3+}$  will be needed to complete the formation mechanism of  $\text{CuCr}_2\text{Se}_4$ . To support this proposal against the other possible pathway (proposing increasing the  $\text{Cr}^{3+}$  while the amounts of Cu and Se ions remain constant), we have used isolated  $\text{Cr}_{0.5}\text{Cu}_{0.5}\text{Se}_2$  particles as the precursor of  $\text{CuCr}_2\text{Se}_4$  using the same heat-up method and phase pure spinel particles have been prepared at 360 °C.



Scheme 4.1: Schematic view of (a) the similar positions of Cr ions and (b) Cu ions diffusion into the neighboring vacant tetrahedral positions during the pyrite to spinel phase transformation.

#### 4.6 Phase Transformation and Raman Spectroscopy

Raman spectroscopy confirmed the pyrite to spinel phase transformation as the reaction temperature increased from 300 to 330 °C. Figure 4.23 shows the Raman spectra of the materials synthesized at 300, 310, and 330 °C. In general, pyrite structure has five Raman active modes, and usually, the two strongest peaks corresponding to the symmetric  $A_g$  and  $T_g$  modes and attributed to the characteristic stretching modes of the Se–Se pairs could be observed in Raman spectrum.<sup>12,13</sup> On the other hand,  $M\text{Cr}_2\text{X}_4$  spinel structure has five Raman active modes, including  $A_{1g}$ ,  $E_g$ , and three  $F_{2g}$  in general.<sup>14</sup> The Raman spectrum of the  $p\text{-Cr}_{0.5}\text{Cu}_{0.5}\text{Se}_2$  formed at 300 °C shows two peaks at 240 and 258  $\text{cm}^{-1}$  corresponding to  $A_g$  and  $T_g$  modes, respectively.<sup>12</sup>

By increasing the reaction temperature to 310 °C, the intensity of the pyrite  $A_g$  and  $T_g$  peaks decreased and five more peaks attributed to spinel phase were observed. By increasing the reaction temperature, the relative intensity of peaks corresponding to pyrite phase gradually decreased, whereas the intensity of peaks from the spinel phase increased. The Raman spectrum of the  $\text{CuCr}_2\text{Se}_4$  spinel phase formed at 330 °C shows all five expected peaks at 107, 144, 170, 225, and 254  $\text{cm}^{-1}$  corresponding to  $F_{2g}$ ,  $E_g$ ,  $F_{2g}$ ,  $F_{2g}$ , and  $A_{1g}$  modes, respectively.<sup>14</sup>

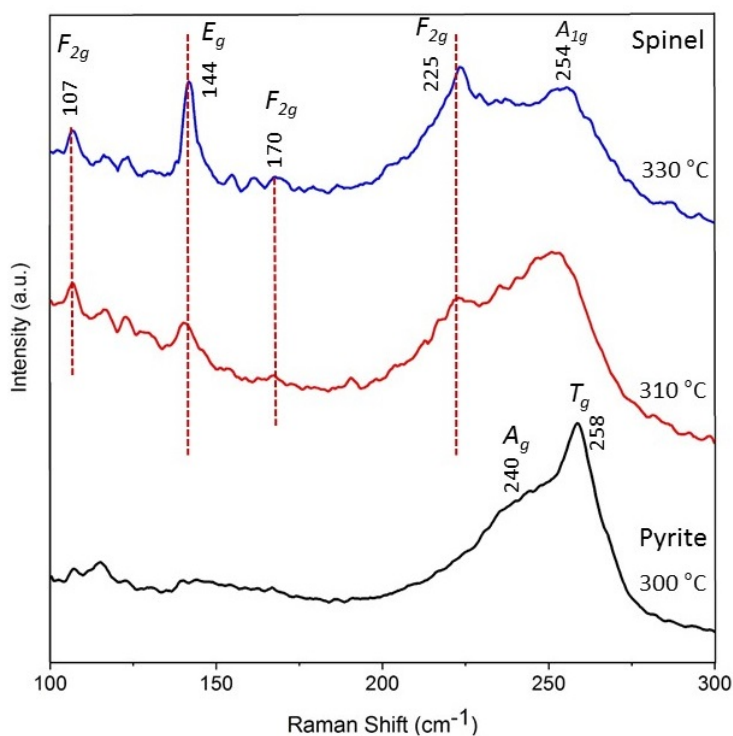


Figure 4.23: Raman Spectra of the NCs formed at 300, 310, and 330 °C, confirming the pyrite to spinel phase transformation by increasing the reaction temperature.

#### 4.7 Magnetic Properties of Spinel $\text{CuCr}_2\text{Se}_4$ NCs

Figure 4.24 shows the hysteresis loop of the nanoneedles of  $\text{CuCr}_2\text{Se}_4$  at 300 K and 5 K. Similar to the previously reported works, the prepared NCs are superparamagnetic at 300 K with

no hysteresis and zero remanence. On the other hand, they exhibit ferromagnetic behavior at 5 K with relatively low coercivity. The obtained saturation magnetization value is 29 emu g<sup>-1</sup> which is lower than the same parameter obtained for NCs prepared via HI method by Wang et al. (37, 43 emu g<sup>-1</sup>)<sup>1</sup> and Pang et al. (43 emu g<sup>-1</sup>)<sup>2</sup> but higher than reported parameter by Ramasamy (23 emu g<sup>-1</sup>)<sup>3</sup> indicating the influence of the size and morphology of the NCs on the saturation magnetization.

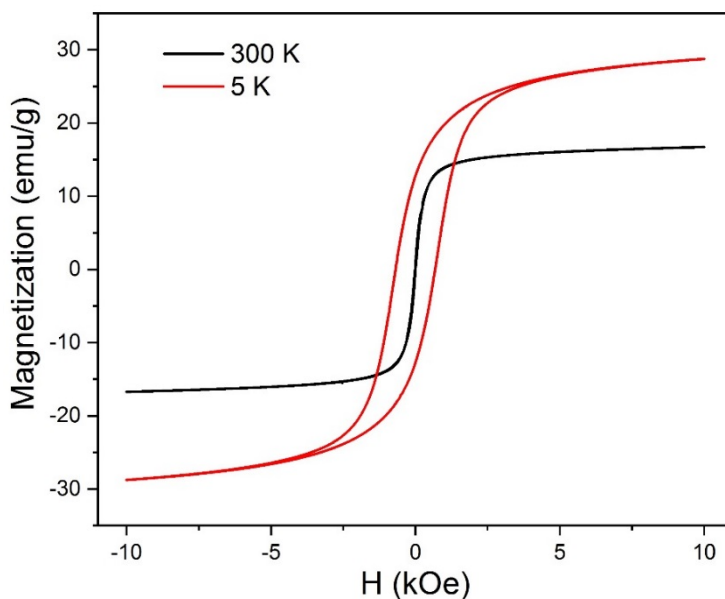


Figure 4.24: Magnetization ( $M$ ) as a function of external field ( $H$ ) diagram at 300 K and 5 K for NCs of  $\text{CuCr}_2\text{Se}_4$ , prepared by HU method at 360 °C.

#### 4.8 Heat-Up (HU) versus Hot-Injection (HI)

In order to rationalize the influence of the preparation method on the composition and morphology of the NCs, we have employed the hot-injection method using the same precursors, capping agent, and reaction condition, including time and temperature. Hot-injection of the mixture of  $\text{CuCl}_2$  (0.25 mmol) and  $\text{Cr}(\text{acac})_3$  (0.5 mmol) dissolved in ODA, into the solution of

Se (in ODA) at 330 °C formed anisotropic-shaped nanocrystals of  $\text{CuCr}_2\text{Se}_4$ . As indicated in figure 4.25, the prepared NCs exhibit a mixture of triangular and hexagonal nanoparticles. The size and shape of the obtained NCs are similar to what has been already made via the HI method and reported by Pang et al.<sup>2</sup> Interestingly, decreasing the reaction temperature never led to the formation of any pyrite phase. Therefore, the synthesis method has a significant influence on the composition and shape of the prepared NCs.

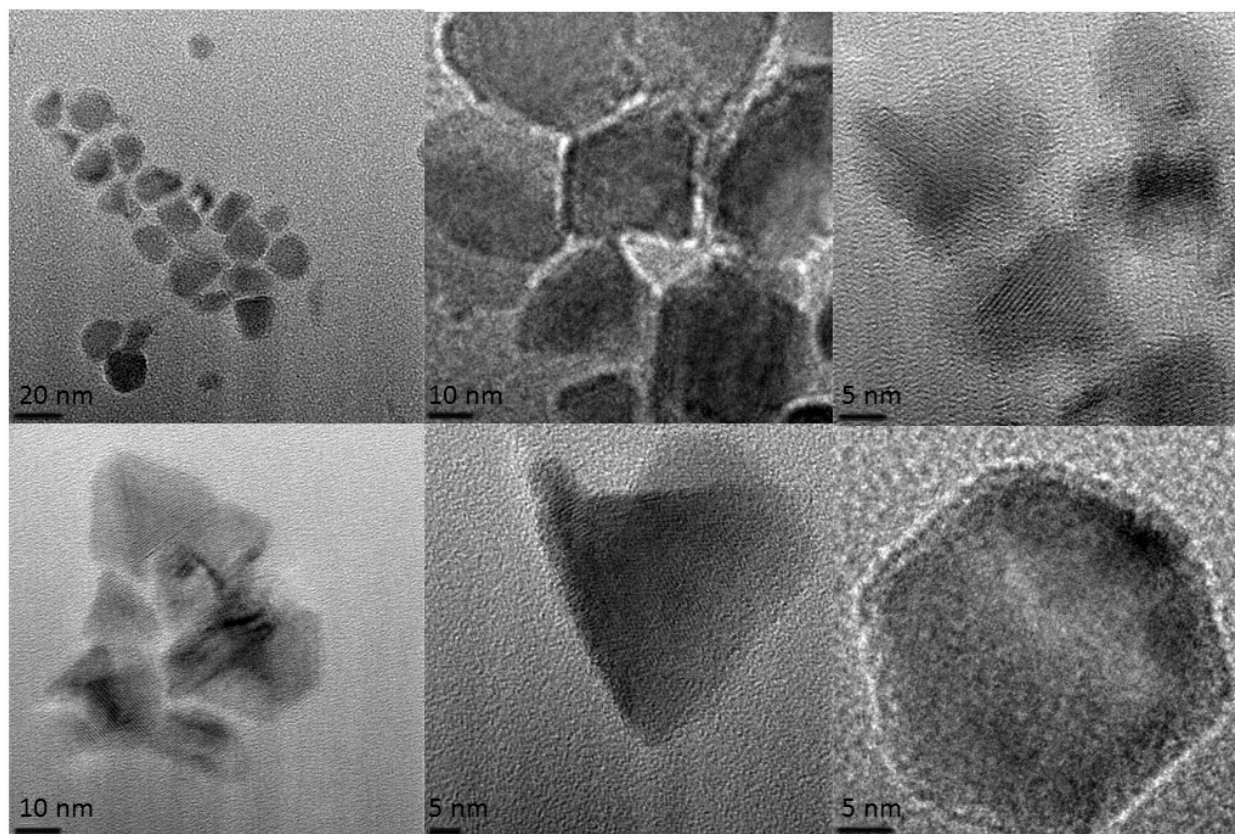


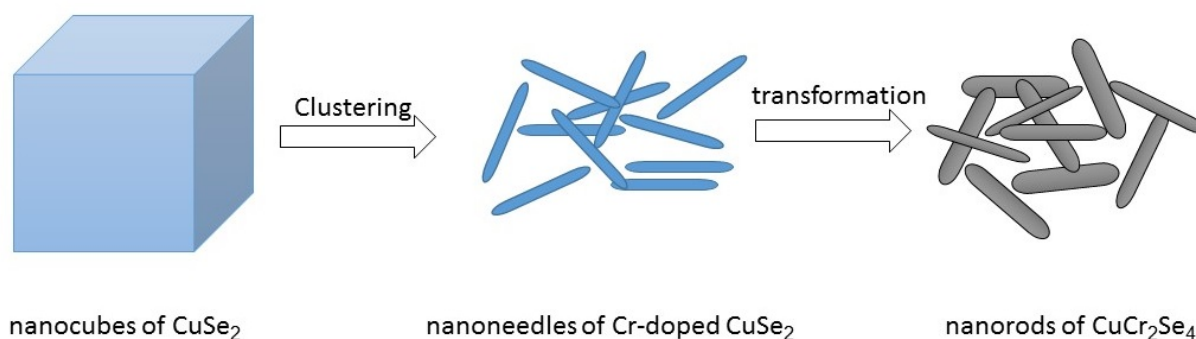
Figure 4.25: TEM images of triangular and hexagonal NCs of  $\text{CuCr}_2\text{Se}_4$  made by HI method.

#### 4.9 Conclusion

The control of materials formation requires a detailed understanding of events occurring during synthesis. The main purpose of this chapter was to rationalize the reaction mechanism of

the formation of colloidal selenospinel  $\text{CuCr}_2\text{Se}_4$  NCs during the HU method. The reaction consists of crystal-to-crystal chemical and structural phase transformation of initial  $p$ - $\text{Cr}_{0.5}\text{Cu}_{0.5}\text{Se}_2$  NCs to the spinel  $\text{CuCr}_2\text{Se}_4$  phase. The results indicated that the reaction temperature plays a predominant role, and influences the composition and structure of the products.  $\text{Cr}^{3+}$  ions occupied the octahedral sites of the pyrite structure and formed  $\text{Cr}_x\text{Cu}_{1-x}\text{Se}_2$  ( $x = 0.1-0.5$ ) NCs, and by reaching the temperature to above  $300\text{ }^\circ\text{C}$ , the 50% doped pyrite phase  $\text{Cr}_{0.5}\text{Cu}_{0.5}\text{Se}_2$  transformed to spinel  $\text{CuCr}_2\text{Se}_4$  NCs. The formation of the pyrite phase was influenced by the occupation of the octahedral positions with  $\text{Cr}^{3+}$  ions, and this process induced the direct structural transformation from pyrite to spinel phase.

The results suggested that the insertion of the  $\text{Cr}^{3+}$  ions into the octahedral positions of the pyrite structure is the main driving force for the formation of the metastable pyrite phase and the nanoneedles were formed during the morphological evolution of the initial nanocubes turned into the nanorods of the spinel phase (Scheme 4.2). This work is the first reported pyrite to spinel phase transformation and offers an outlook on the new forms of transformation mechanisms of nanoscale particles during the colloidal synthesis methods.



Scheme 4.2: Depiction of clustering of the initial nanocubes and pyrite to spinel phase transformation.

#### 4.10 References

1. Wang, Y. H. A.; Bao, N.; Shen, L.; Padhan, P.; Gupta, A. Size-Controlled Synthesis of Magnetic  $\text{CuCr}_2\text{Se}_4$  Nanocrystals. *J. Am. Chem. Soc.* **2007**, *129*, 12408–12409.
2. Pang, C.; Yang, R.; Singh, A.; Chen, H.; Bowman, M. K.; Bao, N.; Shen, L.; Gupta, A. Colloidal Synthesis and Magnetic Properties of Anisotropic-Shaped Spinel  $\text{CuCr}_2\text{Se}_4$  Nanocrystals. *RSC Adv.* **2017**, *7*, 31173–31179.
3. Ramasamy, K.; Sims, H.; Keshavarz, S.; Naghibolashrafi, N.; Gupta, A. Nanocrystals of  $\text{CuCr}_2\text{S}_{4-x}\text{Se}_x$  Chalcospinels with Tunable Magnetic Properties. *J. Mater. Chem. C*, **2016**, *4*, 3628–3639.
4. Yin, Y.; Rioux, R. M.; Erdonmez, C. K.; Hughes, S.; Somorjai, G. A.; Alivisatos, A. P. Formation of Hollow Nanocrystals Through the Nanoscale Kirkendall Effect. *Science* **2004**, *304*, 711–714.
5. Wang, W.; Dahl, M.; Yin, Y. Hollow Nanocrystals through the Nanoscale Kirkendall Effect. *Chem. Mater.* **2013**, *25*, 1179–1189.
6. Mu, L.; Wang, F.; Sadtler, B.; Loomis, R. A.; Buhro, W. E. Influence of the Nanoscale Kirkendall Effect on the Morphology of Copper Indium Disulfide Nanoplatelets Synthesized by Ion Exchange. *ACS Nano* **2015**, *9*, 7419–7428.
7. Feng, J.; Yin, Y. Self-Templating Approaches to Hollow Nanostructures. *Adv. Mater.* **2019**, *31*, 1802349.
8. Cao, G. Atomic level understanding of the nanoscale Kirkendall effect. *Science Bulletin* **2017**, *62*, 818–819.
9. Koh, S.; Kim, W. D.; Bae, W. K.; Lee, Y. K.; Lee, D. C. Controlling Ion-Exchange Balance and Morphology in Cation Exchange from  $\text{Cu}_{3-x}\text{P}$  Nanoplatelets into InP Crystals. *Chem. Mater.* **2019**, *31*, 1990–2001.
10. Hergert, F.; Jost, S.; Hock, R.; Purwins, M. A Crystallographic Description of Experimentally Identified Formation Reactions of  $\text{Cu}(\text{In,Ga})\text{Se}_2$ . *J. Solid State Chem.* **2006**, *179*, 2394–2415.
11. Olvera, A.; Sahoo, P.; Tarczynski, S.; Poudeu, F. P. Topochemical Solid-State Reactivity: Redox-Induced Direct Structural Transformation from  $\text{CuSe}_2$  to  $\text{CuInSe}_2$ . *Chem. Mater.* **2015**, *27*, 7179–7186.
12. Liu, T.; Jin, Z.; Li, J.; Wang, J.; Wang, D.; Laia, J.; Du, H. Monodispersed Octahedral-Shaped Pyrite  $\text{CuSe}_2$  Particles by Polyol Solution Chemical Synthesis. *CrystEngComm*. **2013**, *15*, 8903–8906.

13. V. Lemos, G. M. Gualberto, J. B. Salzberg and F. Cerdelra, First-Order Raman Scattering in  $\text{NiS}_{2-x}\text{Se}_x$ . *Phys. Status Solidi B* **1980**, *100*, 755.
14. Ivanov, V. G.; Iliev, M. N.; Wang, Y. –H. A.; Gupta, A. Ferromagnetic Spinel  $\text{CuCr}_2\text{Se}_4$  Studied by Raman Spectroscopy and Lattice Dynamics Calculations. *Physical Review B* **2010**, *81*, 224302.

## CHAPTER 5

### CONTROLLED SYNTHESIS OF MAGNETIC $\text{CuCr}_2\text{S}_4$ CHALCOSPINEL NANOCRYSTALS USING SINGLE SOURCE PRECURSORS

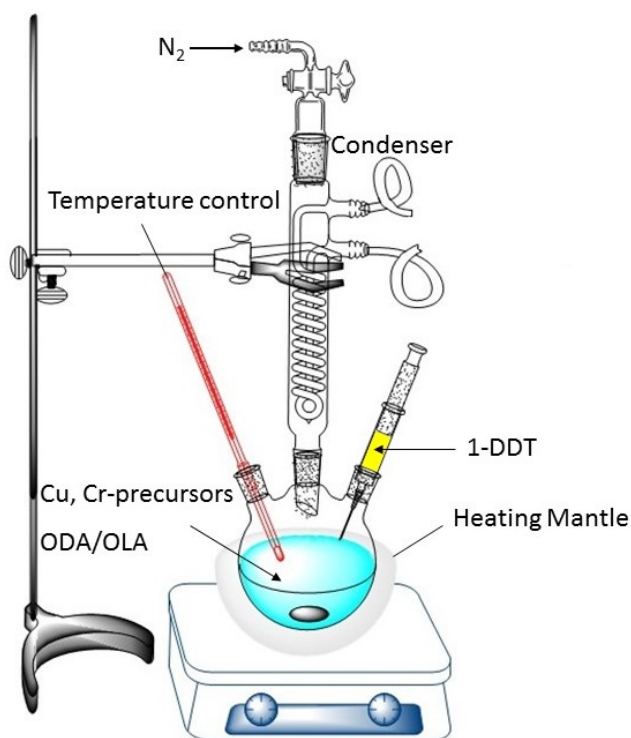
#### 5.1 Abstract

In this chapter, we present a colloidal synthesis of thiospinel  $\text{CuCr}_2\text{S}_4$  NCs via HI method using metal-complexes of diethyldithiocarbamate (DDTC) as the precursors. The effect of the single-source precursor on the composition, crystallinity, and structure of the products has been studied. Moreover, the influence of various important parameters such as reaction time and temperature, capping ligand, surfactant, etc. on the crystalline phase, shape, and size of the NCs have been systematically studied. We have also compared HI with HU method in order to rationalize the influence of the synthesis strategy on the products. The morphological changes and magnetic properties of the NCs were also presented. The obtained materials were analyzed and characterized using X-ray diffraction, SEM, TEM, HRTEM, HAADF-STEM, and EDS-STEM. The result indicates the formation of uniform NCs of  $\text{CuCr}_2\text{S}_4$  along with the formation of a small amount of sulfur impurity. The presence of sulfur in the structure of the organic ligand of DDTC facilitates the formation of a sulfur phase as an impurity. The annealing process under the sulfur vapor atmosphere influences the evolution of the sulfur phase. Our results indicate that the controlling of the formation of pure-phase nanoparticles using metal-DDTC precursors is more challenging than using metal salts, which reported earlier. However, this work is the first successful effort to prepare NCs of  $\text{CuCr}_2\text{S}_4$ , employing single-source precursors.

## 5.2 Introduction

### 5.2.1 Colloidal Nanocrystals of Spinel $\text{CuCr}_2\text{S}_4$

For the first time, Ramasamy et al. reported the synthesis of phase-pure  $\text{CuCr}_2\text{S}_4$  NCs using the thermal-decomposition method, including hot-injection of 1-dodecanethiol (1-DDT) into a hot solvent containing  $\text{CuCl}_2$  and  $\text{CrCl}_3 \cdot 6\text{H}_2\text{O}$  as the precursors. They used oleylamine (OLA;  $\text{C}_{18}\text{H}_{37}\text{N}$ ) and octadecylamine (ODA;  $\text{C}_{18}\text{H}_{39}\text{N}$ ) as coordinating solvents (or capping agent).<sup>1</sup> Scheme 5.1 represents the general scheme of the HI method for the synthesis of  $\text{CuCr}_2\text{S}_4$  nanocrystals.



Scheme 5.1: Schematic representation of the HI synthesis of  $\text{CuCr}_2\text{S}_4$  NCs.

The X-ray diffraction results (Figure 5.1) indicate the phase purity of the synthesized spinel NCs (fcc, space group  $Fd3m$ ). The morphology and composition of the product can be

controlled by adjustment of the temperature, time, and chemistry and composition of the precursors, surfactants, and capping ligands. The reaction temperatures below 350 °C favor the formation of the low-temperature phase  $\text{CuCrS}_2$  nonmagnetic material with a layered structure (Figure 5.2). Therefore temperature control of the reaction is critical.

For the synthesis of  $\text{CuCr}_2\text{S}_4$ , after deaeration of the mixture of  $\text{CrCl}_3 \cdot 6\text{H}_2\text{O}$  (0.5 mmol),  $\text{CuCl}_2$  (0.25 mmol), and 10 g of ODA for 15 min, the mixture was heated to 360 °C under the  $\text{N}_2$  atmosphere. At 360 °C, 3.0 mmol (2.0 ml) of the hot 1-DDT (250 °C) was rapidly injected into the precursor containing vessel. Controlling the temperature of the reaction above 350 °C is the crucial factor during the injection process. After stirring the resulting mixture at 360 °C for 1 hour, the black product  $\text{CuCr}_2\text{S}_4$  was cooled to ambient temperature, washed with ethanol and hexane, and finally isolated via centrifugation. As illustrated in TEM images (Figures 5.3 and 5.4), using ODA and OLA as the capping ligands yield to cube-shaped nanocrystals (with an average size of 20 nm), and nanoclusters (with an average size of 30 nm), respectively.

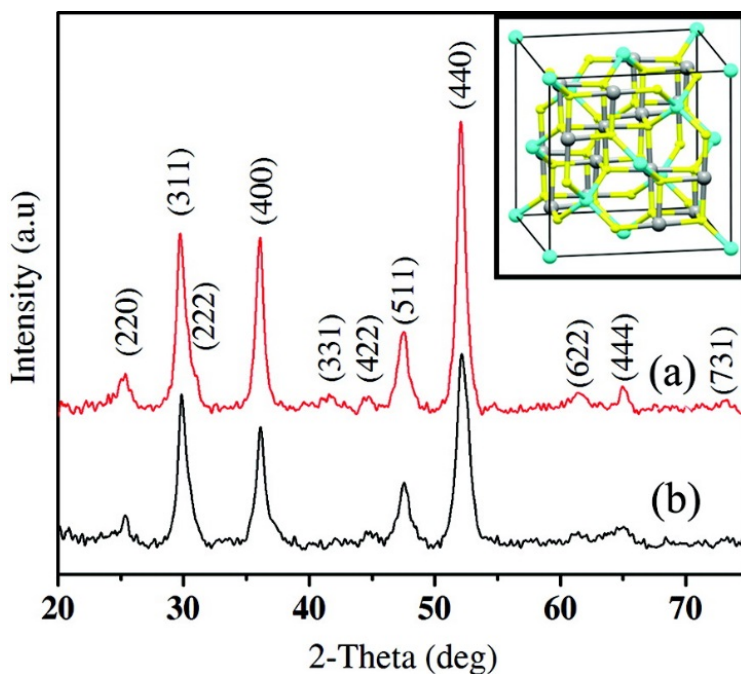


Figure 5.1: The XRD patterns of (a) nanocubes and (b) nanoclusters of  $\text{CuCr}_2\text{S}_4$ . Reprinted with permission from ref. 1.

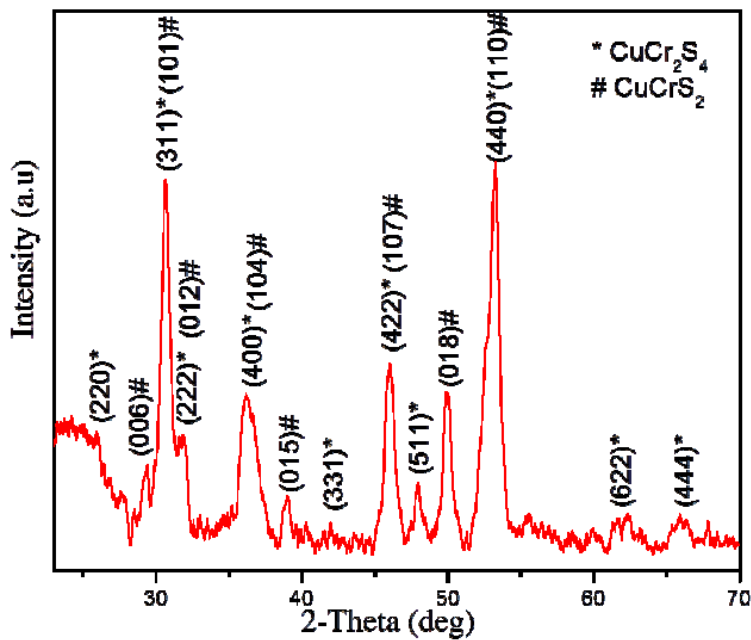


Figure 5.2: The XRD pattern of the NCs prepared at 340 °C, indicating the formation of the secondary phase of  $\text{CuCrS}_2$  as an impurity. Reprinted with permission from ref. 1.

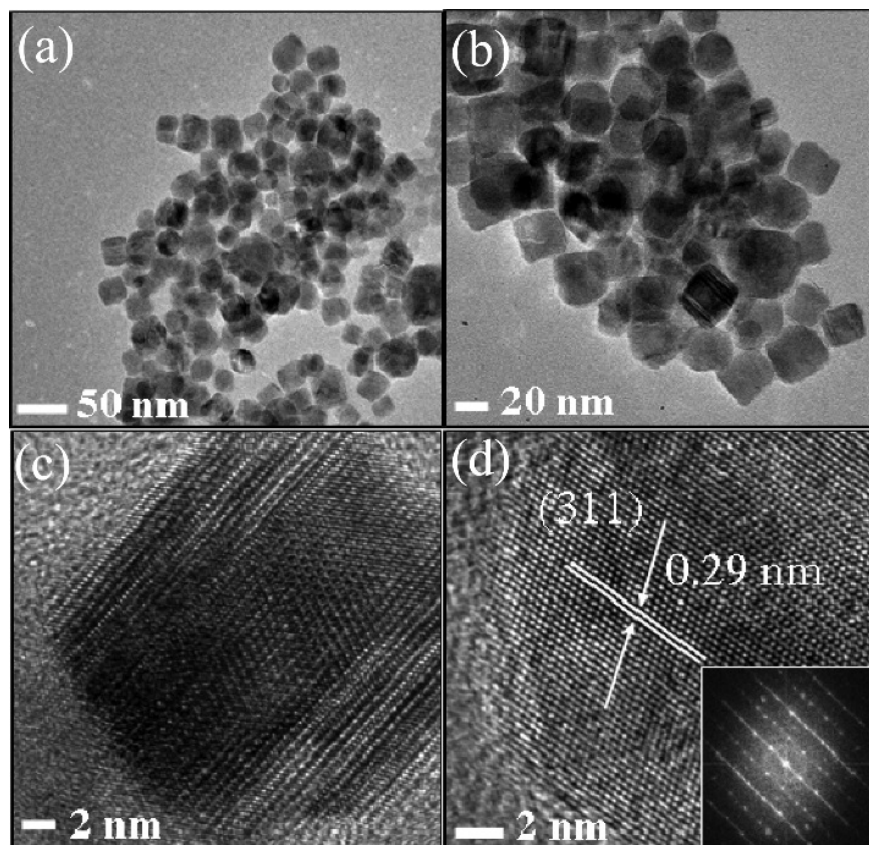


Figure 5.3: TEM, HRTEM images, and SAED pattern of the nanocubes of CuCr<sub>2</sub>S<sub>4</sub> formed in the presence of ODA. Reprinted with permission from ref. 1.

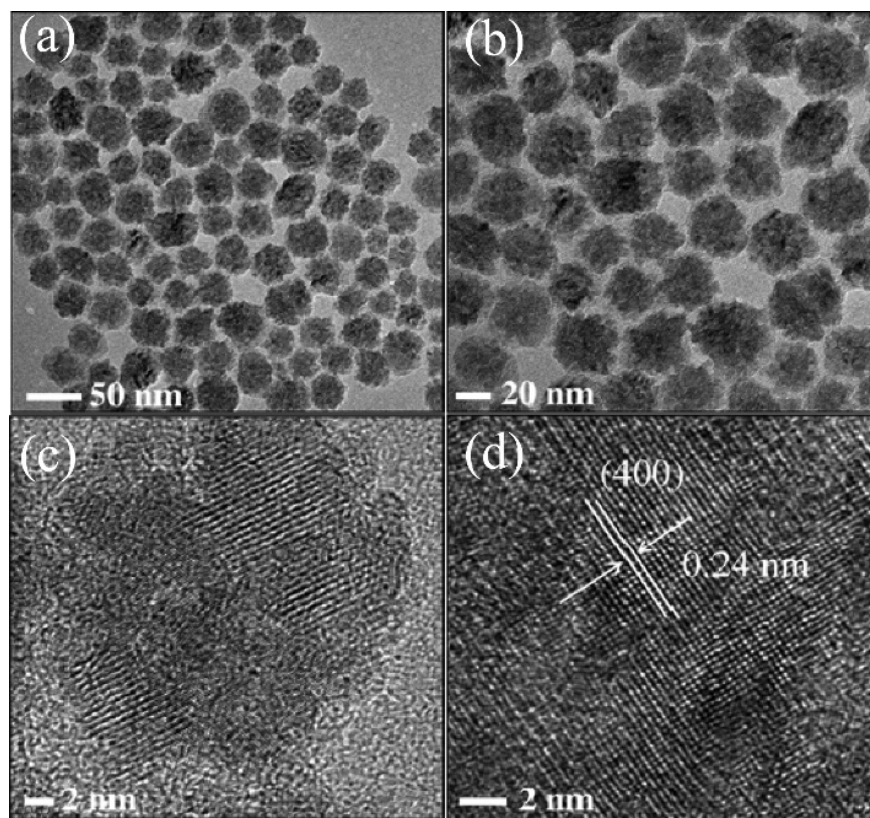


Figure 5.4: TEM and HRTEM images of the nanoclusters of  $\text{CuCr}_2\text{S}_4$  formed in the presence of OLA. Reprinted with permission from ref. 1.

### 5.2.2 Magnetic Properties of $\text{CuCr}_2\text{S}_4$ NCs

Figure 5.5 indicates the temperature dependence of the field-cooled (FC) and the zero-field-cooled (ZFC) magnetization of  $\text{CuCr}_2\text{S}_4$  NCs using applied magnetic fields ( $H$ ) of 50 and 100 Oe.<sup>1</sup> The obtained blocking temperature ( $T_b$ ) deduced from low-field (50 Oe) are 290 and 300 K, for nanocubes and nanoclusters, respectively. For both samples there is a drop in the magnetization value to almost zero at temperatures between 340 and 345 K. It could be because of their Curie temperatures which are under the bulk value of 377 K.

Measurement of the magnetizations ( $M$ ) as a function of the external magnetic field ( $H$ ) has been done to determine the saturation magnetization ( $M_s$ ) at 300 and 5 K. Based on the figure

5.5 nanocubes and nanoclusters reveal superparamagnetic (SP) behavior near the room temperature (300 K). On the other hand, at 5 K, both nanocrystals exhibit ferromagnetic behavior with relatively low coercivity values. The observed coercivity values are almost 350 and 750 Oe for nanocubes and nanoclusters, respectively.<sup>1</sup> The loops did not exhibit magnetization saturation for the NCs. The highest observed magnetization values at 5 K were 30 emu g<sup>-1</sup> and 33 emu g<sup>-1</sup> for nanocubes and nanoclusters, respectively which are significantly lower than the reported bulk value,<sup>2</sup> since parameters such as broken symmetry at the surface of nanoparticles and defects at the cation and anion sites could dramatically decrease the net magnetization and unsaturation of the loops due to significant decrease of the effective number of spins and possible antiferromagnetic coupling.<sup>3</sup> However, the 30 and 33 emu g<sup>-1</sup> values reported in this work are higher than the reported value for the nanoparticles previously made by ball milling method.<sup>2</sup>

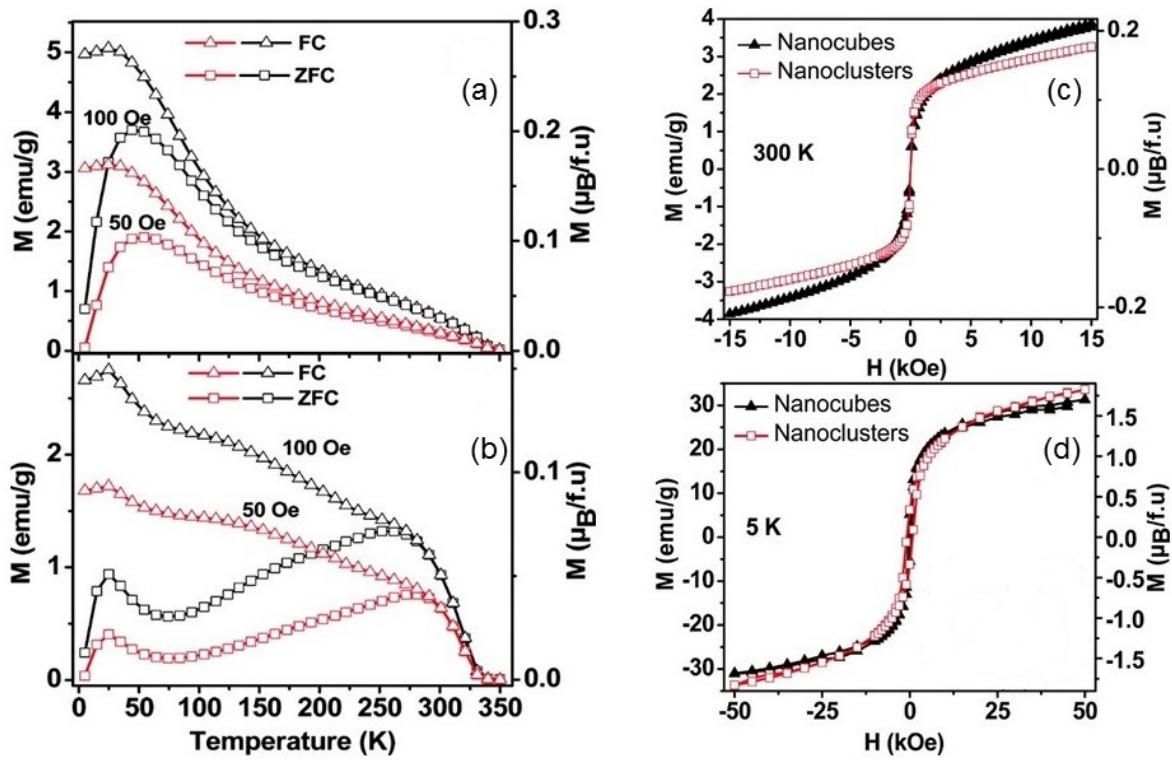


Figure 5.5: Magnetization ( $M$ ) as a function of temperature ( $T$ ) for (a) nanocubes and (b) nanoclusters and (c) as a function of field ( $H$ ) at (c) 300 K and (d) 5 K. Reprinted with permission from ref. 1.

### 5.3 Synthesis and Characterization of $\text{CuCr}_2\text{S}_4$ NCs Using Single-Source Precursors

The main purpose of the work presented in this chapter is the design and preparation of  $\text{CuCr}_2\text{S}_4$  NCs using the new and suitable single-source precursors in order to control the size and morphology of the phase-pure nanoparticles. For this purpose, we have chosen Cu- and Cr-diethyl dithiocarbamate (DDTC) complexes as the precursors. Figure 5.6 represents the structure of  $\text{Cu}(\text{DDTC})_2$ , and  $\text{Cr}(\text{DDTC})_3$ .<sup>4,5</sup>

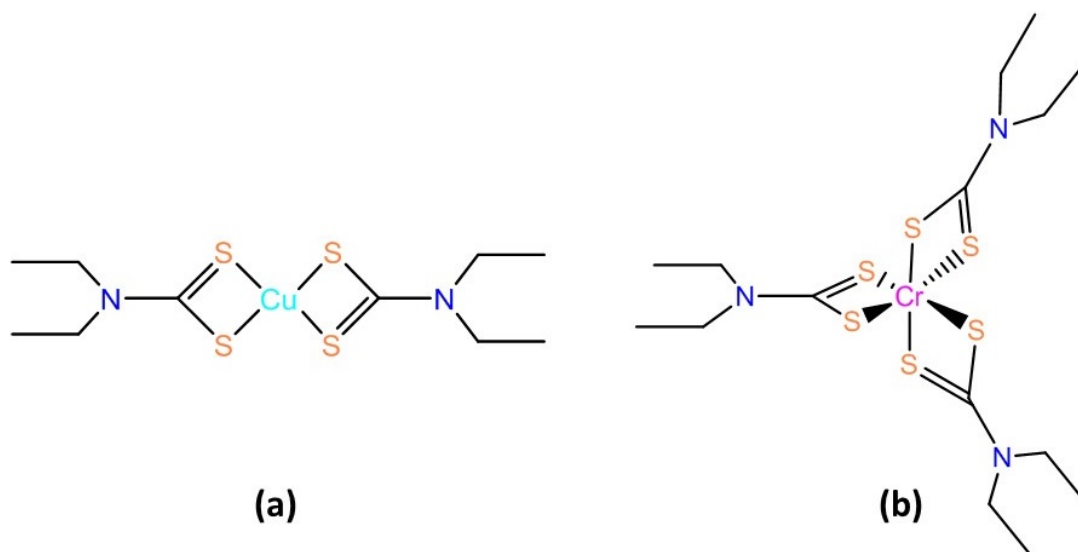
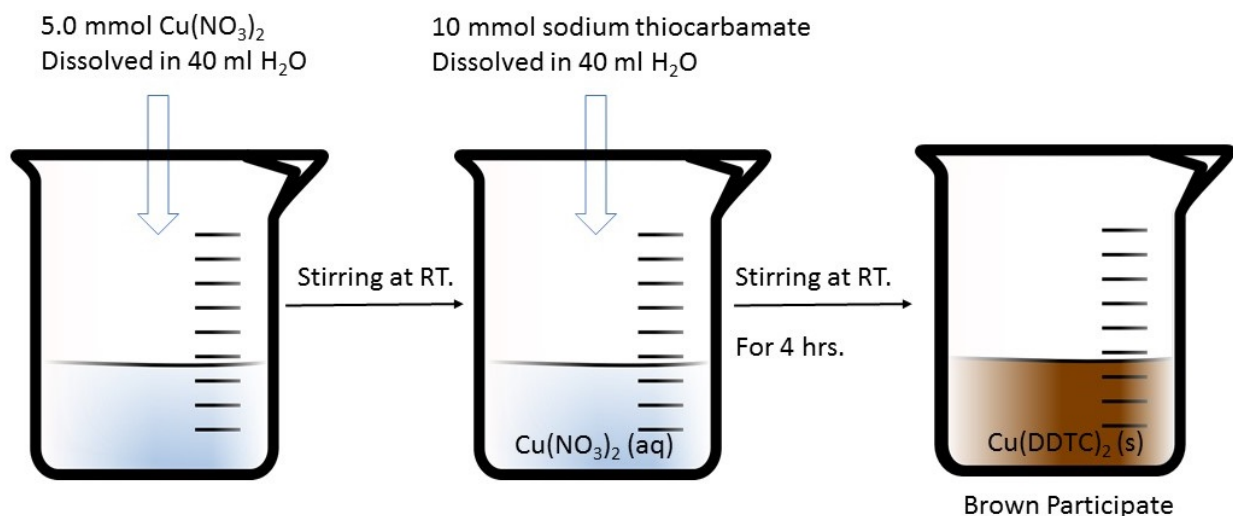


Figure 5.6: The molecular structures of (a)  $\text{Cu}(\text{DDTC})_2$ , and (b)  $\text{Cr}(\text{DDTC})_3$ .

#### 5.3.1 Synthesis of the Precursors

$\text{Cu}(\text{DDTC})_2$  has been synthesized according to the literature method.<sup>6</sup> 5.0 mmol (1.21 g) of copper nitrate dissolved in 40 ml of water. 40 ml of the aqueous solution of 10 mmol (2.25 g) sodium diethyldithiocarbamate trihydrate was added dropwise into the stirred solution of copper

nitrate at room temperature. After 4 hours, the resulting brown particulate was filtered and washed with deionized water and dried (Scheme 5.2). The purified  $\text{Cr}(\text{DDTC})_3$  complex was synthesized during the following procedure; 3.4 mmol (0.49 g) of  $\text{CrCl}_3 \cdot 6\text{H}_2\text{O}$  and 10 mmol (2.25 g) of sodium diethyldithiocarbamate trihydrate dissolved in 20 and 40 ml of isopropanol, respectively. The resulting solution of sodium diethyldithiocarbamate was sonicated for 20 min, and the chromium solution was added dropwise into the stirred sodium diethyldithiocarbamate solution at 70 °C. The resulting solution stirred for 5 hours at 70 °C. The dark teal solid has been cooled, collected by filtration, washed, and dissolved in chloroform. Finally, the resulting solution was centrifuged to the separation of a dark blue precipitate, which washed with isopropanol and dried.



Scheme 5.2: Depiction of the synthesis process of  $\text{Cu}(\text{DDTC})_2$ .

According to the thermal gravimetric analyses (TGA) of the precursors,  $\text{Cu}(\text{DDTC})_2$  and  $\text{Cr}(\text{DDTC})_3$  decompose at around 250 and 350 °C, respectively.<sup>7,8</sup>

### 5.3.2 Synthesis of NCs

As the first trial, we have used the same hot-injection method that already reported by Ramasamy et al. by using  $\text{Cu(DDTC)}_2$  instead of  $\text{CuCl}_2$ .<sup>1</sup>

0.25 mmol of  $\text{Cu(DDTC)}_2$  (0.09 g) and 0.5 mmol of  $\text{CrCl}_3 \cdot 6\text{H}_2\text{O}$  (0.133 g) were added to the 10 g of ODA and the mixture were heated to 360 °C under  $\text{N}_2$ . Extra amount (3.0 mmol; 2.0 ml) of 1-DDT was heated to 250 °C in a separated flask. The 250 °C 1-DDT was quickly injected to the stirred solution of the precursors and the stirring of the mixture continued for 1 h. The resulting black mixture was cooled, washed, isolated via centrifugation process, and dried in air.

As already mentioned, the critical point of this reaction is maintaining the temperature of the reaction at 360 °C because the temperatures under 360 °C form the secondary nonmagnetic phase of  $\text{CuCrS}_2$  as an impurity. In order to find the role of the reaction temperature, we did several reactions at different temperatures. We continued our systematic work by changing other reaction parameters such as reaction time, and composition of the precursors, surfactants, and capping ligands. Next, we will discuss the influence of each parameter on the formation of the nanoparticles.

## 5.4 Influence of the Reaction Parameters on the Formation of the Nanoparticles

### 5.4.1 Reaction Temperature

The temperature range of 310-330 °C formed phase pure particles of layered material  $\text{CuCrS}_2$  as the main product. Figure 5.7 indicates the XRD patterns of the three  $\text{CuCrS}_2$  nanoparticles prepared at 310, 320, and 330 °C, respectively. Therefore, nanoparticles of spinel phase  $\text{CuCr}_2\text{S}_4$  start to form at the temperatures higher than 340 °C.

Doing the same reaction at 340 and 350 °C led to the formation of the mixed-phase of  $\text{CuCrS}_2$  and  $\text{CuCr}_2\text{S}_4$  (Figure 5.8). The XRD pattern of the materials formed at 350 °C, shows diffraction peaks corresponding to spinel  $\text{CuCr}_2\text{S}_4$  (ICDD No. 21-0287) and layered  $\text{CuCrS}_2$  (ICDD No. 23-0952) phases along with a small amount of a sulfur allotrope ( $2\theta = 22, 25, 29, 33, 39, 43$  degrees; ICDD No. 20-1227). It demonstrated that after the mixture was heated to above 350 °C, part of the sulfur transformed to another sulfur allotrope.<sup>9</sup> No peaks correspond to sulfur were detected when the reaction was done at the temperatures below 340 °C, indicating the sulfur formed at the temperatures higher than 340 °C.

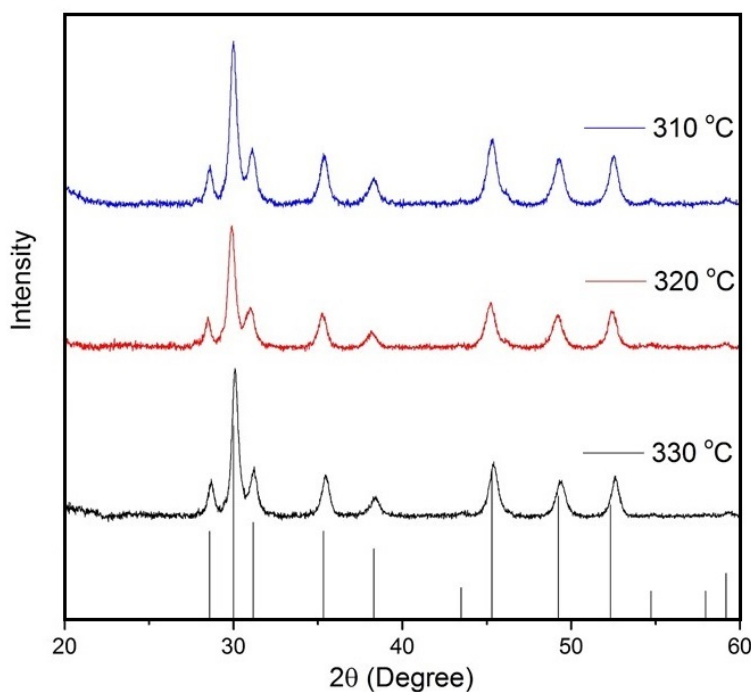


Figure 5.7: XRD patterns of the layered  $\text{CuCrS}_2$  nanoparticles formed at the temperature range of 310-330 °C (ICDD No. 23-0952).

By doing the reaction at 360 °C, we could avoid the formation of the nonmagnetic phase of  $\text{CuCrS}_2$  and the obtained NCs can be indexed to the cubic spinel  $\text{CuCr}_2\text{S}_4$  structure with the

main diffraction peaks of (220), (311), (222), (400), (331), (422), (511), (440), and (622), respectively (ICDD No. 21-0287). However, the problem is still the formation of a small amount of sulfur impurity (Figure 5.9). We have studied the possibility of the formation of other phases by comparing the XRD pattern of the prepared nanoparticles with different metal sulfide phases made by sulfur, copper and/or chromium. The only ternary metal sulfide produced by three elements of Cu, Cr, and S are nonmagnetic  $\text{CuCrS}_2$  and magnetic  $\text{CuCr}_2\text{S}_4$  materials. However, many binary metal sulfides, including Cu or Cr and S, are available. The XRD patterns of the reported metal sulfides, e.g.,  $\text{CuS}$ ,  $\text{Cu}_2\text{S}$ ,  $\text{Cu}_9\text{S}_5$ ,  $\text{CrS}$ ,  $\text{Cr}_2\text{S}_3$ , and  $\text{Cr}_5\text{S}_6$  and also metal chlorides ( $\text{CuCl}_2$  and  $\text{CrCl}_3$ ) did not match with the XRD pattern of the prepared nanoparticles. Therefore, the impurity is only sulfur.

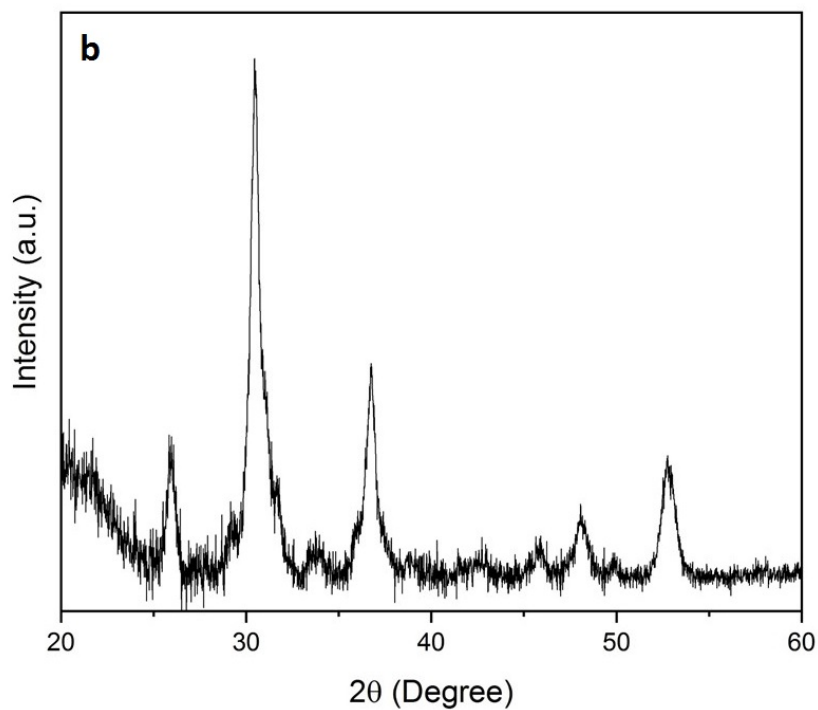
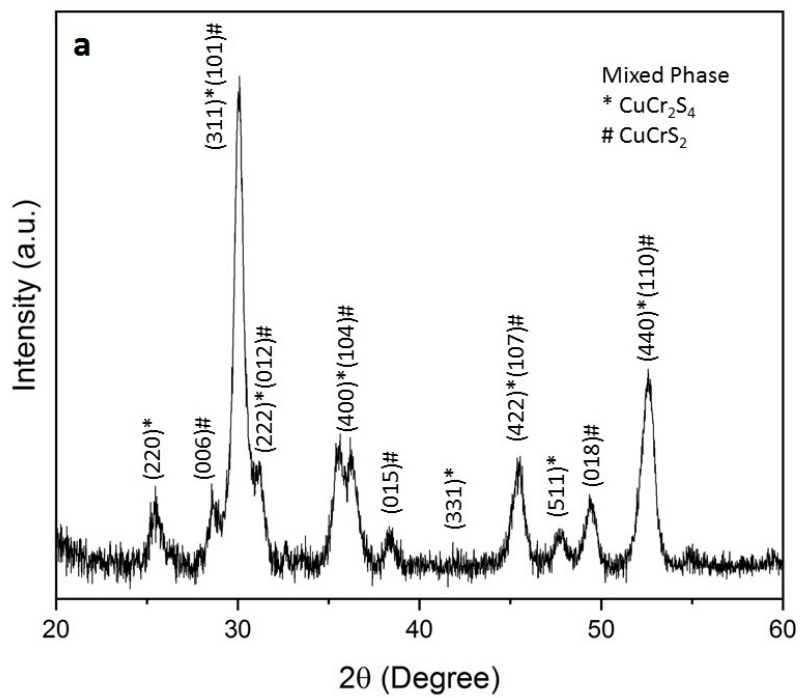


Figure 5.8: XRD patterns of the prepared particles at (a) 340, and (b) 350 °C. The relative intensity of the  $\text{CuCrS}_2$  peaks decreases by increasing the reaction temperature.

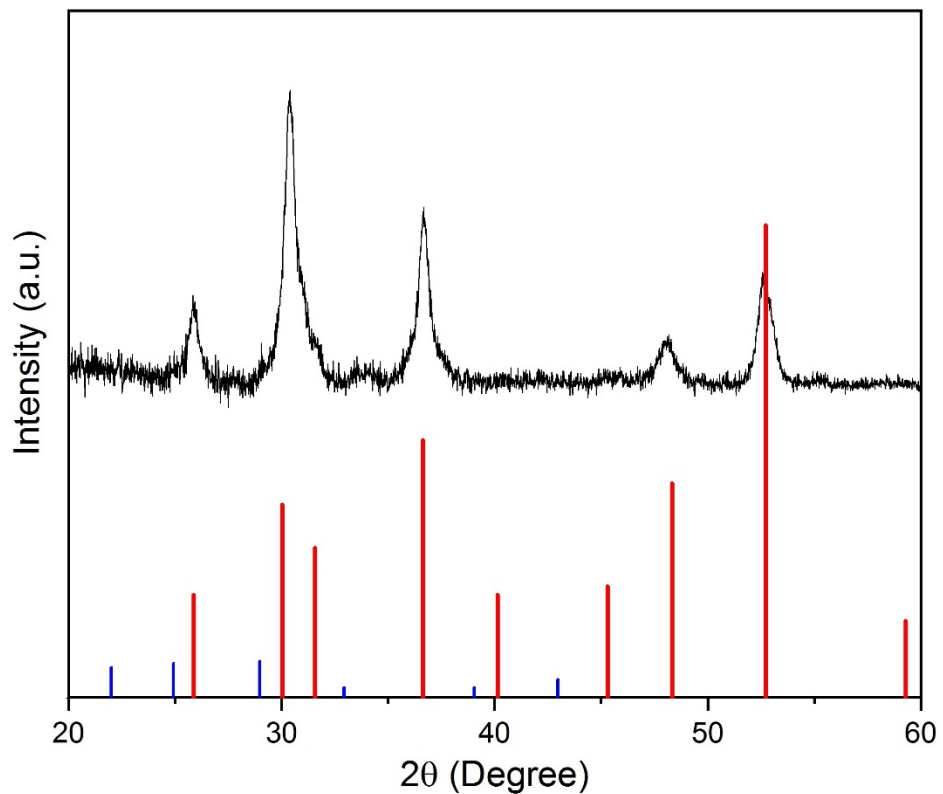


Figure 5.9: XRD pattern of NCs synthesized at 360 °C. The standard XRD stick patterns of bulk  $\text{CuCr}_2\text{S}_4$  (Red; ICDD No. 21-0287) and Sulfur (Blue; ICDD No. 20-1227) are also shown.

The TEM micrograph of the synthesized  $\text{CuCr}_2\text{S}_4$  NCs indicated the formation of nearly cube-shaped crystals with an average size of 30 nm (Figure 5.10).

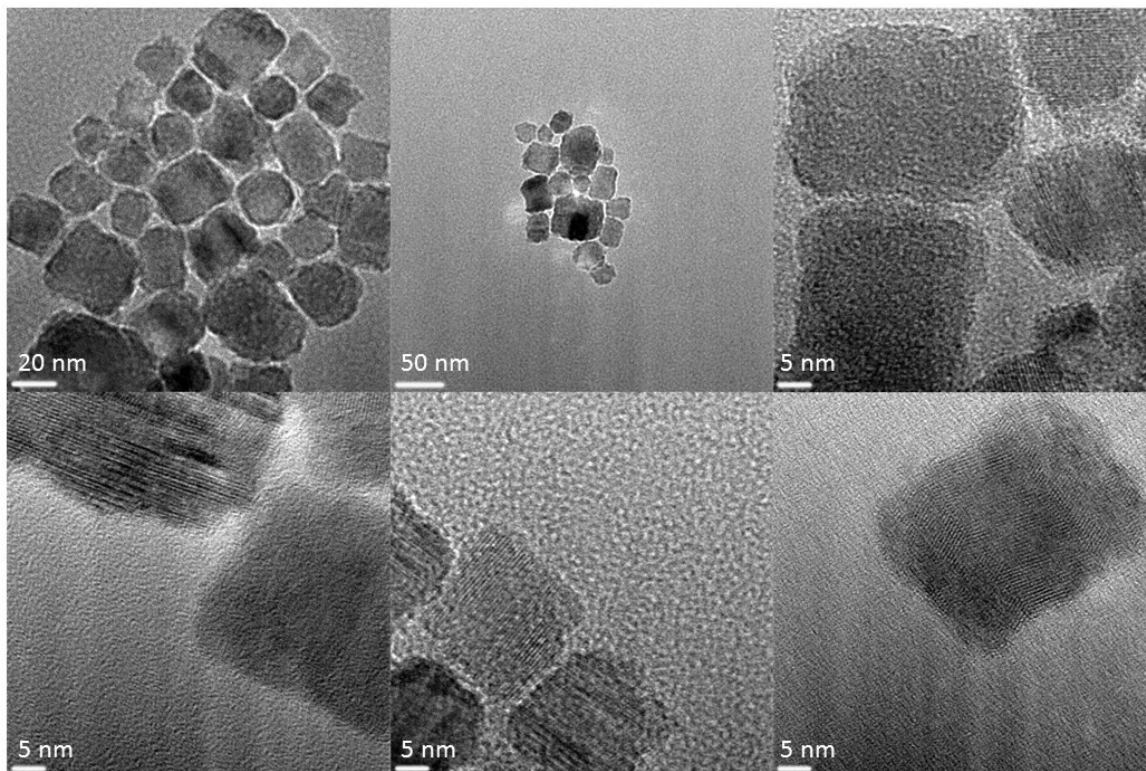


Figure 5.10: TEM images of CuCr<sub>2</sub>S<sub>4</sub> nanocubes made by Cu(DDTC)<sub>2</sub> and ODA as a capping agent.

#### 5.4.2 Reaction Time

Generally, NCs size increases with increasing reaction time (as more materials add to nanocrystal surfaces), and temperature, because the rate of nucleation increases as a function of time and temperature.<sup>10,11</sup> Hot-injection synthesis was done at different reaction times, including 15, 30, 45, and 60 min, by keeping the temperature at 360 °C. The XRD patterns of all synthesized particles show the sulfur impurity, and it seems that by approaching the temperature to 350 °C the byproduct is forming at the very first steps of the reaction. Comparing the collected XRD data at different temperatures reveals that shorter reaction times (15, or 30 min) show more

noisy patterns, and the main peaks of the magnetic  $\text{CuCr}_2\text{S}_4$  particles become less intense (Figure 5.11).

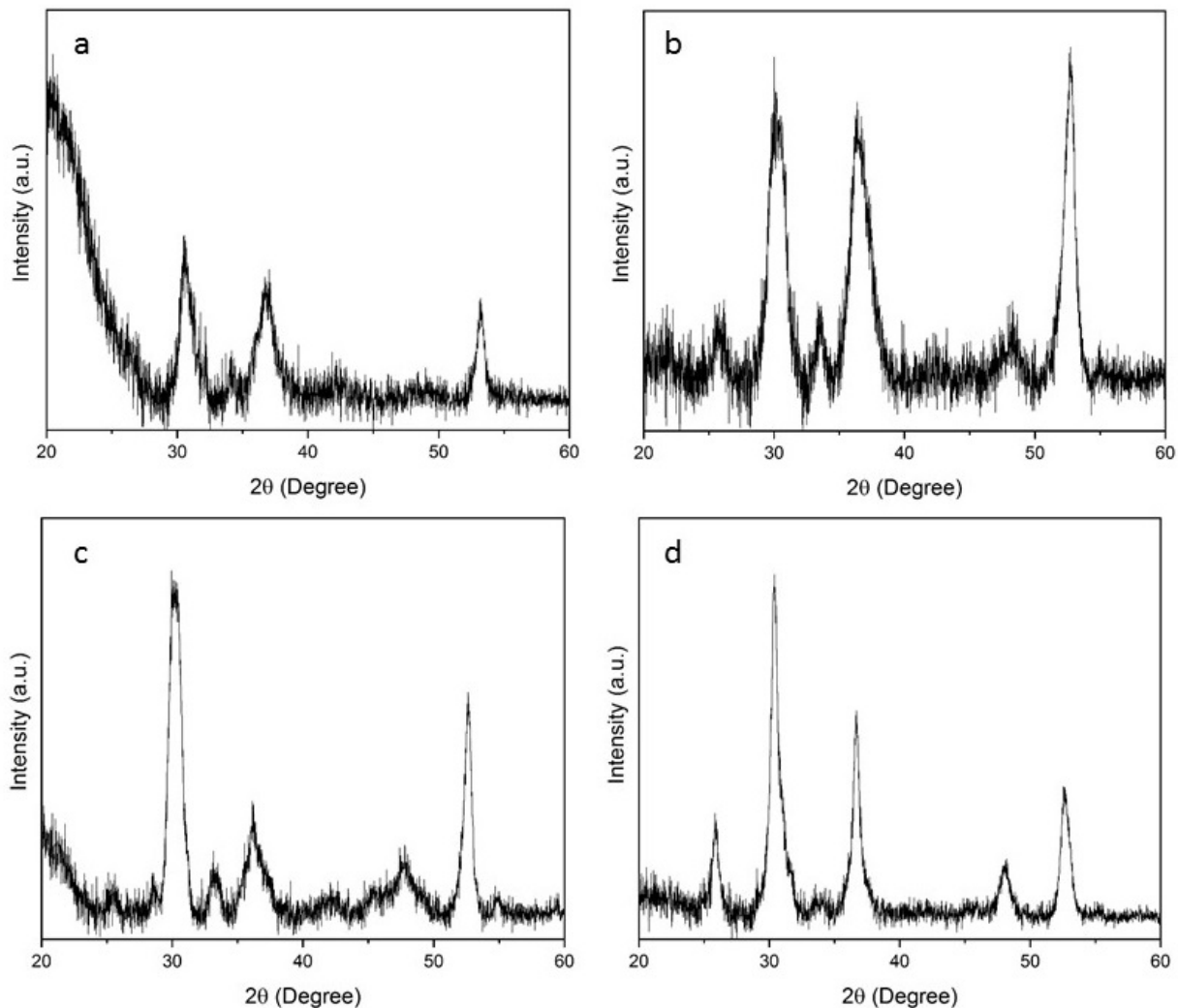


Figure 5.11: Effect of reaction time on the formation of  $\text{CuCr}_2\text{S}_4$  NCs. The XRD patterns of the NCs formed after (a) 15 min, (b) 30 min, (c) 45 min, and (d) 60 min.

### 5.4.3 Sulfur Source and Capping Agent

1-DDT could be used as both surface capping agent (and help the growth of NCs), and source of sulfur and plays an essential role in preparing suitable nanoparticles.<sup>12</sup> The alternative

sulfur source could be tert-dodecanethiol (tert-DDT), which is structurally similar to 1-DDT. Changing the reaction surfactant from 1-DDT to tert-DDT did not make any significant change, and the problem of the byproduct formation was not resolved (Figure 5.12).

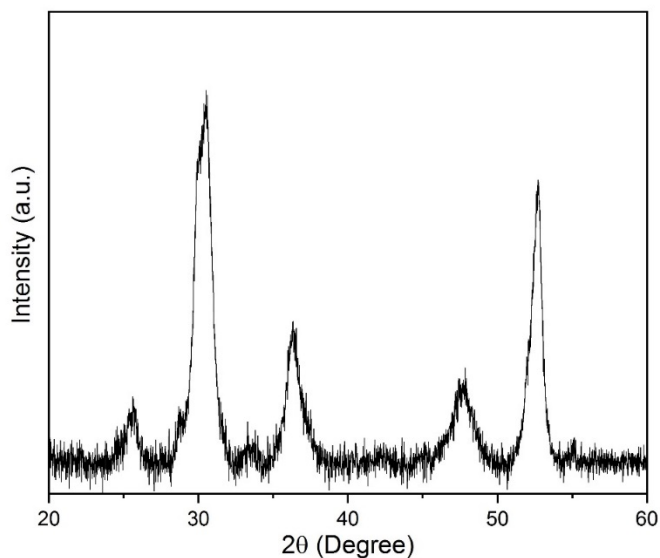


Figure 5.12: XRD pattern of the  $\text{CuCr}_2\text{S}_4$  NCs prepared by using tert-DDT instead of 1-DDT.

We have also applied HU method in the absence of external sulfur source (e.g., 1-DDT and tert-DDT). Employing  $\text{Cu}(\text{DDTC})_2$  and  $\text{CrCl}_3$  as the precursors dissolved in 10 g ODA formed the mixed phase of  $\text{CuCr}_2\text{S}_4$ ,  $\text{CuCrS}_2$ , and sulfur. We also employed HI method in which the solution of  $\text{CrCl}_3$  dissolved in 2.0 g ODA (at 250, 300, and 350 °C) was injected into preheated  $\text{Cu}(\text{DDTC})_2$  in ODA (8.0 g) solution at 360 °C. Although no secondary phase of  $\text{CuCrS}_2$  was detected, the small amount of sulfur formed again. Therefore, the formation of the sulfur phase at the temperatures above 350 °C, is not related to the nature of the external sulfur source.

ODA has bi-functional application as the solvent and capping ligand during the crystallization process.<sup>13-15</sup> When we used OLA instead of ODA as the capping agent of the reaction, the morphology of the prepared nanoparticles changed. The TEM images of the nanoparticles formed in the presence of OLA, illustrated in figure 5.13. Nanoclusters of  $\text{CuCr}_2\text{S}_4$  with an average size of 50 nm were formed. In sum, the TEM micrograph of the NCs of  $\text{CuCr}_2\text{S}_4$  revealed that the size and morphology of the prepared nanoparticles are similar to the reported work by Ramasamy et al., and we prepared nanocubes, and nanoclusters by using ODA and OLA, respectively. Compare to Ramasamy's work, the average size of the particles made by the single-source precursor was bigger (~50 nm). Therefore, the effect of capping ligands on the morphology of the produced NCs is more significant than the effect of precursors.

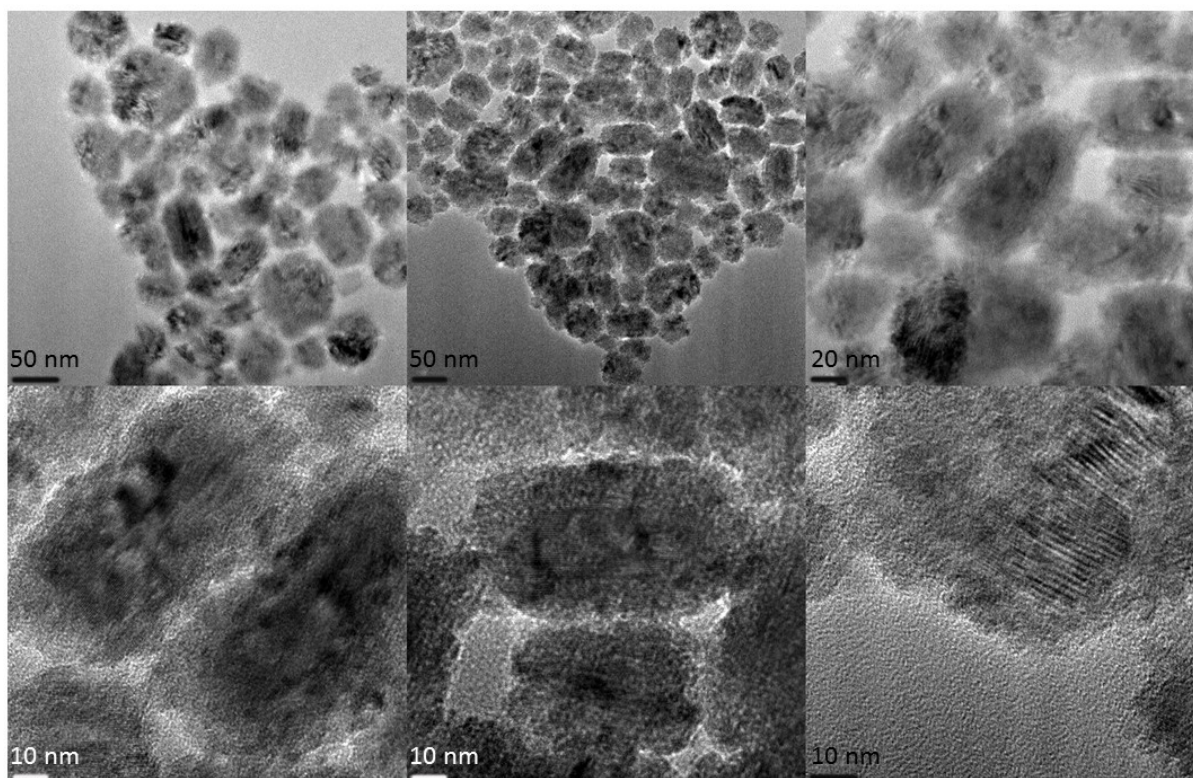


Figure 5.13: TEM images of  $\text{CuCr}_2\text{S}_4$  nanoclusters made by  $\text{Cu}(\text{DDTC})_2$  and OLA as capping agent.

#### 5.4.4 Synthesis Method; HU versus HI

In chapters 3 and 4, we discussed the formation mechanism of the selenospinel  $\text{CuCr}_2\text{Se}_4$  phase made by HU process compared to HI method. The HU synthesis pathway formed the  $p$ - $\text{Cr}_x\text{Cu}_{1-x}\text{Se}_2$  at lower temperatures, and by increasing the reaction temperature, the pyrite  $\text{Cr}_{0.5}\text{Cu}_{0.5}\text{Se}_2$  phase transformed to the spinel  $\text{CuCr}_2\text{Se}_4$ . Focusing on the same idea, encouraged us to design a similar HU method for  $\text{CuCr}_2\text{S}_4$  system. However, the XRD patterns of the products formed at the lower temperatures indicated the formation of the layered  $\text{CuCrS}_2$  phase, and no pyrites ( $\text{CuS}_2$ ) formed in this case (Figure 5.14). The nonmagnetic ternary phase of  $\text{CuCrS}_2$  formed by reaching the HU temperature to the range of 310-340 °C and it is not possible to make the pure phase of magnetic  $\text{CuCr}_2\text{S}_4$  chalcospinel using the HU method.

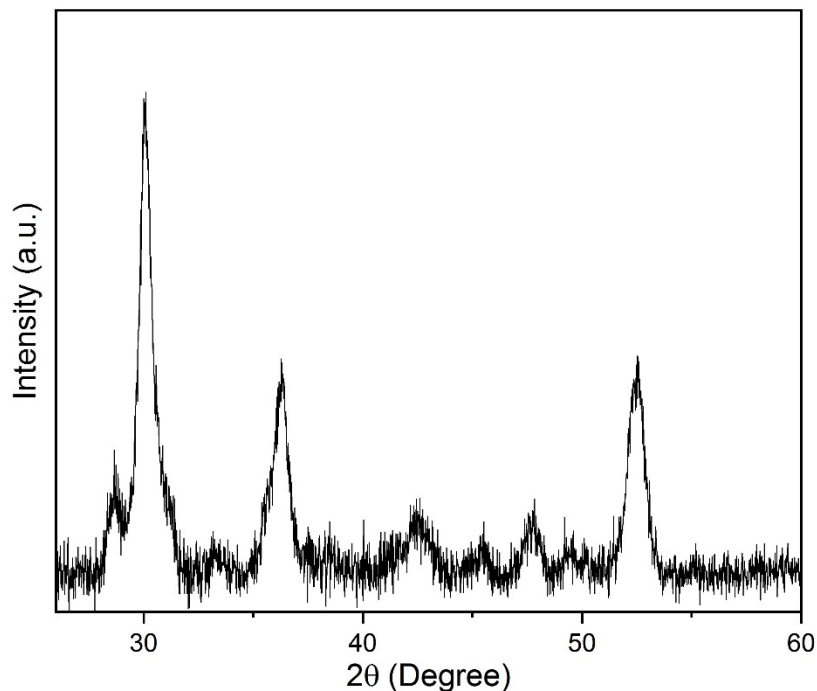


Figure 5.14: XRD pattern of the nanoparticles prepared by HU method indicating the formation of  $\text{CuCrS}_2$  and sulfur along with  $\text{CuCr}_2\text{S}_4$  phase.

### 5.4.5 Precursors

Cu-complex of dimethyldithiocarbamate  $\text{Cu}(\text{DMDTC})_2$  was used instead of  $\text{Cu}(\text{DDTC})_2$  as the copper precursor to check the effect of the chemical composition of the precursors. The relative intensity of the XRD peaks corresponding to the sulfur impurity increased by replacing  $\text{Cu}(\text{DDTC})_2$  precursor with  $\text{Cu}(\text{DMDTC})_2$  (Figure 5.15).

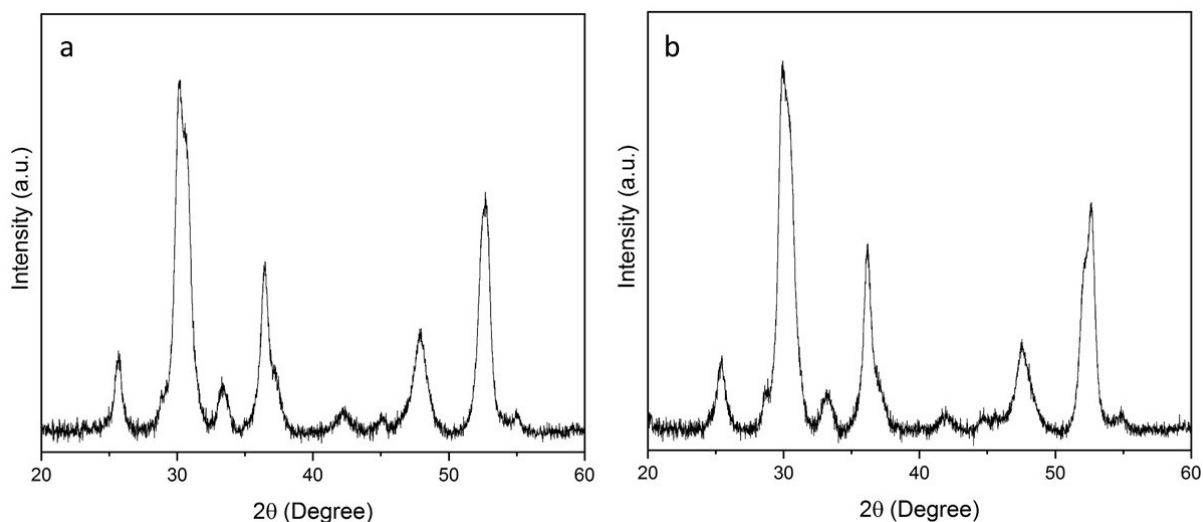


Figure 5.15: XRD patterns of the nanoparticles made by  $\text{Cu}(\text{DMDTC})_2$  in the presence of (a) OLA, and (b) ODA, indicating the mixed phase of magnetic and nonmagnetic phases.

In our next step, we replaced  $\text{CrCl}_3 \cdot 6\text{H}_2\text{O}$  with the metal complex of  $\text{Cr}(\text{DDTC})_3$  to study the effect of chromium precursor on the formation of products. The XRD pattern of the NCs of  $\text{CuCr}_2\text{S}_4$  formed in the presence of 1-DDT and ODA (Figure 5.16) indicated no significant change, and the sulfur impurities were still detected. TEM, HRTEM, HAADF-, and EDS-STEM imaging of the isolated phase pure  $\text{CuCr}_2\text{S}_4$  NCs formed in ODA represented in figures 5.17-5.19. HRTEM image of a representative nanocrystal of  $\text{CuCr}_2\text{S}_4$  exhibits lattice fringes of 0.30 nm and 0.35 nm, corresponding to (3 1 1) and (2 2 0) lattice planes, respectively. The elemental composition of the  $\text{CuCr}_2\text{S}_4$  nanocubes measured by EDS-STEM is shown in table 5.1.

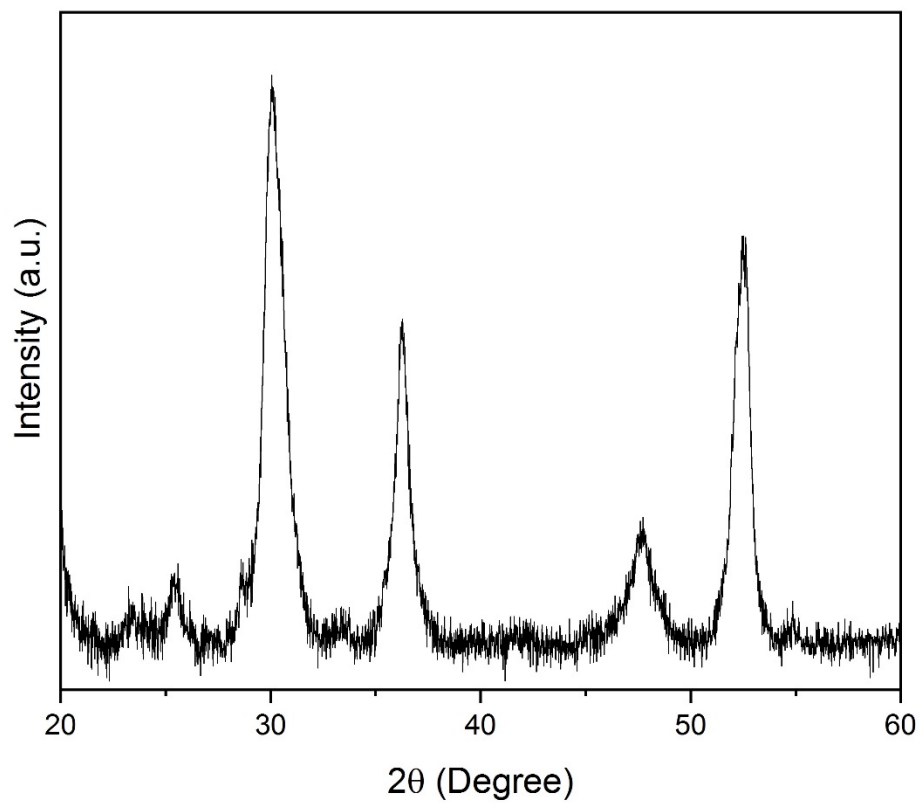


Figure 5.16: XRD pattern of the  $\text{CuCr}_2\text{S}_4$  NCs prepared by  $\text{Cu}(\text{DDTC})_2$  and  $\text{Cr}(\text{DDTC})_3$  single-source precursors.

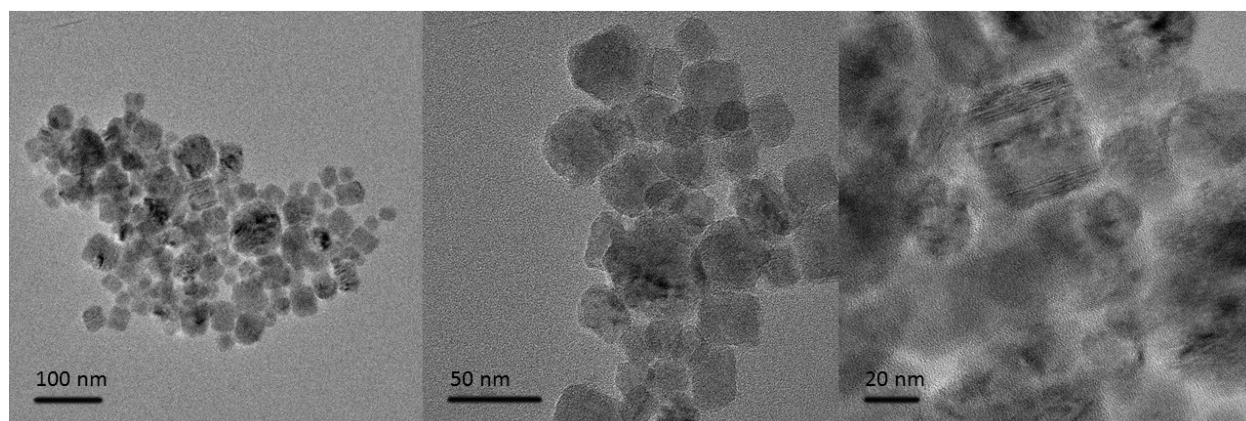


Figure 5.17: TEM images of  $\text{CuCr}_2\text{S}_4$  nanocubes with the average size range of 20-40 nm made using  $\text{Cu}(\text{DDTC})_2$  and  $\text{Cr}(\text{DDTC})_3$  precursors and ODA.

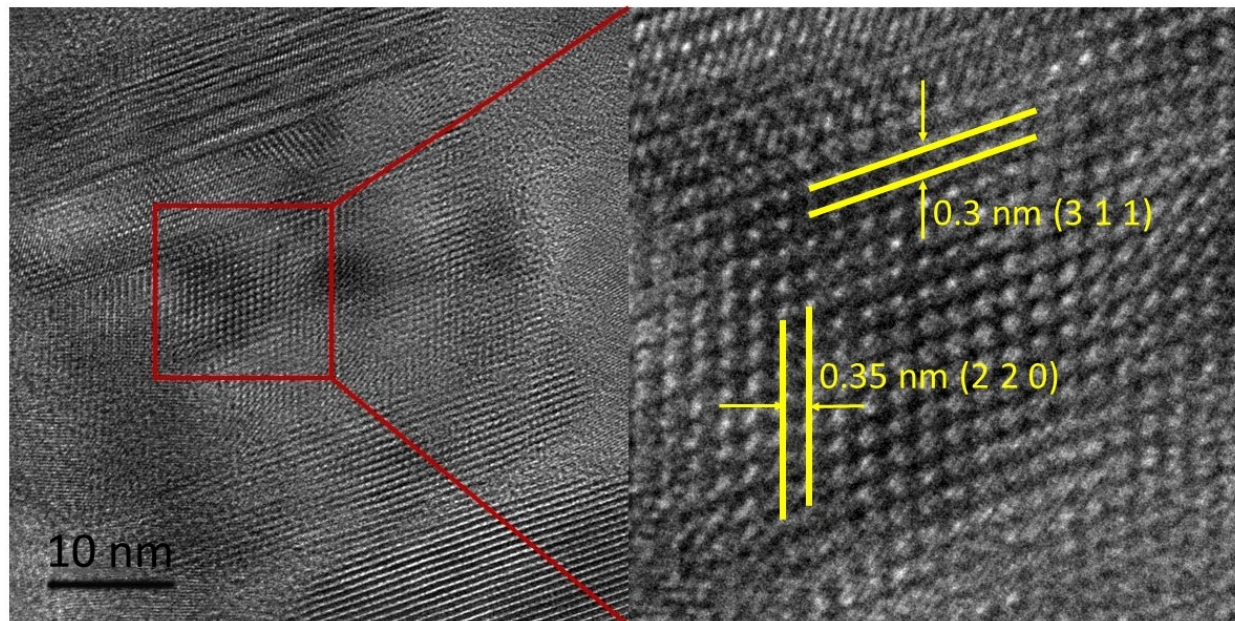


Figure 5.18: HRTEM image of the CuCr<sub>2</sub>S<sub>4</sub> nanocubes.

Table 5.1: Elemental composition of the CuCr<sub>2</sub>S<sub>4</sub> nanocubes determined by EDS.

Element	Weight %	Atomic %	Ratio
Cu K	22.29	14.82	1.00
Cr K	34.02	27.63	1.86
S K	43.69	57.55	3.88

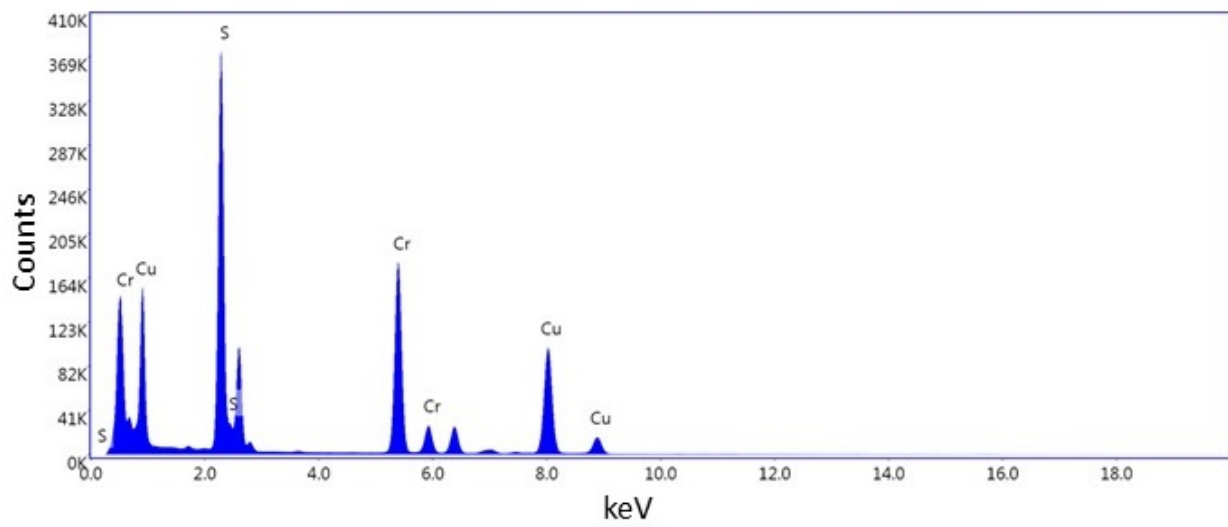
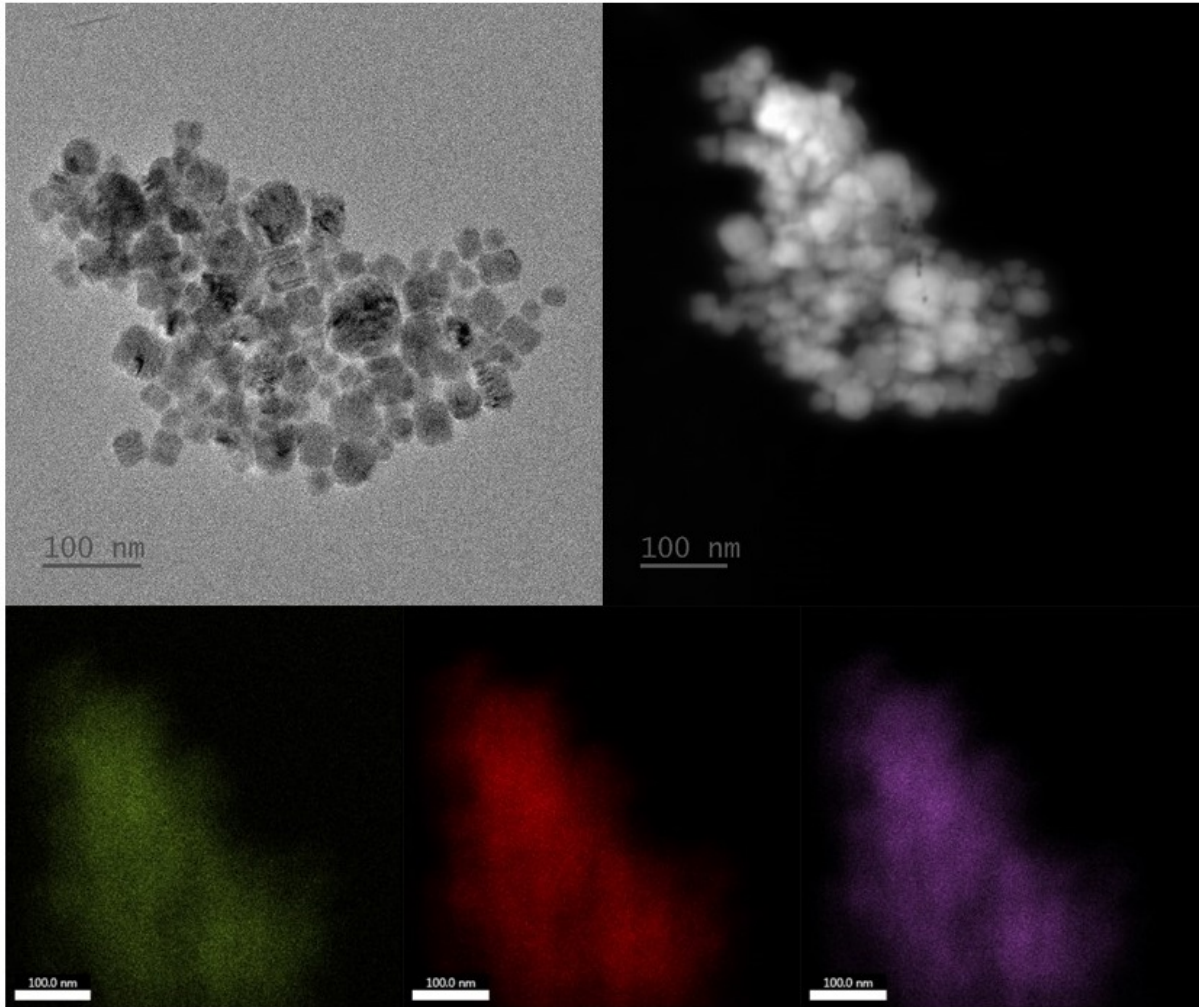


Figure 5.19: HAADF-, EDS-STEM imaging, and EDS-diagram of  $\text{CuCr}_2\text{S}_4$  nanocubes.

The excess sulfur is detected via EDS analysis of a broader area using Scanning Electron Microscopy (SEM). Figure 5.20 indicates the SEM image of  $\text{CuCr}_2\text{S}_4$  nanocubes, and figure 5.21 shows the SEM-EDS spectra of the selected regions in Figure 5.20. The elemental compositions of the selected areas are summarized in table 5.2.

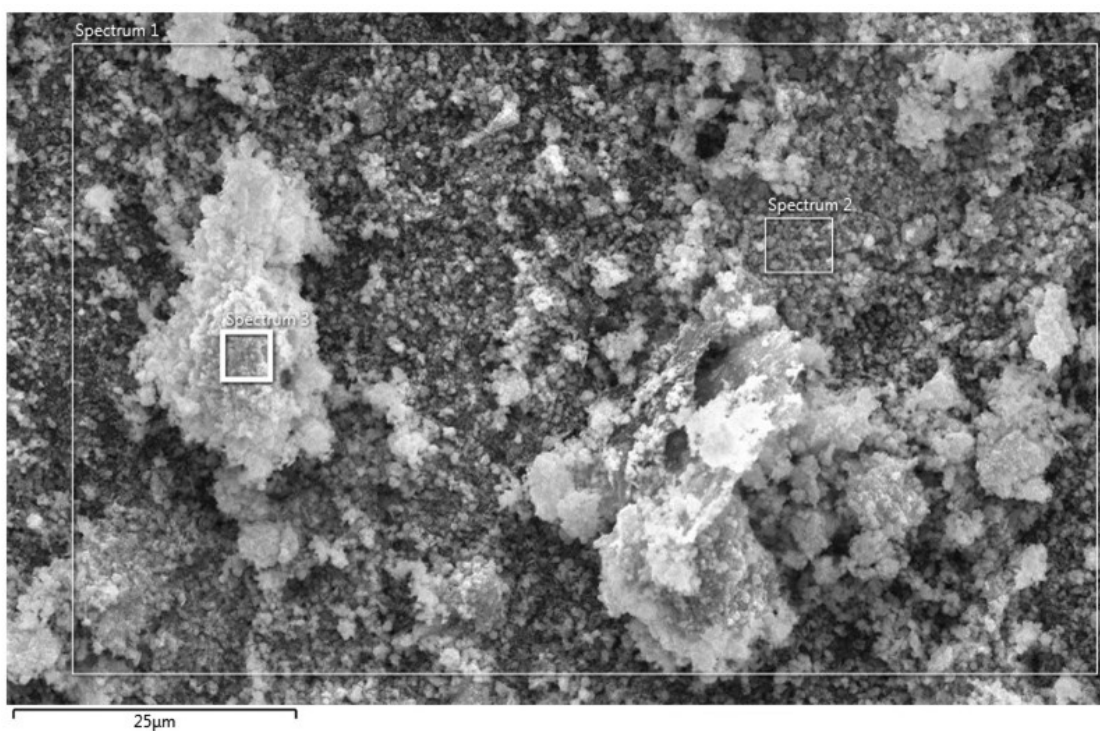


Figure 5.20: SEM image of  $\text{CuCr}_2\text{S}_4$  nanocubes.

Table 5.2: Elemental composition of the spectra 1-3.

Material	Element	Weight %	Atomic %	Ratio
Spectrum 1	Cu K	21.44	14.11	1.00
	Cr K	33.21	26.72	1.89
	S K	45.35	59.17	4.19
Spectrum 2	Cu K	21.16	13.94	1.00
	Cr K	33.72	27.15	1.94
	S K	45.12	58.91	4.23
Spectrum 3	Cu K	20.83	13.65	1.00
	Cr K	33.05	26.46	1.94
	S K	46.12	59.89	4.39

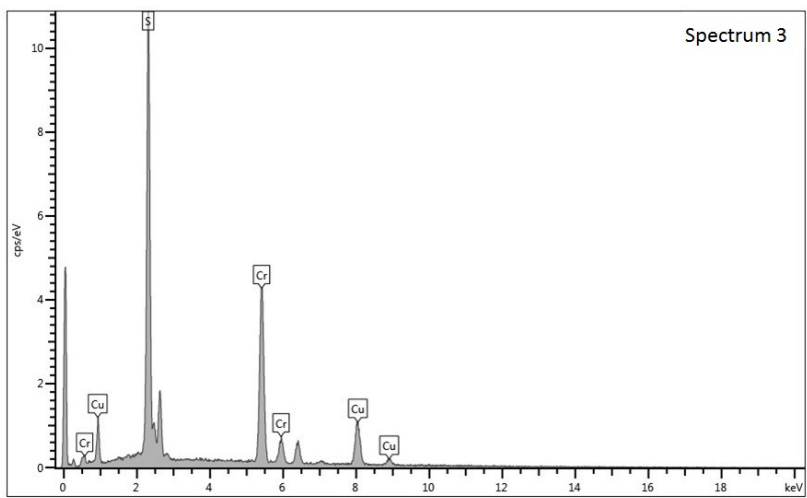
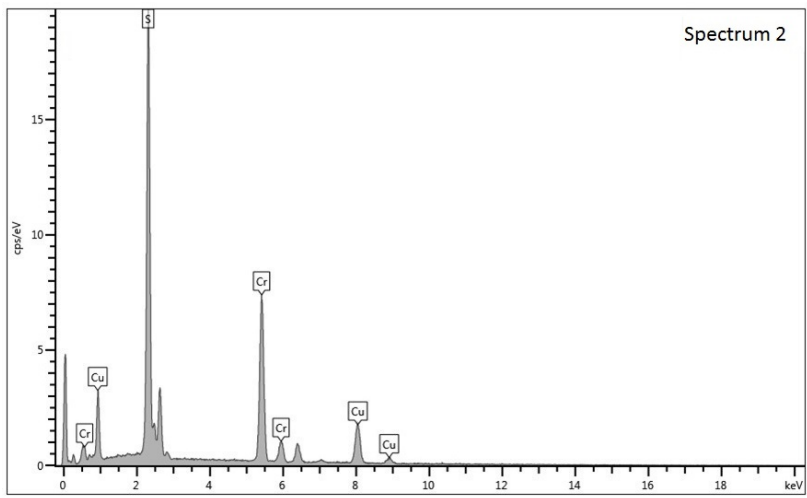
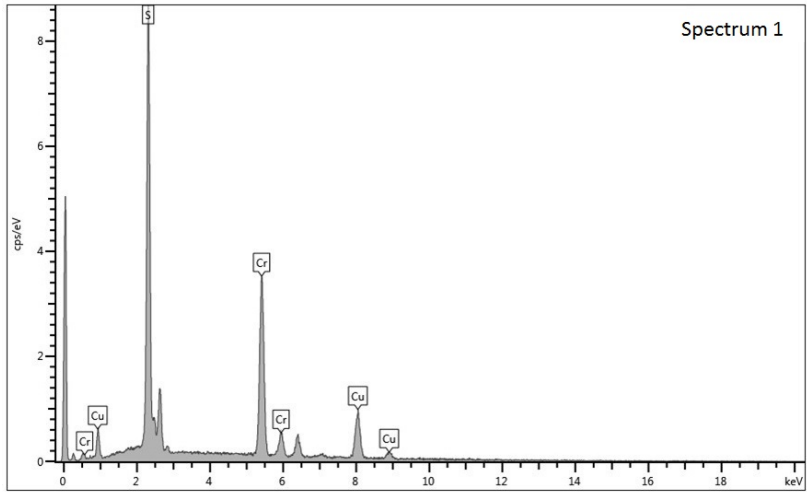
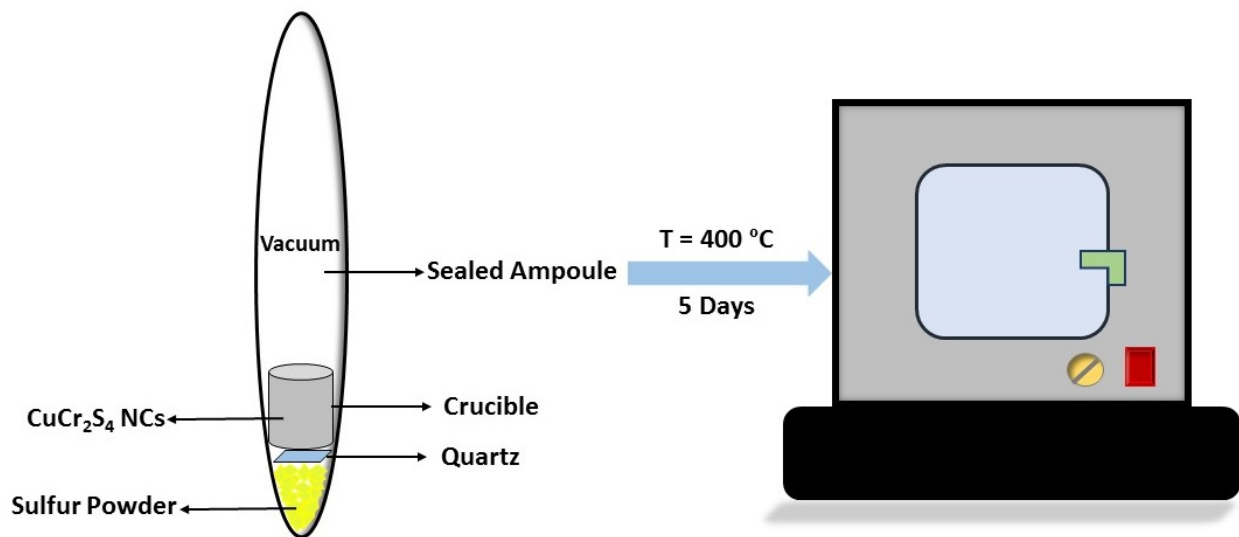


Figure 5.21: SEM-EDS diagram of spectra 1-3.

## 5.5 Stabilization of the Sulfur Rich Phase by Annealing

Obtained NCs were annealed under sulfur vapor atmosphere in order to stabilize the  $\text{CuCr}_2\text{S}_4$  phase and explore the post-annealing effect on the crystallinity of the prepared NCs. Scheme 5.3 shows a schematic depiction of experimental details of the annealing procedure. The synthesis was carried out in a vacuumed sealed quartz ampoule. 160 mg of the as-synthesized colloidal  $\text{CuCr}_2\text{S}_4$  nanocubes (located in a crucible) along with 160 mg of sulfur powder transferred into the ampoule as depicted in scheme 5.3.

$\text{CuCr}_2\text{S}_4$  NCs and sulfur powder were separated by a piece of quartz to allow only the sulfur vapor to be present proximal to the nanoparticles. Therefore, there was no physical contact between the materials. The materials were heated in a furnace to  $400\text{ }^\circ\text{C}$  and maintained at this temperature for 5 days. After cooling the crucible to ambient temperature, annealed NCs washed with a small amount of ethanol and hexane and dried in air.



Scheme 5.3: Depiction of the annealing process of  $\text{CuCr}_2\text{S}_4$  NCs under the atmosphere of sulfur vapor.

As illustrated in figure 5.22, the intensity of the diffraction peaks of annealed  $\text{CuCr}_2\text{S}_4$  particles increased, and the peaks became sharper and less noisy. The same evolution is detected on the diffraction peaks of the sulfur impurity, and the corresponding peaks became sharper, narrower, and more intense. Therefore, the mentioned high-temperature thermal treatment had a similar influence on the crystallinity and stabilization of both the main phase of  $\text{CuCr}_2\text{S}_4$  and sulfur.

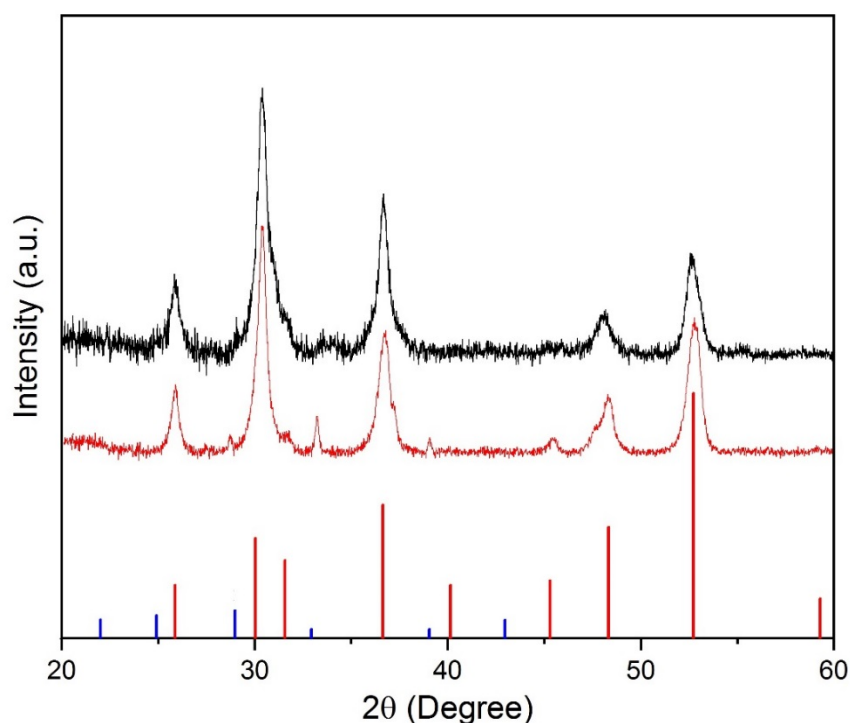


Figure 5.22: XRD patterns of the as-synthesized colloidal (black) and annealed (red)  $\text{CuCr}_2\text{S}_4$  NCs under the atmosphere of sulfur vapor.

Figure 5.23 shows the TEM micrograph of the annealed particles. Although the majority of small NCs are still cubic, larger size particles (with the size range of 60-100 nm) were also formed in a spherical shape.

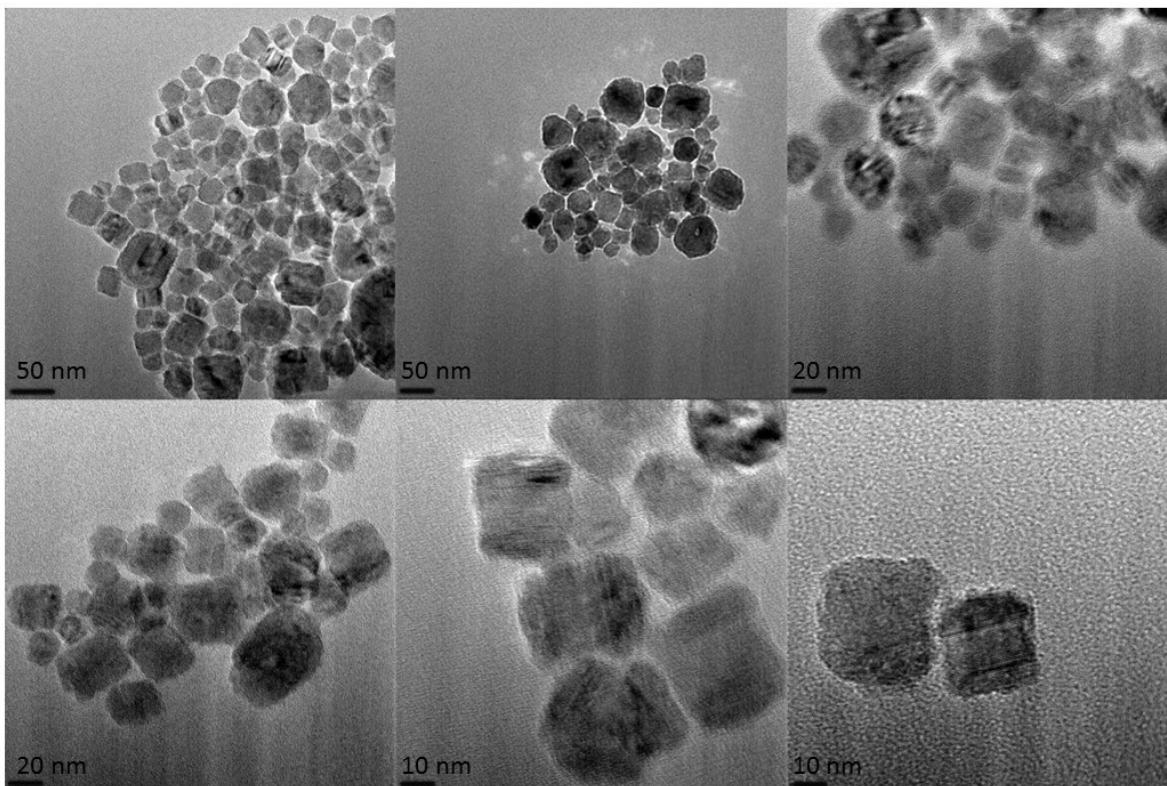


Figure 5.23: TEM images of annealed CuCr<sub>2</sub>S<sub>4</sub> NCs.

## 5.6 Magnetic Measurements

The magnetization ( $M$ ) of CuCr<sub>2</sub>S<sub>4</sub> nanocubes was measured as a function of the external magnetic field ( $H$ ) at 5 K and 300 K (Figure 3.24). As expected from the previous observations,<sup>1</sup> ferromagnetic behavior with a low coercivity of 350 Oe was observed at 5 K, whereas superparamagnetic (SP) behavior was observed at 300 K. Similar to the previous work, the loops do not exhibit magnetization saturation, and the highest observed magnetization value at 5 K was 32 emug<sup>-1</sup>, which was close to the previously reported values.<sup>1,16</sup>

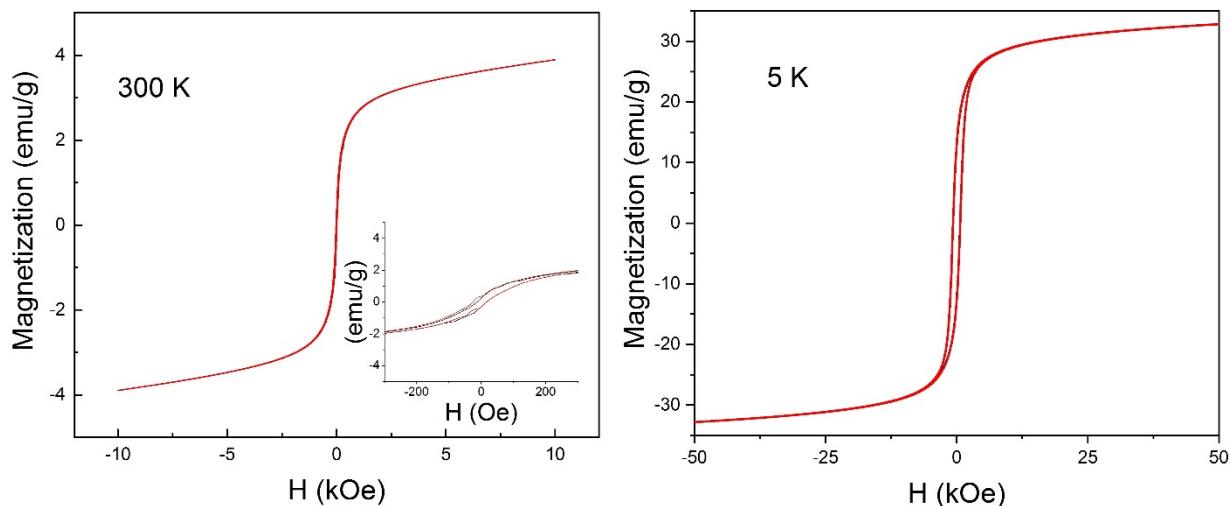


Figure 5.24: Magnetization ( $M$ ) as a function of field ( $H$ ) for nanocubes of  $\text{CuCr}_2\text{S}_4$  at 300 K and 5 K.

## 5.7 Conclusion

Because of the importance of magnetic chalcospinels, our primary purpose was doing a systematic work to find a facile and highly efficient method for the controlled preparation of phase pure chalcospinel NCs with uniform size and desirable morphologies. The first and the only reported colloidal  $\text{CuCr}_2\text{S}_4$  NCs made by using metal salts ( $\text{CuCl}_2$  and  $\text{CrCl}_3$ ) as the precursors along with 1-DDT as the source of sulfur. Since the thermal decomposition of metal-DDTC complexes as the single-molecular precursors was found as a successful one-pot method to synthesis of several binary and ternary metal sulfides, we decided to use Cu- and Cr-DDTC complexes as the single-source precursors to obtain Cr-based magnetic chalcospinels. Under the new reaction conditions, we could prepare magnetic NCs of  $\text{CuCr}_2\text{S}_4$  in both cubic and cluster forms, and we could avoid the formation of the unwanted nonmagnetic phase of  $\text{CuCrS}_2$  by controlling the reaction temperature.

Comparing the results of the current research with previously published work in which the inorganic metal salts were used as precursors, reveals that the sulfur-containing DDTC-metal complexes form a small amount of sulfur beside the main phase of  $\text{CuCr}_2\text{S}_4$ . According to the results presented in this chapter, the presence of sulfur in the structure of the organic ligand (DDTC) influences the formation of the unwanted sulfur phase.

The annealing process under the sulfur vapor atmosphere facilitates the evolution of the sulfur phase. Therefore, controlling the formation of pure-phase nanoparticles using metal-DDTC precursors is more challenging than using simple metal salts. However, this work is the first successful effort in order to prepare shape- and size-controlled NCs of  $\text{CuCr}_2\text{S}_4$  using single-source precursors. Several other sulfur-containing compounds such as metal complexes of thiobiurets, dithioburets, and thiourea derivatives, which have already used to design and preparation of binary metal sulfides, could potentially be the next choices to apply as the single-source precursors.

## 5. 8. References

1. Ramasamy, K.; Mazumdar, D.; Zhou, Z.; Wang, Y. H. A.; Gupta, A. Colloidal Synthesis of Magnetic  $\text{CuCr}_2\text{S}_4$  Nanocrystals and Nanoclusters. *J. A. Chem. Soc.* **2011**, *133*, 20716–20719.
2. Muroi, M.; Street, R.; McCormick, P. G. Magnetic Localization and Field-Dependent Variable-Range Hopping in Disordered  $\text{CuCr}_2\text{S}_4$ . *Phys. Rev. B* **2001**, *63*, 052412.
3. Luigjes, B.; Woudenberg, S. M. C.; Groot, R. D.; Meeldijk, J. D.; Galvis, H. M. T.; Jong, K. P. D.; Philipse, A. P.; Erne, B. H. Diverging Geometric and Magnetic Size Distributions of Iron Oxide Nanocrystals. *J. Phys. Chem. C* **2011**, *115*, 14598–14605.
4. Deng, M.; Shen, S.; Zhang, Y.; Xu, H.; Wang, Q. A Generalized Strategy for Controlled Synthesis of Ternary Metal Sulfide Nanocrystals. *New. J. Chem.* **2014**, *38*, 77–83.
5. Bonamico, M.; Dessy, G.; Mugnoli, A.; Vaciago, A.; Zambonelli, L. Structural Studies of Metal Dithiocarbamates. II. The Crystal and Molecular Dtructure of Copper Diethyldithiocarbamate. *Acta Crystallogr.* **1965**, *19*, 886–897.
6. Raston, C, L.; White; A, H. Crystal Structure of Tris(N,N-diethyldithiocarbamato) Chromium(III). *Aust. J. Chem.* **1977**, *30*, 2091–2094.
7. Linkoln, K, R. Preparation and Characterization of Chromium-Based Chalcospinels Materials, Georgetown University, Washington, Dc, **2011**.
8. D'Ascenzo. G.; Wendlandt, W, W. The Thermal Properties of Some Metal Complexes of Diethyldithiocarbamic Acid New Volatile Metal chelates. *J. Therm. Anal.* **1969**, *1*, 423–434.
9. Zhang, Y.; Dong, K.; Liu, Z.; Wang, H.; Ma, S.; Zhang, A.; Li, M.; Yu, L.; Li, Y. Sulfurized Hematite for Photo-Fenton Catalysis. *Progress in Natural Science: Materials International* **2017**, *27*, 443–451.
10. Murray, C. B.; Sun, S.; Doyle, H.; Betley. T. Monodisperse 3d Transition-Metal (Co, Ni, Fe) Nanoparticles and Their Assembly into Nanoparticle Superlattices. *New Aspects in Nanocrystal Research* **2001**, *26*, 985–991.
11. Castro, S. L.; Bailey, S. G.; Raffaele, R. P.; Banger K. K.; Hepp, A. F. Synthesis and Characterization of Colloidal  $\text{CuInS}_2$  Nanoparticles from a Molecular Single-Source Precursor. *J. Phys. Chem. B* **2004**, *108*, 12429–14435.
12. Zhuang, Z.; Peng, Q.; Wang, X.; Li, Y. Tetrahedral Colloidal Crystals of  $\text{Ag}_2\text{S}$  Nanocrystals. *Angew. Chem., Int. Ed.* **2007**, *46*, 8174–8177.

13. Mourdikoudis, S.; Liz-Marzán, S. M. Oleylamine in Nanoparticle Synthesis, *Chem. Mater.* **2013**, *25*, 1465–1476.
14. Wang, D.; Li, Y. Effective Octadecylamine System for Nanocrystal Synthesis. *Inorg. Chem.* **2011**, *50*, 5196–5202.
15. Ma, Y.; Zeng, J.; Li, W.; McKiernan, M.; Xe, Z.; Xia, Y. Seed-Mediated Synthesis of Truncated Gold Decahedrons with a AuCl/Oleylamine Complex as Precursor. *Adv. Mater.* **2010**, *22*, 1930–1934.
16. Ramasamy, K.; Sims, H.; Keshavarz, S.; Naghibolashrafi, N; Gupta, A. Nanocrystals of  $\text{CuCr}_2\text{S}_{4-x}\text{Se}_x$  chalcospinels with tunable magnetic properties. *J. Mater. Chem. C* **2016**, *4*, 3628–3639.

## CHAPTER 6

### CONCLUSION

#### 6.1 Summary

A general overview of binary and ternary metal chalcogenides and their nanocrystals has been provided. We have provided an overview of the wet-chemical colloidal methods as an essential approach to size and shape-controlled synthesis of nanocrystals. We have also discussed the importance of metal doping reactions as a pathway to create previously unavailable multielemental materials and the formation of a pure phase of novel compounds for high-performance applications. The role of different parameters on the phase and morphology of the nanomaterials obtained during the heat-up and hot-injection reactions have been studied too. A library of a series of colloidal binary and multinary metal chalcogenides, along with preparation conditions, has also been provided.

We discussed that among a large number of possible candidates of metal chalcogenides, chromium-based chalcospinels of  $\text{CuCr}_2\text{S}_4$ ,  $\text{CuCr}_2\text{Se}_4$ , and  $\text{CuCr}_2\text{Te}_4$  gained attention because they are the only ferromagnetic materials at room temperature and these properties make them unique.<sup>1-10</sup> Nanocrystals of  $\text{CuCr}_2\text{S}_4$  and  $\text{CuCr}_2\text{Se}_4$  have been synthesized via colloidal methods, and the mechanistic details of the formation of nanomaterials were discussed in this study.

We presented a heat-up synthesis of nanocrystals of  $p\text{-Cr}_x\text{Cu}_{1-x}\text{Se}_2$  ( $x = 0.1-0.5$ ). By increasing the reaction temperature, the  $\text{Cr}^{3+}$  ions occupy the octahedral positions of the pyrite structure and influenced the formation of the pyrite phase, which is not stable in bulk form. The predominant phase formed at the temperature range of 250-300 °C was pyrite, and  $\text{Cr}_x\text{Cu}_{1-x}\text{Se}_2$

pyrite phase was preserved regardless of the degree of doping. The magnetic measurements of the  $p\text{-Cr}_x\text{Cu}_{1-x}\text{Se}_2$  nanocrystals indicated that the occupation of the octahedral sites of the pyrite structure via  $\text{Cr}^{3+}$  ions led to tunneling magnetic properties and large enhancement of ferromagnetic moment in  $p\text{-Cr}_x\text{Cu}_{1-x}\text{Se}_2$ . The isolated  $p\text{-CuSe}_2$  NCs showed perfect cubic shape, whereas, the nanocrystals of the  $p\text{-Cr}_x\text{Cu}_{1-x}\text{Se}_2$  did undergo degradation during the doping of  $\text{Cr}^{3+}$  ions in the pyrite crystal structure as a function of reaction temperature.

This mechanism provided a pathway to phase transformation from  $\text{Cr}_{0.5}\text{Cu}_{0.5}\text{Se}_2$  NCs to ternary spinel  $\text{CuCr}_2\text{Se}_4$  NCs at above 300 °C. The reaction temperature plays a predominant role and influences the composition and structure of the products. Phase pure nanorods of  $\text{CuCr}_2\text{Se}_4$  formed at the temperature range of 330-360 °C.

The formation mechanism of the spinel phase during the heat-up process was studied. Nanocrystals of  $\text{Cr}_{0.5}\text{Cu}_{0.5}\text{Se}_2$  as the structural template result in the formation of  $\text{CuCr}_2\text{Se}_4$  NCs during the pyrite to spinel phase transformation. It appears that at 50% Cr-content, the pyrite phase is saturated, and then the spinel phase is formed at higher temperatures. The occupation of the octahedral sites of the pyrite structure with  $\text{Cr}^{3+}$  ions during the cationic substitution induced the direct structural transformation. This work is the first reported pyrite to spinel transformation.

In our next study, nanoparticles of  $\text{CuCr}_2\text{S}_4$  were prepared by employing single-source precursors of Cu- and Cr-diethyl dithiocarbamate (DDTC) complexes and the effect of different reaction parameters on the composition, phase purity, size, and shape of the resulting products has been studied. The results were compared to the previously reported work that has been done in our research group. Our results indicated that the controlling of the formation of phase-pure nanoparticles using metal-DDTC precursors is more challenging than using metal salts, which reported earlier, and the presence of sulfur in the structure of the organic ligand of DDTC

influenced the formation of sulfur phase as an impurity. However, this work is the first successful effort to prepare NCs of  $\text{CuCr}_2\text{S}_4$  employing single-source precursors.

## 6.2 Outlook

In general, the thermal-decomposition strategy is an easy, cost-effective, and highly efficient method, and both HU and HI methods could be employed to control the synthesis of binary and multinary metal chalcogenides with pure crystalline phase, uniform size, and desirable morphologies. However, the design and preparation of NCs with desirable morphologies, size, and compositions depend on many different factors, and there is still a long way to go to develop and introduce a generalized synthesis strategy. Paying close attention to the formation mechanism of NCs in solution shows smart ways to make new crystalline materials that are not stable in bulk form or even have never been formed before.

We have successfully prepared NCs of  $p\text{-Cr}_x\text{Cu}_{1-x}\text{Se}_2$  in solution and showed that the  $\text{Cr}^{3+}$  ions enhanced the ferromagnetic moment of the pyrite structure. Methods such as neutron diffraction could be useful in further exploring these newly found magnetic materials. Moreover, the discovered Cr-induced phase transformation in this study could open the doors to the future works on pyrite and spinel phases with regards to (i) the synthesis of metastable materials and (ii) the possible pyrite to spinel phase transformations. Binary and ternary metal chalcogenides such as  $M\text{Se}_2$  and  $M\text{Cr}_2\text{Se}_4$  ( $M = \text{Fe}, \text{Co}, \text{Zn}$ ) are excellent candidates to be considered as the next systems for Cr-induced pyrite to spinel phase transformation.

Lastly, we recommend that other ternary and multinary chalcospinel similar to the ones we covered in this scope of research to be considered for processing and characterization, especially magnetic chalcospinel such as  $\text{CuCr}_2\text{Te}_4$  and  $\text{CdCr}_2\text{S}_4$ .

## REFERENCES

1. Kocsis, V.; Bordács, S.; Varjas, D.; Penc, K.; Abouelsayed, A.; Kuntscher, A.; Ohgushi, K.; Tokura, Y.; Kézsmárki, I. Magnetoelasticity in  $\text{ACr}_2\text{O}_4$  Spinel Oxides. *Physical Review. B* **2013**, *87*, 064416.
2. Baltzer, P. K.; Lehmann, H. W.; Robbins, M. Insulating Ferromagnetic Spinels. *Phys. Rev. Lett.* **1965**, *15*, 493–495.
3. Ramesha, K.; Seshadri, R. Solvothermal Preparation of Ferromagnetic Sub-Micron Spinel  $\text{CuCr}_2\text{Se}_4$  Particles. *Solid State Sci.* **2004**, *6*, 841–845.
4. Kim, D.; Gedanken, A.; Tver'yanovich, Y. S.; Lee, D. W.; Kim, B. K. Synthesis and Characterization of Nanocrystalline  $\text{CuCr}_2\text{Se}_4$  particles. *Mater. Lett.* **2006**, *60*, 2807–2809.
5. Ramasamy, K.; Mazumdar, D.; Zhou, Z.; Wang, Y. H. A.; Gupta, A. Colloidal Synthesis of Magnetic  $\text{CuCr}_2\text{S}_4$  Nanocrystals and Nanoclusters. *J. A. Chem. Soc.* **2011**, *133*, 20716–20719.
6. Ramasamy, K.; Sims, H.; Keshavarz, S.; Naghibolashrafi, N; Gupta, A. Nanocrystals of  $\text{CuCr}_2\text{S}_{4-x}\text{Se}_x$  Chalcospinels with Tunable Magnetic Properties. *J. Mater. Chem. C*, **2016**, *4*, 3628–3639.
7. Ramasamy, K.; Mazumdar, D; Bennett R. D.; Gupta. A. Syntheses and Magnetic Properties of  $\text{Cr}_2\text{Te}_3$  and  $\text{CuCr}_2\text{Te}_4$  Nanocrystals. *Chem. Commun.* **2012**, *48*, 5656–5658.
8. Wang, Y. H. A.; Bao, N.; Shen, L.; Padhan, P.; Gupta, A. Size-Controlled Synthesis of Magnetic  $\text{CuCr}_2\text{Se}_4$  Nanocrystals. *J. Am. Chem. Soc.* **2007**, *129*, 12408–12409.
9. Pang, C.; Yang, R.; Singh, A.; Chen, H.; Bowman, M. K.; Bao, N.; Shen, L.; Gupta, A. Colloidal Synthesis and Magnetic Properties of Anisotropic-Shaped Spinel  $\text{CuCr}_2\text{Se}_4$  Nanocrystals. *RSC Adv.* **2017**, *7*, 31173–31179.
10. Lin, C. R.; Yeh, C. L.; Lu, S. Z.; Lyubutin, I. S.; Wang, S. C.; Suzdalev, I. P. Synthesis, Characterization and Magnetic Properties of Nearly Monodisperse  $\text{CuCr}_2\text{Se}_4$  Nanoparticles. *Nanotechnology* **2010**, *21*, 235603.